

Investigating molecules of astrochemical interest using rotational and infrared spectroscopy

Dissertation

zur Erlangung des Doktorgrades
der Mathematisch-Naturwissenschaftlichen Fakultät
der Christian-Albrechts-Universität zu Kiel

angefertigt am
Deutschen Elektronen-Synchrotron,
ein Forschungszentrum der Helmholtz-Gemeinschaft

Gayatri Batra

Hamburg, Dezember 2023

Gutachter der Dissertation:

Prof. Dr. Melanie Schnell

Prof. Dr. Gernot Friedrichs

Tag der mündlichen Prüfung: 25-01-2024

For my grandparents, my mother, my uncle, and my siblings, for their unwavering support and love. I am eternally grateful.

List of publications

1. B. E. Arenas, G. Batra, A. L. Steber, L. Bizzocchi, B. M. Giuliano, P. Caselli, B. J. Harris, B. H. Pate, A. Pietropolli Charmet, M. Schnell *Rotational spectroscopy of imidazole: Three vibrationally excited states and a molecular structure based on an extended frequency range*, Journal of Molecular Spectroscopy **378** 111452 (2021).
2. * G. Batra, P. Pinacho, A. L. Steber, V. M. Rivilla, J. M. Pintado, I. J. Serra, M. Schnell *The missing conformer: A comprehensive rotational spectroscopy study and astronomical search of two conformers of methyl cyanoacetate*, Frontiers in Astronomy and Space Sciences, **9**, 977488 (2022).
3. A. K. Lemmens, P. Ferrari, D. Loru, G. Batra, A. L. Steber, B. Redlich, M. Schnell, B. Martinez-Haya *Wetting of a Hydrophobic Surface: Far-IR Action Spectroscopy and Dynamics of Microhydrated Naphthalene*, Journal of Physical Chemistry Letters, **14**(48), 10794-10802 (2023).

*This manuscript is presented as Chapter 4 in this dissertation

Abstract

“The important thing is not to stop questioning. Curiosity has its own reason for existing.” -
Albert Einstein

The interstellar medium, comprising of matter and radiation in the space between stars, plays a crucial role in the formation of celestial bodies. It is mainly composed of regions of gas and dust known as interstellar clouds. The chemical diversity of molecules within the interstellar medium, particularly complex organic molecules, has intrigued astronomers and astrochemists for decades. To date, over 300 molecular species have been detected in space, ranging from simple diatomic compounds to complex organic structures like Buckminster fullerene. Most of these chemical species have been detected with the help of radio astronomy, since its advent in the 1960s. The objective of this thesis is to investigate molecules of astronomical interest, specifically complex organic molecules, with a multi-spectroscopic approach, to better determine the chemical inventory of interstellar molecules. This in turn will also contribute towards a more comprehensive understanding of their formation mechanisms in the interstellar medium.

The primary emphasis of this thesis is on rotational spectroscopy, providing detailed line lists and rotational parameters for studied molecules. The rotational spectra have been obtained over a broad frequency range (2-110 GHz), which aligns well with radio telescopes such as Atacama Large Millimeter/submillimeter Array and the Effelsberg radio telescope. This makes the laboratory data directly applicable to radio astronomy. However, rotational spectroscopy is limited to studying molecules with a permanent electric dipole moment, while for infrared spectroscopy (IR), a change in electric dipole moment is required for a vibrational mode to be IR-active. For this, infrared spectroscopic techniques, including infrared reflection absorption spectroscopy and IR-UV ion dip spectroscopy, were employed. With the launch of the James Webb Space Telescope, vibrational spectroscopy data will be crucial for detecting molecules, especially molecules with small or no dipole moments.

The complex organic molecules investigated in this thesis are methyl cyanoacetate, 2,4,6-cycloheptatriene-1-carbonitrile, and organosilicon molecules like phenylsilane and diphenylsilane. Rotational spectroscopy and vibrational spectroscopy, both coupled with electrical discharge sources, were employed to characterize these molecules and study their relevance to astrochemistry. The work strongly emphasizes the importance of laboratory studies of astrochemically relevant molecules in understanding the chemical makeup of the interstellar medium. These laboratory studies lay the foundation for the potential astronomical detection of the molecules investigated in this thesis in various regions of space.

Zusammenfassung

“Wichtig ist, dass man nicht
aufhört zu hinterfragen. Die
Neugierde hat ihre eigene
Daseinsberechtigung.”
-Albert Einstein

Das interstellare Medium, bestehend aus Materie und Strahlung im Raum zwischen Sternen, spielt eine entscheidende Rolle bei der Entstehung von Himmelskörpern. Es besteht hauptsächlich aus Gas- und Staubregionen, die als „interstellare Wolken“ bezeichnet werden. Die chemische Vielfalt der Molekülverbindungen im interstellaren Medium, insbesondere komplexer organischer Moleküle, wird seit Jahrzehnten intensiv im Bereich der Astronomie sowie Astrochemie erforscht. Bis heute wurden über 300 Moleküle im Weltraum entdeckt, die von einfachen zweiatomigen Verbindungen bis hin zu komplexen organischen Strukturen wie etwa den Buckminsterfullerenen reichen. Die meisten dieser chemischen Verbindungen wurden seit den 1960er Jahren mit Hilfe von Radioteleskopen entdeckt. Das Ziel dieser Arbeit ist die Untersuchung von Molekülen von astronomischem Interesse, insbesondere komplexen organischen Molekülen, mittels eines multispektroskopischen Ansatzes, um die chemischen Zusammensetzungen interstellarer Moleküle besser zu bestimmen. Die umfassende Erforschung soll auch zu einem besseren Verständnis ihrer Entstehung im interstellaren Medium beitragen. Der Schwerpunkt dieser Arbeit liegt auf der Methode der Rotationsspektroskopie, welche detaillierte Linienlisten und Rotationsparameter der untersuchten Moleküle liefert. Die Rotationsspektren wurden über einen breiten Frequenzbereich von 2-110 GHz gemessen, welcher sich mit jenen von Radioteleskopen wie dem Atacama Large Millimeter/submillimeter Array und dem Effelsberger Radioteleskop deckt. Somit sind die hier präsentierten Labordaten direkt mit Beobachtungen von Radioteleskopen vergleichbar. Während Rotationsspektroskopie auf die Untersuchung von Molekülen mit permanenten elektrischen Dipolmomenten begrenzt ist, können Moleküle mit Schwingungsanregungen, welche mit einer Änderung des elektrischen Dipolmoments einhergehen, mithilfe

von Infrarotspektroskopie analysiert werden. Aus diesem Grund wurden zusätzlich Infrarot-Reflexions-Absorptions-Spektroskopie und IR-UV-Ion Dip-Spektroskopie eingesetzt. Nicht zuletzt seit dem Start des James-Webb-Space-Teleskops sind derartige vibrationsspektroskopische Datensätze entscheidend für den Nachweis von Molekülen im All, insbesondere Molekülen ohne oder mit kleinem permanenten elektrischen Dipolmoment.

Die in der vorliegenden Arbeit untersuchten Moleküle sind Methylcyanoacetat, 2,4,6-Cycloheptatrien-1-carbonitril und siliziumorganische Moleküle wie Phenylsilan und Diphenylsilan. Rotationsspektroskopie und Schwingungsspektroskopie, beide gekoppelt mit elektrischen Entladungsquellen, wurden zur Charakterisierung eingesetzt. Die hier präsentierte Arbeit unterstreicht nachdrücklich die Bedeutung von Laboruntersuchungen astrochemisch relevanter Moleküle für das Verständnis des chemischen Aufbaus des interstellaren Mediums. Die vorliegenden Laborstudien bilden die Grundlage für den potenziellen astronomischen Nachweis der in dieser Arbeit untersuchten Moleküle in verschiedenen Regionen des Weltraums.

Contents

1	Introduction	1
1.1	Astrochemistry and complex organic molecules	1
1.2	Thesis outline	7
2	Theoretical Background	9
2.1	Rotational spectroscopy	9
2.1.1	Moments of inertia and types of rotors	10
2.1.2	The rigid-rotor rotational Hamiltonian	11
2.1.3	The semi-rigid rotor Hamiltonian	15
2.1.4	Large amplitude motions	15
2.1.5	Nuclear electric quadrupole coupling	17
2.1.6	Rotational and vibrational partition function	19
2.1.7	Spectral analysis and quantum chemical calculations	21
2.1.8	Structure determination	22
2.2	Infrared spectroscopy	24
2.2.1	Infrared reflection-absorption spectroscopy (IRRAS)	26
2.2.2	IR-UV ion dip spectroscopy	27
3	Experimental Details	29
3.1	The COMPACT spectrometer	29
3.2	The K-band spectrometer	30
3.3	The W-band spectrometer	32
3.4	Electrical discharge setup	34
3.5	Approaches to sample introduction: Room-temperature measurement and supersonic expansion	34
3.5.1	Room-temperature measurements	34
3.5.2	Supersonic expansion	36
3.6	Molecular beam setup at FELIX	39
3.6.1	Probing the structures of silicon-containing discharge products with IR-UV ion dip spectroscopy	39
3.7	Ultra-high vacuum-reflection absorption infrared spectroscopy	41

4	The missing conformer: A comprehensive rotational spectroscopy study and astronomical search of two conformers of methyl cyanoacetate	43
4.1	Introduction	43
4.2	Theoretical work	46
4.3	Experimental details and fitting procedure	48
4.4	Results and discussion	50
4.4.1	Rotational partition function and transition intensities for MCA_1 and MCA_2	55
4.4.2	Interstellar search towards the G+0.693-0.027 molecular cloud	56
4.4.3	Structure determination	58
4.5	Conclusions	60
5	Rotational spectroscopy of 2,4,6-cycloheptatriene-1-carbonitrile: Facilitating the search for complex cyclic molecules in the ISM	63
5.1	Introduction	63
5.2	Experimental details	65
5.3	Theoretical details	67
5.4	Spectroscopic analysis	67
5.5	Results and discussion	70
5.5.1	Vibronic ground state	70
5.5.2	Structure determination	74
5.5.3	Vibrationally excited states	77
5.5.4	Rotational and vibrational partition functions of CHT-1-CN-1	78
5.6	Conclusions	80
6	Insights into the gas phase structure and rotational dynamics of diphenylsilane: A broadband rotational spectroscopy study	83
6.1	Introduction	83
6.2	Experimental and theoretical details	85
6.3	Results and discussions	86
6.4	Summary	92
7	Infrared reflection absorption spectroscopy of water ice and naphthalene	95
7.1	Introduction	95
7.2	Experimental details	97
7.3	Results and discussion	99
7.4	Summary	104

8	Silicon chemistry under the harsh conditions of an electrical discharge	107
8.1	Introduction	107
8.2	Experimental and computational details	109
8.2.1	Electrical discharge coupled with IR-UV ion dip spectroscopy	109
8.2.2	Electrical discharge coupled with rotational spectroscopy . . .	111
8.3	Results and discussion	112
8.3.1	Electrical discharge of phenylsilane probed by mass-resolved IR-UV ion dip spectroscopy	113
8.3.2	Summary	123
8.3.3	Bottom-up growth of silicon-containing aromatic molecules under the conditions of an electrical discharge	124
8.3.4	Facilitating astronomical searches	131
8.3.5	Summary	134
8.4	Appendix for FELIX data	136
8.4.1	IR spectra of all the masses observed with the two-color REMPI (266+193 nm).	136
8.4.2	IR spectra of all the masses observed with the two-color REMPI (269+193 nm).	141
8.4.3	Supplementary figures	144
9	Summary and outlook	151
10	Appendices	181
10.1	The missing conformer: A comprehensive rotational spectroscopy study and astronomical search of two conformers of methyl cyanoacetate	181
10.2	Rotational spectroscopy of 2,4,6-cycloheptatriene-1-carbonitrile: Facilitating the search for complex cyclic molecules in the ISM	188
10.3	Insights into the gas phase structure and rotational dynamics of diphenylsilane: A broadband rotational spectroscopy study	191
10.4	Infrared reflection absorption spectroscopy of water ice and naphthalene	193

Chapter 1

Introduction

1.1 Astrochemistry and complex organic molecules

The interstellar medium (ISM) is defined as the matter and radiation that exist in the space between stars. It is mainly composed of regions of gas and dust known as interstellar clouds, ranging in size from a few to 100s of light years. These interstellar clouds are the birthplaces of planets and stars. The material present in these clouds greatly affect the compositions of systems that are formed there [1]. This material serves as a tool to explore the physical aspects of the ISM, such as temperatures and densities in the regions of investigation. The chemical richness and complexity of molecules in the ISM are thus intriguing topics for astronomers, astrophysicists, and astrochemists alike.

With the advent of radio astronomy in the 1960s, an important chapter in astronomy began with the first ever discovery of a molecular species, the OH radical in 1963 [2]. Five years later, emission lines were observed at 1.26 and 1.35 cm which led to the discovery of the first polyatomic molecules, ammonia [3] and water [4] respectively, paving the way for future searches of larger and more complex species. Fast forward to 2023, and the tally of molecules identified in space has surpassed 300, unveiling its rich chemical complexity ranging from the simplest diatomic, H₂ [5], to sizable molecules like buckminsterfullerene (C₆₀) [6]. Radio astronomy has played a crucial role in detecting the majority of these molecules. The updated catalogs can be accessed on the Cologne Database for Molecular Spectroscopy (CDMS)* and Astrochymist† websites. The last decade has seen an unprecedented exponential growth in detection rates. This increase can be attributed to two factors; on the one hand, to the technical advances in the field of radio astronomy and facilities such as

*<https://cdms.astro.uni-koeln.de>

†<https://www.astrochymist.org/>

the Atacama Large Millimeter/submillimeter Array (ALMA)[‡], the Green Bank Telescope (GBT)[§] or the Yebes 40 m telescopes[¶], *etc.* [7]; and on the other hand, to the increase in laboratory-based rotational spectroscopy studies of potential molecules of astrochemical interest, which provide detailed spectroscopic parameters required for their search in the ISM. This factor is attributed to the development of chirped-pulse Fourier transform microwave (CP-FTMW) spectrometers [8], which reduced the measurement times for broadband, high-resolution microwave spectra by several orders of magnitude than what was previously possible. A significant portion of these detected molecules are organic and considered “large”, by astronomical standards, and come under the broad sphere of Complex Organic Molecules (COMs). These COMs are usually defined as carbon-bearing molecules with six or more atoms (may contain oxygen, nitrogen, and/or hydrogen). They were first detected in and are typically associated with warm, dense concentrations of gas and dust within the interstellar medium and in various protoplanetary environments [9–14]. They range from simple organic molecules like alcohols and acids to linear unsaturated cyanopolynes HC₁₁N [15], as well as detected PAHs [16], and fullerenes in space [6].

In addition to the most commonly observed elements like hydrogen, carbon, nitrogen, and oxygen, silicon is also abundant in space, being only one order of magnitude less than C, N, and O [17]. A significant fraction of the elemental silicon is believed to be locked up in relatively volatile dust components [18], which provide the surface for the ice grain chemistry in the cold regions of the ISM. The presence of silicon in the interstellar environments was first detected in Sagittarius B2 more than 50 years ago in the form of silicon monoxide (SiO) [19]. Since then, more than 15 silicon-containing molecules have been detected, ranging from diatomic silicon monoxide (SiO) to COMs containing silicon in it, such as methylsilane, CH₃SiH₃ and linear silicon carbide chains, like (SiC₄) [20]. The in-depth study of COMs using a combination of observational facilities and laboratory-based spectroscopic techniques can help unravel the physical conditions and the chemistry taking place in the regions of interest. In addition, COMs are often associated with the building blocks of life due to their organic nature and provide insights into prebiotic chemistry [21].

There has been, and continues to be, extensive research performed in trying to elucidate the formation mechanisms of observed COMs. The widely accepted mechanisms are explored in more depth below. The formation mechanisms of COMs in different interstellar environments involve a combination of various processes, mainly in the gas phase, on the surface of bare dust particles and in the ice mantles that cover the bare grains in cold dense interstellar clouds [22].

[‡]<https://www.eso.org/public/teles-instr/alma/>

[§]<https://greenbankobservatory.org/science/telescopes/gbt/>

[¶]<https://rt40m.oan.es/>

The observation of significant abundance of COMs in assorted interstellar sources can be explained with gas phase reactions involving ion-neutral and neutral-neutral reactions [23]. For example: one of the most fundamental ions for interstellar chemistry is H_3^+ which acts as a universal proton donor for the formation of new molecules. Another commonly acknowledged approach for the synthesis of COMs is the gas-grain model [24]. This model encompasses the chemical processes occurring on exposed silicate and carbonaceous dust surfaces, referred to as dust chemistry, prior to the development of ice mantles. Additionally, it explores the chemical evolution during and after the formation of ice mantles around the grains, known as ice chemistry, occurring both on the surfaces and within the ice. A pictorial representation of ice chemistry in brief is shown in Figure 1.1.

On the surfaces of dust grains, atoms and molecules can accrete and react, leading

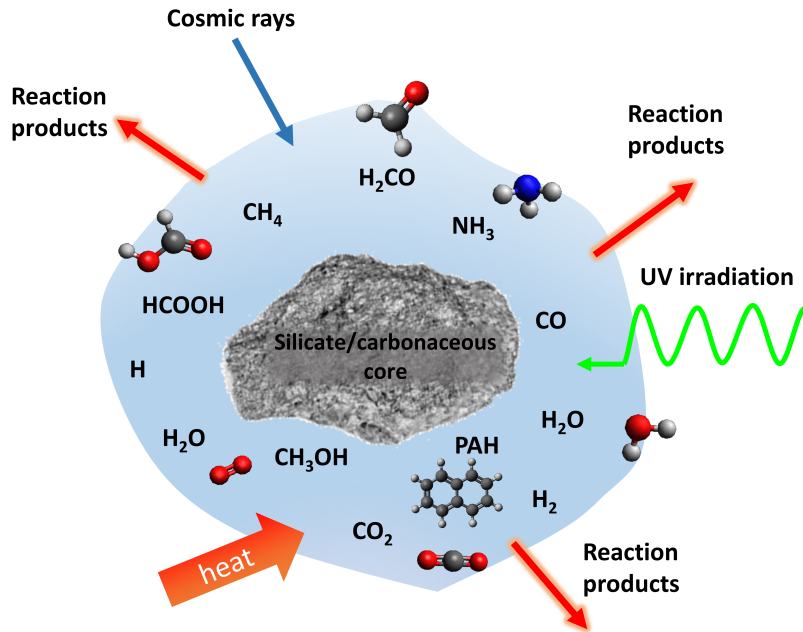


Figure 1.1: Pictorial representation of the surface reactions taking place in and on the surface of ices. The ice depicted here is grown on the silicate or carbonaceous dust grain. It's important to note that the ice chemistry extends beyond the presented model. This model serves as a representation of a few selected reaction mechanisms transpiring within or on interstellar ices.

to the formation of more complex molecules. These surface reactions are particularly important in the dense regions of molecular clouds.

Once sufficient material starts to accrete on grains, and chemistry occurs, a mantle of ice gradually builds up in cold dense regions. It is normally assumed that the reactions occur via the Langmuir–Hinshelwood mechanism [22], although this might be a great oversimplification given the complexity of the ice surface as well as the bulk material underneath the surface.

Another prevailing theory explains the formation of COMs in hot cores by radical-radical reactions on and in the ice mantles as well as cosmic ray bombardment of these ice mantles, in addition to bombardment of UV photons to produce reactive radicals in and on ice mantles [25].

Our existing knowledge of the chemical make-up of the ISM is obtained by studying the molecules present in it. This is done primarily by spectroscopy. For instance, diffuse clouds can be studied in the visible and ultra-violet regions of the spectrum by line absorption of light from background stars, while dense clouds must be studied at longer wavelengths [26]. The dominant approach to investigate gas phase species in dense clouds is via rotational spectroscopy in the microwave-to-submillimeter range and with vibrational spectroscopy. With the former technique, the measurements can be undertaken from the ground based telescopes like ALMA, GBT, the Effelsberg 100-m radio telescope[‡], *etc.* but the latter, i.e. vibrational spectroscopy, is not well suited for ground based observations because infrared radiation is partially blocked by the terrestrial atmosphere, and satellite or airborne spectrometers are often needed, like Infrared Space Observatory (ISO, 1995 - 1999)^{**}, Stratospheric Observatory for Infrared Astronomy (SOFIA, 2014 - 2022)^{††}, and the very recently commissioned James Webb Space Telescope (JWST, 2022 - expected up to 10 years)^{‡‡}. Figure 1.2 provides a brief overview of the different techniques that can be used to study the vastness of space and how the atmosphere plays a role in it.

The observational facilities that are relevant for the work produced in this thesis involve radio astronomy and vibrational astronomy. Radio astronomy relies on the collection of microwave emission from the astronomical object under study. This emission contains the “molecular fingerprints”, which are the rotational transitions. Indeed, the rotational features are extremely sensitive to the molecular species, and even allows for discriminating among different conformers, vibrational states, and the isotopic species of the same molecule. This is the reason behind the overwhelming majority of gas phase chemical species has been identified via their rotational signatures [7]. Radio telescopes provide millimeter-/submillimeter-wave line surveys, which contain the rotational features of all molecules present in the interstellar cloud

[‡]<https://www.mpifr-bonn.mpg.de/effelsberg>

^{**}<https://science.nasa.gov/mission/infrared-space-observatory/>

^{††}<https://science.nasa.gov/mission/sofia>

^{‡‡}<https://webb.nasa.gov/>

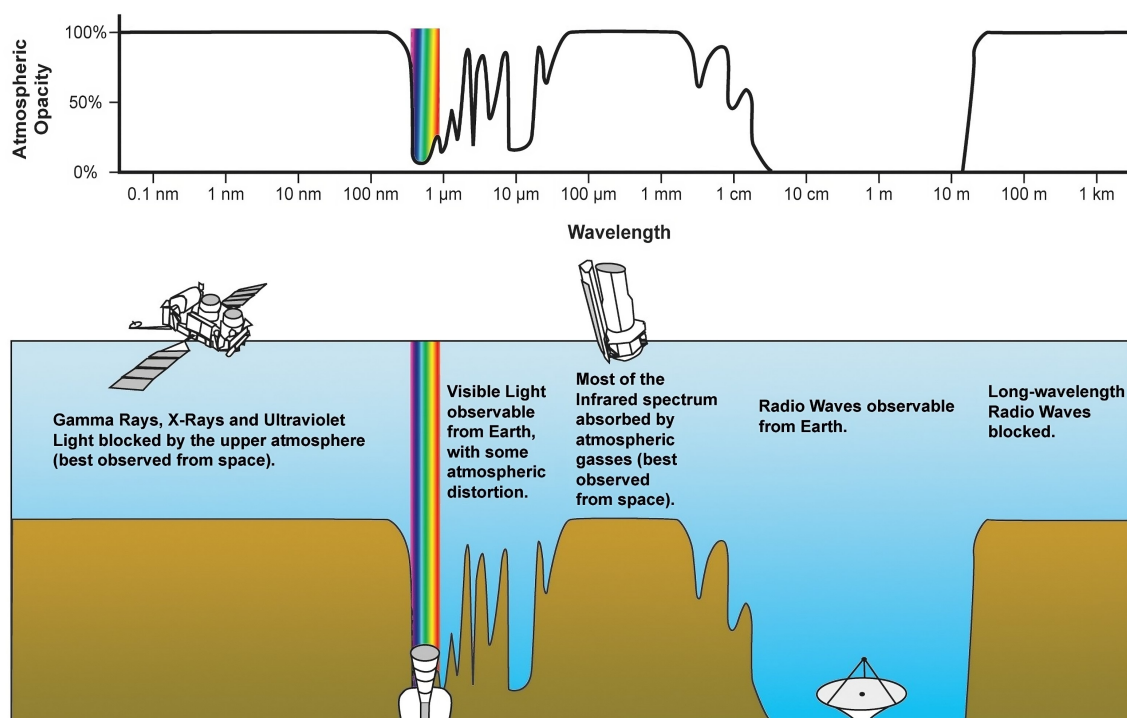


Figure 1.2: Atmospheric windows: types of electromagnetic waves that pass through the Earth’s atmosphere. Note that the atmosphere is “transparent” to visible light and radio waves, but opaque to infrared radiation. Source: NASA public domain.

under investigation. As a consequence, their assignment requires accurate knowledge of the rotational transitions of all molecules that are expected to be present. This knowledge is obtained from rotational spectroscopy laboratory experiments. However, the observations with radio astronomy are limited to molecules with a permanent electric dipole moment. But for vibrational spectroscopy, this is not a limiting factor. Especially now with the launch of JWST, operating between $100\text{--}3500\text{ cm}^{-1}$, the molecules with small or no dipole moments can be also be observed via their vibrational features. In order for a molecule to be vibrationally active, its electric dipole moment must change during the vibrations. With the array of instruments on JWST, notably the Mid-Infrared Instrument (MIRI), JWST facilitates comprehensive studies of ice characteristics across diverse astronomical environments [27].

The unprecedented sensitivity of observational facilities like ALMA, GBT, JWST, *etc.* are producing data that can only be fully characterized with the help of high-resolution laboratory studies. This highlights the pressing need for laboratory studies of molecules of astrochemical interests.

The survey of the chemical inventory within the ISM [7] reveals a diverse range

of compounds, consisting of familiar terrestrial complex organic molecules (COMs) and exotic variants. Surprisingly, the list does not end here. In addition to the observation of these molecules in their ground state, the observational data sets also contain emissions from their isotopologues and vibrationally excited states [28]. Indeed, as noted in Ref. [29], these are believed to be the source of many unidentified lines, which can be as much as 70% in very deep observations at ALMA Bands 3 and 6, covering between 84-116 GHz and 211-275 GHz, respectively [30].

The determination of the experimental rotational constants and the line lists of isotopologues and vibrationally excited states (especially for the molecules already detected in the ISM) facilitate their searches in the ISM. For instance, *iso*-propyl cyanide is the first branched molecule ever detected in the ISM [31]. In addition to its microwave study, Arenas *et al.* [32] studied its vibrationally excited states in the millimeter range which were later detected in the Sgr B2(N2b) region [33]. Moreover, the lines generated by isotopologues and vibrationally excited states of already detected molecules are also be considered as weeds [34] or hindrance, to identifying new COMs in the observational data sets. Therefore, their elimination from the astronomical data sets is a crucial step in simplifying complex and confusion limited spectra. In addition, vibrationally excited states also act as a temperature probes for the regions they are detected in, and can thus aid the characterization of warm regions in the ISM, for example, hot cores [35].

Similarly from an astrochemical perspective, the detection of isotopologues of already detected molecules could be important for elucidating the formation pathway of the parent molecule. This is further described in detail by Furey *et al.* [36] where the authors demonstrated the use of isotopic species to deduce the likely formation routes of interstellar molecules. In addition to this, isotopologues are also important for structural determination of molecules in the gas phase. One can use the rotational constants of the singly-substituted isotopologues to construct the gas phase structure of the molecule using the famous Kratichman method (r_s) and least-squares fitting method (r_0). The details on these methods can be found in Section 2.1.8.

In addition to the “terrestrial-type” molecules, there is a whole new class of molecules that are exotic in nature. Examples include linear carbon chains like polyynes (up to $C_{10}H^-$) [37] and cyanopolyynes (upto $HC_{11}N$) [15], silicon-carbide molecules such as *c*- SiC_3 [38], and highly reactive species like *o*-benzyne [39]. In order to generate exotic species in the laboratory for the purpose of understanding their formation mechanisms in space (for the ones that are already detected) or perhaps for conducting a search for new species in the ISM, high energetic conditions are required. A highly effective method for synthesizing these species *in situ* involves utilizing electrical discharge sources coupled with spectroscopic techniques such as high-resolution rotational spectroscopy and IR-UV ion dip spectroscopy. The discharge

set-up has the capability to generate new molecular species, including transient molecules, facilitating their characterization in the laboratory. This approach allows for the exploration of novel molecular classes in the ISM, including doubly functionalized molecules and open-shell molecules, which are relatively underrepresented in the ISM’s chemical inventory. Numerous studies have focused on the application of electrical discharge sources to produce molecules of astronomical interest [40–43]. Beyond generating these molecules, it also offers insights into potential pathways and mechanisms for their formation under the conditions of electrical discharge. The electrical discharge setup used in the present work is described in Section 3.4. This thesis delivers the necessary rotational constants for the COMs in their ground state and its isotopologues. The COMs that are investigated in this thesis include methyl cyanoacetate (4), 2,4,6-cycloheptatriene-1-carbonitrile (5), and organosilicon molecules like, phenylsilane (8.3.4) and diphenylsilane (8). One can also determine centrifugal distortion constants from the measurements done in the high frequency region (see Section 3.3), which are needed for predicting accurate rest frequencies. In another project, (Chapter 8) we performed IR-UV ion dip spectroscopy of various silicon-containing molecules in the range of 550-3200 cm^{-1} which overlaps with the IR range covered by JWST.

1.2 Thesis outline

Herein, we focus on studying molecules of astronomical interest with a multi-spectroscopic approach with the aim of understanding and exploring the chemical inventory in the ISM. This includes the broadband rotational spectroscopy studies of COMs containing nitrogen and oxygen, and organosilicon molecules like phenylsilane and diphenylsilane. Infrared reflection-absorption (IRRAS) spectroscopy of water ice encapsulating naphthalene, and IR-UV ion dip spectroscopy of the electrical discharge products of phenylsilane are also described.

In Chapter 2, the theoretical background to rotational spectroscopy along with its applications to astrochemistry and molecular structure determination is explained, as well as the basics of vibrational spectroscopy and its application to the IRRAS technique. Chapter 3 details the different spectroscopic techniques used in the scope of this thesis and the different methods of sample introduction- supersonic expansion and room-temperature flow-cell set-up. It also includes the implementation of an electrical discharge source to the rotational spectrometers and the molecular beam set-up at FELIX, Nijmegen, the Netherlands.

Chapter 4 focuses on the rotational spectroscopy of methyl cyanoacetate, which is a cyano derivative of an already detected molecule, methyl acetate. The rotational spectra of methyl cyanoacetate was recorded across the 2-110 GHz frequency range, and deals with methyl internal rotation and nuclear quadrupole coupling due to the

presence of ^{14}N . The molecule was also searched for in the G+0.693-0.027 molecular cloud located in the galactic center. Chapter 5 concentrates on a seven-membered ring with a cyano group attached to it, 2,4,6-cycloheptatriene-1-carbonitrile. This molecule is next in succession in size after the detection of benzonitrile in TMC-1. The assignment included the rotational spectra of vibrational ground state, six low-lying vibrationally excited states, and heavy-atom rare isotopologues in natural abundance. Chapter 6 discusses the rotational spectroscopy study of diphenylsilane in 2-8 GHz. The study includes the gas phase structure determination of the diphenylsilane and a comparison of the tunnelling barrier height with respect to its oxygen analogue, diphenylether. The comparison was also extended to the Si-C bond lengths across different molecules containing Si-C bonds, and the factors responsible for the differences observed.

Chapter 7 investigates the interplay between naphthalene and water ice under ultra-high vacuum conditions using IRRAS. The vibrational dynamics of water ice and naphthalene were compared when grown on different substrates. This study aims to develop a better understanding on the ice-grain chemistry taking place in the ISM. Chapter 8 details the electrical discharge products of phenylsilane probed with mass-resolved IR-UV ion dip spectroscopy. It focuses on the formation of silicon substituted aromatic and cyclic hydrocarbons. The vibrational spectra were recorded in the $550\text{-}3200\text{ cm}^{-1}$ range, which overlaps with the frequency region covered by JWST. The second part of this chapter discusses the complimentary nature of microwave spectroscopy and IR-UV ion dip spectroscopy by highlighting the formation of phenylsilane from benzene and silane discharge with microwave spectroscopy and the formation of diphenylsilane from the electrical discharge of phenylsilane probed with IR-UV ion dip spectroscopy. The chapter considers the chemistry occurring in the discharge plasma and explores the astrochemical relevance of such studies.

Chapter 2

Theoretical Background

The International Union of Pure and Applied Chemistry (IUPAC) defines spectroscopy as the study of physical systems by the electromagnetic radiation with which they interact or that they produce. It is the interaction between the electromagnetic radiation and the quantized energy levels of the matter at the microscopic scale.

2.1 Rotational spectroscopy

This section deals with rotational spectroscopy which uses radiation lying in the centimeter-wave (1-30 GHz), in the millimeter-wave (30-300 GHz), and in the sub millimeter-wave (>300 GHz) regions to interact with the rotational energy levels of a molecular system. The description of the rotational spectrum begins by obtaining the quantized energies of the rotational levels. For a molecular system, the quantized energy levels can be calculated with the time-independent Schrödinger equation,

$$\hat{H}\psi = E\psi \quad (2.1)$$

where ψ is the eigenfunction of the Hamiltonian \hat{H} and E is its corresponding eigenvalue.

Considering the Born-Oppenheimer approximation, the electronic and nuclear motion can be separated as they occur at different timescales [44]. Hence the total Hamiltonian \hat{H} can be written as a sum of the translational, rotational, vibrational, and electronic components, all of which can be treated independently within the Born-Oppenheimer approximation.

$$\hat{H}_{tot} = \hat{H}_{trans} + \hat{H}_{rot} + \hat{H}_{vib} + \hat{H}_{elec} \quad (2.2)$$

and the corresponding energy can be written as:

$$E_{tot} = E_{trans} + E_{rot} + E_{vib} + E_{elec} \quad (2.3)$$

In this section, the rotational energy of the system in the electronic and vibrational ground states is evaluated using rotational spectroscopy. The time-independent Schrödinger equation in focus is:

$$\hat{H}_{rot}\psi_{rot} = E_{rot}\psi_{rot} \quad (2.4)$$

where ψ_{rot} is the rotational eigenfunction and E_{rot} is the corresponding eigenvalue.

2.1.1 Moments of inertia and types of rotors

For the purpose of studying the rotational spectra of molecules, it is essential to classify them according to their principal moments of inertia. The moment of inertia (I) for any molecule about any axis through the center of mass is given by

$$I = \sum_{i=0} m_i r_i^2 \quad (2.5)$$

where m_i and r_i are the distance of atom i from the axis. For a system containing N atoms with mass m_i located at x_i, y_i, z_i coordinates in a cartesian axis system, the inertia tensor I can be written as,

$$I = \sum_{i=0}^N m_i \begin{pmatrix} y_i^2 + z_i^2 & -x_i y_i & -x_i z_i \\ -y_i x_i & x_i^2 + z_i^2 & -y_i z_i \\ -z_i x_i & -z_i y_i & x_i^2 + y_i^2 \end{pmatrix} r_i^2 = m_i \begin{pmatrix} I_{xx} & I_{xy} & I_{xz} \\ I_{yx} & I_{yy} & I_{yz} \\ I_{zx} & I_{zy} & I_{zz} \end{pmatrix} r_i^2 \quad (2.6)$$

In the inertia matrix on the right hand side, the diagonal components are the moments of inertia and the non-diagonal elements are the products of inertia. For a molecule to be in the principal axis system, given by the principal moments of inertia, the three axes (a, b , and c) pass through the centre of mass of the molecule. The axes are labelled in a way that the moment of inertia has its maximum value about the c axis and its minimum value about the a axis. Three axes (a, b , and c) are orthogonal to each other and the corresponding moments of inertia (I_a, I_b , and I_c) are the principal moments of inertia, according to the convention $I_c > I_b > I_a$. Based on the symmetry, the molecules can be classified into four different categories:

- Linear tops ($I_a = 0, I_b = I_c$), e.g., carbon dioxide (CO_2), carbonyl sulfide (OCS)
- Spherical tops ($I_a = I_b = I_c$), e.g., methane (CH_4), carbon tetrachloride (CCl_4)
- Symmetric top molecules

- Oblate symmetric tops ($I_a = I_b < I_c$) e.g. ammonia (NH_3), benzene (C_6H_6)
- Prolate symmetric tops ($I_a < I_b = I_c$) e.g. propyne (CH_3CCH), chloroform (CH_3Cl)
- Asymmetric tops ($I_a < I_b < I_c$): This is the largest category of molecules. All the molecules studied in this thesis with the help of rotational spectroscopy belong to this category.

Table 2.1: The six representations for the adjustment of the (x, y, z) coordinate system into the (a, b, c) principal axis system.

	I^r	I^l	II^r	II^l	III^r	III^l
x	b	c	c	a	a	b
y	c	b	a	c	b	a
z	a	a	b	b	c	c

There are six different ways that the Cartesian coordinates can be transformed into the principal axis system a , b , and c , as tabulated in Table 2.1. For example, in Figure 2.1, the molecule 2,4,6-cycloheptatriene-1-carbonitrile is represented in (a, b, c) principal axis system in I^r representation, where the three orthogonal axis a , b , and c passes through the centre of mass.

2.1.2 The rigid-rotor rotational Hamiltonian

The rotational energy of a molecule E_{rot} can be calculated using the rigid rotor approximation, where the rotational energy of a rigid body is given by Ref. [45]:

$$E_{rot} = \frac{1}{2} \omega \cdot I \cdot \omega, \quad (2.7)$$

where I is the inertia tensor and ω is the angular velocity.

Based on the rigid-rotor model, the energy expression for the different types of rotors discussed above, can be described as the following:

- For linear molecules:
 $I_b = I_c$; $I_a = 0$ (for a diatomic molecule), the energy levels are given by the formula

$$E_J(\text{cm}^{-1}) = BJ(J+1) \quad (2.8)$$

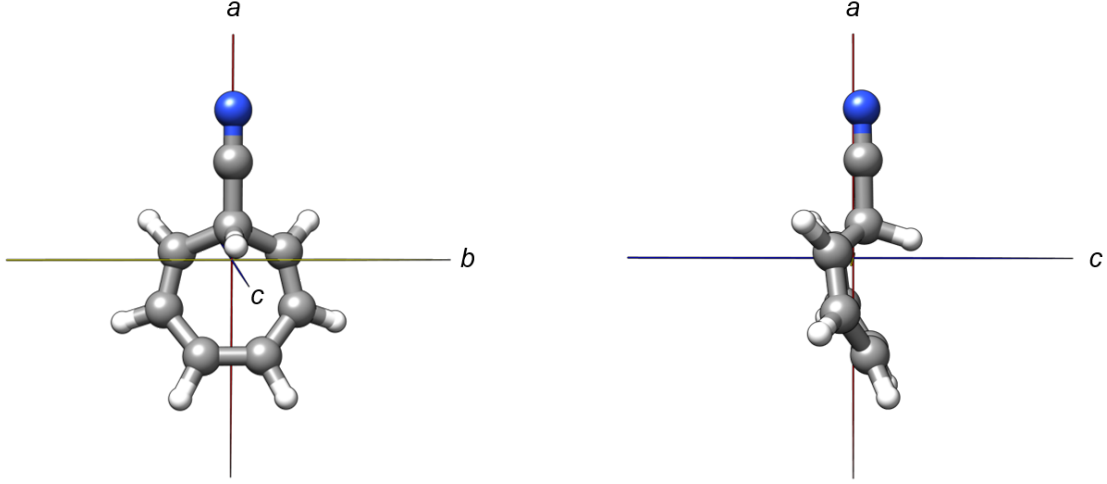


Figure 2.1: Representation of 2,4,6-cycloheptatriene-1-carbonitrile in the principal axis system

where J is the rotational quantum number and B is the rotational constant defined as, $B = \frac{\hbar^2}{8\pi^2 I}$.

- For symmetric tops:

The energies of the rotational energy levels for the oblate symmetric top are defined as:

$$E_{oblate}(cm^{-1}) = AJ(J+1) + (C - A)K^2, \quad (2.9)$$

The energies of the rotational energy levels for the prolate are defined as:

$$E_{prolate}(cm^{-1}) = BJ(J+1) + (A - B)K^2 \quad (2.10)$$

The quantum number K accounts for the projection of the total angular momentum onto the symmetry axis of the molecule. It takes values from $-J$ to $+J$ in integer steps.

- For asymmetric tops:

In the principal axis system, the rotational energy of an asymmetric top molecule takes the form:

$$E_{asymmetric}(cm^{-1}) = \frac{1}{2} (I_a \omega_a^2 + I_b \omega_b^2 + I_c \omega_c^2) \quad (2.11)$$

This expression can also be written as the function of angular momentum components, considering that $\vec{J} = I\vec{\omega}$,

$$E_{asymmetric}(cm^{-1}) = \frac{1}{2} \left(\frac{J_a^2}{I_a} + \frac{J_b^2}{I_b} + \frac{J_c^2}{I_c} \right) \quad (2.12)$$

It follows that the rotational Hamiltonian for a molecule in the principal axis system within the rigid rotor approximation can be written as:

$$\hat{H}_{rig} = \frac{\hbar^2 \hat{J}_a^2}{2I_a} + \frac{\hbar^2 \hat{J}_b^2}{2I_b} + \frac{\hbar^2 \hat{J}_c^2}{2I_c} = A\hat{J}_a^2 + B\hat{J}_b^2 + C\hat{J}_c^2 \quad (2.13)$$

where $A = \frac{\hbar^2}{2I_a}$, $B = \frac{\hbar^2}{2I_b}$, and $C = \frac{\hbar^2}{2I_c}$ are the rotational constants. Within the confines of this thesis, only asymmetric top molecules are examined using rotational spectroscopy.

The selection rules governing the allowed transitions for asymmetric tops are summarised in Table 2.2.

It is to be noted that for asymmetric top molecules, the quantum number K is not sufficient to describe the rotational energy level, as the K component of angular momentum is not constant along the symmetry axis of the rotating asymmetric molecule [45]. Therefore, the labels K_a and K_c are used to represent the projection of the total angular momentum onto the symmetry axes in the limit of prolate and oblate top molecules, respectively [46]. The rotational energy levels of asymmetric tops are labeled as $J_{K_a K_c}$ and the degree of asymmetry can be characterized by the value of Ray's asymmetry parameter [47],

$$\kappa = \frac{2B - A - C}{A - C} \quad (2.14)$$

where A , B , and C are the rotational constants. The limiting cases of $\kappa = -1$ and $\kappa = +1$ represent a symmetric prolate and oblate top, respectively. The value of κ is a valuable indication of which of Watson's reduced Hamiltonian (the A - or the S - reduced Hamiltonian [48]) is to be used to describe the molecule (Subsection 2.1.3). The highest degree of asymmetry is reached when $\kappa = 0$. The energy level scheme of an asymmetric-top molecule relating the two limiting cases of κ is illustrated in Figure 2.2. The condition of $\Delta J = 0$ gives rise to Q-branch, $\Delta J = -1$ to P- branch and $\Delta J = +1$ to R-branch transitions. In addition, the asymmetric top molecules must have at least one nonzero dipole moment component (μ_a , μ_b , or μ_c) to give rise to the types of selection rules summarized in Table 2.2.

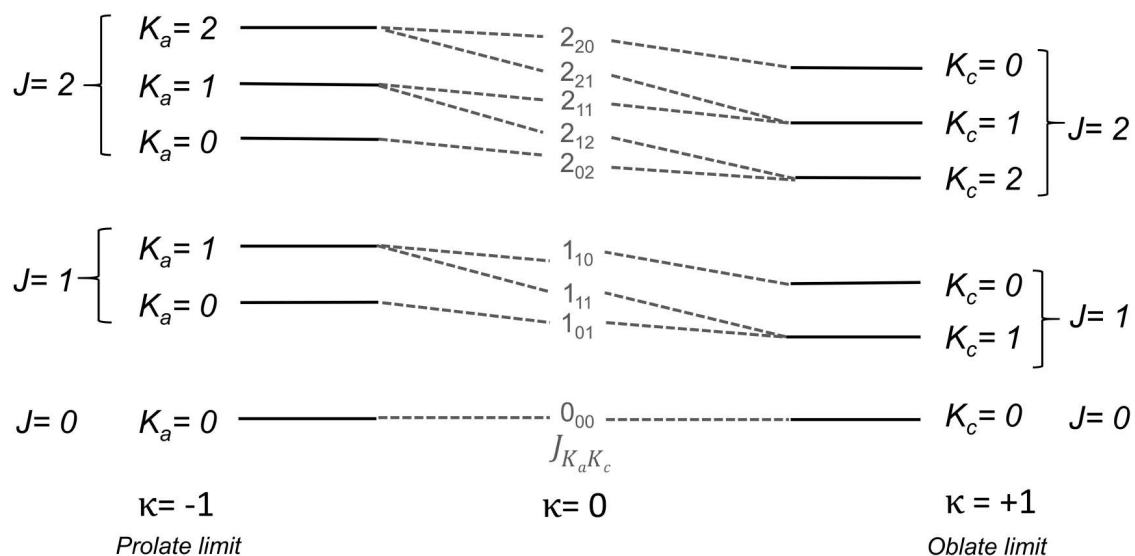


Figure 2.2: Correlation diagram for the asymmetric top energy levels with the prolate and oblate limits. Only the three lowest J levels are depicted.

Table 2.2: A summary of the selection rules for rotational transitions in an asymmetric top molecule.

dipole moment component	transition type	ΔJ	ΔK_a	ΔK_c
μ_a	a -type	$0, \pm 1$	$0, \pm 2, \dots$	$\pm 1, \pm 3, \dots$
μ_b	b -type	$0, \pm 1$	$\pm 1, \pm 3, \dots$	$\pm 1, \pm 3, \dots$
μ_c	c -type	$0, \pm 1$	$\pm 1, \pm 3, \dots$	$0, \pm 2, \dots$

However, the rigid rotor model fails to take into account that bonds do not act like a rod with a fixed distance, but rather like a spring. This means that as the angular velocity of the molecule increases so does the distance between the atoms. This leads us to the semi-rigid rotor model in which centrifugal distortions are taken into account for this stretching during rotation.

2.1.3 The semi-rigid rotor Hamiltonian

The rigid-rotor model is an approximation in which molecules are treated as point nuclei held by rigid bonds. However, real molecules are not rigid and undergo distortions in their average nuclear positions as rotation occurs. The semi-rigid rotor Hamiltonian takes the flexible nature of the molecule into account by adding various correction terms from perturbation theory to the rigid rotor Hamiltonian. These distortions from the average nuclear positions are referred to as centrifugal distortions. The centrifugal distortions cause the frequency of rotational transition to shift (to a lower frequency) relative to that predicted by the rigid rotor Hamiltonian. This is because when rotating molecules are subjected to a centrifugal force, it tends to distort the molecular geometry (stretching of the bonds) and hence increases the moments of inertia which causes the energy levels to be closer than predicted by rigid-rotor model. These shifts are significant when dealing with high-frequency data sets as the effects of centrifugal distortions are larger for increasing J .

The correction terms are added to the rigid rotor Hamiltonian to account for the centrifugal distortion forces. For an asymmetric rotor, the rotational Hamiltonian \hat{H}_{rot} becomes

$$\hat{H}_{rot} = \hat{H}_{rig} + \frac{\hbar^4}{4} \sum_{\alpha\beta\gamma\delta} \tau_{\alpha\beta\gamma\delta} \hat{J}_\alpha \hat{J}_\beta \hat{J}_\gamma \hat{J}_\delta \quad (2.15)$$

where \hat{H}_{rig} is the rigid-rotor Hamiltonian, α, β, γ , and δ can take any value of a, b , or c coordinates in the principal axis system. Watson demonstrated that the number of these terms in the correction part of the Hamiltonian can be reduced to five determinable linear combinations of the fourth-order corrections [45, 49, 50]. To analyze the centrifugal distortion, Watson also proposed two possible combinations of terms giving rise to the reduced Hamiltonian, the S (symmetric) and A (asymmetric) reductions. The A -reduced Hamiltonian in the I^r representation is most suited for asymmetric top molecules, and the quartic centrifugal distortion constants that can be determined under this reduction are Δ_J , Δ_{JK} , Δ_K , δ_J , and δ_K . The S -reduced Hamiltonian in the III^l representation is most suited for slightly asymmetric top molecules, and the quartic centrifugal distortion constants that can be determined under this reduction are D_J , D_{JK} , D_K , d_1 , and d_2 .

2.1.4 Large amplitude motions

Large amplitude motions (LAM) refer to vibrational or rotational movements that deviate significantly from the average or equilibrium positions, with an amplitude on the order of bond length. This can significantly alter the structure of a molecule or convert a molecule from one equivalent structure to another via quantum tunneling. Examples include ring puckering, proton tunneling, and inversion tunnelling

[51]. One of the commonly observed LAM in rotational spectra is methyl ($-\text{CH}_3$) internal rotation. The rotational angular momentum of the rotating methyl group within the molecule couples with the overall rotational angular momentum of the molecule. This coupling perturbs the rotational energy levels and splits them into non-degenerate levels, which leads to the splitting of each rotational transitions into many components.

In an asymmetric top molecule, such as toluene or methyl cyanoacetate (as shown in the Figure 2.3), the effect of methyl internal rotation leads to an equivalent minimum position repeated over 120° of the methyl group in the dihedral scan. (as shown in Figure 2.3). As a result, every rotational energy level is split into a doublet consisting of a non-degenerate A state, and a doubly degenerate E state. The splitting of transitions is dependent on the height of the barrier and the transition being considered.

The addition of methyl internal rotation significantly enhances the complexity of the rotational spectrum, compared to the case without. Therefore the corresponding rotational Hamiltonian, \hat{H}_{rot} , must be extended to include the effect of methyl internal rotation:

$$\hat{H}_{rot} = \hat{H}_{rig} + \hat{H}_I \quad (2.16)$$

where \hat{H}_{rig} is the rigid-rotor Hamiltonian and \hat{H}_I is the Hamiltonian of the internal rotation.

The Hamiltonian of the internal rotation is defined as:

$$\hat{H}_I = F(\hat{j}_\alpha - \hat{J})^2 - V(\alpha), \quad (2.17)$$

\hat{j} is the angular momentum operator of the internal rotation, \hat{J} is the total angular momentum operator, and $V(\alpha)$ is the potential energy as a function of the internal rotation angle α . F is the rotational constant for the internal rotor, given by

$$F = \frac{\hbar^2}{2I_r} \quad (2.18)$$

and I_r is the reduced moment of inertia for the relative motion of the two groups. In the case of the methyl top, which has $2\pi/3$ periodicity, the potential energy can be expressed as:

$$V(\alpha) = \frac{1}{2}V_3(1 - \cos(3\alpha)) + \frac{1}{2}V_6(1 - \cos(6\alpha)) + \dots \quad (2.19)$$

In the scope of this thesis, we only deal with the three-fold barrier, V_3 . Usually, the value of V_3 is much higher than the value of V_6 and therefore higher order terms can be ignored, reducing the expression to:

$$V(\alpha) = \frac{1}{2}V_3(1 - \cos(3\alpha)) \quad (2.20)$$

An additional selection rule arises, according to which, the transitions are only allowed between states of the same symmetry, A to A or E to E.

The determination of the barrier to hindered internal rotation is possible through the analysis of the rotational spectrum of a molecule and the evaluation of the splitting between A- and E- state transitions [45]. For this type of analysis (as shown in chapter 4), we used the analysis program XIAM [52], available from the PROSPE website [53]. XIAM uses the internal axes method (IAM), proposed by Woods [52], to treat internal rotation in symmetric and asymmetric top molecule. It deals with the angles between the local C_3 axis of the internal rotor (depicted by α in Figure 2.3) and the principal inertial axis of the molecule. The polar coordinates defined as δ and ϵ , are the angles between the C_3 axis and the a -inertial axis of the molecule and between the b -axis and the projection of the C_3 axis onto the bc - plane, respectively.

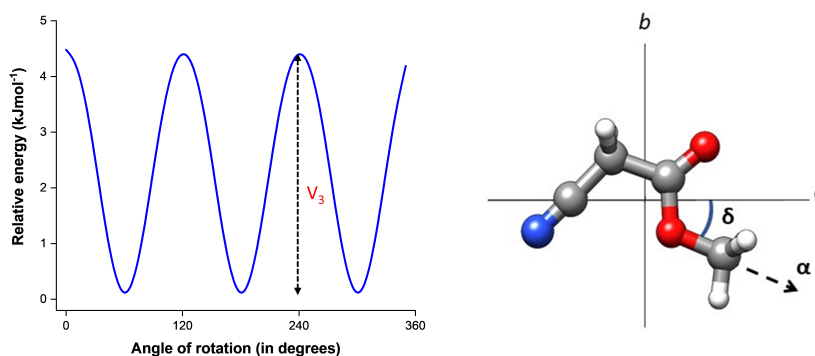


Figure 2.3: Calculated representation of the V_3 hindering potential in methyl cyanoacetate. Identical minima are repeated over 120° rotations of the methyl group by scanning the dihedral angle C-O-C-H.

2.1.5 Nuclear electric quadrupole coupling

When a molecule contains one or more nuclei with a non-spherical distribution of nuclear charges, its rotational spectrum can exhibit hyperfine structure. The non-spherical distribution of nuclear charges generates the nuclear electric quadrupole moment, eQ , and an electric field gradient (EFG) on the nucleus q . The hyperfine structure in the rotational spectrum arises through the coupling of eQ of the nucleus with spin $I \geq 1$ with the EFG of the oscillating electric field. It is important to note that this effect only exists if $I_{(nucleus)} \geq 1$.

For a rotating molecule with one quadrupole nucleus in the presence of an external electric field, the nuclear spin I couples with the angular momentum of molecular rotation J to generate total angular momentum F . The resulting quantum numbers

are related by the following expressions,

$$F = J + I \quad (2.21)$$

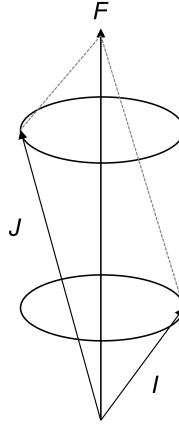


Figure 2.4: Schematic representation of coupling between the angular momentum J and the nuclear spin I resulting in the total angular momentum F .

and F can take values from,

$$F = J + I, J + I - 1, J + I - 2, \dots, |J - I| \quad (2.22)$$

The selection rules for the allowed hyperfine transitions in rotational emission spectra are $\Delta J = 1$, $\Delta F = 0 \pm 1$, and $\Delta I = 0$.

Analysing the hyperfine structure of the rotational transitions leads to the determination of nuclear quadrupole coupling constants, χ , from the quadrupole coupling tensor:

$$\chi = \begin{pmatrix} \chi_{aa} & \chi_{ab} & \chi_{ac} \\ \chi_{ba} & \chi_{bb} & \chi_{ba} \\ \chi_{ca} & \chi_{cb} & \chi_{cc} \end{pmatrix} \quad (2.23)$$

For nuclei with small quadrupole moments, such as $^{14}\text{N}(I = 1)$, usually only the diagonal elements can be determined, which are sensitive to subtle changes in the electronic environment of the quadrupole nucleus. The three diagonal nuclear quadrupole coupling constants are not linearly independent and follow the condition:

$$\chi_{aa} + \chi_{bb} + \chi_{cc} = 0 \quad (2.24)$$

χ_{ii} can be defined as

$$\chi_{ii} = eQq_{ii} \quad (2.25)$$

where q_{ii} are the tensor elements of the electric field gradient. This makes the value of χ_{ii} useful for characterizing the local electronic environment of a quadrupolar nucleus in the molecule and for differentiating between structural isomers as the local electronic distribution can change from one structural isomer to the other. It is also of use in confirming potential astronomical observations of molecules containing quadrupolar nuclei with $I \geq 1$, for example, benzonitrile [54].

The hyperfine structure collapses with increasing J , with hyperfine lines tending to be blended at higher J values. This is seen for the molecules investigated in this thesis (lying in the range of medium to large size molecules) studied across a large frequency range, 2–110 GHz, where resolvable hyperfine splitting is observed up to 26 GHz (low J values) and in the 75–110 GHz range (higher J values), the hyperfine splitting is collapsed, for example, in Chapter 4 and 5.

2.1.6 Rotational and vibrational partition function

The molecular partition function Q corresponds to the number of energy levels that are thermally accessible to a molecule at the temperature of the system. Q is defined as

$$Q = \sum_i g_i \cdot \exp\left(-\frac{E_i}{k_B T}\right) \quad (2.26)$$

where g_i is the degeneracy, i.e., the number of states with the same energy, k_B is the Boltzmann constant and T is the temperature in Kelvin. [55]

As already described in equation (2.3), within the Born-Oppenheimer approximation, the total energy of a molecule can be written as

$$E_{total} = E_{electronic} + E_{vibrational} + E_{rotational} + E_{translational} \quad (2.27)$$

and the partition function factorizes into a product of contributions:

$$Q_{total} = Q_{electronic} \cdot Q_{vibrational} \cdot Q_{rotational} \cdot Q_{translational} \quad (2.28)$$

The electronic energy levels are generally widely separated in energy as compared to the thermal energy $k_B T$ at room temperature. In each electronic level there are several vibrational levels and within each vibrational level lies several rotational levels. Since, $E_{electronic} > E_{vibrational} > E_{rotational} > E_{translational}$, $Q_{electronic}$ is nearly unity at room temperature for singlet state molecules.

In radio astronomy, Q is often composed almost entirely of rotational component, with small additional contributions from vibrational components. This is because radio astronomy deals with the rotational emissions of the molecules, which at high

temperatures can also include rotational emissions from molecules in vibrationally excited states. Therefore, the equation 2.28 becomes

$$Q_{total} = Q_{vibrational} \cdot Q_{rotational} \quad (2.29)$$

The rotational partition function $Q_{rotational}$, is often calculated according to the high-temperature approximation, stating that the temperature is so high that numerous states are occupied. For that case, equation (2.26) can be approximated by integrals, leading to the semi-empirical approximation for $Q_{rotational}$. For an asymmetric molecule, Q can be written as [55]:

$$Q_{rotational}^{asymmetric} = \frac{1}{\sigma} \sqrt{\left(\frac{k_B T}{h}\right)^3} \sqrt{\left(\frac{\pi}{ABC}\right)} \quad (2.30)$$

Which can be further simplified to

$$Q_{rotational}^{asymmetric} = \frac{5.34 \times 10^6}{\sigma} \sqrt{\left(\frac{T^3}{ABC}\right)} \quad (2.31)$$

where σ is a symmetry parameter, T is the temperature (K), and A , B , and C are the rotational constants (MHz). It is important to note that this approximation does not take into account many of the additional sources of complexity in rotational spectra, like internal rotation and nuclear quadrupole coupling.

The vibrational contribution $Q_{vibrational}$ is given by

$$Q_{vibrational} = \prod_i \frac{1}{1 - \exp\left(\frac{h\nu_{vib,i}}{k_B T}\right)} \quad (2.32)$$

In order for $Q_{vibrational}$ to have contribution to Q_{total} , the temperature must be sufficiently high to populate the low-lying vibrationally excited states. Often the vibrational contribution is $< 1\%$ up to 30–40 K but it could be significant at warmer temperatures [7].

In practice, the value of the rotational partition function can be calculated using an analysis software, such as the SPCAT program [53]. This program performs the direct summation across the rotational energy levels that are predicted from the experimentally determined rotational and centrifugal distortion constants (and, if applicable, nuclear quadrupole coupling constants).

Partition functions can also be used to calculate the relative transition intensities at different rotational temperatures. The proportionality of the partition function to the temperature is reflected in the calculated and observed transition intensities, as the increase in the temperature redistributes the population into the accessible vibrationally excited states resulting in an overall lower signal intensity of rotational transitions. This can be seen in Figure 3.6 which shows the comparison of simulated transition intensities as a function of temperature (K) for one of the conformers of 2,4,6-cycloheptatriene-1-carbonitrile, CHT-1-CN-1.

Vibrationally excited states

Depending on the size of the molecules, at temperatures higher or equal to the room-temperature, vibrationally excited states are populated. Therefore, it is important to consider the value of the vibrational partition function, Q_{vib} , as given in equation (2.32), which can then be incorporated in the evaluation of the total partition function. The anharmonic energies of the vibrationally excited states can be obtained from anharmonic frequency calculations and the Q_{vib} can be calculated with these values using the equation (2.32).

In practice, The room-temperature configuration in the W-band instrument (refer to Section 3.5.1) allows for probing the low-lying vibrationally excited states. The rotational spectra of the vibrationally excited states is analyzed the same way as the rotational spectra in the ground vibrational states, using the same theories and programs for analysis. However, the analysis can become complicated if the vibrational excited states are too close in energy that allowing them to perturb each other. One example is Fermi resonance which happens if the wavefunctions of two energetically close states with the same symmetry mix. This results in shifted energy levels and altered intensities [45]. More precisely, the rotational transitions arising from the higher energy mode shift to higher frequency, and the ones from the lower energy mode shift to lower frequency. For the intensity part, it is the opposite. The higher intensity transitions show a decrease, and the lower intensity ones show an increase in the intensities. Another type of coupling that occurs due to the interaction of rotational and vibrational energy levels is called ro-vibrational or Coriolis coupling. Coriolis effects become significant when there is coupling between different vibrational modes, leading to interactions between rotational levels associated with these vibrational states. These interactions can cause changes in the rotational energy levels, resulting in shifts and splittings in the rotational spectrum. The Coriolis coupling constants can be used to describe the effect of the ro-vibrational coupling on the rotational spectrum. These constants take into account the coupling of the overall rotation of the system with the coordinate system of the motion or interaction, and they measure the angular momentum caused by the vibration-rotation interaction. In this thesis, only unperturbed vibrational excited states are analyzed, as can be seen in Chapter 5, where six vibrationally excited states were assigned for the lowest energy conformer in the room temperature flow cell experiment for CHT-1-CN.

2.1.7 Spectral analysis and quantum chemical calculations

There are several fitting programs available to assist the assignment of rotational spectra, e.g. JB95 [56], PGOPHER [57], AABS program suite [58, 59], and XIAM [52]. The latter two programs can be found on the PROSPE homepage [53]. All of

these programs are developed to fit the rigid rotor and non-rigid rotor Hamiltonian to the assigned rotational transitions for determining the experimental rotational parameters, including rotational constants, centrifugal distortion constants, if applicable (nuclear quadrupole coupling constants). In the work presented in this thesis, the spectra were first fit using the PGOPHER program and then further refined using Pickett’s SPFIT/SPCAT programs as implemented in the AABS program suite. The analysis of the observed tunneling splitting arising from methyl group internal rotation in Chapter 4 was performed using the XIAM program. A detailed description of the properties of the programs can be found in the corresponding literature. Other than these, KRA and EVAL [53] programs were used for structure determination and the calculations of the structural parameters (bond lengths, bond angles, etc), respectively.

Quantum chemical calculations are used to aid the assignment of the rotational spectra. Two main types of calculations were performed: structure optimization calculations and anharmonic frequency calculations with ORCA 5.0 [60, 61] and Gaussian 09 [62].

Structure optimizations were performed in order to obtain theoretical rotational constants, electric dipole moments, and if needed, nuclear quadrupole coupling constants of the molecular structures under investigation. These constants were used as an input for the preliminary assignment of the rotational spectrum. For molecules studied with the W-band spectrometer (Section 3.3) at room temperature in the flow-cell setup, anharmonic frequency calculations were required to obtain theoretical rotational constants of low-lying vibrationally excited states. These calculated rotational constants were adjusted by applying the difference between the experimental and theoretical rotational constants for the vibronic ground state of the molecule at the same level of theory and basis set. B3LYP-D3(BJ)/aug-cc-pVTZ and MP2/aug-cc-pVTZ are the most commonly used levels of theories in the scope of this thesis. For the analysis of IR-UV ion dip spectra, structure optimizations were performed using B3LYP-D3/def2-SVP level of theory (see Chapter 8 for more details). Where relevant, initial conformational searches were performed using the SPARTAN 14 program [63], for example in Chapter 5. These were complemented with manual dihedral scans using ORCA 5.0 [60, 61].

2.1.8 Structure determination

Experimentally determined rotational constants give information about the molecular structure, since the rotational constants are related to the moments of inertia by equation (2.13). For an asymmetric molecule consisting of N atoms, the molecular structure can be determined from its $3N - 6$ independent parameters: $N - 1$ bond lengths, $N - 2$ bond angles, and $N - 3$ dihedral angles.

It is possible to determine the precise position of an atom within a molecule using the rotational constants of the isotopologues. Each isotopologue has its unique set of rotational constants, which is a consequence of the change in the moment of inertia upon the isotopic substitution of an atom in the parent molecule. From this information, the molecular structures can be constructed.

Due to the high resolution and high sensitivity offered by rotational spectroscopy, it is often possible to observe singly-substituted heavy-atom isotopologues in natural abundance, such as ^{13}C (1.1%), ^{29}Si (4.6%), ^{30}Si (3.1%), ^{15}N (0.4%), and ^{18}O (0.2%). When their observation is not possible in natural abundance, isotopically enriched samples can be used.

In the scope of this thesis, two different methods can be employed to obtain the experimental structure of the molecule, as discussed in the following sections [64, 65].

The effective structure (r_0)

The effective structure represents the experimental structure in a specific vibrational state, usually in the ground vibrational state, $v = 0$, and is known as r_0 structure. It is calculated by the least-squares fitting of the structural parameters which reproduce the experimentally obtained rotational constants of the parent and all the fitted isotopologues. The method is implemented in the STRFIT program and a detailed description of the method and program used can be found in Ref. [53]. This method is not reliable in the case where the molecule under investigation exhibits LAM.

The substitution structure (r_s)

Kraitchman's substitution structure, r_s [66], exploits changes in the moments of inertia upon single isotopic substitution. This approach allows for the determination of the coordinates of each isotopically substituted atom in the principal inertial axis system. The r_s structure is based on the application of Kraitchman's equations, with an assumption that there is no change in molecular structure upon isotopic substitution. The equations for determining the coordinates of the atom in asymmetric top molecules are:

$$|a| = \left[\frac{\Delta P_a}{\mu} \left(1 + \frac{\Delta P_b}{I_a - I_b} \right) \left(1 + \frac{\Delta P_c}{I_a - I_c} \right) \right]^{1/2} \quad (2.33)$$

$$|b| = \left[\frac{\Delta P_b}{\mu} \left(1 + \frac{\Delta P_c}{I_b - I_c} \right) \left(1 + \frac{\Delta P_a}{I_b - I_a} \right) \right]^{1/2} \quad (2.34)$$

$$|c| = \left[\frac{\Delta P_c}{\mu} \left(1 + \frac{\Delta P_a}{I_c - I_a} \right) \left(1 + \frac{\Delta P_b}{I_c - I_b} \right) \right]^{1/2} \quad (2.35)$$

where P_i are the planar moments, which are defined as:

$$\Delta P_a = \frac{1}{2}(-\Delta I_a + \Delta I_b + \Delta I_c) \quad (2.36)$$

$$\Delta P_b = \frac{1}{2}(-\Delta I_b + \Delta I_a + \Delta I_c) \quad (2.37)$$

$$\Delta P_c = \frac{1}{2}(-\Delta I_c + \Delta I_a + \Delta I_b) \quad (2.38)$$

μ is the reduced mass and is given by:

$$\mu = \frac{M\Delta m}{M + \Delta m} \quad (2.39)$$

where M is the total mass of the molecule and Δm is the change in the mass upon isotopic substitution [45].

As can be seen from the equations given above, the method only provides the absolute values for the coordinates of each atom. The sign of each value can be confirmed by comparing the experimentally determined coordinates with the ones obtained from structure optimization calculations or from chemical intuition. The method may perform poorly by returning imaginary numbers when determining the position of an atom close to an inertial axis or the center of mass. It is common practice to artificially designate these coordinates as zero along the relevant axes. We used the KRA [66] program, the coordinates of the isotopically substituted atoms can be calculated and the gas phase structure of the molecule can be constructed.

2.2 Infrared spectroscopy

Infrared spectroscopy relies on the interaction between infrared (IR) radiation and molecules. The absorption of IR radiation by molecules leads to transitions between quantized vibrational energy levels. A certain vibration is called IR-active if it has a changing net dipole moment μ during the vibration: $\frac{\partial \mu}{\partial Q_i} \neq 0$, where Q_i is the normal coordinate to describe the motion of atoms during the vibration and the intensity of the absorption band is characterized by

$$I \propto \left(\frac{\partial \mu}{\partial Q} \right)^2 \quad (2.40)$$

In the simplest model, the vibrations between two atoms can be modelled by the harmonic approximation, obeying Hooke's law, where the vibrational energy states are given by:

$$E = h\nu \left(v + \frac{1}{2} \right) \quad (2.41)$$

where h is the Planck constant, v is the vibrational quantum number, and ν is the frequency. The harmonic approximation is only valid for low quantum numbers and deviates significantly if v is large. Therefore, the potential has to be extended to a more physical expression and to explain the dissociation at higher values of v (or at higher internuclear distances). This is done by an anharmonic potential by defining the energy of the vibrational eigenstates (following the Maclaurin expansion of the Morse potential).

$$V = h\nu \left(v + \frac{1}{2} \right) - h\nu x \left(v + \frac{1}{2} \right)^2 \quad (2.42)$$

where x is the anharmonicity constant (typically the value of x lies between 0.001-0.02) [67]. Figure 2.5 shows the potential energy curve of the stretching vibration

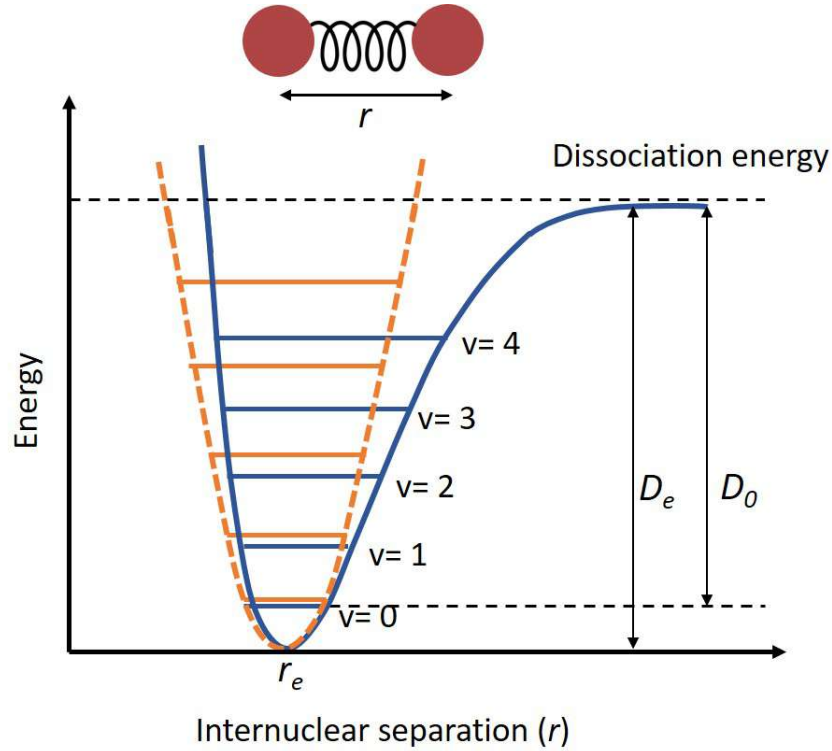


Figure 2.5: Potential energy of a vibration of a diatomic molecule as a function of the internuclear distance r in a harmonic (solid blue line) and anharmonic (orange dashed line) potential.

of a diatomic molecule for the harmonic (orange dashed line) and anharmonic (solid blue line) approximation. For our experiments, we used Fourier transform infrared (FT-IR) spectroscopy as a technique to investigate the adsorption of molecules onto the surface of Iridium single crystal, Ir(111) in our case. The FT-IR technique has

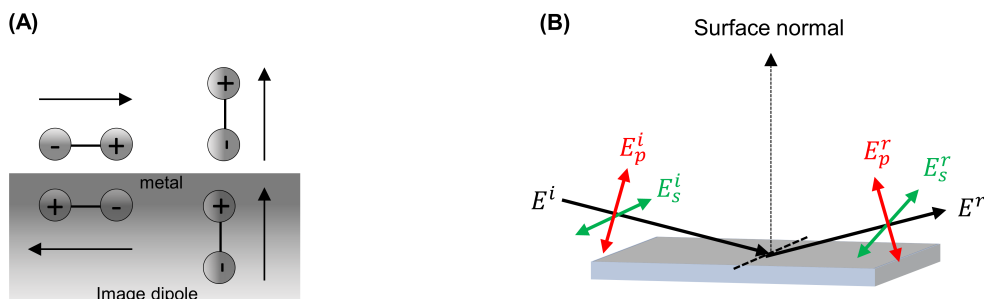


Figure 2.6: Interaction of IR radiation with the metal surface. Panel (A) demonstrates the surface selection rule and panel (B) describes the incident (E^i) and reflected (E^r) radiation after hitting the metal surface at an angle.

been extensively used to study the interfaces with the use of state-of-the-art FT-IR spectrometers that offer a high resolution, high signal-to-noise ratio, and fast acquisition time over a wide scanning range [68, 69].

2.2.1 Infrared reflection-absorption spectroscopy (IRRAS)

For investigating the geometry of adsorbed molecules on reflecting surfaces, an important aspect is the surface selection rule for adsorbed molecules. The two limiting cases of adsorbed molecules on metal surfaces would be a flat-oriented or a perpendicular-oriented molecule with respect to the surface normal, as shown in Figure 2.6a. In both cases the dipole of the adsorbed molecule is mirrored below the metal surface with opposite charge distribution.

In the case of the dipole moment parallel to the surface, the image dipole moment is also parallel resulting in the destructive interference of the effective dipole moment. For the case of the perpendicular orientation of the dipole moment, the mirrored dipole moment has the same orientation, resulting in constructive interference. This phenomenon is called the metal surface selection rule and it explains why only vibrations with a transition dipole moment non-parallel to the metal surface are visible in IRRAS [70]. To predict the orientation of the adsorbed molecules, it is necessary to look at the different electric field components of the incoming IR beam, as described in Figure 2.6b. The electric field oriented parallel to the surface and perpendicular to the plane of incidence is called s-polarized (E_s) light and p-polarized (E_p) light is the one which is perpendicular to the surface and parallel to the plane of incidence. The arrows represent the direction of the dipole moment component. E^i indicates the incident light and E^r indicates the reflected light.

2.2.2 IR-UV ion dip spectroscopy

The IR-UV ion dip technique was first developed by Lee and coworkers in the 1980s [71] and is a well established double resonance method. In IR-UV ion dip spectroscopy, an IR laser is used as the pump source, and a UV laser(s) is used as a probe. For this technique, we require a constant ion signal of our molecule of interest, which is generated via resonance-enhanced multiphoton ionization (REMPI) spectroscopy. This ion signal is depleted by the depopulation of a vibrational state in the electronic ground state of the molecule, resulting in a dip of the ion signal. REMPI spectroscopy, as the name indicates is an approach to effectively ionize molecules through excitation via a resonant electronic state. In this technique, a molecule is resonantly excited by a photon(s) from the ground electronic state S_0 , to the electronically excited state, usually S_1 , and is then ionized using another photon of the same or different wavelength. For this to happen, the sum of the two photons must be higher than the ionization energy of the molecule. If the molecule is resonantly ionized using two photons of the same energy, it is called a one-color resonant two photon ionization or [1+1] REMPI process. If two photons of different energies are employed, it is referred to as [1+1'] REMPI, as shown in Figure 2.7. In the scope of this thesis, the molecules of interest are resonantly ionized using the [1+1'] REMPI process. The resulting ions can then be detected using time-of-flight (TOF) mass spectrometry to determine the mass/charge (m/z) ratio of the species under investigation. One of the requirements for recording the REMPI spectra is to have a sufficiently long-lived electronic excited state, to allow for the absorption of the second photon. For the work presented in this thesis, pulsed nanosecond lasers were employed, requiring lifetimes at least in the nanosecond regime. To perform IR-UV

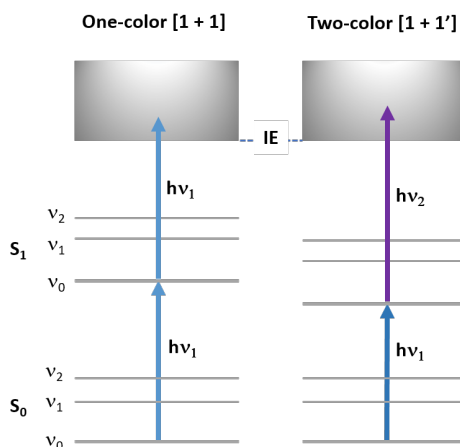


Figure 2.7: Schematics of [1+1] and [1+1'] REMPI technique, where ν_1 and ν_2 correspond to the two different UV frequencies.

ion dip spectroscopy, the UV laser is fixed on a transition of the REMPI spectrum of a specific m/z to generate a constant ion signal, and the IR laser is scanned over the frequency range of interest, which in our case is $550 - 3200 \text{ cm}^{-1}$. Provided the IR laser frequency is in resonance with a vibrational transition of the molecule probed by $[1+1']$ REMPI, the vibrational population in the electronic ground state of that molecule is depopulated and a dip in the ion current is observed (as shown in Figure 2.8), resulting in a mass selective IR-UV ion dip spectrum [72]. In our experiment, we also coupled the electrical discharge source with the IR-UV setup giving rise to the mass-resolved IR-UV ion dip spectra of the formed discharge products in the experiment. The schematics of the IR-UV ion dip technique used in the FELIX laboratory is shown in Section 3.6.1 where the IR pulse (provided by FELIX) is spatially aligned with the UV pulse, and is introduced before the UV pulse.

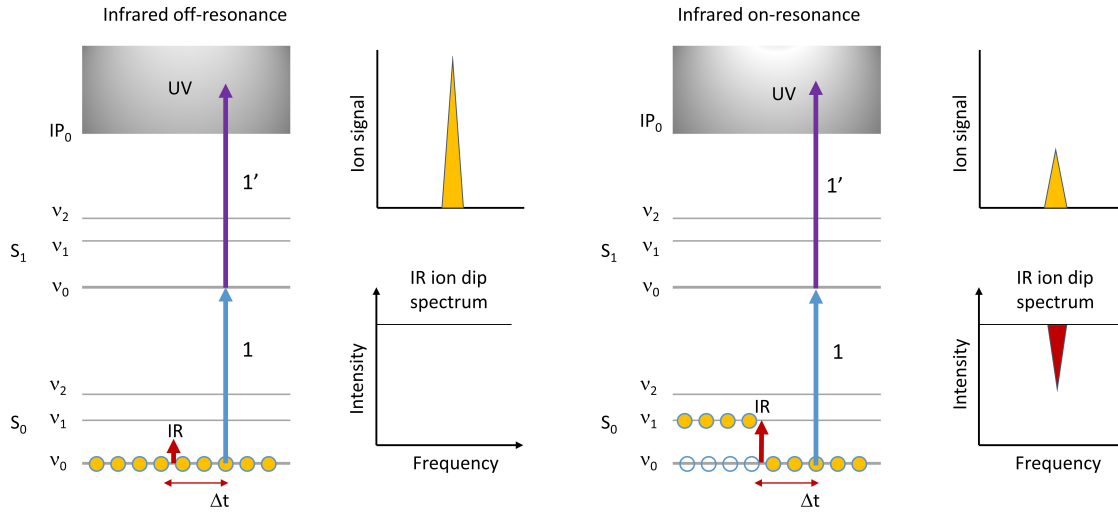


Figure 2.8: Description of the working of the IR-UV ion dip spectroscopy depicted using two level system. The left panel shows IR radiation not being resonant with the vibrational level. In the right panel, the IR radiation is in resonance with the vibrational level and hence successfully depopulating the ground vibrational state, leading to a reduction in the ion signal and the dip in the ion current is observed.

Chapter 3

Experimental Details

The work in this thesis is performed using three different spectroscopic techniques: rotational spectroscopy, IR-UV ion dip spectroscopy, and IR- reflection absorption spectroscopy (IRRAS). The rotational spectra were recorded over a broad frequency range, 2-110 GHz, the IR-UV ion dip spectra were collected from 550-3200 cm^{-1} , and the IRRAS measurements were performed between 500 and 4500 cm^{-1} .

This chapter describes the instrumentation, the different methods of sample introduction, which leads to the two distinct experimental methods (supersonic expansion and the room temperature measurement), and the electrical discharge setup for initiating reactions that can form chemical species relevant for ISM.

3.1 The COMPACT spectrometer

The 2-18 GHz compact-passage acquired coherence technique (COMPACT) spectrometer is a home-built instrument [73], undergoing constant developments to improve its performance. The design of the spectrometer follows the CP-FTMW approach introduced by Brown *et al.* [8] and is based on the design proposed by Grabow [74]. The instrument operates in the frequency region from 2 to 18 GHz, divided in two segments; 2-8 GHz [73, 75] and 8-18 GHz [76]. The scheme of the COMPACT spectrometer is as follows: A 24 GS/s arbitrary waveform generator (AWG, Tektronik 7122C) creates a 4 μs excitation chirped pulse from 2-8 GHz, subsequently amplified to 300 W using a traveling wave tube (TWT) amplifier. For the 8-18 GHz frequency range, chirps of 2 μs duration are generated between 4-9 GHz with the AWG, later amplified and doubled to 8-18 GHz. The doubler multiplies the bandwidth of the chirp by a factor of two without changing the pulse duration. The generated chirped pulses are then amplified with a 50 W solid-state amplifier (SSA, Mercury Systems L0618-46-T680) operating between 6-18 GHz.

After amplification, the excitation chirped pulse is transmitted into the vacuum

chamber (operating pressure in the range of 10^{-5} mbar) and broadcast via a microwave horn antenna. The molecules, seeded in an inert gas (usually Ne, He, or Ar), are supersonically expanded into the vacuum chamber using a pulsed valve (Parker General pulsed valve, series 9) modified to be equipped with a heatable reservoir close to the orifice. Upon interaction with the excitation pulses, a macroscopic polarization is induced when the frequencies of the chirped pulse are resonant with molecular rotational transitions of the sample under investigation. The relaxation of the induced macroscopic polarization is recorded in the form of a free induction decay (FID). The FID is then amplified with a low-noise amplifier (LNA) and digitized on a 100 GS/s oscilloscope (Tektronix DPO 72004C). The oscilloscope is able to process multiple FIDs per molecular pulse, which is referred to as the fast frame method. The COMPACT spectrometer uses a fast frame method in which each molecular gas pulse is probed by a successive train of eight excitation chirps, followed by recording the resulting eight FIDs. When the fast-frame is combined with the gas pulse repetition rate of 8 Hz it yields an effective repetition rate of 64 Hz. The oscilloscope has an adjustable digitization rate and is set to 25 GS/s and 50 GS/s for 2-8 GHz and 8-18 GHz, respectively. The FIDs are collected for 40 μ s and 20 μ s, and Fourier transformed using a Kaiser Bessel windowing for baseline improvement, giving a frequency resolution of 25 kHz for 2-8 GHz and 50 kHz for 8-18 GHz.

3.2 The K-band spectrometer

The K-band spectrometer, operating in the 18-26 GHz region, is another home-built chirped-pulse Fourier transform microwave spectrometer, shown in Figure 3.2. This instrument takes advantage of the cost-effectiveness linked with the segmented approach in instrument construction [76, 77]. This new design decreased the total cost of instrumentation by at least two-thirds compared to the commercial ones, without compromising the quality of the data. The complete details of the design and characterization of the instrument can be found in ref. [76].

Similar to the fast-frame method employed in the COMPACT spectrometer, here, each molecular pulse is probed by three pulse trains (multi-train). The 18-26 GHz spectrometer utilizes the segmented approach, whereby the total bandwidth of the instrument is covered by several shorter segments stitched together in an automatic fashion to obtain the whole spectrum. The 25 GS/s AWG (Textronix AWG70000A series) synthesizes 1.5 μ s of excitation pulses in the range of 7-3 GHz, the bandwidth is divided into ten segments, each spanning 400 MHz. Subsequently, these chirps are upconverted to 9-13 GHz and then doubled to 18-26 GHz. Before being transmitted in the vacuum chamber, each pulse train is amplified by a 6 W SSA (Quinstar QPP-18273840MPI). Upon interaction with the molecular gas pulse, at the repetition

rate of 10 Hz, the molecular ensemble undergoes polarization, and the subsequent FIDs are collected for usually $10\ \mu\text{s}$. This is followed by amplification, frequency down-conversion, digitization on a high-speed digitizer card ((Keysight U5303A), and lastly fast-Fourier transformation into the frequency domain, resulting in a resolution of around 100 kHz. The multi-frame method of probing each gas pulse with three pulse trains, with a 10 Hz repetition rate of the molecular gas pulse, gives an effective repetition rate of 30 Hz.

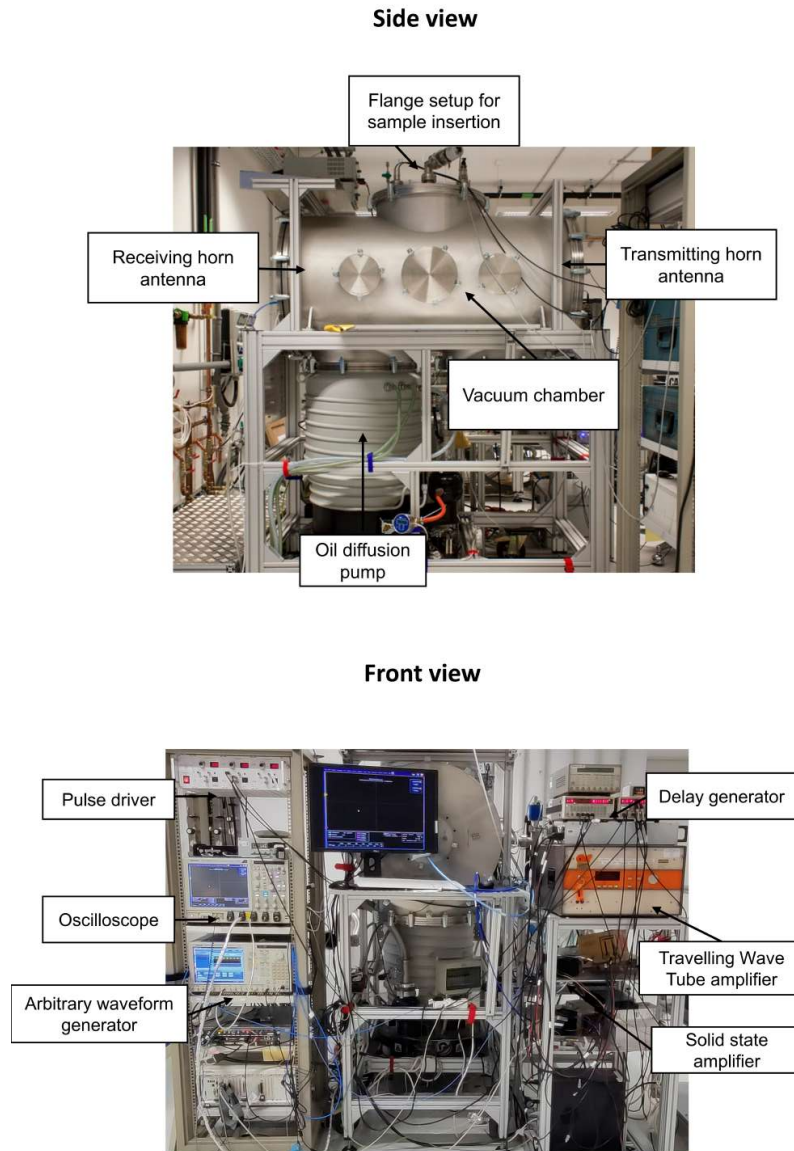


Figure 3.1: The COMPACT spectrometer

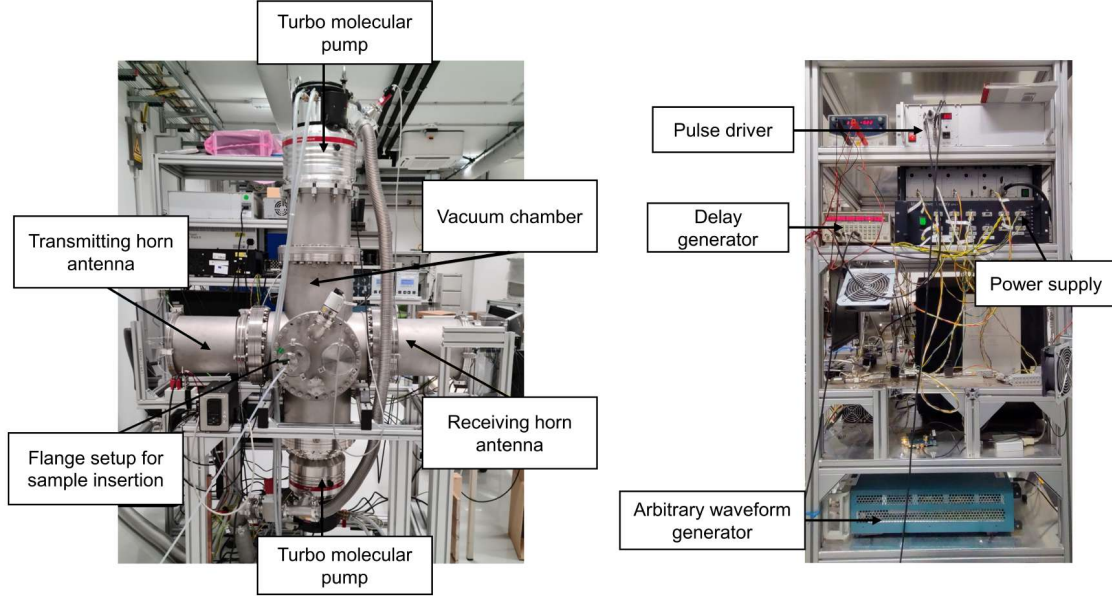


Figure 3.2: The K-band spectrometer

3.3 The W-band spectrometer

The W-band spectrometer, shown in Figure 3.3, operates between 75-110 GHz. This instrument was developed by BrightSpec, Inc., and is based on the developments from the University of Virginia, where the chirped-pulse technique was expanded into the millimeter-wave region [78]. Similar to the 18-26 GHz spectrometer, the W-band spectrometer also utilizes the segmented approach to cover the spectral bandwidth of 35 GHz. The electronic components of the instrument are controlled by the Edgar program and by the BrightSpec user interface. A thorough description of the instrument's working can be found in reference [79]. The instrument was primarily designed for the room temperature flow-cell configuration and was later modified to include supersonic expansion capabilities as well. In the scope of this thesis, only room-temperature experiments were performed and a brief description of the same is given below.

For the majority of the experiments, the instrument was operated in two segmented modes: fast mode and high dynamic range (HDR) mode. The excitation pulses are

created by a 12 GS/s AWG (Keysight M8190A) initially in the range of 1.56-2.28 GHz. These pulses are then frequency up-converted and multiplied by an active multiplier chain (AMC, x6) to generate millimeter-wave radiation in the range of 75-110 GHz. The synthesized radiation is then transmitted into the vacuum chamber through a Teflon window. In fast mode, the excitation pulse length is 250 ns long, and the entire 35 GHz frequency bandwidth is covered by 48 segments, each 720 MHz wide. Before the excitation chirp for the next segment is transmitted into the chamber, there is a $2.35 \mu\text{s}$ delay between the two segments to allow for the collection of the FID corresponding to the first segment. For recording one acquisition, the complete spectrum is covered in $131 \mu\text{s}$. In HDR mode, each 720 MHz segment is further divided into 30 MHz segments, increasing the measurement time as compared to the fast mode, and in return, decreasing the number of spurious signals in the spectrum. The typical excitation pulse length for an HDR experiment is 500 ns, and the resulting FID is collected for $4 \mu\text{s}$.

The FID of the molecular response is coupled out of the chamber through the second Teflon window, collected by the receiving horn antenna, frequency down-converted, digitized on a 4 GS/s real-time digitizer (Keysight U1084), and fast Fourier transformed into the frequency domain. A typical measurement strategy is to optimize the experimental conditions with the fast mode, such as the pressure in the flow cell or the heating temperature if the sample needs to be heated. Once the experimental conditions are optimized, the spectrum can then be recorded using the HDR mode, increasing the signal-to-noise ratio and decreasing the content of spurious signals in the spectrum relative to the one obtained with fast mode. When the final spectrum is recorded using the HDR mode, the achieved frequency accuracy of the instrument is 30 kHz, and the full width at half maxima (FWHM) of about 550 kHz.

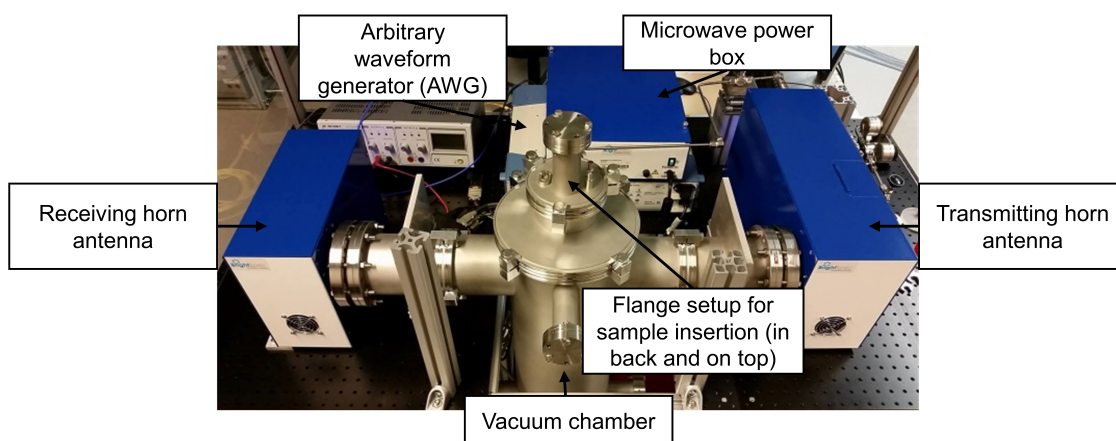


Figure 3.3: The W-band spectrometer

3.4 Electrical discharge setup

All the instruments described above can be coupled with an electrical discharge setup, where the molecular gas pulse is subjected to high voltage (usually between 0.6-1.2 kV) before expanding into the vacuum chamber. The discharge voltage to be applied depends on various factors, for example, the precursor molecules to be discharged and more importantly, on the carrier gas used to achieve a certain amount of current produced (in mA). To perform discharge experiments, an additional nozzle is attached at the bottom of the pulsed valve containing the sample. This additional piece (Figure 3.4), also referred to as a discharge nozzle, consists of two oxygen-free copper electrodes, separated by Teflon spacers, in the Teflon housing. The first (top) electrode is grounded and the second (bottom) electrode (with negative polarity) is connected to a high-voltage supply. Following the second electrode, another spacer is added to introduce a recombination zone which allows for the generated chemical species to recombine before entering the vacuum chamber. Subsequently, the formed discharge products interact with the microwave radiation, and the ones in resonance with the chirped-pulse will be investigated. The design of the discharge nozzle is inspired by the ones described in McCarthy *et al.* [80, 81] and is shown in Figure 3.4.

In this thesis, electrical discharge experiments were performed to produce *in situ* the species of astronomical interest, which can be stable molecules, open-shell species, or transient species that are otherwise inaccessible or short-lived to perform spectroscopic investigations. We have coupled the electrical discharge source with the microwave spectrometers. One of the projects discussed in this thesis involves the electrical discharge experiment of silane (1 % in Ne) with benzene to explore the silicon-substituted aromatic molecules using microwave spectroscopy. Detailed information about that specific experiment can be found in Chapter 8. We also used the electrical discharge setup coupled with the molecular beam instrument at FELIX laboratory [82] to perform IR-UV ion-dip spectroscopy on the discharge products of phenylsilane (discussed in detail in Section 3.6).

3.5 Approaches to sample introduction: Room-temperature measurement and supersonic expansion

3.5.1 Room-temperature measurements

According to the Boltzmann distribution, the probability of finding the particles (molecules in our case) in higher energy states in a system at thermal equilibrium,

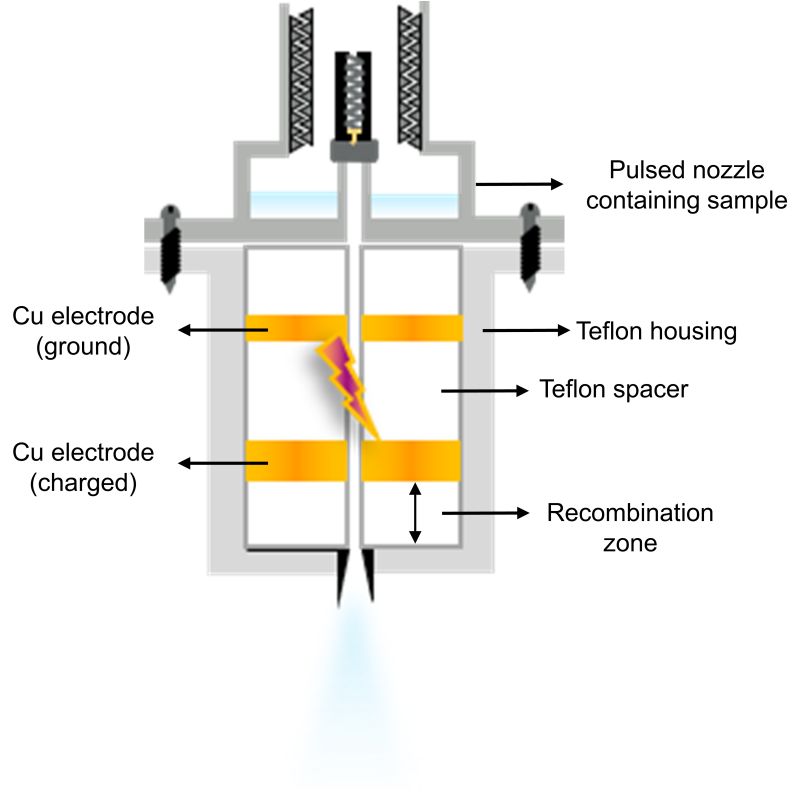


Figure 3.4: Schematics of the discharge nozzle

decreases exponentially with increasing energy difference, and it is directly proportional to the inverse of the temperature, as shown in equation (3.1).

$$\frac{N_2}{N_1} = \exp\left(\frac{-\Delta E}{k_B T}\right) \quad (3.1)$$

N_2 and N_1 correspond to the population in the respective energy states, ΔE being the energy difference between the two states, k_B and T are Boltzmann constant and temperature (in K), respectively. Considering the energy level diagram of a molecular system, at room temperature, typically multiple rotational and vibrational states are occupied. Moreover, in experiments where heating of the sample is required, more and more states are populated. The room-temperature measurement configuration allows access to pure rotational spectra of low-lying vibrational states. The W-band spectrometer, capable of operating under both supersonic expansion and room-temperature conditions, was operated in a room-temperature slow-flow set-up for most experiments.

For experiments where commercial liquid samples were used, the sample was loaded

into an external reservoir, and a freeze-pump-thaw cycle was performed at least twice to remove the dissolved air present in the sample before starting the measurement. The approach consists of freezing the liquid sample by subjecting the reservoir to liquid nitrogen atmosphere, followed by pumping the reservoir such that the dissolved air is removed and only the frozen sample remains. As a last step of the process, the frozen sample is allowed to thaw to return to room temperature, and the whole cycle is repeated until the sample is free of air. The freeze-pump-thaw method ensures that any increase in the pressure inside the vacuum chamber upon sample introduction is due to molecular vapors. The room-temperature flow-cell set-up is an open system where the incoming rate of the vapors of the sample is equal to the pumping or outgoing rate from the vacuum chamber. If the vapor pressure of the molecular sample to be investigated is not enough to be measured in the flow-cell set-up, then the room-temperature cell can also be used as a static cell. The static cell is a closed system rather than an open one and hence does not exchange matter with the surroundings.

3.5.2 Supersonic expansion

Contrary to the room-temperature measurements, a supersonic expansion leads to an internally cooled molecular jet where the translational, vibrational, and rotational degrees of a molecule are cooled in the absence of any condensation. This technique has seen tremendous applications in spectroscopy [83–85], like increasing the intensities by cooling down the population to the low-energy states, and narrowing the spectral line widths due to the low translation temperature relative to the room-temperature experiment. A schematic of a supersonic expansion [86] is shown in Figure 3.5. The reasoning behind supersonic expansion is explained as follows: The molecule of interest and inert carrier gas are mixed in the pre-expansion region such that only a few percent of the molecular sample is present in the mixture. The velocity distribution can be described using the Maxwell-Boltzmann distribution, $f(v)$:

$$f(v) = 4\pi \left(\frac{m}{2\pi k_B T} \right)^{\frac{3}{2}} v^2 e^{-\frac{mv^2}{2k_B T}} \quad (3.2)$$

where $f(v)$ is the probability distribution function, m is the mass of the particle, T is the temperature, k_B is the Boltzmann constant, and v is the particle velocity. The equation describes the probability distribution as a function of velocity, which in turn is affected by the temperature. If we consider our gaseous system to be ideal, the most probable velocity can be calculated using the expression:

$$v_{mp} = \sqrt{\frac{2k_B T}{m}} \quad (3.3)$$

The most probable velocity is the velocity most likely to be possessed by any particle of mass m in the system and corresponds to the maximum value of the $f(v)$.

The expansion of a gas from the high pressure of the pre-expansion region, P_0 , into the low pressure of the vacuum chamber, P_B through a small orifice, converts the random motion of the particles into a directed flow with the reduced velocity distribution. This reduction in velocity distribution can be used to define the decrease in the so-called translational temperature of the ensemble. This expansion is called a supersonic expansion when the diameter of the orifice is much larger than the mean free path length λ of the atoms. This enables many inelastic collisions between the molecule of interest and the carrier gas atoms during the early stages of expansion. The extent of the vibrational and rotational cooling depends on the carrier gas with which the molecule of interest undergoes two-body collisions. As the carrier gas atoms become heavier, the associated collision energy increases and hence lowers vibrational and rotational temperatures. The advantages of supersonic expansion utilized in our experiments are the low translational temperature leading to narrow spectral line width, and reduced number of populated states owing to low vibrational and rotational temperatures. These effects combined, simplify the recorded spectrum by increasing the population in the low-lying energy states which results in increased observed intensities as compared to the room-temperature experiments. An example can be seen in Figure 3.6 which shows simulated rotational spectra of CHT-1-CN-1 (Chapter 5) at different temperatures.

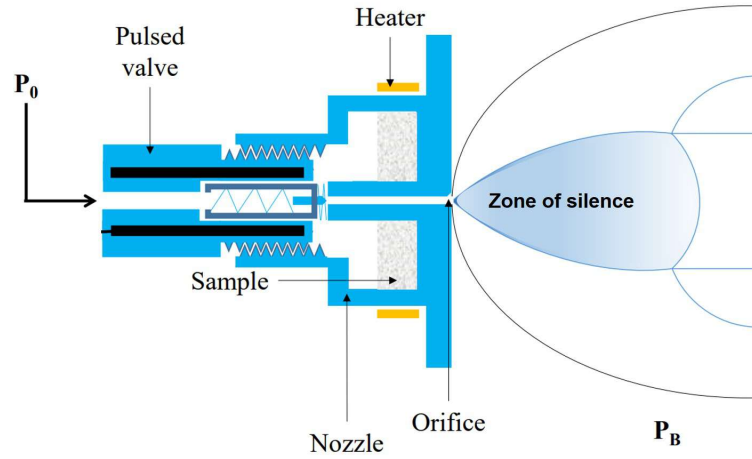


Figure 3.5: Schematic of the supersonic expansion propagating from a pulsed nozzle set-up, adapted from Ref.[86]

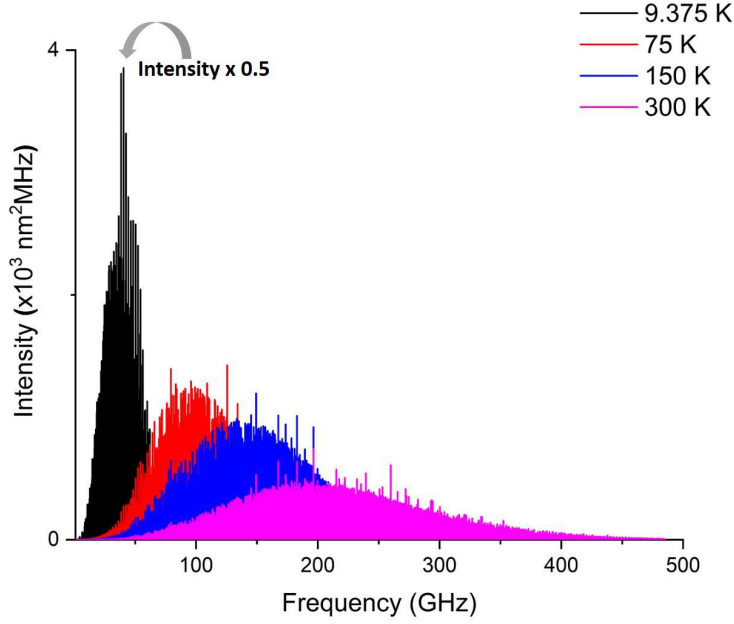


Figure 3.6: Distribution of rotational transitions at different temperatures. It is important to note that the intensity scale for $T = 9.375$ K has been halved for better comparison.

In the experimental set-ups discussed above, the pre-expansion region (P_0) and the expansion region (P_B) are separated by a pulsed nozzle. With each pulse, the ensemble of molecules seeded in the carrier gas is introduced into the vacuum chamber. This is followed by the interaction with the excitation radiation in the zone of silence (as shown in Figure 3.5). It is called the zone of silence due to the low density of particles and the lack of collisions between the particles that are present. The length of the zone of silence, x , can be calculated by the following expression, where D is the diameter of the orifice separating the pre- and post-expansion zones.

$$x = 0.67D\sqrt{\frac{P_0}{P_B}} \quad (3.4)$$

For our experiments, we usually use backing pressure, P_0 , in the range of 1-3 bar, and the vacuum chamber has the pressure, P_B in the order of 10^{-5} bar. This allows for the zone of silence to be long enough for spectroscopy to take place.

3.6 Molecular beam setup at FELIX

FELIX stands for: Free-Electron Lasers for Infrared eXperiments. The molecular beam set-up is located in the FELIX laboratory, Nijmegen, the Netherlands [82] where we performed mass selected IR-UV ion dip spectroscopy. The molecular beam setup is coupled with the infrared free electron laser (FELIX) that can operate in the range of $66 - 3600 \text{ cm}^{-1}$. The detailed description of the different IR lasers available at the facility can be found at the website*. We used this technique to study the electrical discharge of a silicon-containing molecule, phenylsilane to gain spectroscopic insights into the formation of various silicon-substituted cyclic molecules. Using resonance-enhanced multiphoton ionization (REMPI), the majority of discharge products (with electronic energy levels resonant with the UV lasers) formed can be efficiently ionized. Following this, IR-UV ion dip spectroscopy was performed to obtain the vibrational spectra of the discharge products in their electronic ground state. Together with quantum chemical calculations, we can then assign the structures of the various silicon-containing molecules formed as a result of the electrical discharge experiment of phenylsilane. The technique can be divided into the following parts:

- Electrical discharge (discussed in Section 3.4)
- Supersonic expansion (discussed in Section 3.5.2)
- Resonance-enhanced multiphoton ionization (REMPI) as discussed in Section 3.6.1
- IR-UV ion dip spectroscopy (discussed below)

3.6.1 Probing the structures of silicon-containing discharge products with IR-UV ion dip spectroscopy

The electrical discharge experiment of phenylsilane was performed at the FELIX laboratory [82] using mass-selective IR-UV ion dip spectroscopy coupled with an electrical discharge source. Argon (at 5 bar) was passed through the reservoir containing phenylsilane and the molecular gas pulse was created using a general valve. Prior to supersonic expansion into the vacuum chamber, the gas pulse was subjected to a voltage of 0.75 kV. A current of 50 mA was found optimal for the formation of a m/z ratio larger than that of the precursor molecule. The expanding gas pulse containing the mixture of newly formed species, precursor molecule, and carrier gas was passed through the skimmer before it could interact with the laser beams

*<https://www.ru.nl/felix/about-felix/about-felix/felix-laboratory/>

to perform IR-UV ion dip spectroscopy and mass spectrometry. Subsequently, the formed fragments and products present in the molecular beam were ionized using $[1+1']$ REMPI with excitation by a dye laser at 266 nm and ionization with an ArF laser (193 nm). For each mass channel with decent intensities in the $[1+1']$ REMPI mass spectrum, an IR spectrum was recorded in the $550 - 3200\text{ cm}^{-1}$ region using the IR-UV ion dip method with the free electron laser FELIX-2. The repetition rate of the IR laser was set to half with respect to the rest of the experiment (10 Hz) to acquire alternating IR on and IR off shots to avoid shot-to-shot ion signal fluctuations. Detailed information about the experiment can be found in Chapter 8.

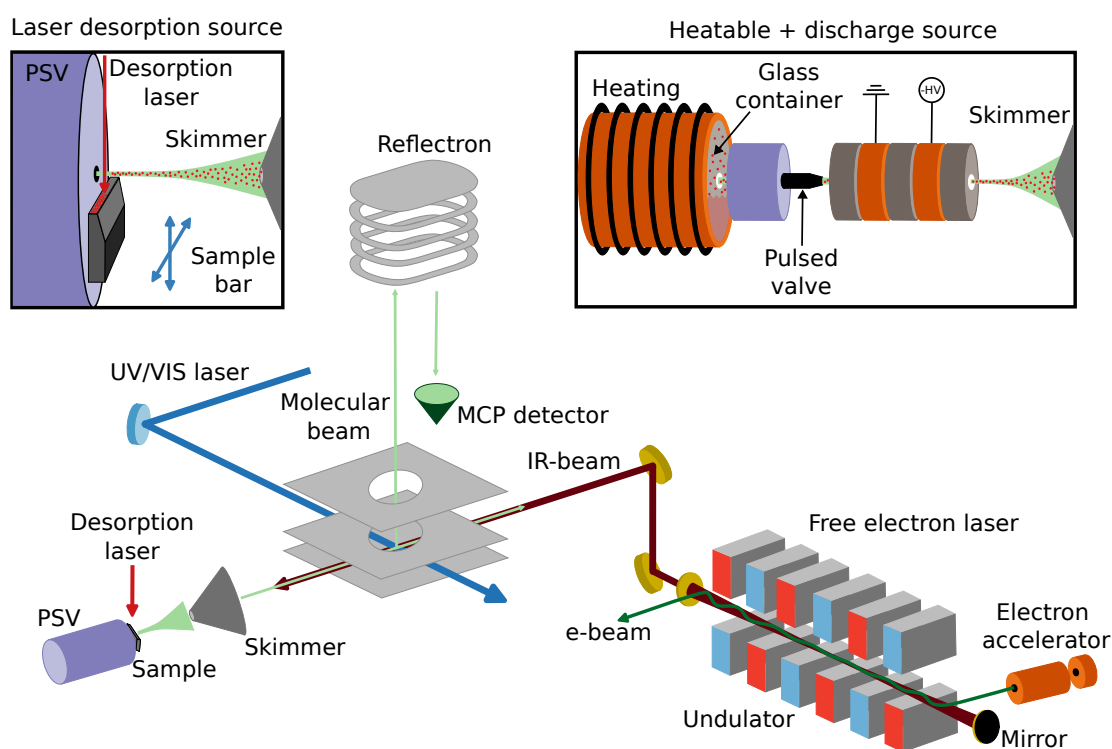


Figure 3.7: Schematics of the mass resolved IR-UV ion dip spectroscopy set-up at FELIX

3.7 Ultra-high vacuum-reflection absorption infrared spectroscopy

An ultra-high vacuum apparatus consisting of a tunnel chamber connected to the load-lock, growth/preparation chamber, reflection absorption infrared spectroscopy (RAIRS or IRRAS), and X-ray photoelectron spectroscopy (XPS) is available in the DESY NanoLab [87]. This facility can be used for surface preparation and controlled nanoparticle growth that allows the user to use surface science techniques like IRRAS to investigate the growth processes on well-defined metal and oxide single-crystal surfaces in ultra-high vacuum (UHV) conditions. Moreover, controlled adsorption experiments on clean single-crystal surfaces require ultra-high vacuum (UHV) conditions, as it is important for adsorption studies to ensure that only the desired molecules reach the surface. UHV is typically referred to as the pressure range below 10^{-8} mbar, however, most UHV setups operate below 10^{-9} mbar. At this pressure, the number of residual gas molecules is below 10^8 per cm^3 and it takes around an hour for a substrate to be covered by a complete monolayer of adsorbates. The mean free path, which denotes the distance a molecule can travel without hitting another molecule, is then in the order of 50 km [88]. UHV conditions are essential to study clean surfaces since they become covered with water, carbon (from CO_2), or other contaminants within milliseconds when working in the atmospheric or low vacuum pressure range. We used a state-of-the-art Fourier transform IR spectrometer (Bruker, VERTEX 80v) to carry out reflection-absorption IR experiments to study the growth of water ice on naphthalene, the simplest polycyclic aromatic hydrocarbon under UHV conditions.

An iridium single crystal surface, Ir(111) which was mounted on a molybdenum sample holder by tantalum clips, was used to grow the naphthalene and water ice layers and reflect the signal into an external mercury cadmium telluride (MCT) infrared (IR) detector that was cooled using liquid nitrogen. The Ir(111) surface was first cleaned in the preparation chamber by repeated cycles of Ar sputtering and O_2 annealing and checked with low-energy electron diffraction (LEED) and Auger electron spectroscopy (AES). A thorough description of the cleaning process is given in Chapter 7. Both naphthalene and water were placed in separate glass vials on the gas supply line of the IR chamber and their vapors were sequentially introduced into the chamber in steps via the leak valves and absorbed on the cooled Ir(111) surface. The polarized IRRAS spectra were measured for each exposure step. The sample exposures were reported in units of Langmuir (L) ($1 \text{ L} = 1.33 \times 10^{-6} \text{ mbar/s}$). The base pressure in the IR measurement chamber is 2×10^{-10} mbar. All IRRAS spectra were collected by averaging 200 scans at a resolution of 2 cm^{-1} between 500 and 4500 cm^{-1} using the *p*-, *s*-, and non-polarized IR light, respectively.

FT-IR spectroscopy under UHV conditions allows us to study the surface proper-

ties during deposition of molecules of interest on the surface. As a result of it the change in the vibrational spectra can be monitored. Measurement techniques that can quantify and possibly separate the surface signal from the bulk signal are of sheer importance here. Spectroscopic techniques such as Fourier transform infrared reflection absorption spectroscopy (FT-IRRAS) are used to investigate the characteristic molecule vibrations and provide insights into the adsorption geometry.

Chapter 4

The missing conformer: A comprehensive rotational spectroscopy study and astronomical search of two conformers of methyl cyanoacetate

This chapter is based on the following publication:

- G. Batra, P. Pinacho, A. L. Steber, V. M. Rivilla, J. M. Pintado, I. J. Serra, M. Schnell *The missing conformer: A comprehensive rotational spectroscopy study and astronomical search of two conformers of methyl cyanoacetate*, *Frontiers in Astronomy and Space Sciences*, **9**, 977488 (2022).
- Own contributions:
 - rotational spectroscopic measurements
 - quantum-chemical calculations
 - data analysis
 - writing of paper draft

4.1 Introduction

In the recent years, there has been an acceleration in the pace of detection of molecules in the interstellar medium (ISM). As of August 2022, around 270 molecules have been detected in the interstellar medium or circumstellar shells, comprising of

19 different chemical elements. The majority of these molecules have been detected using radio astronomy since the 1960s with an approximate rate of ~ 4 detections/year since 1968 and ~ 6 detections/year since 2005 [20]. The detection rate has increased significantly, for instance, around 45 new molecules have been detected in the last 1.5 years. Updated lists of detected molecules in space can be found in the Cologne Database for Molecular Spectroscopy* and on astrochymist.org†. This increase in the detection rate can be attributed to two factors; on one hand, to the technical advances in the field of radio astronomy and facilities such as the Atacama Large Millimeter/submillimeter Array, the Green Bank Telescope or the Yebes 40-m telescopes [20]; and on the other hand, to the increase in laboratory-based rotational spectroscopy studies of potential molecules of astrochemical interest, which provide detailed spectroscopic parameters required for their search in the ISM. With the development of chirped-pulse Fourier-transform microwave (CP-FTMW) spectrometers [8], the measurement times for broadband, high-resolution microwave spectra have become several orders of magnitude faster than what was previously possible. Due to a combination of both factors, larger and more complex molecules are becoming targets for searches in the ISM. As a starting point for the detection of a new compound, it is useful to study derivatives of molecules which have already been detected, for example, by including additional functional groups. One of the most abundant functional groups in the ISM is the cyano group ($-\text{C}\equiv\text{N}$). It is present in more than 15% of the detected molecules [20]. The prevalence of cyano-containing molecules can be attributed to the substantial electric dipole moment of the molecule introduced by the cyano group. Since most of the molecules are detected based on their rotational fingerprint, a large value of the electric dipole moment facilitates their observation, as the rotational transition intensities are dependent on the electric dipole moment.

Additional features, such as the observation of transitions from highly excited torsional states or splittings due to large amplitude motions, could direct towards the detection of certain classes of molecules [89, 90]. The internal rotation of a methyl top ($-\text{CH}_3$) is hindered by a finite three-fold potential. This induces a quantum tunneling effect, which leads to the splitting of each rotational level into a non-degenerated A state and a doubly degenerated E state. Internal rotors play an important role in the astrophysical environment. Not only do they act as unique indicators of the chemical structure of Complex Organic Molecules (COMs) [91] through the observation of the A/E splitting, they also carry valuable information about the physical conditions of the surrounding environment. For example, the population of torsionally excited states of the molecules containing internal rotors can provide information on the temperature of the surrounding region [90]. To date,

*<https://cdms.astro.uni-koeln.de/classic/molecules>

†<http://www.astrochymist.org/>

many complex molecules with internal rotors have been identified in the ISM [91], as well as in comets, meteorites and asteroids [90, 92, 93]. The millimeter wave spectra of hot cores, such as Sagittarius B2 or the Orion molecular cloud, are dominated by the rotational-torsional spectra of small molecules with internal rotors, such as methanol (CH_3OH) and methyl formate (HCOOCH_3). An insightful review of the spectroscopy of interstellar internal rotors is given in reference [89].

To obtain a more detailed catalog of the detected molecules in the ISM, their different low-energy conformers must be considered. The majority of the detections in the ISM are reported for the lowest energy conformer, but extending this study to other energetically accessible conformers can help to evaluate the physical and chemical environment of the detection region. Moreover, it is possible to obtain accurate column densities when all the populated conformers are included, rather than based on the presence of the lowest energy variant. This is described in detail for the case of the *trans* and *gauche* conformations of ethanol [94, 95].

Methyl cyanoacetate (MCA), $\text{NCCH}_2\text{COOCH}_3$, is an excellent candidate for a future astronomical detection, as it is a derivative of an already detected molecule, methyl acetate, $\text{CH}_3\text{COOCH}_3$ [96]. MCA contains an ester and a cyano functional group, responsible for fine and hyperfine structure, respectively. The fine structure is due to the internal rotation of the $-\text{CH}_3$ group linked to the ester oxygen, while the hyperfine structure is generated due to nuclear quadrupole coupling, caused by the presence of a ^{14}N nucleus ($I = 1$) in the cyano part of the molecule.

MCA has been studied previously using vibrational spectroscopy in the liquid [97] and in the solid phases [98] to obtain information regarding the different geometries and relative energies of the conformers. Both studies concluded the presence of more than one conformer based on several unassigned bands in the infrared spectra. Later on, a detailed infrared study was conducted to obtain more information on the lowest energy conformers by analyzing data from the vapor phase and from solutions in liquid argon [99]. This was followed by an in-depth analysis of the vibrational features in liquid [100], solution [101], and by matrix isolation techniques [102, 103]. Based on the previous studies and chemical intuition, MCA can adopt four possible geometries in view of the orientation of the methyl group of the ester fragment and the cyano fragment in the *syn* or *anti* orientation with respect to the carbonyl group. Recently, a high-resolution rotational spectroscopy study of MCA was reported for the lowest energy conformer, with insights into the internal rotation barrier for the methyl top and the nuclear quadrupole coupling constants for the ^{14}N nucleus [104]. However, all the previous vibrational spectroscopy studies and the theoretical calculations predict the presence of a second conformer with a large dipole moment of around 5 Debye and close in energy with respect to the first conformer.

In the present work, we report the detailed characterization of the second conformer of MCA as well as an extension of the spectral range for the first conformer up

to 110 GHz using rotational spectroscopy. The comprehensive rotational spectroscopic characterization of both conformers covering a broad spectral range (2-110 GHz in selected frequency regions) can aid their detection in the ISM using the high-sensitivity radio telescopes. It also emphasizes the need of extending the observational searches not only to the lowest energy conformer but to other energetically accessible conformers as well. This can also be seen in the study reporting the interstellar detection of conformer pairs of ethyl formate ($\text{C}_2\text{H}_5\text{OCHO}$) [105] and C-cyanomethanimine (HNCHCN) [106], where the energy difference between their conformers is small enough for both conformers to exist in the thermodynamic equilibrium at the kinetic temperature (T_k) of the gas.

4.2 Theoretical work

To facilitate the experimental analysis, quantum-chemical calculations were performed using the ORCA program package [60, 61] and Gaussian 09 program package [62]. The geometry optimization calculations for the different conformers of MCA were performed with the Gaussian 09 program [62] employing anharmonic force fields. The set of obtained rotational constants, nuclear quadrupole coupling constants, dipole moments, and centrifugal distortion constants were used to simulate the rotational spectrum. A relaxed scan of the torsional potential was performed to obtain an initial value for the barrier height of the internal rotation motion of the methyl top. A more detailed description of the calculations is provided below.

The conformational space of MCA can be described by the possible values of two dihedral angles, θ and ϕ , given by $\text{NC-CH}_2\text{-C=O}$ and $\text{H}_3\text{C-O-C=O}$, respectively, as shown in Figure 4.1. As a result, four different conformations are possible for MCA, as listed in Table 4.1 with both functional groups, $-\text{C}\equiv\text{N}$ and $-\text{COOCH}_3$, being in -syn or -anti arrangement with respect to the carbonyl group. Geometry optimizations and anharmonic frequency calculations for the four possible conformers of MCA were performed at the B3LYP-D3/aug-cc-pVTZ level of theory. The two lowest energy conformers (hereafter, MCA_1 and MCA_2) with an energy difference of 1.4 kJ/mol are energetically accessible under our experimental conditions. The other two conformers, MCA_3 and MCA_4, are significantly higher in energy (~ 30 kJ/mol and ~ 36 kJ/mol, respectively) with respect to the lowest energy conformer MCA_1 and hence are not expected to be observed under our experimental conditions. The computed rotational constants, dipole-moment components, and zero-point corrected relative energies are given in Table 4.1. The energy difference between the two lowest energy conformers computed at the B3LYP-D3/aug-cc-pVTZ level of theory is within the method uncertainty. Consequently, additional single-point energy calculations were performed using the RI-MP2/cc-pVTZ level of theory and the DLPNO-CCSD(T)/CBS extrapolation based on aug-cc-pVnZ ($n=\text{T}, \text{Q}$) cal-

culations, with TightPNO settings using the geometries obtained with the B3LYP-D3/aug-cc-pVTZ structure optimization calculation. The energy difference between MCA_1 and MCA_2 calculated at different levels of theory is summarized in Table 10.5 in Appendix 10.1. Interestingly, the energy difference between MCA_1 and MCA_2 decreases from 1.4 kJ/mol at the B3LYP-D3/aug-cc-pVTZ level of theory to only 0.1 kJ/mol at the DLPNO-CCSD(T)/CBS level of theory. To obtain theo-

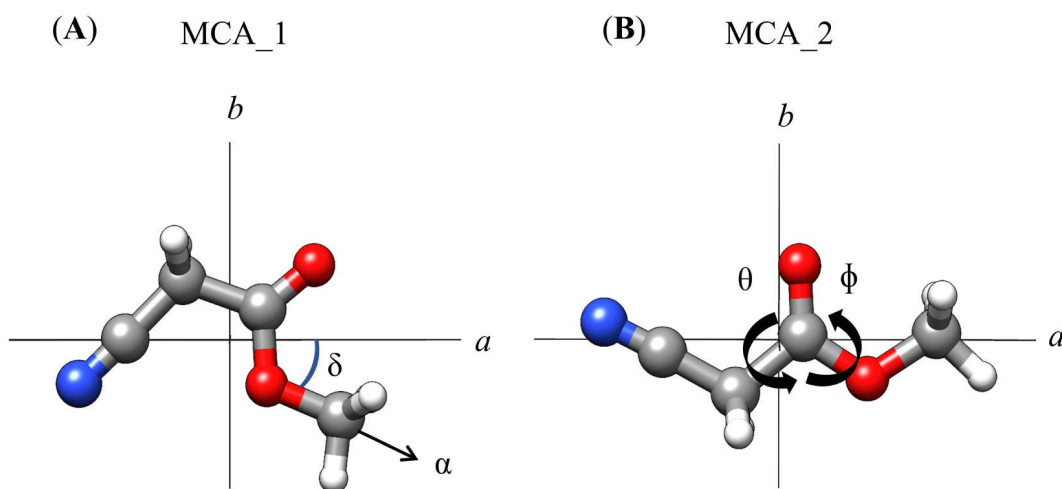
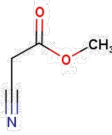
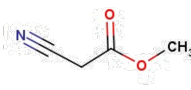
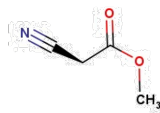
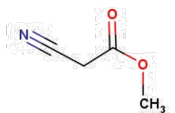


Figure 4.1: Molecular structure and principal inertial axes of MCA_1 (panel (A)) and MCA_2 (panel (B)). The c -axis is perpendicular to the ab -molecular plane. α is the methyl internal rotor axis and δ is the angle between the methyl internal rotor axis and the principal axis a . θ and ϕ are the dihedral angles. The nitrogen atoms are shown in blue, the oxygen atoms in red, the carbon atoms in grey, and the hydrogen atoms are shown in white color.

retical values of the barrier heights for the methyl top internal rotation for both of the lowest energy conformers, one-dimensional potential energy scans (PES) were performed at two different levels of theory, B3LYP-D3/aug-cc-pVTZ and MP2/aug-cc-pVTZ. In the scans, the dihedral angle H-CH₂-O-C was varied in steps of 10°. For each point, all the other parameters were relaxed and the resulting PES is given

in Figure 10.2 in Appendix. The obtained values were used as a starting point for the analysis of experimental barrier height. The comparison of the experimental and theoretical barrier height at both levels of theory is shown in Figure 10.2 in Appendix 10.1.

Table 4.1: Calculated parameters for the conformers of MCA at the B3LYP-D3/aug-cc-pVTZ level of theory.

Rotational parameters	MCA_1	MCA_2	MCA_3	MCA_4
				
A^a/MHz	5077	9509	3786	6231
B/MHz	1830	1407	2264	1624
C/MHz	1368	1244	1592	1309
$\mu_a, \mu_b, \mu_c^b/\text{D}$	2.3/0.6/0	4.5/-3.0/0.0	-0.016447368	4.8/4.7/0.0
$\Delta E^c/kJmol^{-1}$	0	1.4	30.4	36

^a A, B, and C are the rotational constants

^b μ_a, μ_b, μ_c are the electric dipole-moment components

^c Relative zero-point energy

4.3 Experimental details and fitting procedure

The rotational spectrum of MCA was recorded in several frequency ranges, covering 2-26 and 75-110 GHz. Three broadband chirped-pulse Fourier transform microwave/millimeter wave (CP-FTMW) spectrometers were employed, namely, the COMPACT spectrometer (2-18 GHz) [73, 75, 76], the K- band spectrometer (18-26 GHz) [76] and the W-band spectrometer (75-110 GHz) [79]. For the measurements in the range of 2-26 GHz, the sample of MCA was held in a modified pulsed nozzle (Parker Series 9 valve modified to be equipped with an internal heatable reservoir) and heated at 55 °C to increase its vapor pressure. The molecular vapor was then introduced into the vacuum chamber using a supersonic expansion with 2.5 bar of neon as a backing gas. Owing to the supersonic expansion, the resulting rotational temperature goes down to $T_{rot} \sim 1\text{-}3$ K. In the W-band spectrometer, the spectrum

was recorded at room temperature conditions with $T_{rot} \sim 300$ K.

The through description of the spectrometers is given in Chapter 3. Therefore, only a brief description of the working is as follows. The spectrum of MCA in the region between 2-18 GHz was recorded with the COMPACT spectrometer in three parts, 2-8, 8-13, and 13-18 GHz [73, 75, 76]. The excitation chirp is generated by an arbitrary waveform generator (AWG), amplified and transmitted into the vacuum chamber. For the 2-8 GHz region, the excitation chirp is amplified by a 300 W traveling wave tube (TWT) amplifier, while for the 8-13 GHz and 13-18 GHz regions, a 50 W solid state amplifier (SSA) is employed. These excitation pulses are then transmitted into the vacuum chamber and broadcast via a horn antenna, where a macroscopic polarization is induced when a frequency of the chirped excitation pulse is resonant with a molecular rotational transition of the sample. The relaxation of the induced macroscopic polarization of the molecular ensemble is recorded in the form of a free induction decay (FID). The spectrometer uses the fast-frame method, in which each molecular pulse is probed by a successive train of eight excitation chirps followed by recording the respective FIDs. Combined with the gas pulse repetition rate of 8 Hz, an effective repetition rate of 64 Hz was achieved. For the 2-8 GHz experiment, 4 million FIDs (each collected for 40 μ s) were co-added and converted into the frequency domain by a fast Fourier transformation. For both 8-13 and 13-18 GHz, 4.5 million FIDs were co-added (each collected for 20 μ s) and converted into the frequency domain by applying a fast Fourier transformation.

The spectrum across 18-26 GHz was recorded using the K-band spectrometer, which uses the segmented approach [76, 77]. The bandwidth of 8 GHz is divided into 800 MHz segments, which are then concatenated together to produce a spectrum across the whole bandwidth. Similar to the COMPACT spectrometer, this instrument uses a fast-frame set-up of several excitation-detection cycles per molecular gas pulse. The AWG synthesizes 1.5 μ s of excitation pulses in the range of 7-3 GHz. These chirps are then frequency upconverted to 9-13 GHz and doubled to 18-26 GHz. For each gas pulse, the molecular ensemble is polarized by a series of three pulse trains. The multi-train setup was performed simultaneously with a gas pulse repetition rate of 10 Hz, giving an effective repetition rate of 30 Hz. The FIDs were collected (each for 10 μ s), frequency down-converted and co-added, and converted into the frequency domain by fast Fourier transformation. For this experiment, a total of 2.5 million acquisitions were recorded. Unlike the COMPACT and the K-band spectrometer, the spectrum was recorded at room temperature conditions in the W-band spectrometer. The experiment was set up in a slow flow cell condition in order to maintain a constant pressure inside the vacuum chamber. The liquid sample was heated to 55 °C resulting in a constant pressure of 1.5 mTorr in the spectrometer chamber. The instrument also works with the segmented approach in which the 35 GHz bandwidth was covered in segments of 720 MHz each. For this experiment the

high dynamic range (HDR) mode was used, which addresses each segment of 720 MHz by 30 chirps of 24 MHz spectral width each to reduce the spurious content in the measured spectrum [79]. The AWG synthesizes the excitation pulse in the 1.5-2.3 GHz range, which is then frequency upconverted and multiplied through a series of mixing stages and an active multiplier chain ($\times 6$) to produce the radiation in the millimeter-wave regime. A total of one million FIDs (each recorded for 4 μ s) were collected followed by conversion into the frequency domain by fast Fourier transformation. For all the experiments discussed above, the sample of MCA (>97% purity, purchased from Sigma Aldrich) was used without further purification.

The initial spectral analysis of the rotational spectra of MCA was done using the PGOPHER program [57]. The final fitting of the rotational parameters was achieved by using the XIAM program [52] for the simultaneous fitting of the A and E states for the parent species. For the assignment of the singly substituted ^{13}C and ^{15}N isotopologues in natural abundance, the SPFIT/SPCAT suite of programs [107] was used to fit the A state transitions. The r_s structure analysis was performed with the KRA program package, followed by the calculation of the bond lengths and angles using the EVAL program. The effective structure $r_m^{(1)}$ was performed with the STRFIT program. All of these programs are available on the PROSPE website [53]. More details on the methods of structure determination can be found in Section 2.1.8. The AABS package [53, 108] was used for displaying the predicted transitions and measuring the experimental frequencies.

4.4 Results and discussion

The structures and principal axes for MCA_1 and MCA_2 are shown in Figure 4.1. Both conformers have a near prolate symmetry, as depicted by the values of Ray's asymmetry parameter, κ :

$$\kappa = \frac{2B - A - C}{A - C} \quad (4.1)$$

The experimentally obtained value of κ is -0.75 for MCA_1 and -0.96 for MCA_2. Note that MCA_1 consists of an enantiomeric pair where the cyano group is rotated out of the plane of the ester fragment by $\pm 20^\circ$. The interconversion pathway between the two enantiomers is essentially barrierless, as the calculated vibrational ground state lies above the calculated interconversion transition state at the B3LYP-D3/aug-cc-pVTZ level of theory, as shown in Figure 10.1 in Appendix 10.1. The interconversion pathway of MCA_1 is also discussed in detail by Gregory *et al.* [104]. From the dihedral scan around NC-CH₂-CO, the barrier height between MCA_1 and MCA_2 was found to be ~ 2 kJ/mol, as shown in Figure 4.3 [104]. For both conformers of MCA, the spectra recorded with the COMPACT and the K-band spectrometers show resolvable fine structure due to internal rotation and hyperfine structure

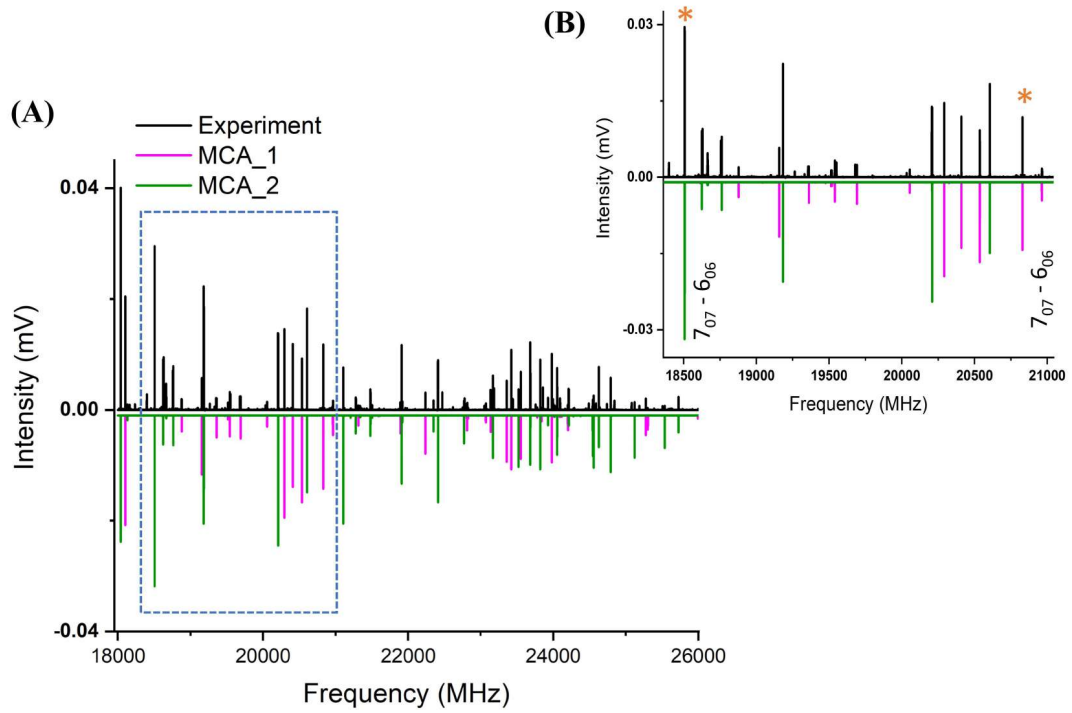


Figure 4.2: Panel (A) shows the rotational spectrum of MCA recorded with the K-band spectrometer in the 18-26 GHz region. The upper black trace is the experimental spectrum, the lower colored traces are the simulated spectra based on the fitted rotational constants at 3 K for both conformers of MCA (MCA_1 in magenta and MCA_2 in green). The zoom-in (panel (B)) illustrates the assignment and the intensity ratio of the two conformers. The rotational transition $J_{K_a, K_c} - J'_{K'_a, K'_c} = 7_{0,7} - 6_{0,6}$ is marked with an asterisk to highlight the difference in intensities for MCA_1 and MCA_2. Note that the transition intensities in different parts of the spectrum can be influenced by frequency-dependent instrumental effects, such as the amplifier performances.

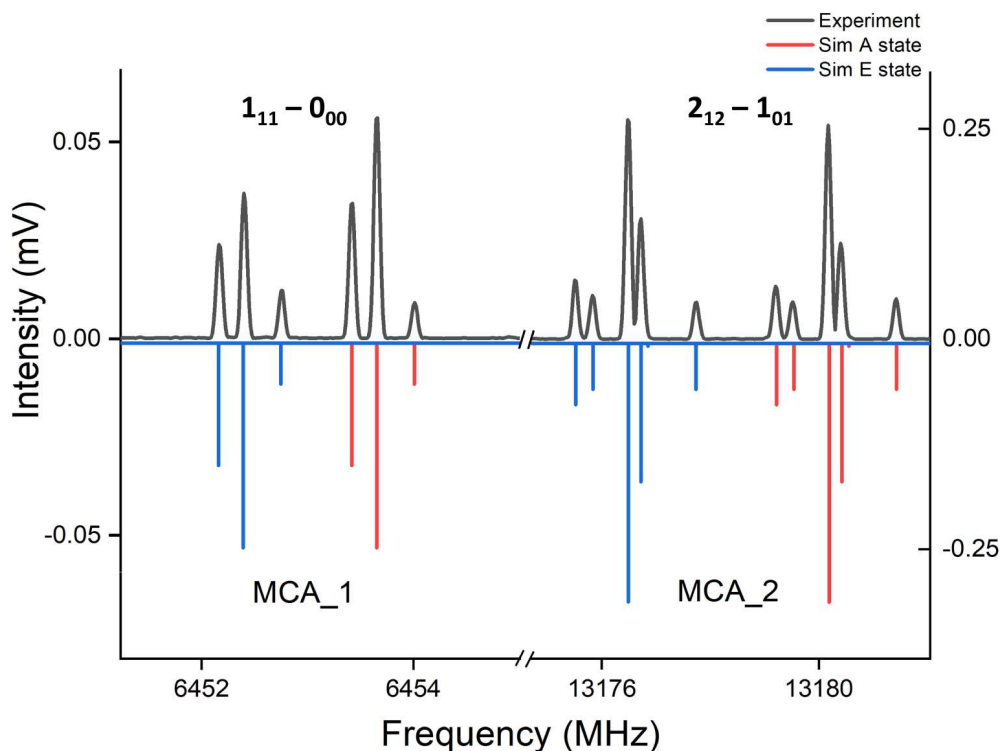


Figure 4.3: The upper trace shows a part of the experimental rotational spectrum of MCA, highlighting the internal rotation splitting (red and blue) followed by the splitting due to nuclear quadrupole coupling. The bottom trace shows the simulation based on the fitted rotational constants.

(HFS) due to nuclear quadrupole coupling. Each rotational transition is split into A and E components due to the internal rotation of the methyl group, and it is further split due to the interaction of the nuclear spin, $I(^{14}\text{N})=1$, with the electric field gradient. The pattern and the span of the splitting for one of the transitions can be clearly seen in the Figure 4.3, where a section of the rotational spectrum is shown together with the simulated spectra employing the fitted constants for MCA_1 and MCA_2. The comprehensive analysis of the above-mentioned effects on the rotational spectra allowed us to effectively determine the nuclear quadrupole coupling constants for ^{14}N and the experimental barrier height (V_3) for the methyl internal rotor for both conformers of MCA. The comparison between the experimental and theoretical rotational constants is shown in Table 4.2. The two sets of rotational constants agree well within less than 1%. The comparison is further extended to the previous rotational spectroscopy study done on MCA_1 [104]. In the present

work, more than 600 new transitions are added to the existing line list of MCA_1 while extending the probed J quantum number up to 39 in comparison to $J = 6$ as reported in reference [104].

The set of experimentally determined rotational parameters given in Table 4.2 are obtained from the global fit (combined fit for the low and high frequency dataset) for each of the conformers, including the transitions between 2-110 GHz. The data were fit to a Watson S reduction Hamiltonian in an I'' representation. The XIAM software [52] was used for the fitting procedure as it can yield the barrier height (V3) of the methyl internal rotation and nuclear quadrupole coupling constants simultaneously. The experimentally obtained barrier heights (4.4822(20) kJ/mol for MCA_1 and 4.7909(7) kJ/mol for MCA_2) are closer to the value predicted using MP2/aug-cc-pVTZ (4.5 kJ/mol for MCA_1 and 4.6 kJ/mol for MCA_2) as compared to the ones predicted using B3LYP/aug-cc-pVTZ (3.2 kJ/mol for MCA_1 and 3.2 kJ/mol for MCA_2). In the XIAM fit, the internal rotation parameter, ε , was fixed to zero. ε is the angle between the projection of the methyl axis onto the bc -plane and the b -axis, but as the molecule lies in the ab -inertial plane, it makes the methyl internal rotation axis and b -axis coplanar, as shown in Figure 4.1.

In the high frequency region (75-110 GHz), the HFS is not resolved as the splitting collapses with increase in the J quantum number. Hence the nuclear quadrupole coupling constants were determined from the low-frequency dataset alone. To obtain a global fit included all covered frequency regions, the transitions with resolved HFS and transitions with unresolved HFS were included together in the same line list. In the high frequency region, for each rotational transition with unresolved HFS we assigned the three most intense HFS components to the same experimental frequency without increasing the uncertainty for these merged transitions.

In addition to the XIAM fit, fits including only the A-state transitions for both MCA_1 and MCA_2 were performed with the SPFIT/SPCAT suite of programs [107] for the astronomical searches in different regions of the ISM. The experimental constants obtained for both conformers are given in Table 10.1 and Table 10.2 in Appendix 10.1. The line list contains the assigned experimental frequencies together with their uncertainties. The .cat files generated with the SPCAT program contain predicted transition frequencies up to 150 GHz based on the fitted rotational parameters. The predicted uncertainties for transitions up to 150 GHz are predominantly less than 1 MHz and therefore should be highly reliable for the search of MCA in the ISM. For instance, there are more than 250 transitions for MCA_1 and more than 2000 transitions for MCA_2 with uncertainties below 40 kHz in the frequency range of 84-116 GHz (ALMA Band 3).

Table 4.2: Experimental and theoretical rotational parameters for the two observed conformers of MCA. The theoretical rotational parameters were obtained at the B3LYP-D3/aug-cc-pVTZ level of theory.

Rotational parameters	MCA_1			MCA_2	
	Experiment (This work)	Previous study [104]	Theory	Experiment (This work)	Theory
A^a/MHz	5069.2812(13) ^h	5069.2803(10)	5077	9429.0621(20)	9509
B/MHz	1842.95598(29)	1842.95524(23)	1830	1413.55699(12)	1407
C/MHz	1383.81701(17)	1383.81674(17)	1368	1249.82319(12)	1244
D_J^b/kHz	0.5057(18)	0.5087(19)	0.13	0.136320(42)	0.11
D_{JK}/kHz	1.074(38)	1.102(12)	6.64	-0.46472(26)	4.09
D_K/kHz	4.50(13)	[2.07]	10.25	12.24(47)	9.63
d_1/kHz	-0.17502(95)	-0.1769(20)	-0.02	-0.020225(30)	0.03
d_2/kHz	-0.04112(25)	-0.0458(14)	-0.03	-0.001776(37)	0
χ_{aa}^c/MHz	-1.1936(60)	-1.1924(24)	-1.39	-2.9569(53)	-3.38
χ_{bb-cc}/MHz	-2.767(10)	-2.7648(12)	-3.23	-1.103(10)	-1.23
$V_3^d/\text{kJ} \cdot \text{mol}^{-1}$	4.4822(20)	4.579(6)	4.5 ⁱ	4.7909(7)	4.6 ⁱ
F_0^e/GHz	161.84	160.34(22)	-	159.6052	-
δ^f/rad	0.4706(40)	0.4829(7)	-	2.6672(20)	-
σ^g/kHz	45	2.4	-	44	-
No. of lines	794	153	-	1580	-
J/K_a	39/4	6/3	-	43/27	-

^a A, B, and C are the rotational constants.

^b D_J , D_{JK} , D_K , d_1 , and d_2 are the quartic centrifugal distortion constants.

^c χ_{aa} , χ_{bb} , and χ_{cc} represent the diagonal elements of the ^{14}N nuclear quadrupole coupling tensor.

^d V_3 is the potential barrier in a three-fold methyl internal rotation top.

^e F_0 is the rotational constant of the methyl top.

^f δ is the angle between the internal rotation axis and the a -axis.

^g Microwave root-mean-square deviation of the fit.

^h Statistical uncertainties are given in parentheses in units of the last digit.

ⁱ Theoretical potential barrier to the methyl internal rotation computed at the MP2/aug-cc-pVTZ level of theory.

4.4.1 Rotational partition function and transition intensities for MCA_1 and MCA_2

To facilitate the astronomical searches for MCA, in addition to providing accurate rest frequencies for the two assigned conformers, information on the relative intensities of the rotational transitions at different temperatures is also calculated from the rotational partition function. The rotational partition function, Q_{rot} , represents the accessible rotational energy states at a given temperature for a molecule. For an asymmetric top, it is approximated as

$$Q_{\text{rot}}^{\text{asymmetric}} = \frac{5.34 \times 10^6}{\sigma} \sqrt{\left(\frac{T^3}{ABC}\right)} \quad (4.2)$$

where σ is the symmetry parameter, T the sample temperature (K), and A , B , and C the rotational constants of the molecule (MHz) [45]. The rotational partition function can be useful for calculating absorption coefficients and hence the transition intensities, which can be further used for the calculation of column densities of the species of interest [109].

As Q_{rot} depends on the temperature, changing the temperature results in a change of the intensity distribution of the observed rotational transitions. This can be seen in Figure 4.4, which shows the simulated spectra for MCA_1 and MCA_2 based on their μ_a dipole-moment components and calculated partition functions at 3 K and 300 K, respectively. In the present work, Q_{rot} is calculated for two spin states, $I = 0$, spin degeneracy $2I + 1 = 1$, where hyperfine structure is not considered, and for $I = 1$, spin degeneracy $2I + 1 = 3$, considering the hyperfine structure caused by nitrogen with $I(^{14}\text{N})=1$, as shown in Table 4.3. The rotational partition function is calculated for the A state transitions of both MCA_1 and MCA_2, across standard temperatures, as implemented in the JPL database (Table 4.3) [110].

The rotational transition intensities are proportional to the product of $\mu^2 \cdot N_i$, μ being the dipole-moment component associated with the transition, and N_i being the fraction of molecules in the ground state of that transition. MCA_1 and MCA_2 can be considered to be essentially isoenergetic, although all our quantum-chemical calculations predict MCA_2 to be slightly higher in energy than MCA_1. However, the substantially higher dipole-moment component of MCA_2 compensates for it. In general, the observed a-type transitions for MCA_2 are of similar intensity or more intense than those for MCA_1, as μ_a is 2.3 D for MCA_1, while μ_a is 4.5 D for MCA_2. In Figure 4.2, the rotational spectrum recorded in 18-26 GHz is shown. Panel B highlights the intensity difference observed for MCA_1 and MCA_2 (marked by an asterisk) for the rotational transition $7_{07}-6_{06}$. Note that these marked transitions are ~ 2.5 GHz apart, so that instrumental effects, such as the frequency dependencies of the horn antennas and the amplifier gains, can influence the absolute intensity. However, the overall higher intensity of rotational transitions for MCA_2

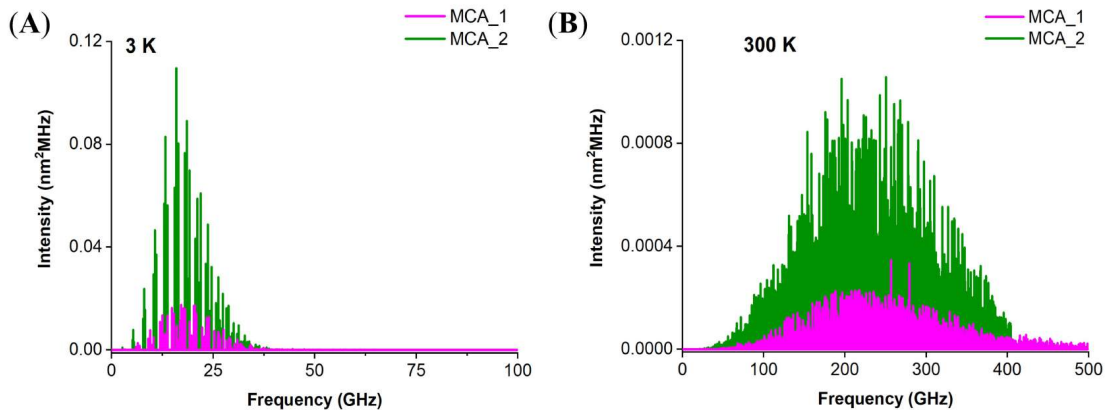


Figure 4.4: The distribution of the rotational transitions of MCA_1 (magenta) and MCA_2 (green) at 3 K (left, panel (A)) and at 300 K (right, panel (B)). The spectra were simulated up to 500 GHz and J quantum numbers up to 100. The plot was made for the case of $2I + 1 = 1$, considering only a -type transitions. Note the different intensity scales for the two panels.

compared to MCA_1 has been observed in our experiments, especially in the W -band region (75–110 GHz). This observation is supported by the total number of assigned transitions. For MCA_1, a total of 794 transitions were assigned with a J quantum number up to 39 in comparison to 1580 assigned transitions for MCA_2 with a J quantum number up to 43, shown in the Table 4.2.

4.4.2 Interstellar search towards the G+0.693-0.027 molecular cloud

We conducted a search for both conformers of MCA using a high sensitivity spectral survey carried out towards the G+0.693-0.027 molecular cloud (hereafter G+0.693), located in the Sgr B2 region of the Galactic Center. This region is one of the most chemically rich sources in the ISM, including many species with the cyano group ($-C\equiv N$), such as cyanoacetylene (HC_3N), acetonitrile (CH_3CN), cyanamide (NH_2CN), the cyanomethyl and the cyanomidyl radicals (H_2CCN and $HNCN$, respectively), C-cyanomethanimine ($HNCHCN$), cyanic acid ($HOCN$), and glycolonitrile ($HOCH_2CN$) [106, 111–113]. This makes G+0.693 a suited interstellar source to search for MCA.

We used the IRAM 30m telescope (Granada, Spain) and the Yebes 40m telescope (Guadalajara, Spain). The observations were centred at $\alpha(J2000.0) = 17^h47^m22^s$, and $\delta(J2000.0) = -28^\circ21'27''$. The position switching mode was used in all the ob-

Table 4.3: Rotational partition function (Q_{rot}) calculated across the standard temperatures implemented in the JPL database [110]

	MCA_1		MCA_2	
T/K	$Q_{rot}[2I + 1 = 1]^a$	$Q_{rot}[2I + 1 = 3]^b$	$Q_{rot}[2I + 1 = 1]^a$	$Q_{rot}[2I + 1 = 3]^b$
300	130946.9811	392806.8398	109601.70	328691.10
225	104461.3874	313353.2984	86967.91	260811.73
150	70438.5067	211294.9274	59020.07	177000.75
75	29606.4782	88819.4714	25600.40	76785.97
37.5	10768.9748	32309.4462	9470.87	28411.75
18.75	3811.7874	11435.8468	3356.85	10070.55
9.375	1349.1161	4047.4297	1188.08	3564.25
1.5	87.4177	262.2544	76.90	230.69

^a $I = 0$, assuming no hyperfine structure

^b $I = 1$, considering hyperfine structure

servations with the off position located at $\Delta\alpha = -885''$, $\Delta\delta = 290''$ from the source position. In this work, we have used data covering the spectral windows from 31.3 GHz and to 50.6 GHz (Yebes telescope) and from 71.8 to 116.7 GHz (IRAM 30m telescope). The line intensity of the spectra was measured in units of T_A^* (antenna temperature as a scale) as the molecular emission toward G+0.693 is extended over the beam [114], [111, 115, 116]. More details about the observations can be found in references [112, 117].

MCA was searched for in the observational data using the SLIM (Spectral Line Identification and Modelling) tool within the MADCUBA package (version 11/03/2022) [118]. The rotational spectroscopy data for the A state transitions presented in this work was implemented into the SLIM tool, which enabled us to generate the synthetic spectra of both conformers of MCA under the assumption of local thermodynamic equilibrium (LTE).

None of the MCA conformers were detected towards the G+0.693 molecular cloud. Therefore, we have computed upper limits for their molecular column densities (N) using the brightest transitions according to the synthetic LTE model generated by SLIM. We used typical values for the physical parameters: excitation temperature, $T_{ex}=10$ K, full width half maximum, FWHM=10 km s⁻¹, and velocity, $v_{LSR}=69$

km s⁻¹. The brightest transitions predicted by the LTE model within the spectral survey are the 120,12-110,11 transitions, at 34.528700 GHz ($E_{up} = 11.01$ K) and at 31.320023 GHz ($E_{up} = 9.78$ K) for MCA_1 and MCA_2, respectively. Figure 4.5 shows the observed spectrum around these frequencies, where no clear line emission is detected. We measured a noise level (σ) in the velocity range of ± 300 km s⁻¹ around these transitions (Figure 4.5) of 1.5 and 2.7 mK for MCA_1 and MCA_2, respectively. We derived the column density upper limits (A states) of $< 1.2 \times 10^{13}$ cm⁻² for MCA_1 and $< 0.4 \times 10^{13}$ cm⁻² for MCA_2, using the 3σ value of the integrated intensity, see further details in reference [118]. Using the column density of molecular hydrogen, $N(\text{H}_2) = 1.35 \times 10^{23}$ cm⁻², the molecular abundances (A states) were derived to be $< 9 \times 10^{-11}$ and $< 3 \times 10^{-11}$ for MCA_1 and MCA_2, respectively. Despite the noisier spectrum around the MCA_2 transitions, the most stringent upper limit was obtained for this higher energy conformer, due to its larger dipole moment. Note that since we only focus on the A state transitions here, the actual upper limits for the abundances of MCA_1 and MCA_2 can be expected to be somewhat higher than the values reported here.

MCA is a complex organic molecule with twelve atoms, containing seven heavy atoms, namely, four carbon (C), two oxygen (O), and one nitrogen (N) atoms. So far, the most complex CON-bearing species detected in the ISM are ethyl isocyanate ($\text{CH}_3\text{CH}_2\text{NCO}$) [39] and ethanolamine ($\text{NH}_2\text{CH}_2\text{CH}_2\text{OH}$) [44], both detected towards G+0.693. These two molecules are somewhat lighter than MCA, since they contain ten and eleven atoms, respectively, and only four heavy atoms. The abundances found for ethyl isocyanate and ethanolamine are $\sim (0.5-1.5) \times 10^{-10}$. The upper limits of the A states of two MCA conformers derived in this work are $< (0.3-0.9) \times 10^{-10}$, i.e., similar to the abundances of the simpler CNO-species ethyl isocyanate and ethanolamine. Since MCA is a more complex molecule, it is not surprising that its abundance in the ISM is lower. This is in good agreement with the observed general trend of decreasing abundances with increasing chemical complexity found for several chemical families [111, 118]. Therefore, to detect more complex species such as MCA, and to study the growth of chemical complexity in the ISM, deeper observations with higher sensitivities are needed, which will allow us to address the detection of complex species with abundances $< 10^{-11}$.

4.4.3 Structure determination

Due to the high signal-to-noise ratio for the two conformers in the 2-26 GHz frequency range, we were able to assign the rotational spectra of the singly substituted ¹³C and ¹⁵N isotopologues in natural abundances of 1.1% and 0.4%, respectively. From this information, we could determine the structures of the two conformers of MCA using the substitution structure and the effective structure methods.

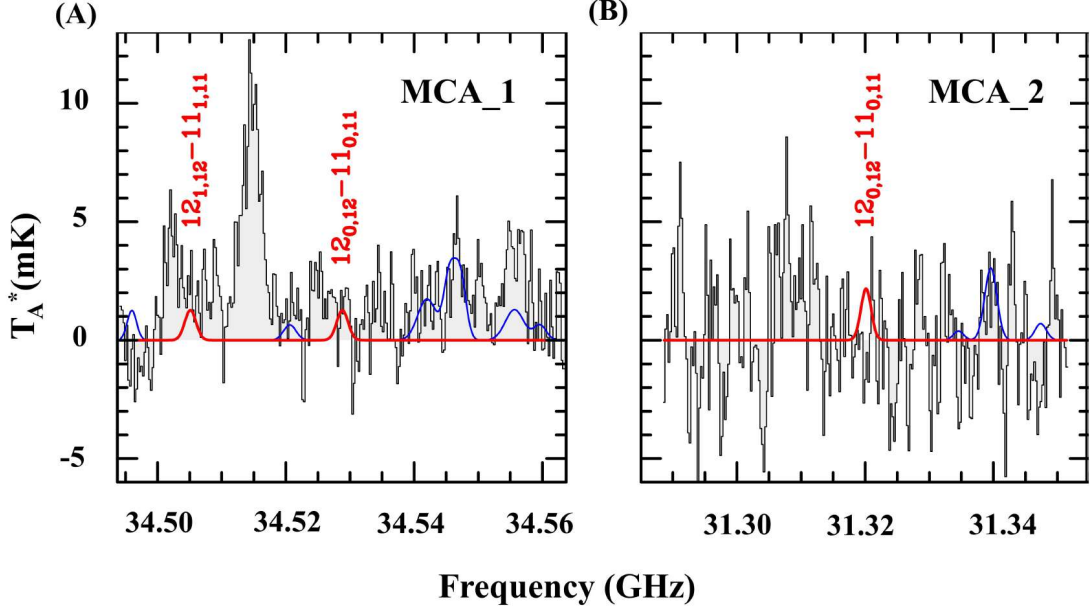


Figure 4.5: The brightest transitions of MCA_1 (panel (A)) and MCA_2 (panel (B)) according to the local thermodynamic equilibrium (LTE) towards the G+0.693-0.027 molecular cloud. The synthetic spectrum (red solid line) is derived using the upper limits to the column densities for the typical parameters (T_{ex} , FWHM, and VLSR) found in this source, as outlined in the text. The black solid line and gray histogram correspond to the observed spectra towards the source. The blue solid line shows the contribution from other molecular species already identified in the spectral survey.

Kraitchman's substitution method, r_s [66], exploits changes in the moments of inertia upon single isotopic substitution. This approach allows us to unambiguously determine the coordinates of each isotopically substituted atom in the principal inertial axis frame (the signs can be assigned from the theoretical or effective structure coordinates). Another way to exploit the single-isotopic information is to obtain the bond distances and angles from a least-squares fit of all the available rotational parameters. This method allows us to determine a total or partial effective ground state r_0 structure [119]. In our analysis, we employed the $r_m^{(1)}$ method [120], as it incorporates additional terms that account for vibration - rotation corrections, which are not considered in the r_s and r_0 methods. The results of the application of the r_s and $r_m^{(1)}$ methods given in the Table 10.3 and Table 10.4 (in Appendix 10.1) are

summarized in Figure 4.6, where they show the good consistency between experimental and theoretical data.

One of the drawbacks from the Kraitchman’s method is that it frequently gives imaginary values for some coordinates if they are close to 0. In the case of MCA, most of the c coordinates for the atoms are close to 0 since they lie almost directly on the ab -inertial plane. As a result of this, we kept the c coordinates fixed to zero giving rise to a planar r_s structure. The values of the planar moments of inertia P_{cc} (4.3519(1) amu·Å² for MCA_1 and 3.03803(1) amu·Å² for MCA_2) suggest the ground state structure to be near planar, with the -CN group slightly tilted with respect to the ab -inertial plane. This is also supported by the equilibrium structure r_e obtained from the theoretical calculations performed at the B3LYP-D3/aug-cc-pVTZ level of theory.

Figure 4.6 shows the overlay of the experimentally obtained r_s and $r_m^{(1)}$ structures (in bold spheres) and the theoretical structure, obtained at the B3LYP-D3/aug-cc-pVTZ level of theory (partially transparent back bone) for both MCA_1 and MCA_2. The structure of MCA can be compared with a similar molecule, cyanoacetic acid [121], as MCA is a methyl ester of cyanoacetic acid. The most stable conformer of cyanoacetic acid is the *cis* configuration of the -CN group with respect to the carbonyl oxygen. This arrangement corresponds to MCA_2 in our study, while, in the most stable configuration of MCA (MCA_1), the -CN group is *gauche* with respect to the carbonyl group. This can be attributed to the combination of the attractive forces between the H atoms of the methyl rotor and the carbonyl carbon and the lone pair of electrons on the ester oxygen and the carbon of the -CN group, as discussed thoroughly in reference [104], making the conformation of MCA_1 slightly more stable.

4.5 Conclusions

We present an extensive laboratory study of the rotational spectra of the two lowest energy conformers of MCA in which the internal rotation and nuclear quadrupole coupling splittings have been resolved. We report the detailed characterization of MCA_2, which has not been investigated before, while extending the previous microwave investigation for MCA_1 into the millimeter wave region. The final analysis comprises of the assignment of rotational transition frequencies between 2-26 GHz and 75-110 GHz and the precise determination of the rotational parameters up to the quartic centrifugal distortion constants, including the internal rotation barrier (V_3) of the methyl group and the nitrogen nuclear quadrupole coupling constants, for both conformers of MCA. In addition, the assignments in the high-frequency data set lead to the accurate determination of the centrifugal distortion constants, which in turn allowed us to compute reliable rest frequencies up to 150 GHz, with line

uncertainties clearly below 1 MHz for most of the predicted transitions. Precisely, more than 250 transitions for MCA_1 and more than 2000 transitions for MCA_1 are predicted with accuracy better than 0.1 km/s (< 40 kHz) in the frequency range of ALMA Band 3. We also provide precise structural information for both MCA_1 and MCA_2.

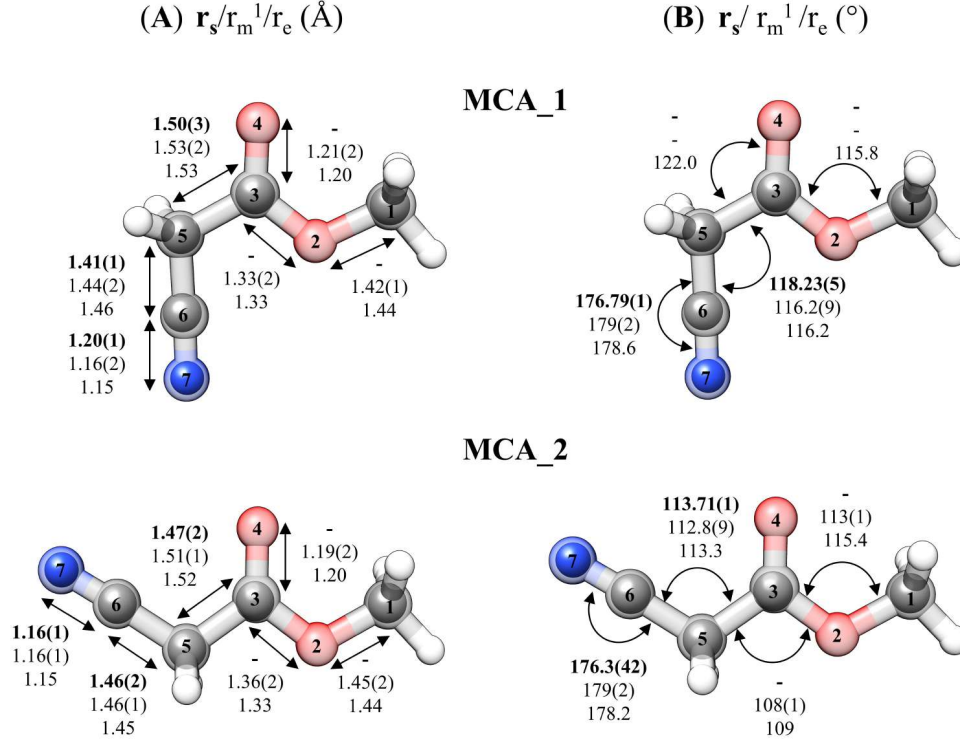


Figure 4.6: The experimental structures of MCA_1 and MCA_2. The inner bold spheres represent the r_s positions of the atoms, whereas the partially transparent backbone gives the theoretical r_e structures (B3LYP-D3/aug-cc-pVTZ level of theory). The bond distances (panel (A)) and angles (panel (B)) obtained by the three methods, r_s , $r_m^{(1)}$, and r_e , are also included where applicable.

One of the notable results from this study is that despite the fact that MCA_2 is slightly higher in energy than MCA_1, the intensities of MCA_2 are generally more intense than those of MCA_1, owing to the higher value of electric dipole moment of MCA_2. The number of assigned transitions especially in the higher frequency region, where MCA_1 can scarcely be seen while MCA_2 dominates the rotational spectrum, further supports this finding. This result is of great interest as it em-

phasizes the need to also consider higher-energy conformers as promising candidates for interstellar detection, especially in the warmer regions of the ISM, since at elevated temperatures, the higher energy conformers are expected to be more populated as compared to the colder regions. Based on our results, MCA_2 is a more favorable conformer of MCA to be detected in the ISM.

Using the precise spectral predictions based on our laboratory spectra, a search for both MCA_1 and MCA_2 was attempted towards the G+0.693 molecular cloud located in the Sgr B2 region of the Galactic Centre. None of the MCA conformers were detected. We derived a column density upper limit of $< 1.2 \times 10^{13} \text{ cm}^{-2}$ for MCA_1 and $< 0.4 \times 10^{13} \text{ cm}^{-2}$ for MCA_2, based on the A state predictions. Such a comprehensive study, which covers the assignment of the rotational transitions in the low and high frequency regime, is essential for interstellar searches, as the large frequency range allows the experimental transition frequencies to be directly compared with the observational spectra. For example, the data in the 2-26 GHz range can be used for searches using the Effelsberg telescope and the line frequencies in 75-110 GHz can be directly compared with the observational data from the Atacama Large Millimeter/submillimeter Array Band 3. The detection of two conformers of MCA in the ISM will be a step forward in the direction of increasing structural complexity of the molecules present in the ISM.

Chapter 5

Rotational spectroscopy of 2,4,6-cycloheptatriene-1-carbonitrile: Facilitating the search for complex cyclic molecules in the ISM

5.1 Introduction

The advent of radio astronomy in the late 1960s has facilitated the astronomical detections of well-known as well as highly unusual molecular systems primarily via their rotational signatures, indicating the astonishingly rich chemical inventory present in the interstellar medium (ISM). With the state-of-the-art facilities and high-sensitivity telescopes available today, more complex molecules are becoming the target of astronomical searches. Recent discoveries are not only the subject of chemical curiosity but also underline many open questions [122], for example, what degree of chemical complexity exists in molecular clouds, what pathways are responsible for their formation, and is there a correlation between the highly abundant unsaturated linear chains such as polyynes and cyanopolyynes and the comparatively scarcely observed cyclic analogues?

Among the vast array of molecular species, exceeding 300, identified in the interstellar medium or circumstellar shells ^{*†}, most of the detections were made via their rotational spectra. For a direct detection via their rotational signature, a molecule must possess a permanent electric dipole moment. Although molecular H₂ is the most abundant molecule in the ISM, its direct observation is limited to the weak quadrupole allowed transitions in the IR region. As a result, polar molecules, despite

^{*}<https://cdms.astro.uni-koeln.de/classic/molecules>

[†]<http://www.astrochymist.org/>

their considerably lower abundances, serve as highly convenient and sensitive tracers of the molecular gas present in the ISM. This further indicates the existing predominance in the detection of CN-containing molecules ($> 15\%$ of the total detected molecules so far) [7], as they possess high values of electric dipole moments leading to an intense rotational spectra, which facilitate their astronomical search. Even though terrestrial organic chemistry is dominated by the presence of molecules containing five- and six-membered rings as building blocks of many biological compounds, it was only in the year 2018 that the first cyclic aromatic molecule was identified in the cold starless core TMC-1; the CN-functionalized benzene ring, benzonitrile [54]. This molecule was then subsequently detected in four other prestellar, and possibly protostellar, sources: Serpens 1A, Serpens 1B, Serpens 2, and MC27/L1521F [123], suggesting a high degree of chemical complexity in the early star formation regions. Shortly thereafter, evidence was found for cyano-functionalized cyclopentadiene [124] in TMC-1 by using the 100m Green Bank Telescope. It is to be noted that the detection of the CN-functionalized hydrocarbons can act as a proxy for the unsubstituted molecule as most of the studied reactions of unsaturated hydrocarbons, like benzene, with a CN radical are found to be barrierless and exothermic in nature [125]. The detection of the five-membered and six-membered rings with CN functionalization has evoked interest in the seven-membered CN functionalized ring: 2,4,6-cycloheptatriene-1-carbonitrile (hereafter CHT-1-CN). In this work, we conducted a thorough rotational spectroscopy study of CHT-1-CN at two different rotational temperatures to facilitate its detection in cold as well as in warm regions of the ISM.

In warm regions of the ISM, a considerable proportion of complex molecules resides in the low-lying vibrationally excited states. The transitions arising from these vibrationally excited states are commonly referred to as weeds in radio astronomy data [34]. These weeds can occupy many channels in a warm and dense astronomical dataset, and therefore their characterization is an important step in simplifying a complex and confusion-limited spectra. Vibrationally excited states, together with isotopologues, constitute a large fraction of the many unidentified lines in the observational datasets. The percentage of these unidentified lines can be as high as 70% in deep observations at ALMA band 3 and 6 (covering 84-116 GHz and 211-275 GHz, respectively) [30]. The assignment of vibrationally excited states and isotopologues, especially of already detected molecules, is also important for the completeness of the astronomical catalogues, especially in the millimeter-wave region. In addition to vibrationally excited states, isotopologues are important species not only from a spectroscopic but also from a structural point of view. The assignment of singly substituted isotopologues in the rotational spectrum provides the experimentally determined rotational constants, which then leads to the construction of a comprehensive structure of the molecule in the gas phase. For CHT-1-CN, elucidating

structural information is fascinating as it is a seven-membered ring with six sp^2 - and one sp^3 -hybridized carbon atoms. The structures of cycloheptatrienes and their derivatives, investigated with vibrational and rotational spectroscopic techniques [126–129] have been a subject of discussion since the early 1960s.

In this chapter, we present an extensive analysis of the rotational spectra of CHT-1-CN covering the 2-110 GHz frequency region (in parts of 2-8, 18-26, and 75-110 GHz) in two different experimental settings using the isolated, cold conditions of a supersonic expansion in 2-26 GHz and a room-temperature flow-cell experiment in 75-110 GHz. The broad frequency ranges probed and the different experimental conditions used are of significant importance here, as not only do we analyze the vibronic ground state of the molecule but we also study vibrationally excited states and determine the molecular structure in the vibronic ground state. The determination of the rotational constants, quartic centrifugal distortion constants, and nuclear quadrupole coupling constants have allowed us to accurately predict the rotational transition frequencies for the ground state and vibrationally excited states into the millimeter-wave region for facilitating the astronomical searches.

5.2 Experimental details

The rotational spectra of CHT-1-CN were recorded over a wide frequency range spanning from 2-110 GHz. The comprehensive analysis was achieved using three chirped-pulse Fourier transform rotational spectrometers: the COMPACT spectrometer, operating within the 2-18 GHz [73, 75, 76], the K-band spectrometer operating within 18-26 GHz [76], and the W-band spectrometer operating within 75-110 GHz [79]. The detailed description of the instruments used in this work can be found in Chapter 3. The liquid sample of CHT-1-CN purchased from Sigma Aldrich (> 95%) was used without any further purification. The molecule was first measured in the range of 18-26 GHz using the K-band spectrometer, as for a molecule of this size, most intense transitions simulated with a rotational temperature of 3 K lie in the range of the K-band spectrometer. Further, the measurement was extended to the low-frequency range (2-8 GHz) employing the COMPACT spectrometer to better resolve the nuclear hyperfine split transitions due to the presence of the ^{14}N nucleus. For these measurements, the sample of CHT-1-CN was loaded into a modified pulsed nozzle (a modified Parker Series 9 valve equipped with an internal heatable reservoir with an orifice diameter of 1 mm) and heated to ~ 311 K. With neon used as a carrier gas at 2.5 bar, the molecular vapor was supersonically expanded into the vacuum chamber. The supersonic expansion of the molecular vapor into the vacuum chamber results in a rapid decrease of the rotational temperature, T_{rot} , to the range of 1-3 K. In contrast to the spectra recorded in the low-frequency region, the measurement in the high-frequency region (75-110 GHz) was performed

under room temperature flow-cell condition. The liquid sample was heated to 323 K resulting in a constant vapor pressure of 2-3 mTorr ($2.6 - 4 \times 10^{-3}$ mbar) in the spectrometer chamber.

A brief description of the measurements performed in this work is given as follows. The COMPACT spectrometer[73, 75, 76] was used to record the spectrum in the 2-8 GHz range. A series of eight chirped pulses (each 4 μ s long) is generated by the arbitrary waveform generator (AWG) and amplified with a 300 W travelling wave tube amplifier. These excitation pulses are then transmitted into the vacuum chamber containing a package of supersonically expanded, cold molecules, and the interaction between the molecules and the pulses induces a macroscopic polarization of the molecular ensemble. Eight chirp pulses per gas-pulse combined with the gas-pulse repetition rate of 8 Hz, an effective repetition rate of 64 Hz was thus achieved. Following each excitation, the resulting free induction decays (FIDs) were recorded for 40 μ s. In total, one million FIDs were co-added in the time domain, followed by the fast Fourier transformation into the frequency domain.

The K-band spectrometer, operating in the range of 18-26 GHz [76], combines the segmented approach and the multi-train method. The bandwidth of 8 GHz is split into smaller segments of 800 MHz, and the spectrum across the whole bandwidth is obtained by stitching these segments together [77]. The multi-train method utilizes multiple pulse trains per molecular pulse, increasing the effective repetition rate of the experiment. The AWG synthesizes 1.5 μ s long excitation pulses in the range of 7-3 GHz. These chirps are then frequency upconverted to 9-13 GHz and doubled to 18-26 GHz. For each gas-pulse, the molecular ensemble is polarized by a series of three pulse trains. The multi-train setup combined with a gas pulse repetition rate of 10 Hz results in the effective repetition rate of 30 Hz. A total of 2.2 million FIDs were collected (each for 10 μ s), frequency down-converted, co-added, and converted into the frequency domain by fast Fourier transformation.

The W-band spectrometer (75-110 GHz) [79] also utilizes the segmented approach. The 35 GHz bandwidth is covered in segments of 720 MHz each. Among the different measurement modes available, the high dynamic range (HDR) mode was used for this experiment, which addresses each segment of 720 MHz by 30 chirps of 24 MHz bandwidth each, thus reducing the spurious content in the collected spectrum. The AWG synthesizes 500 ns excitation pulses in the 1.5-2.3 GHz range, which is then frequency upconverted and multiplied through a series of mixing stages and an active multiplier chain ($\times 6$) to produce the radiation in the millimeter-wave regime. A total of one million FIDs (each recorded for 4 μ s) were collected followed by conversion into the frequency domain by fast Fourier transformation.

5.3 Theoretical details

To explore the conformational flexibility of CHT-1-CN, an automated semi-empirical conformational search was performed with the SPARTAN 14[‡] program using the Austin Model 1 (AM1) method, the Parameterization Method 3 (PM3), and the Parameterization Method 6 (PM6) (Spartan 14). The results from the SPARTAN program combined with chemical intuition yielded two structures differing in the orientation of the cyano group (attached to an sp^3 -hybridised carbon atom) with respect to the seven-membered ring. Moreover, the cycloheptatriene ring systems are known to undergo an equilibrium reaction between the norcaradiene–cycloheptatriene forms [130] in the presence of electron-withdrawing groups, such as the cyano group. Therefore, it is essential to consider the two tautomeric forms of CHT-1-CN that could be present in our experiment as a result of this equilibrium reaction. The geometry optimizations of the four structures (two conformers and two tautomers) were performed at the B3LYP-D3/cc-pVTZ level of theory using the ORCA program package [60, 61]. The computed rotational constants, dipole moment components, and zero-point corrected relative energies along with the optimized structures are summarized in Table 5.1.

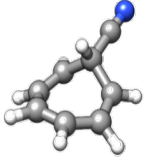
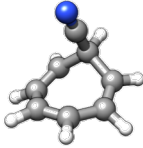
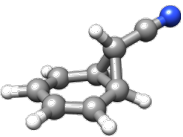
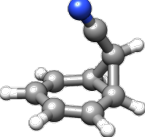
Anharmonic frequency calculations were also performed for the lowest energy conformer in order to aid the analysis of the vibrationally excited states of conformer 1. The program package Gaussian 09 [62] was used to perform structure optimization and anharmonic frequency calculations at the B3LYP-D3/aug-cc-pVTZ level of theory. In addition to the theoretical rotational constants and the nuclear quadrupole coupling constants (NQCCs) for the ^{14}N nucleus, the anharmonic frequency calculations also provided theoretical quartic centrifugal distortion constants, which are of great relevance for the assignment in the high-frequency region (75-110 GHz).

5.4 Spectroscopic analysis

CHT-1-CN is a seven-membered ring molecule containing a cyano group attached to position 1 of the ring. The structure of the two lowest-energy conformers according to the quantum-chemical calculations, with conventional numbering and principal axes are shown in Figure 5.1. The π electrons of the ring are not fully delocalized due to the presence of an sp^3 -hybridised carbon atom at position 1, giving the molecule a bent shape. Spectroscopically, CHT-1-CN is a near-oblate asymmetric top with Ray’s asymmetry parameter, $\kappa = \frac{2B-A-C}{A-C} = -0.79$ and -0.60 for conformer 1 and 2, respectively. The molecule contains one nitrogen nucleus, which has

[‡]<https://www.wavefun.com>

Table 5.1: Rotational parameters and relative energies of the calculated lowest energy conformers and tautomers for CHT-1-CN at the B3LYP-D3/cc-pVTZ level of theory.

Rotational parameters	Conformer 1	Conformer 2	Tautomer 1	Tautomer 2
				
A^a / MHz	3579.6	2274.5	4297.6	2427.8
B / MHz	1252.4	1683.2	1160.7	1733.3
C / MHz	990.9	1540.2	996.7	1626.5
$\mu_a / \mu_b / \mu_c / ^b D$	4.3/0.0/0.2	2.8/0.0/2.9	4.3/0.0/0.2	2.5/3.3/0.0
$\Delta E^c / kJ \cdot mol^{-1}$	0	6.3	22	24.6

^a A, B, and C are the rotational constants.

^b $\mu_a / \mu_b / \mu_c /$ are the electric dipole moment components.

^c Zero-point energy corrected relative energies.

nuclear spin $I(^{14}\text{N})=1$. The spin of the ^{14}N couples with the electric field gradient of the molecule, resulting in splitting of each rotational transition into several hyperfine components. This hyperfine splitting (HFS) is prominent in the low-frequency datasets (up to 26 GHz in the present work), whereas in the high-frequency region, the HFS collapses with the increase in the rotational quantum number J and hence cannot be resolved.

For the preliminary spectral assignment, the calculated parameters for the ground state as well as for low-lying vibrationally excited states were used as initial inputs to fit the experimental spectra with PGOPHER [57]. The fits were then refined with Pickett's SPCAT/SPFIT programs [107] using Watson's A -reduction Hamiltonian in the I^r representation. The AABS package [53, 108] was used for displaying the predicted transitions and measuring the experimental frequencies. For the vibronic ground state, a global fit (combining the rotational transitions from the low-frequency and high-frequency region) was performed in a way that the transitions with resolved HFS and the transitions with unresolved HFS were included

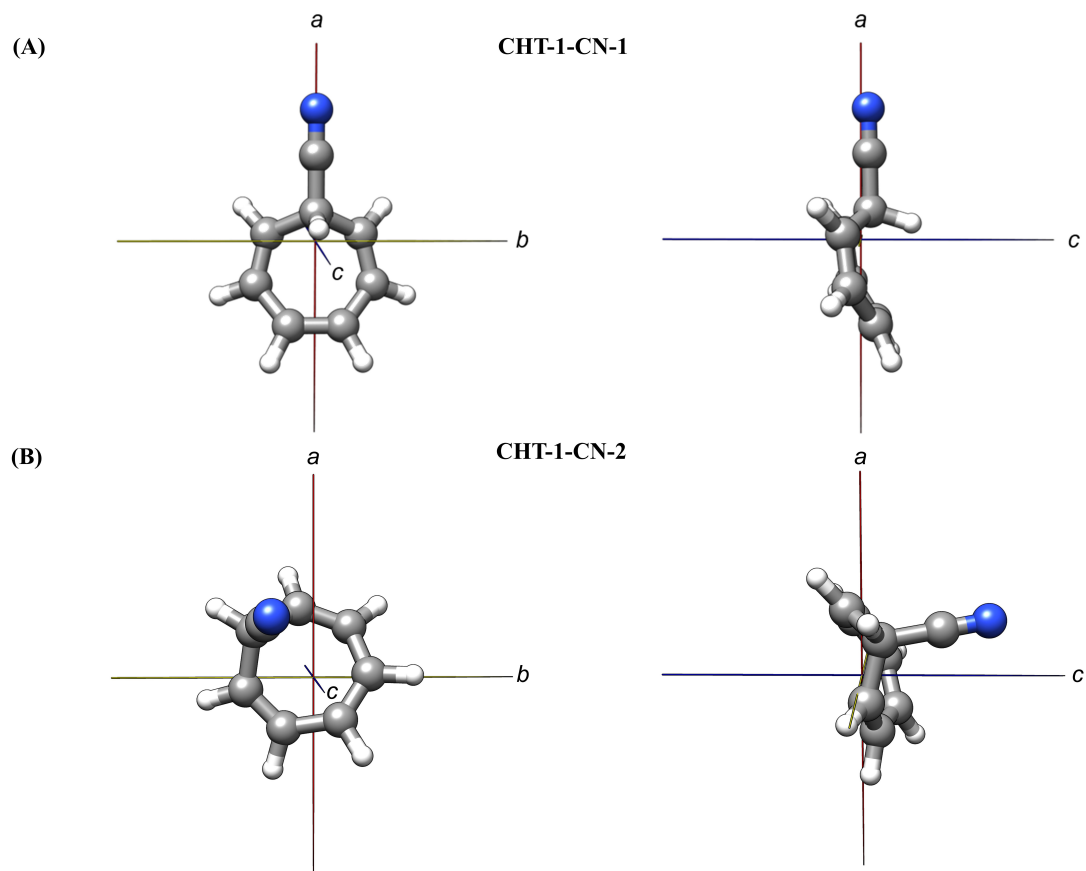


Figure 5.1: Molecular structures and principal inertial axes of the lowest energy conformers (A) CHT-1-CN-1(top trace) and (B) CHT-1-CN-2 (bottom trace) in the ab plane (left) and in the ac plane (right).

together in the same line list. This fitting procedure has been reported before for the rotational spectroscopy of imidazole in the frequency range of 2-295 GHz [131, 132].

For the determination of the substitution structure of CHT-1-CN, the KRA program package [133] was used. The EVAL program [53] was then employed to calculate the various structural parameters, such as bond lengths, bond angles, and dihedral angles.

5.5 Results and discussion

5.5.1 Vibronic ground state

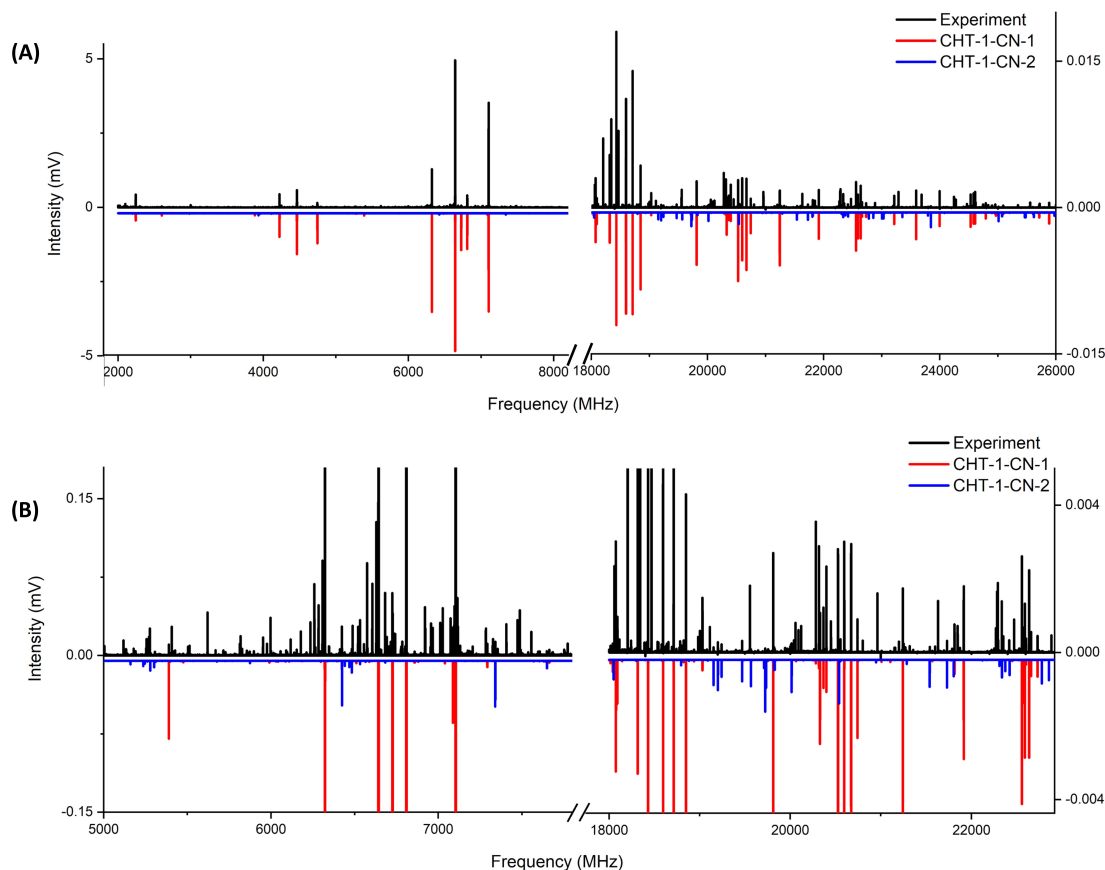


Figure 5.2: Panel (A) shows the rotational spectra of two lowest energy conformers in the frequency range of 2-8 and 18-26 GHz. The black trace represents the experimental spectra; the red trace and the blue trace corresponds to the simulated spectra based on the fitted rotational constants of CHT-1-CN-1 and CHT-1-CN-2, respectively, at a rotational temperature of $T_{rot} = 3$ K. Panel (B) shows the zoom-in to emphasize the presence of the second conformer (in blue). The left and right intensity axes correspond to the experiments performed in the different frequency regions.

Among the four different structures studied computationally, only the two lowest energy structures were observed in the experimental spectra as the rest of the struc-

tures are more than 8 kJ/mol higher in energy with respect to the lowest energy one. Hereafter, the abbreviation CHT-1-CN-1 refers to the lowest energy conformer and CHT-1-CN-2 refers to the conformer next in energy.

The spectra recorded below 26 GHz (Figure 5.2) show resolvable HFS. The pattern of the HFS observed for the *a*-type transitions can be found in Figure 10.3 in Appendix 10.2. The NQCCs obtained at the B3LYP-D3/cc-pVTZ level of theory were used to simulate HFS caused by the nuclear spin ($I=1$) of the ^{14}N nucleus. In the present work, ~ 150 transitions with resolved HFS were assigned.

The rotational spectrum in the W-band region, described in Figure 5.3, does not show a resolvable HFS as the HFS collapses with the increasing rotational quantum number, J . For such transitions, the experimentally measured frequencies were assigned to the corresponding pure rotational transitions. In total, our data set contains 1272 and 123 assigned transitions for the vibronic ground state of CHT-1-CN-1 and CHT-1-CN-2, respectively. For CHT-1-CN-1, the majority of the transitions are *a*-type transitions due to the high dipole-moment component along the *a*-axis. Some *c*-type transitions were also assigned but no *b*-type transitions could be assigned due to the very low dipole-moment component along the *b*-axis. A global fit incorporating the rotational transitions from both low- and high-frequency regions was performed. In the case of CHT-1-CN-2, both *a*-type and *c*-type transitions were assigned due to the significant dipole moment component along the *a*- and *c*-axes. No transitions for CHT-1-CN-2 could be assigned in the high-frequency region, due to the combination of factors, such as lower overall intensities due to the room-temperature setup and higher relative energy of CHT-1-CN-2 (~ 6 kJ/mol) with respect to the lowest energy conformer, CHT-1-CN-1.

The experimental and theoretical rotational parameters for the vibronic ground state of both conformers are given in Table 5.1. In the global fit (2-110 GHz), as for the case of CHT-1-CN-1, the NQCCs were included only for the transitions in the low-frequency regions, *i.e.*, for the transitions exhibiting nuclear hyperfine splitting. Analyzing high-frequency data sets allows for the accurate determination of the centrifugal distortion constants, which are crucial for the astronomical community, as this leads one to compute reliable rest frequencies in the higher frequency region more precisely than predictions based on the rigid rotor models alone. In this work, the transition frequencies of CHT-1-CN-1 were predicted up to 150 GHz based on the fitted rotational parameters, with the use of the SPCAT program. For the vast majority of the predicted transitions, the uncertainties are well under 200 kHz. Besides the centrifugal distortion constants, the experimentally determined NQCCs, χ_{aa} and χ_{bb-cc} , are also important for interstellar searches, as the observation of the nuclear hyperfine splitting can act as a further validation mechanism for interstellar detections. For example, the elucidation of the hyperfine splitting patterns of several interstellar molecules like cyanoallene [134] and benzonitrile [54] led to their

conclusive identification in the ISM.

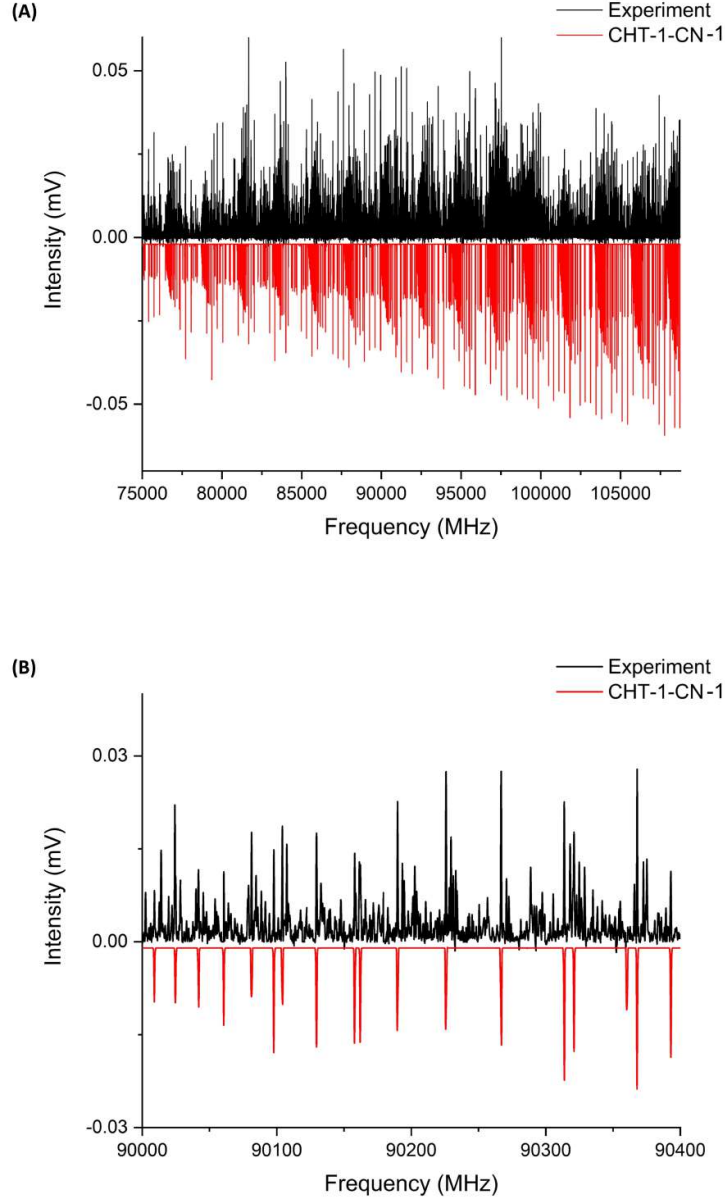


Figure 5.3: Panel (A) shows the experimental (black trace) and simulated (red trace) rotational spectrum of CHT-1-CN-1 in the W-band region (75-110 GHz) recorded at room-temperature conditions in a flow-cell setup. The simulated spectrum was obtained using the fitted rotational constants at a rotational temperature of $T_{rot} \sim 323$ K. Panel (B) shows the zoom-in highlighting the well resolved rotational transitions at the room-temperature experimental conditions.

Table 5.2: Experimental and theoretical rotational parameters for the two lowest energy conformers, CHT-1-CN-1 and CHT-1-CN-2. The experimental rotational parameters were obtained as a result of the global fit in the frequency range 2-110 GHz and 2-26 GHz for CHT-1-CN-1 and CHT-1-CN-2, respectively. The rotational transitions were fit using Watson’s A -reduction Hamiltonian in an I^r representation. The theoretical rotational parameters were calculated at the B3LYP-D3/aug-cc-pVTZ level of theory.

	CHT-1-CN-1		CHT-1-CN-2	
Rotational parameters	Experiment	Theory	Experiment	Theory
A^a/MHz	3538.12661(62)	3584.3	2232.1100(22)	2274.5
B/MHz	1251.39700(13)	1253.3	1702.8285(16)	1683.2
C/MHz	990.61360(11)	991.4	1573.6604(20)	1540.2
Δ_J^b/kHz	0.055512(30)		0.626(25)	
Δ_{JK}/kHz	0.20096(13)		-1.228(92)	
Δ_K/kHz	0.830(20)		1.08(12)	
δ_J/kHz	0.006708(17)			
δ_K/kHz	0.27771(99)			
χ_{aa}^c/MHz	-4.251(8)	-4.7	0.132(24)	-
χ_{bb-cc}/MHz	0.077 (17)	0.09	4.424(44)	-
σ^d/kHz	24.64		32	
No. of lines	1272		123	
J/K_a^e	54/38		5/7	

^a A, B, and C are the rotational constants

^b Δ_J , Δ_{JK} , Δ_K , δ_J , and δ_K are the quartic centrifugal distortion constants.

^c χ_{aa} , χ_{bb} , and χ_{cc} represent the diagonal elements of the ^{14}N nuclear quadrupole coupling tensor.

^d Microwave root-mean-square deviation of the fit.

^e Maximum values of J and K_a assigned in the fit.

5.5.2 Structure determination

In addition to the lowest energy conformer CHT-1-CN-1, we also observed the rotational spectra of its singly substituted ^{13}C and ^{15}N isotopologues in natural abundance (1.1% and 0.4%, respectively) in the 2-26 GHz region. For the second conformer CHT-1-CN-2, the signal-to-noise ratio (SNR) for the main isotopologue was not high enough to observe its singly substituted ^{13}C and ^{15}N isotopologues in natural abundance. In the W-band region, no rotational transition arising from the heavy-atom isotopologues could be assigned in natural abundance. This is due to the fact that in the room-temperature measurement of CHT-1-CN, the vibrationally excited states are also populated, which increases the partition function of the molecule. This affects the relative intensities of rotational transitions, which in turn makes the assignment of the singly substituted ^{13}C and ^{15}N isotopologues difficult in natural abundance; as a result only the main isotopologue of CHT-1-CN-1 could be assigned in the W-band region.

The presence of a symmetry plane σ in CHT-1-CN-1 causes the effective natural abundance of the mirrored carbon atoms, labelled as $^{13}\text{C}(5)$, $^{13}\text{C}(6)$, and $^{13}\text{C}(7)$, to be 2.2% instead of 1.1% (Figure 5.4). Since the change in the mass of the mirrored carbon atoms have the same effect on the center of mass, the moments of inertia and hence the rotational constants are identical for the mirrored carbon atoms. The experimentally determined rotational parameters for all the observed isotopologues of CHT-1-CN-1 are given in Table 10.7 in Appendix 10.2. These experimentally obtained rotational constants were then utilized to determine the positions of each isotopically substituted atom with respect to the molecule’s center of mass by employing Kraitchman’s equations [66]. The comparison of the experimentally determined substitution structure (r_s) and the theoretical equilibrium structure (r_e) optimized at the B3LYP-D3/aug-cc-pVTZ level of theory is shown in Figure 5.4. The bold spheres represent the experimentally determined atom positions (r_s) and the partially transparent backbone represents the equilibrium geometry (r_e) of the molecule.

The structure of CHT-1-CN-1 can be compared to the structures of related molecules, benzonitrile [134] and cycloheptatriene (CHT) [126]. Figure 5.5 depicts the ring structure of three molecules along with their relevant bond lengths and bond angles, as shown in Table 5.3. For CHT, the values are taken from structure optimization calculations performed at the B3LYP-D3/aug-cc-pVTZ level of theory, which were performed for this work because of the absence of an experimental gas phase structure for CHT in literature. The primary distinction in the structures of benzonitrile and CHT-1-CN-1 is the degree of saturation of the bonds in the ring (i.e., the presence of the sp^3 - hybridized carbon atom at position 1 and this impacts the resulting bond lengths. The structural differences between CHT and CHT-1-CN-1 arises from the substitution of a hydrogen atom with a CN group at the C(1)

position. The differences in the degree of saturation between the above-mentioned systems also affect the aromaticity of the molecules. For example, benzonitrile is an aromatic molecule while CHT and CHT-1-CN-1 are non-aromatic. As a result, benzonitrile is a planar molecule, while CHT and CHT-1-CN-1 are not. The boat shape arrangement of CHT-1-CN-1 makes the angle at the sp^3 - hybridized carbon atom C(1) the smallest (106.9°) and the bond length associated with C(1) to be the longest $r_{C(1)-C(2)} = 1.5201(20)$ Å. All the relevant bond lengths and bond angles are given in Table 5.3.

Table 5.3: A comparison of bond lengths, in Å, and bond angles in $^\circ$ determined in this work for CHT-1-CN-1 and by Casado *et al.* for benzonitrile [135], and from the structure optimised using B3LYP-D3/aug-cc-pVTZ level of theory.

Bond lengths (Å)				
CHT-1-CN-1 ^a		CHT ^b [127]	Benzonitrile ^a [135]	
C(1)-C(2)	1.5241(62)	1.503	C(1)-C(2)	1.3876(5)
C(2)-C(3)	1.3078(130)	1.345	C(2)-C(3)	1.3956(4)
C(3)-C(4)	1.4510(36)	1.441	C(3)-C(4)	1.3974(4)
C(4)-C(5)	1.3582(32)	1.359	C*-N	1.1581(2)
C(1)-C*	1.4829(22)			
C*-N	1.1570(93)			
Bond angles ($^\circ$)				
CHT-1-CN-1 ^a		CHT ^b [127]	Benzonitrile ^a [135]	
C(1)-C(2)-C(3)	120.4 (6)	121.8	C(1)-C(2)-C(3)	119.00(4)
C(2)-C(3)-C(4)	124.6(2)	125.3	C(2)-C(3)-C(4)	120.06(3)
C(3)-C(4)-C(5)	125.5(2)	125.8	C(3)-C(4)-C(5)	120.05(3)
C(2)-C(1)-C(7)	106.5(5)	107.8	C(2)-C(1)-C(6)	121.82(5)
C(1)-C*-N	179.3(8)		C(1)-C*-N	

^a parameters calculated by r_s method

^b parameters taken from the calculations performed in [127]

* carbon atom of the cyano group

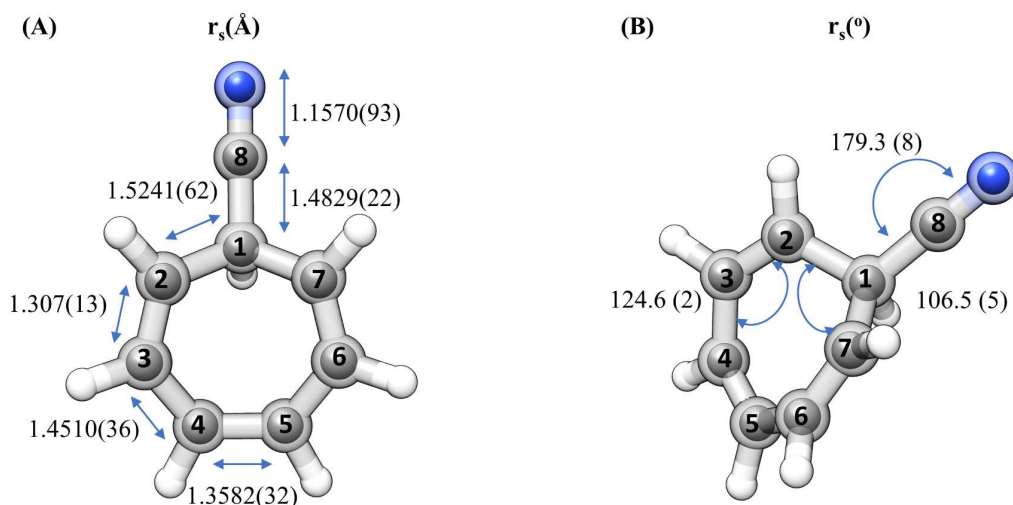


Figure 5.4: The experimental structure of CHT-1-CN-1. The inner bold spheres represent the r_s positions of the atoms, whereas the partially transparent backbone gives the theoretical r_e structures (B3LYP-D3/aug-cc-pVTZ level of theory). The bond lengths are given in panel (A) and the bond angles are given in panel (B). The bond distances and angles obtained by r_s are included where applicable.

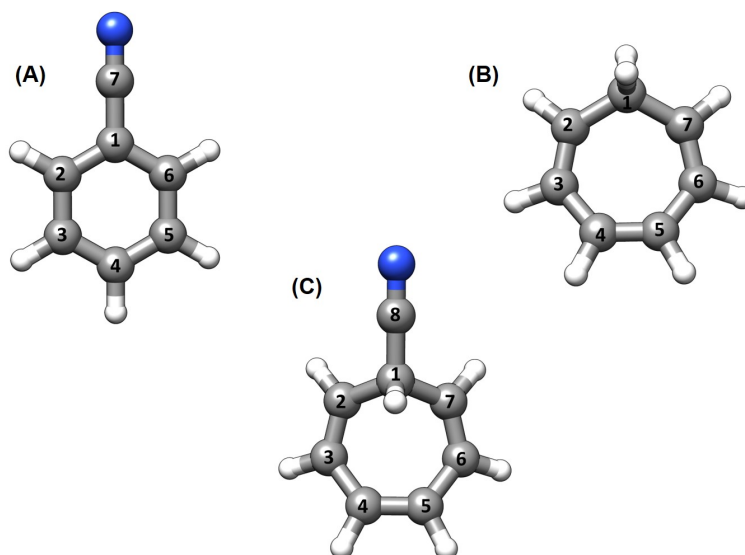


Figure 5.5: Molecular structures of (A) benzonitrile, (B) CHT, and (C) CHT-1-CN-1 with numbering of the atoms for better comparison with the structure of CHT-1-CN-1.

5.5.3 Vibrationally excited states

The flow-cell experiment performed with the W-band spectrometer (75-110 GHz) at room temperature allows the observation of not only the vibronic ground state but also the low-lying vibrationally excited states. The population in these vibrationally excited states can be calculated by using the Boltzmann distribution equation, which gives an estimation of the population distribution based on the energy difference with respect to the vibronic ground state and the temperature. We present here the assignment of the six lowest energy vibrationally excited states of CHT-1-CN-1, namely ν_{42} , ν_{41} , $2\nu_{42}$, $\nu_{42} + \nu_{41}$, ν_{40} , and ν_{38} , within 500 cm^{-1} of energy difference with respect to the ground state of CHT-1-CN-1. A brief description of the fundamental modes follows: ν_{42} (110.4 cm^{-1}) is an out-of-plane bending motion, this can be seen as the movement of the C-CN bond and the ring C atoms in the *ac* plane; ν_{41} (145.7 cm^{-1}) is an in-plane wagging motion along the C-CN bond in the *bc* plane; ν_{40} (269.7 cm^{-1}) is an out-of-plane wagging motion of the CN group in the *ac* plane; ν_{38} (318.2 cm^{-1}) is a breathing motion, shown by the periodic expansion and contraction of the ring structure. Figure 5.6 shows these motions alongside their energies with anharmonic corrections at the B3LYP-D3/aug-cc-pVTZ level of theory.

The spectral assignment of the vibrationally excited states was facilitated by anharmonic frequency calculations performed at the B3LYP-D3/cc-pVTZ level of theory for the corresponding vibrational motions. The theoretical rotational constants obtained for each of the observed vibrationally excited states were shifted by the difference in the theoretical and experimental rotational constants obtained for the vibronic ground state at the same level of theory. The experimentally determined rotational constants and number of assigned transitions for the four fundamental bands as well as the overtone $2\nu_{42}$ and the combination band $\nu_{42} + \nu_{41}$ are listed in Table 10.2 (in Appendix 10.2) along with their derived rotational constants and anharmonic energies computed at the B3LYP-D3/aug-cc-pVTZ level of theory.

The analysis of the vibrationally excited states is an important task, as the detected vibrational states can serve as temperature probes in the region where they are observed, given that, the ground state conformer has already been detected in that region. Moreover, it is useful for the simplification of the complex astronomical datasets by eliminating lines from vibrationally excited states and isotopologues of already known molecules.

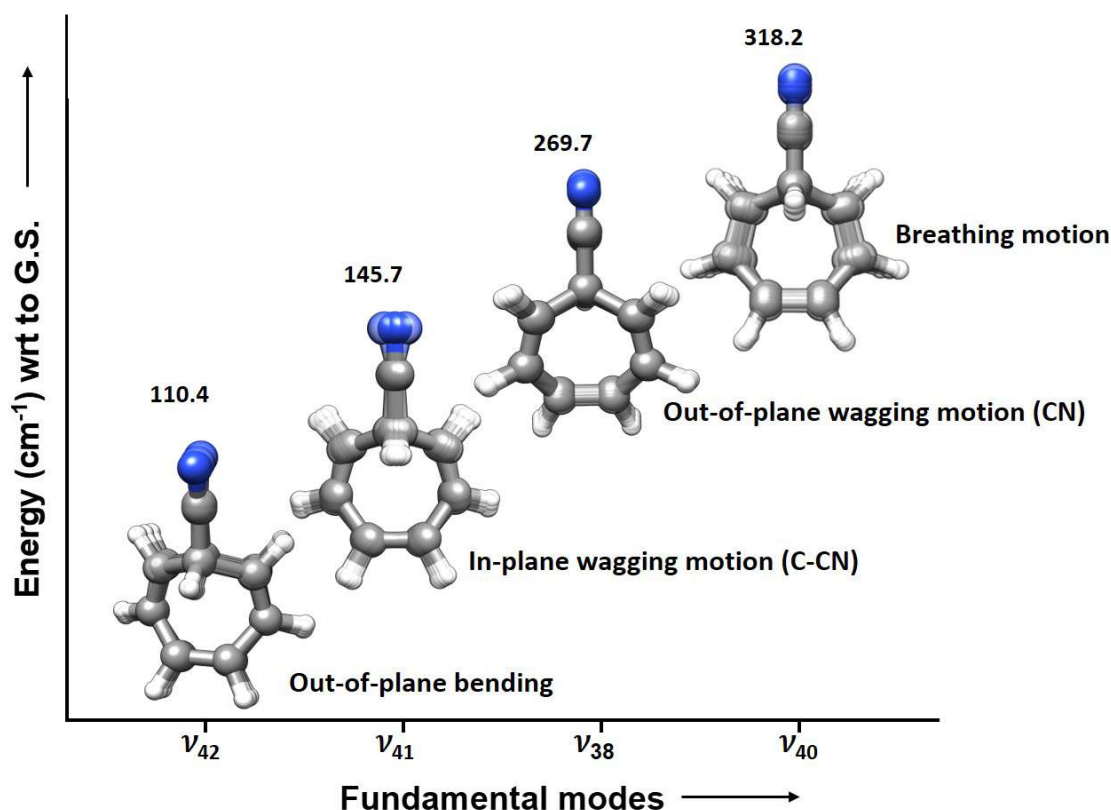


Figure 5.6: A summary of the assigned fundamental vibrations of CHT-1-CN-1. The predominant motion for each mode is indicated by the overlapping transparent structures. The anharmonic energies presented are those calculated at the B3LYP-D3/aug-cc-pVTZ level of theory.

5.5.4 Rotational and vibrational partition functions of CHT-1-CN-1

Interstellar searches for molecules of astronomical interests do not only require accurate rest frequencies but also information on the relative intensities of the rotational transitions. Partition functions can be used to calculate the relative transition intensities at different rotational temperatures, by direct summation over rotational energy levels. Further, the information on the partition functions is important for the calculation of the column densities [109]. The proportionality of the partition function on the temperature is reflected in the calculated and observed transition

intensities, as the increase in the temperature redistributes the population over the accessible vibrationally excited states resulting in overall lower signal intensity of rotational transitions. This is because of the increase in the partition function which leads to the decrease in the intensity. A thorough description of the partition functions can be found in Section 2.1.6. The comparison of the simulated transition intensities at different temperatures for CHT-1-CN-1 is shown in Figure 5.7. The plot was made considering spin degeneracy equal to 0 ($2I + 1 = 1$, i.e., the case where the hyperfine splitting is ignored).

The experiment in the range of 75-110 GHz was performed at ~ 323 K, therefore it is important to consider the vibrational partition function in addition to the rotational partition function. In Table 5.4, we list the rotational (Q_{rot}) and vibrational (Q_{vib}) partition functions of CHT-1-CN-1 calculated for the rotational quantum number J up to 60 without considering the hyperfine splitting due to ^{14}N . The rotational partition functions were calculated using the SPCAT program [107] across the standard temperatures as implemented in the Jet Propulsion Laboratory (JPL) database [110]. The vibrational contributions were calculated through direct summation on all of the vibrational modes up to 500 cm^{-1} . The total partition function (Q_{tot}) of the molecule is the product of Q_{rot} and Q_{vib} , as listed in Table 5.4.

Table 5.4: Rotational and vibrational partition functions calculated for CHT-1-CN-1 across the standard range of temperatures as implemented in the JPL database [110].

CHT-1-CN-1			
T/K	$Q_{rot}[2I + 1 = 1]^a$	Q_{vib}	$Q_{tot} = Q_{rot} \times Q_{vib}$
300	164124.64	4.623	758748.21
225	137771.51	3.41	469800.86
150	100473.94	2.167	217727.03
75	47757.85	1.221	58312.34
37.5	18374.49	1.018	18705.24
18.75	6541.21	1	6541.21
9.375	2314.62	1	2314.62
1.5	149.45	1	149.49

^a $I = 0$ for ^{14}N , ignoring the hyperfine splitting.

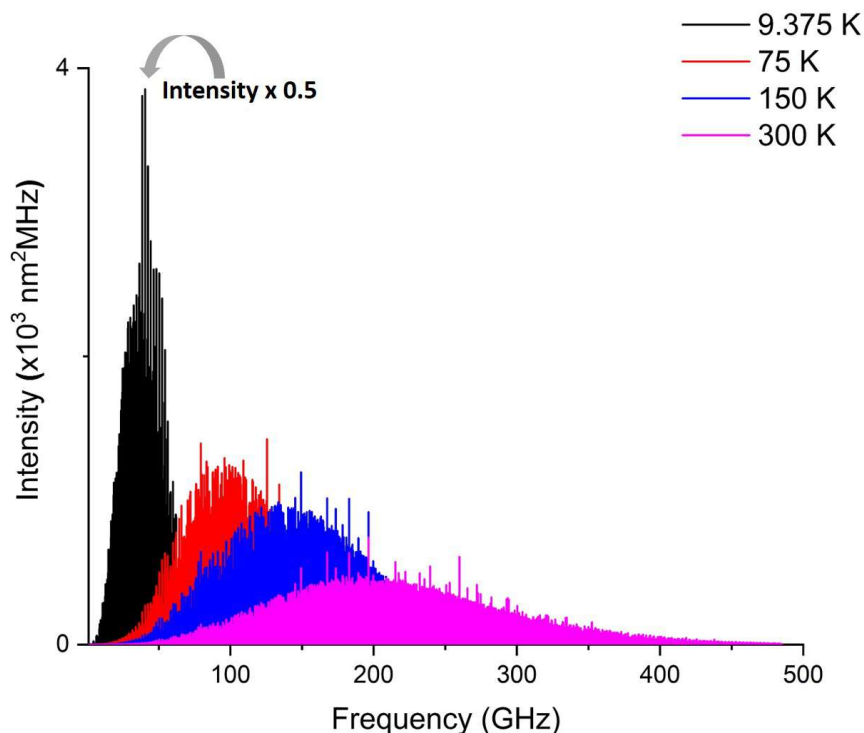


Figure 5.7: The distribution of the rotational transitions of CHT-1-CN-1 across four of the standard temperatures implemented in the JPL database [110]. The frequency simulation is made up to 500 GHz for the case of $2I+1 = 1$. Note that the intensity scale for the prediction at 9.375 K has been halved for clearer comparison with the predictions at higher temperatures.

5.6 Conclusions

This extensive investigation of the rotational spectra of 2,4,6-cycloheptatriene-1-carbonitrile led to the identification and assignment of the two lowest energy conformers, CHT-1-CN-1 and CHT-1-CN-2, in their vibronic ground state isotopologues, including the assignment of the singly substituted ^{13}C and ^{15}N isotopologues in natural abundances. Additionally, six vibrationally excited states of CHT-1-CN-1 were observed and characterized in the room-temperature flow cell measurement. For the lowest energy conformer, CHT-1-CN-1, the assignment comprises of exact rotational frequencies between 2-8, 18-26, and 75-110 GHz, determination of rotational parameters up to quartic distortion constants along with the nuclear quadrupole coupling constants. The accurate determination of centrifugal distortion constants

allowed us to compute reliable rest frequencies in the high-frequency region. For the vast majority of predicted transition frequencies (up to 150 GHz, in this work), the uncertainties are well under 200 kHz, which makes this a reliable study for conducting astronomical searches. Rotational and vibrational partition functions were also calculated for the variety of temperatures as listed in the JPL database [110]. In addition to determining the gas phase structure of CHT-1-CN-1 in the vibronic ground state, its structure can also be compared to other similar molecules like CHT and benzonitrile. The aromatic nature of benzonitrile is a satisfactory explanation for the decrease in bond lengths in the ring structure as compared to those in CHT and CHT-1-CN-1, especially the ones including C(1) carbon atom due to its sp^3 hybridization.

The astronomical detections of cyano substituted five membered and six membered rings, cyanocyclopentadiene [136] and benzonitrile [54], respectively, makes CHT-1-CN-1 (cyano substituted seven membered ring) as a potential candidate to be detected. Moreover, the electric dipole moment of CHT-1-CN-1 (4.3 D) makes it a favourable molecule to be searched for using radio astronomy. The astronomical search for CHT-1-CN-1 is suggested in TMC-1, where other cyclic molecules have been detected recently like benzonitrile [54], *o*-benzyne [137], cyclopentadiene and derivatives [16, 138], and indene [16, 139, 140]. The comprehensive study of large complex molecules like CHT-1-CN-1 opens up the possibility of extending these studies to investigate even more complex or large structures that might be present in the ISM.

Chapter 6

Insights into the gas phase structure and rotational dynamics of diphenylsilane: A broadband rotational spectroscopy study

6.1 Introduction

Silicon is the second most abundant element in the earth’s crust, eighth most abundant in the universe, and has an important role in modern-day technology, medical applications, and industry. The usefulness of silicon was not fully realized until the second half of the 20th century, when the advent of semiconductors marked the onset of the transformative “Silicon Age” [141–143]. Apart from semiconductors, silicon is utilized in the production and development of a wide range of devices and materials. These include biologically active compounds [144, 145], glasses [146], ceramics [147], cement [148], fiber optics [149], liquid crystal technology for smart screens [150], silicones (oil, grease, rubber, resin, caulk) [151, 152], and other polymers [153–155]. Recently, silicon gained significant attention in medical applications particularly in the form of organosilicon biomolecules. The inherent advantages of using silicon as a bioisostere of carbon make it an attractive option, such as its tetravalent nature akin to carbon, lack of toxicity [156, 157], and higher lipophilicity [144, 158] than carbon. An interesting example involves modifying the amino acid proline to create sila-proline, which contains two methyl groups attached to silicon instead of a methylene carbon. This modification resulted in a 16-fold increase in cellular uptake compared to proline [144, 145].

Furthermore, organosilicon compounds serve as fundamental building blocks in the synthesis of silicone polymers. The inclusion of silicon in these polymers imparts spe-

cific functionalities such as crosslinking, thermal stability, and chemical resistance [159]. For example, the polymer of diphenylsilane (PDPS) also has applications in fabricating thin films [160] and photovoltaic cells [161]. PDPS’s high hole mobility, due to σ conjugation in its polymers, makes these materials suitable for use in organic thin film solar cells. Moreover, silanediol peptide isosteres are found to be highly active inhibitors of proteolytic enzymes. This unique class of protease inhibitors can be synthesized by a rather direct synthesis using diphenylsilane as a precursor molecule, as reported recently [162].

In addition to their myriad of applications on Earth, small silicon-bearing moieties are notably abundant in the interstellar medium (ISM) and play a key role in the chemical evolution of the ISM [163, 164]. The detection of silicon-containing molecules in space constitutes a substantial portion, accounting for up to 7% of the total number of molecules identified in space so far [7]. Organosilicon molecules like SiC, SiC₂, *c*-SiC₃, SiC₄, *etc.* are believed to be linked to the formation of silicon carbide dust grains in the outflow of circumstellar envelopes of carbon-rich asymptotic giant branch (AGB) stars like IRC+10216 [165–167]. This is considered an important region for astronomical detections of organosilicon molecules for two main reasons. Firstly, it hosts observations of almost half of the known interstellar and circumstellar species, many of which were discovered in space for the first time [168]. Secondly, IRC+10216 provides high densities ($10^8 - 10^{14} \text{ cm}^{-3}$) and temperatures (1000 – 2500 K) for the nucleation and growth of dust grains.

Given the abundance of organosilicon molecules in space, silicon-substituted analogs of known or postulated carbon moieties are likely targets for astronomical searches. Several silicon-containing carbon chain radicals as well as their hydrogenated forms have been previously studied in silane-acetylene electrical discharge experiments using Fourier-transform microwave spectroscopy [169–173]. Detection of cyclic organosilicon molecules will provide valuable insights on the mechanisms for formation of these molecules and contribute to our existing knowledge of silicon chemistry in space. To facilitate the potential detection of such molecules in space, laboratory data are required which contain the spectroscopic signatures specific to that molecule.

Diphenylsilane is a complex organosilicon molecule with two phenyl groups attached to the Si center. We report its microwave spectroscopic analysis in the range of 2-8 GHz along with precise gas phase structure determination. Investigating the structural properties of complex organosilicon molecules like diphenylsilane are the basis to its functional behavior, such as the chemical and biological activity. We also investigate the tunneling barrier height of diphenylsilane and compare it with the oxygen analogue, diphenylether [174]. The comparison is also extended to the structural parameters as replacing oxygen with silicon in a molecule leads to an increase of the bond length from C-O to C-Si (due to the larger size of the silicon atom)

and results in modified shape and reactivity. The comprehensive rotational analysis of diphenylsilane and the generated line lists, rotational constants, and centrifugal distortion constants can aid the astronomical searches for diphenylsilane in the interstellar environments. Its detection will unveil an unexplored area of substituted aromatic and cyclic silicon-containing molecules.

6.2 Experimental and theoretical details

The liquid sample of diphenylsilane was purchased from Sigma-Aldrich (97% purity) and was used without any further purification. The broadband spectrum of diphenylsilane was obtained utilizing the COMPACT spectrometer, which has been described in detail in Chapter 3, and thus only a brief description is given here. The sample is brought into the gas phase using a supersonic expansion, where neon was used as a carrier gas at 2 bar of backing pressure to generate a cold molecular jet. To create sufficient vapour pressure, the sample was heated to 90°C in a specific reservoir directly at the nozzle orifice (1 mm). The gas pulse is expanded into the vacuum chamber using a pulsed nozzle (Parker General Valve Series 9) operating at 8 Hz, where the molecular ensemble is polarised by the 4 μ s chirp ranging from 2 to 8 GHz, resulting in a macroscopic dipole moment. The chirp is generated by an arbitrary waveform generator and amplified by a 300 W travelling wave tube amplifier prior to broadcasting it into the vacuum chamber using a horn antenna. We use eight consecutive excitation chirps per gas pulse, which results in an effective repetition rate of 64 Hz. Upon excitation by the chirped microwave pulses, we record the free induction decay (FID) of the macroscopic dipole moment of the molecular ensemble for 40 μ s. To obtain the final spectrum, 4.5 million FIDs were co-added and Fourier transformed into the frequency domain, with the resulting frequency resolution of 25 kHz and full width half maximum of 50 kHz.

The analysis of the experimental spectrum was facilitated by quantum-chemical calculations using the ORCA 5.0 program package [60, 61]. The geometry optimizations followed by harmonic frequency calculations were performed at the B3LYP-D3/aug-cc-pVTZ level of theory. The set of obtained theoretical rotational constants and electric dipole moments were used to simulate the rotational spectrum. The molecular structure of diphenylsilane and the principal inertial axes are shown in Figure 6.1. In addition, Nudge Elastic Band (NEB) calculations were performed to calculate the barrier between the two equivalent minima.

For the initial spectral assignment, the calculated parameters for diphenylsilane were used as initial inputs to fit the experimental spectrum with PGOPHER [57]. The fits were then refined with Pickett’s SPCAT/SPFIT programs [107] using Watson’s *A*-reduction Hamiltonian in the I^r representation. The AABS package [53, 58] was used for displaying the predicted transitions and measuring the experimental fre-

quencies. Finally, the EVAL program [53] was employed for the calculation of bond lengths, bond angles, and dihedral angles using the Kraitchman's approach.

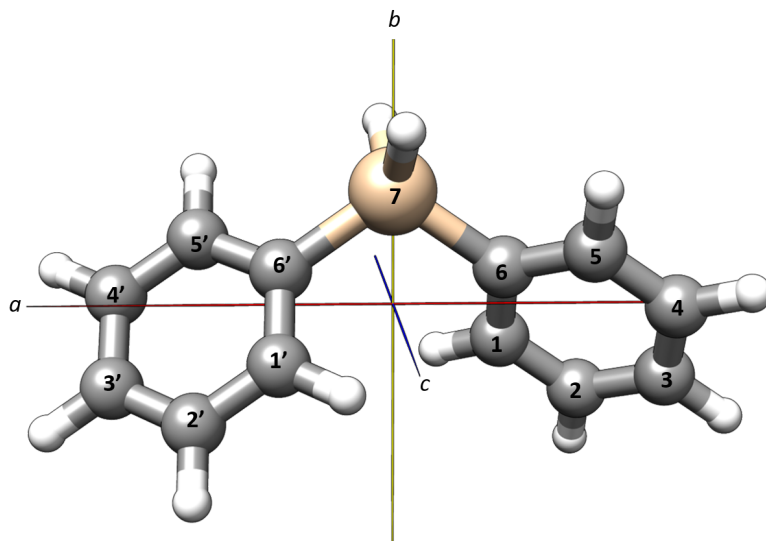


Figure 6.1: Molecular structure and principal inertial axes of diphenylsilane in ab plane.

6.3 Results and discussions

Diphenylsilane is a near-prolate asymmetric top molecule with a value of Ray's asymmetry parameter of $\kappa = -0.95$ and a calculated electric dipole moment of 0.9 D along the b -axis. The calculated minimum energy structure of diphenylsilane has a C_2 point group symmetry, with the symmetry axis C_2 coinciding with the b -inertial axis of the molecule. It is a flexible molecule and exhibits tunnelling motion of the phenyl groups between equivalent minima. The minimum energy structure of diphenylsilane, as shown in Figure 6.1 corresponds to a dihedral angle of 42° between C1'-C6'-Si-C6. The barrier height for the tunnelling motion of the phenyl rings between the two minima through a transition state was calculated using the NEB method at the B3LYP-D3/cc-pVTZ and MP2/cc-pVTZ level of theory. The calculated barrier height was found to be 196 cm^{-1} (2.72 kJ/mol) and 245 cm^{-1} (2.95 kJ/mol) at B3LYP-D3/cc-pVTZ and MP2/cc-pVTZ level of theory, as shown in Figure 6.2, which is too high to cause a resolvable splitting of the experimentally observed rotational transitions in our experiment. This barrier of diphenylsilane can be compared to its oxygen analogue, diphenylether, where the two phenyl rings are connected to an oxygen atom instead of a silicon atom. For diphenylsilane, the barrier is more than double than that of diphenylether ($\sim 100\text{ cm}^{-1}$), explaining the

absence of splitting of rotational transitions due to tunnelling in the former.

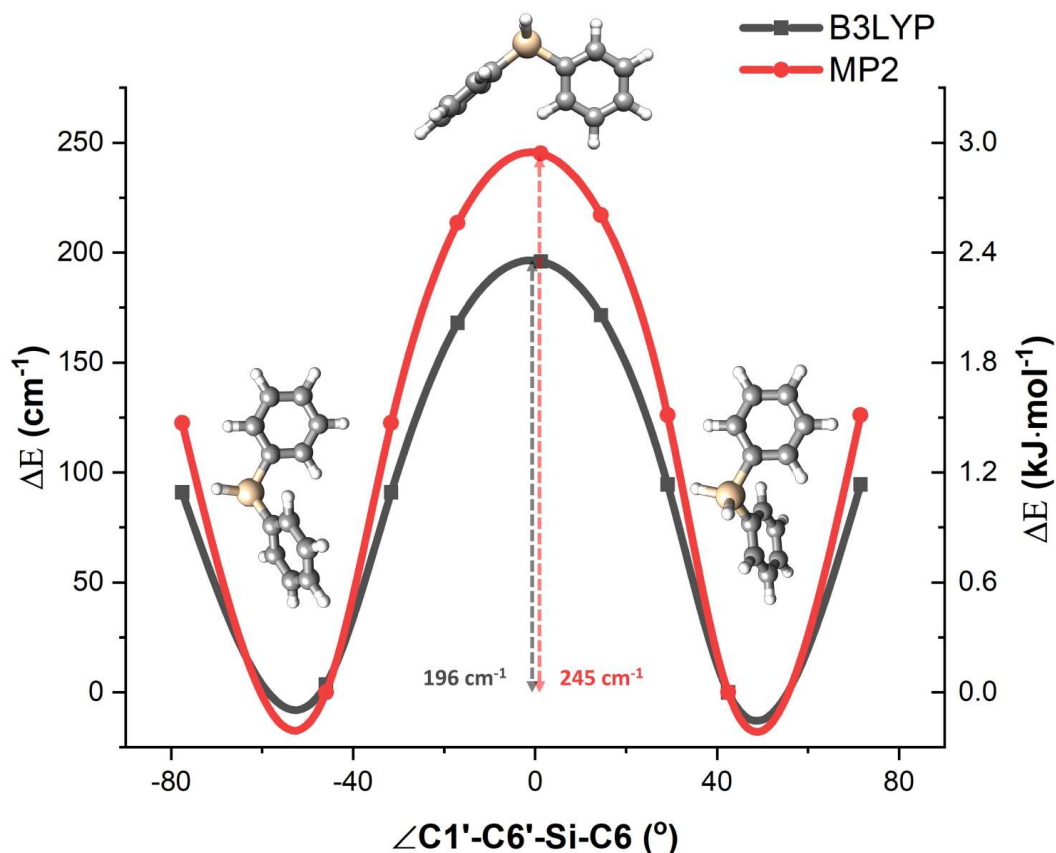


Figure 6.2: Theoretical analysis of the tunnelling barrier height calculated using the NEB method at B3LYP-D3/def2-TZVP level of theory. The x -axis shows the dihedral angle corresponding to the minima and the transition state. On the y -axis, the energy difference between the minima and the transition state is given.

A section of the high-resolution broadband rotational spectrum of diphenylsilane is shown in Figure 6.3 with the experimental spectrum in the top trace (in black) and the simulated spectrum in the bottom trace (in red). Table 6.1 shows the fitted rotational parameters together with the theoretically calculated ones. In total, 71 rotational transitions corresponding to the parent isotopologue were assigned in the 2-8 GHz frequency range with a root-mean-square deviation of the fit of 9 kHz. The signal-to-noise ratio of the experimental spectrum was sufficient to observe the rotational spectra of six singly substituted ^{13}C isotopologues and two singly substituted Si isotopologues, namely ^{29}Si and ^{30}Si , in their respective natural abundances. The natural abundances of ^{13}C , ^{29}Si , and ^{30}Si are 1.1%, 4.6%, and 3.1%, respectively, but due to the overall C_2 symmetry of the molecule, the rotational transitions arising

from ^{13}C isotopologues exhibit double the intensity ($\sim 2.2\%$) as compared to the natural abundance of 1.1%. This effect is further highlighted in Figure 6.4, where a section of the experimental spectrum is shown against the simulated spectra of the single substituted ^{13}C , ^{29}Si , and ^{30}Si isotopologues, for the rotational transition $J_{K_a, K_c} - J'_{K'_a, K'_c} = 4_{14} - 3_{03}$. The merged transitions are shown separately in the zoom-in of Figure 6.4a for better visualization of the observed rotational transitions. The fitted rotational and quartic centrifugal distortion constants of the singly substituted ^{13}C , ^{29}Si , and ^{30}Si isotopologues are summarized in Table 10.9 in Appendix 10.3, along with their theoretically calculated rotational constants.

In general the set of rotational constants obtained from the fits of these isotopologues allow for the determination of the individual atom positions with respect to the center of the mass of the molecule. Thus resulting in an accurate determination of the experimental structure of the molecule in the gas phase, in comparison to the derived structure based on quantum-chemical calculations.

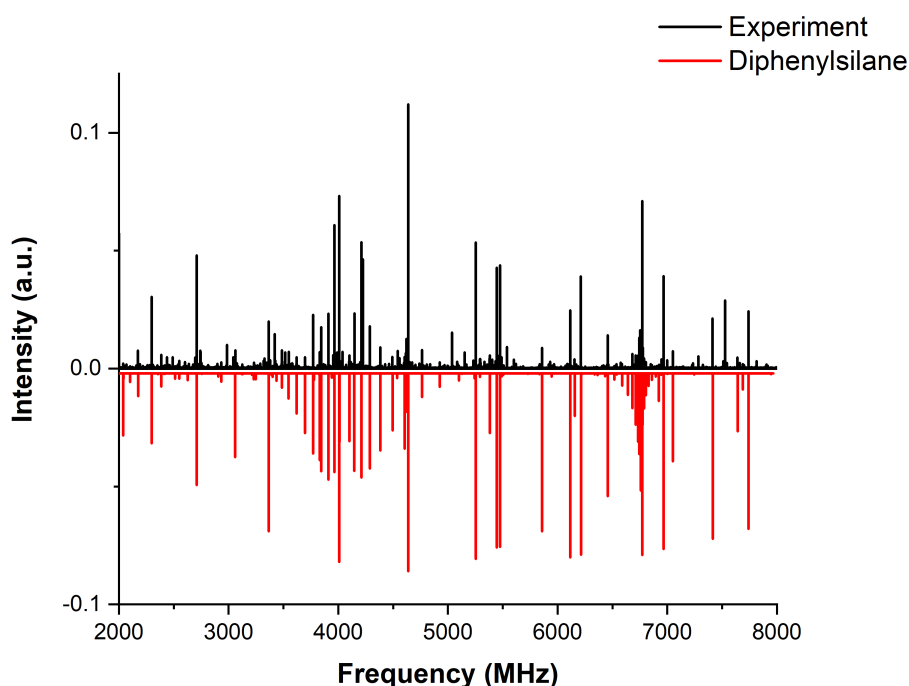


Figure 6.3: Part of the experimental rotational spectrum obtained for diphenyl silane in the frequency range of 2-8 GHz. The black trace represents the experimental spectrum, and the red trace corresponds to the simulated spectrum based on the fitted rotational constants (given in Table 6.1) and a rotational temperature of $T_{rot} = 3$ K.

Table 6.1: Experimental and theoretical rotational parameters for the vibronic ground state of the global minimum structure of diphenylsilane. The rotational transitions were fit using Watson’s A -reduction Hamiltonian in the I^r representation. The theoretical rotational parameters were calculated at the B3LYP-D3/aug-cc-pVTZ level of theory.

Rotational parameters	Experiment	Theory
A^a/MHz	1702.99149(88)	1722.37
B/MHz	366.69745(35)	367.30
C/MHz	335.80765(33)	333.48
Δ_J^b/kHz	0.0351(19)	
Δ_{JK}/kHz	0.2100(70)	
Δ_K/kHz	1.680(70)	
$\mu_a/\mu_b/\mu_c^c/\text{D}$		0.0/0.95/0.0
κ	-0.95	-0.95
σ^d	9	
No. of lines	71	

^a A, B, and C are the rotational constants.

^b Δ_J, Δ_{JK} , and Δ_K are the quartic centrifugal distortion constants.

^c $\mu_a/\mu_b/\mu_c$ are the electric dipole-moment components.

^d Microwave root-mean-square deviation of the fit.

In order to experimentally determine the gas phase structure of a molecule, different approaches can be employed. In this work, Kraitchman’s equations were used to obtain the substitution structure, r_s [66]. The Kraitchman’s substitution method exploits changes in the moments of inertia upon single isotopic substitution. This approach allows for determination of the coordinates of each isotopically substituted atom in the principal inertial axis frame (the signs of the coordinates can be assigned from the theoretical or effective structure coordinates).

The EVAL program [53] was used to calculate the various structural parameters derived from r_s structure determination, such as bond lengths, bond angles, and dihedral angles (given in Table 10.8 in Appendix 10.3). Figure 6.4b shows the overlay of the experimentally obtained r_s structure (in bold spheres) and the theoretical structure r_e obtained at the B3LYP-D3/aug-cc-pVTZ level of theory (in partially

transparent back bone).

The structure of diphenylsilane can be compared with that of diphenylether [174], as the latter is the oxygen analogue of diphenylsilane. It is important to note that different methods were employed to calculate the structural parameters for both molecules, r_s for diphenylsilane and r_0 (least-squares fitting method [119]) for diphenylether. The r_s structure is closer to the equilibrium structure, r_e than the r_0 structure. The detailed description of the structure determination methods can be found in Section 2.1.8.

On comparison, the C-Si bond length is found to be evidently longer than that of C-O as given by 1.855(9) Å for C-Si and 1.406(35) Å for C-O. Similarly, the dihedral angle described by C6'-Si-C6-C1 in diphenylsilane is found to be 47(1)° as compared to 43(2)° for diphenylether. Both longer bond length and larger dihedral angle for diphenylsilane in comparison to diphenylether can be explained by the larger radius of the Si atom (1.17 Å) with respect to the O (0.66 Å) atom*. The angle between C-Si-C is given by 109.61(16)°, which demonstrates the perfect tetrahedral arrangement corresponding to the sp^3 hybridization of the silicon atom. While for the C-O-C angle in diphenylether, given by 116(3)°, the steric hindrance created by two phenyl groups attached to an oxygen atom causes the deviation (increase) in the bond angle due to the smaller size of O as compared to Si. All the relevant bond distances, bond angles, and dihedral angles for the gas phase structure of diphenylsilane determined in this work are given in the Table 10.8 in Appendix 10.3. The structural comparison was also extended to other organosilicon molecules, for comparing the corresponding Si-C bond lengths to the one experimentally observed for diphenylsilane, as shown in Table 6.2. The list includes two rhomboidal isomers of cyclic silicon tricarbid (c-SiC₃) and their corresponding transannular and peripheral Si-C bonds [38, 176], where the Si is included in the cyclic structure of the molecule, trimethylsilyl chloride containing three methyl groups attached to Si [177], phenylsilane [178] and methyl phenylsilane [179], where Si is attached to an aromatic ring. It is to be noted that no rotational spectroscopy data is available for the gas phase structure determination of phenylsilane and methyl phenylsilane. Therefore, the Si-C bond lengths reported here were obtained by computing the equilibrium structure, r_e , at the MP2/aug-cc-pVTZ and at the MP2/6-31G* level of theory for methyl phenylsilane [179] and phenylsilane [180], respectively. For phenylsilane, the Si-C bond length is also reported from the gas phase electron diffraction study by Portalone *et al.* [180].

As can be seen from the Table 6.2, the longest Si-C bond length is reported for the oblate ring structure of SiC₃ (1.893(1) and 2.022(1) Å) for transannular and peripheral Si-C bonds, respectively. This is because in this molecule, silicon is a part of a strained four-membered ring and is connected to three carbon atoms with

*The atomic radii are taken from General Chemistry textbook [175]

a single bond with-in the ring. In order to reduce the ring strain, the silicon atom is pushed away from the ring, giving rise to longer Si-C bond lengths as compared to other members of the table. This can be directly compared to the ground state isomer of $c\text{-SiC}_3$ where the Si atom is connected to two carbon atoms with a single bond, while still being a part of the four-membered ring, resulting in lesser strain and consequently shorter Si-C bond lengths. One can also compare the Si-C bond lengths when the silicon atom is connected to the aromatic or aliphatic carbon atoms as in the case of diphenylsilane and trimethylsilyl chloride, respectively. The Si-C bond length in diphenylsilane is slightly shorter (1.855 ± 0.009 Å) than that in trimethylsilyl chloride (1.8606 ± 0.001 Å), since Si is connected to an aliphatic carbon in the case of trimethylsilyl chloride, giving rise to a longer Si-C bond length.

Table 6.2: A comparison of Si-C bond lengths of different organosilicon molecules, in Å, with the ones determined in this work experimentally and from the structure optimised at B3LYP-D3/ aug-cc-pVTZ level of theory.

Molecule	Bond length/ Å (Si-C)	Reference
$(\text{C}_6\text{H}_5)_2\text{SiH}_2$ (r_s)	1.855(9)	This work
$(\text{C}_6\text{H}_5)_2\text{SiH}_2$ (r_e)	1.876	B3LYP-D3/aug-cc-pVTZ
Ground state- SiC_3 (r_0)	1.834(2)	[38]
Oblate ring- SiC_3 (r_0)	$1.893(1)^a/2.022(1)^b$	[176]
$(\text{CH}_3)_3\text{SiCl}$ (r_0)	1.860(1)	[177]
$\text{C}_6\text{H}_5\text{SiH}_3$ (r_e)	1.872	[180] MP2/6-31G*
$\text{C}_6\text{H}_5\text{SiH}_3$ (ED) ^e	1.870(4)	[180]
$\text{C}_6\text{H}_5\text{SiH}_2\text{CH}_3$ (r_e)	$1.877^c/1.879^d$	[179] MP2/aug-cc-pVTZ

^{a/b}transannular/peripheral Si-C bond length

^{c/d}aromatic/aliphatic Si-C bond length

^eresults from electron diffraction study

6.4 Summary

The broadband rotational spectrum of diphenylsilane is reported in the frequency range of 2-8 GHz. The tunnelling barrier height and the central structure around the Si atom of diphenylsilane was compared with its oxygen analogue, diphenylether[174]. The rotational spectra of the parent isotopologue of diphenylsilane and all its singly substituted ^{13}C , ^{29}Si , and ^{30}Si isotopologues have been assigned with the help of theoretical calculations performed at the B3LYP-D3/aug-cc-pVTZ level of theory. The gas phase structure of diphenylsilane was determined using the Kraitichman's equations employed in the r_s method. The theoretical atomic coordinates agree well with the experimentally determined coordinates. The structural parameters like bond lengths, bond angles and dihedral angles of diphenylsilane, were compared with the structure of its oxygen analogue, diphenylether. This allowed for the identification of changes in the bond angles and bond lengths when the hetero atom is changed from O to Si. This structural comparison was also extended to other silicon containing molecules like silicon tricarbid, trimethylsilyl chloride, phenylsilane, and methyl phenylsilane.

The tunnelling barrier diphenylsilane was found to be quite high (double) than that of diphenylsilane and hence no resolvable splitting were observed experimentally. Given the size difference between the atomic radius of Si (1.17 Å) and O (0.66 Å), one would expect a smaller tunnelling barrier for diphenylsilane than that of diphenylether, as the Si-C (1.855 ± 0.009 Å) bond length is considerably longer than that of O-C (1.406 ± 0.035 Å).

Diphenylsilane is a complex organosilicon molecule with 13 heavy atoms. The comprehensive rotational spectroscopic analysis of this molecule sheds light on its gas phase structure, which influences the activity of the molecule. The structure can affect various applications, for instance, the biological activity, or the semiconductor properties of organosilicon compounds. The broadband rotational spectroscopy study of diphenylsilane can potentially be extended to high frequency regions, such as 75–110 GHz range which overlaps with ALMA band 3 [181]. Such measurements can provide accurate rest frequencies for detecting complex organosilicon molecules like diphenylsilane especially in the regions where other silicon-containing molecules have been previously detected in high abundances, for example, IRC+10216 [182]. The detection of complex organosilicon molecules will enable us to understand the chemical reactions taking place in the ISM and its existing chemical complexity.

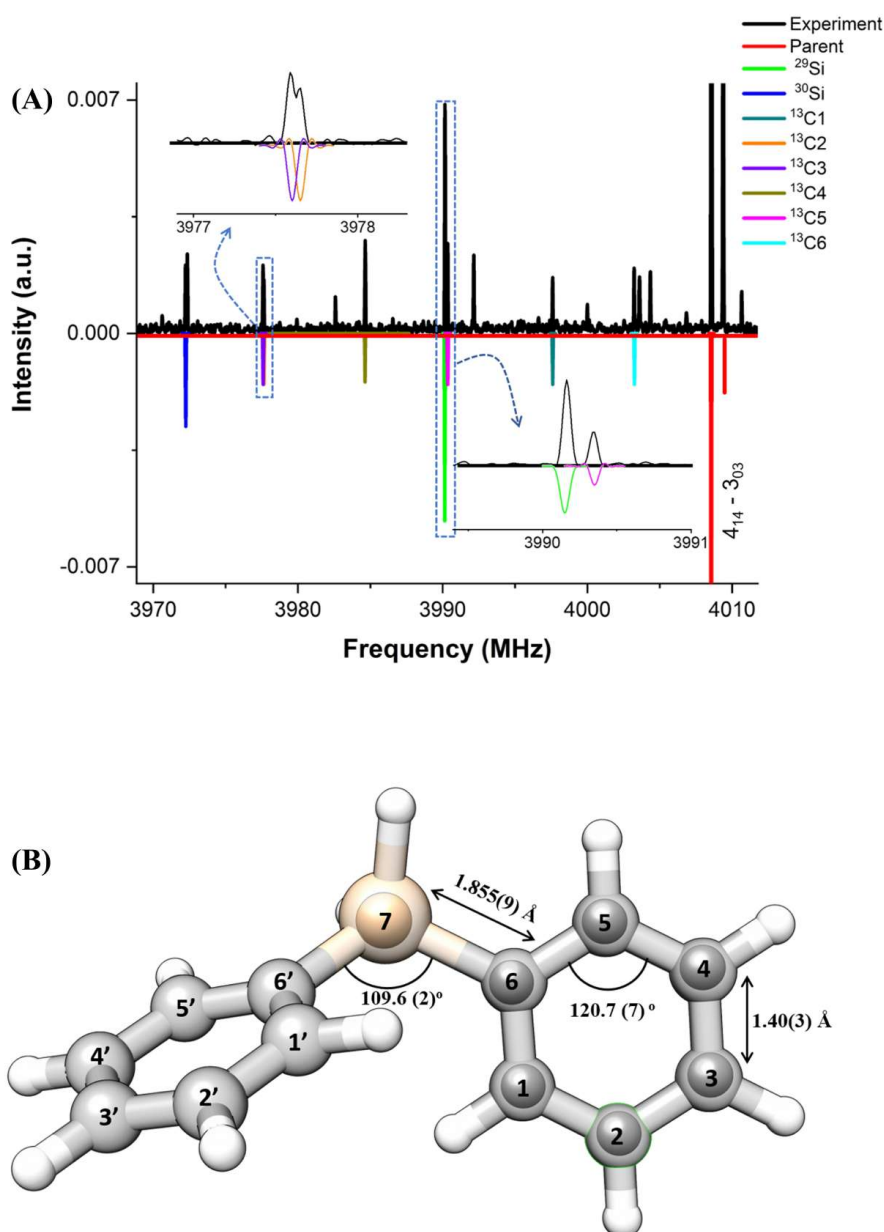


Figure 6.4: Panel A shows a section of the experimental spectrum highlighting the rotational transition $J_{K_a, K_c} - J'_{K'_a, K'_c} = 4_{14} - 3_{03}$ for the parent molecule (in red) and for all the observed singly substituted isotopologues as mentioned in the legend (on the top right of the spectrum). The sections where the rotational transitions arising from different isotopologues are close to each other are shown in the zoom-in of the spectrum. Panel B shows the experimental gas phase structure of diphenylsilane. The inner bold spheres represent the r_s positions of the atoms, whereas the partially transparent backbone gives the theoretical r_e structures (B3LYP-D3/aug-cc-pVTZ level of theory).

Chapter 7

Infrared reflection absorption spectroscopy of water ice and naphthalene

7.1 Introduction

Water is the cradle of life on Earth and water ice is believed to play a crucial role in the prebiotic chemical evolution in molecular clouds [183]. In the cold astrophysical environments, the gas-phase water molecules readily undergo condensation onto the surfaces of the silicate/carbon-rich dust grains, giving rise to the formation of ice grain mantles. Within water ices, the co-condensed small volatiles, such as methane (CH_4) and ammonia (NH_3), could react to form complex organic molecules, such as amino acids, especially when exposed to high-energy UV radiation [184]. Such photochemistry reactions can be influenced by the microstructure and porosity of the ice [185]. Interstellar ices are mainly characterized with the broad O–H stretching band near 3300 cm^{-1} in the mid-infrared (IR) region. The band profile is sensitive to the ice structures, such as amorphous solid water (ASW), cubic crystalline ice (I_c), and hexagonal crystalline ice (I_h), which are formed under distinct astrophysical conditions [186]. In cold molecular clouds, it is widely accepted that porous ASW structure predominantly prevails, which can undergo restructuring into crystalline ice forms upon exposure to elevated temperatures or UV radiation. However, precisely determining the exact composition and structure of interstellar ices still remains challenging, as they likely exist in mixtures of different ice forms and with other small molecules. One unresolved mystery regarding the hypothesis of porous ASW in molecular clouds is the absence of the free or dangling O–H (dOH) features near 3700 cm^{-1} , which typically serve as an indicator of ice porosity [187]. Besides temperature and high-energy radiation, the surface properties of the dust

grains, onto which interstellar ices accrete, can give rise to distinct arrangements of the water molecules at the grain-ice interfaces through surface-water interactions. The resulting ice structure within this contact layer further impacts the formation of bulk ice. In molecular clouds, aromatic carbon nanoparticles, including polycyclic aromatic hydrocarbons (PAHs) and graphite grains, are remarkably abundant and ubiquitous. Their IR emission signatures at wavenumbers of 3050, 1610, 1300, 1160, and 885, and 790 cm^{-1} , dominate the mid-IR spectra observed toward various galactic and extra-galactic sources [188–190]. These carbonaceous materials, exhibiting a diverse range of sizes and structures are not only present in the gas phase, but also constitute a significant portion of interstellar dust grains [191, 192]. Therefore, investigating the ice formation on these aromatic carbon surfaces are of particular interest.

Previously, the water adsorption on a graphene surface, the atomic single layer of graphite, has been experimentally and theoretically investigated [193–195]. These studies revealed that water molecules are physisorbed on the graphene surface through van der Waals interactions instead of hydrogen bonds [194]. At low water coverages (2 monolayers, ML) on the graphene/Pt(111) substrate, two flat hexagonal sheets of water molecules were formed under low temperatures of ~ 100 – 135 K and stacked directly on top of each other through hydrogen bonds, leaving no free O–H bond pointing to graphene or vacuum. The continued ice growth gave rise to infrared reflection-absorption spectroscopy (IRRAS) spectra similar to that of cubic crystalline ice (I_c) [193]. Later experiments conducted with graphene/Ir(111) further revealed that the formed ices exhibit higher degree of internal order compared to the bulk ASW observed on common metal surfaces, such as Pt(111) and Cu(111), where water molecules adsorb on metal surfaces via the oxygen-metal interactions ($\text{H}_2\text{O} \xrightarrow{\delta e^-} \text{M}$) [195–197].

Following the top-down approach, PAH molecules in the interstellar medium are thought to be produced through the combination of graphite sheets or amorphous carbon with reactive atomic hydrogen [198, 199]. The hydrogen edge encases the aromatic carbon surface and consequently acts as a barrier, impeding the diffusion of water molecules between PAH molecules. The movement and accumulation of water molecules have been investigated at the molecular level when weakly bound to PAHs in supersonic jet expansion ($T_{\text{rot}} < 3$ K), suggesting that the single water molecule can diffuse almost freely within the aromatic systems through the process of quantum tunneling [200, 201]. Detailed investigation of water adsorption on such confined surfaces has not been extensively reported yet. Although small PAH molecules were previously excluded as candidates for carriers of the unidentified infrared emission bands (UIRs) [202], recent astronomical observations of two cyano-substituted small-sized PAHs, namely 1- and 2-cyanonaphthalene, toward the molecular cloud TMC-1, where benzonitrile was also detected, strongly indicate the

presence of small aromatic hydrocarbons, such as benzene and naphthalene, in the interstellar medium [54, 203]. In the laboratory experiments, infrared signatures of naphthalene have been extensively studied under various conditions, including the gas phase,[204] the pure solid state,[205] in solid inert-gas matrices,[206] and when mixed in H₂O ice [207].

Herein, we investigate the interplay between naphthalene and water ice under ultra-high vacuum conditions at about 120 K using a high-resolution infrared reflection absorption spectroscopy (IRRAS). The vibrational dynamics of the water ice deposited on the naphthalene/Ir(111) substrate are compared with that from the ice sample directly grown on the clean Ir(111) surface. The interaction between water and different substrates results in the development of ice with varying degrees of internal molecular order, which is evidenced in the peak position and spectral shape of the water O–H stretching feature. In turn, the vibrational motions of naphthalene are affected by the ice sample as well, in contrast to the vibrational bands of naphthalene on Ir(111).

7.2 Experimental details

All experiments were carried out at the DESY Nanolab [208, 209]. The polarized infrared reflection-absorption spectroscopy (IRRAS) measurements were performed with a state-of-the-art Fourier transform IR spectrometer (VERTEX 80v, Bruker), which is part of an ultrahigh vacuum (UHV) apparatus. The optical path inside the IR spectrometer and the space between the spectrometer and the UHV chamber were evacuated so that background signals from the gas-phase species can be eliminated, which enhances the sensitivity and stability of the measurements. The base pressure in the IR measurement chamber is 2×10^{-10} mbar. All IRRAS spectra were collected by averaging 200 scans at a resolution of 2 cm^{-1} between 500 and 4500 cm^{-1} using the p-, s- and non-polarized IR light, respectively. The electric field vector of p-polarized IR light incidence has components both perpendicular and parallel to the surface. At the grazing angle of incidence, p-polarized spectra are dominated by vibrations normal to the surface, whereas s-polarized spectra only measure vibrations parallel to the surface (see Section 2.2.1).

An iridium single crystal surface, Ir(111), which was mounted on a molybdenum sample holder by tantalum clips, was used to grow the naphthalene and water ice layers and reflect the signal into an external mercury cadmium telluride (MCT) detector that was cooled using liquid nitrogen. The Ir(111) surface was first cleaned in the preparation chamber by repeated cycles of Ar sputtering and O₂ annealing and checked with low-energy electron diffraction (LEED) and Auger electron spectroscopy (AES). The cleaning process is similar to that previously described in detail [195]. The cleaned Ir(111) surface was then transferred to the IR chamber within

the UHV system (see Section 3.7). Naphthalene and water were placed in separate glass vials on the gas supply line of the IR chamber. The sample of naphthalene (99% purity) purchased from Sigma Aldrich, is crystal solid at room temperature, and used without any further purification. The gas line was flushed with Ar and subsequently pumped to remove residual air. Both naphthalene and water were degassed through freeze-pump-thaw cycles.

Prior to sample exposures, the polarized (p-, s-) and non-polarized IRRAS spectra of the clean Ir(111) surface, which was maintained at $T \approx 120$ K using liquid nitrogen cooling, were measured and used as background references. Next, vapors of water and naphthalene were sequentially introduced into the chamber in steps via leak valves and adsorbed on the cooled Ir(111) surface. The polarized IRRAS spectra were measured for each exposure step. The sample exposures were reported in units of Langmuir (L) ($1 \text{ L} = 1.33 \times 10^{-6} \text{ mbar}\cdot\text{s}$). Two sets of experiments were conducted, where the sample depositions on the Ir(111) surface are naphthalene (130 L)–ice (400 L) and ice (130 L)–naphthalene (130 L)–ice (9800 L).

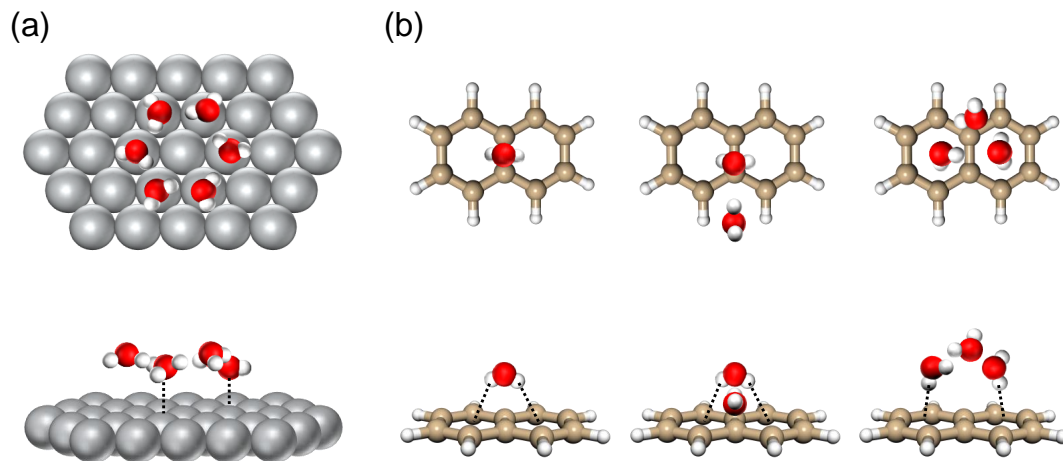


Figure 7.1: (a) Top and front views of the adsorption of the water hexamer on the Ir(111) surface. (b) Top and front views of the water clusters binding to the naphthalene molecule, which are taken from ref [210]. The black dashed lines indicate the interactions of the water molecules with the Ir(111) surface and the naphthalene molecule.

7.3 Results and discussion

Water-surface interactions can influence the formation dynamics and structure of the first monolayer of ice and thus the continued ice growth. In the past few years, enormous efforts have been devoted to obtaining the molecular-level understanding of water adsorption on different surfaces [197]. When using single-crystal transition metals as substrates, the metal surfaces play the role of an electron acceptor so that water molecules bind to metals through the oxygen lone pair orbitals forming the first water layer [211, 212]. A rich diversity of water-surface structures have been reported from different metal surfaces and conditions, such as a one-dimensional ice chain on Cu(110) [213], a two-dimensional water monolayer on Pt(111) [214], and three-dimensional clusters on Cu(111) [215] and Pt(111) [216]. As iridium and platinum are neighboring elements in the periodic table, the lattice constant of monocrystalline iridium is similar to the platinum crystal with a minor difference of about 2%. It can thus be expected that water adsorption on the Ir(111) surface mimics that on Pt(111). A previous study using scanning tunneling microscopy and thermal desorption spectroscopy has shown that the arrangement of the water molecules on Ir(111) and Pt(111) are very similar at low coverages (< 1 ML), where a hydrophobic wetting layer is formed [196]. In this wetting layer, a small fraction of the water molecules are lying flat and sitting in the atop sites of the metal substrates, as demonstrated in Figure 7.1a, whereas the rest are situated slightly higher to the surface and bonded to the bottom water clusters completing the hydrogen-bonded network. For larger coverages (> 1 ML) on Pt(111) with a growth temperature below 125 K, it is observed that multilayer water films are formed, which are predominantly ASW [214, 216, 217]. In this study, we measured the IRRAS spectra of the H_2O adsorption on the low-temperature Ir(111) substrate. The spectra in the O–H stretch region are presented in Figure 7.2 with increasing water exposures. A clear feature was only observed with a H_2O exposure larger than 10 L. The broad absorption band (black lines) with a maximum at 3395 cm^{-1} is consistent with the previously reported IRRAS spectra of ASW in terms of both band position and shape [218–222], which is attributed to the intramolecular O–H stretching vibrations (ν_{OH}) from the fully-coordinated H_2O molecules in bulk ASW. The frequency of this vibrational mode is sensitive to O–H \cdots O distances within the ice structure [223]. The stronger the intermolecular interactions, the shorter the O–H \cdots O distance and the lower the vibrational frequency. Due to the metal surface selection rules, the vibrations with the transition dipole perpendicular to the surface normal cannot be detected [224], so no band was observed with s-polarized light, as shown in Figure 7.2c. In addition, there is a weaker band at 3696 cm^{-1} emerging from 30 L, which is the characteristic feature of the dangling O–H bonds (dOH) protruding into the vacuum [195, 225]. This peak arises from the three-coordinated

H₂O molecules. The counterpart from the two-coordinated H₂O molecules (~ 3720 cm⁻¹) was not observed, as it is not energetically favored above 70 K [219]. When depositing H₂O onto naphthalene, the ν_{OH} band exhibits a distinct profile (red solid lines in Figure 7.2), comparing to that observed with the H₂O/Ir(111) samples. The absorption maximum of ν_{OH} is red-shifted to 3275 cm⁻¹, whereas the feature at 3395 cm⁻¹ appears as a peak shoulder. This band profile is typically observed with ordered ice structures, such as crystalline ice (CI), believed to form at higher temperatures (typically $T > 150$ K) [221, 226]. The red shift of the ν_{OH} mode suggests a reduction in O \cdots O distances and an enhancement of intermolecular hydrogen-bonding interactions within the formed ice on naphthalene [227]. Therefore, the varied peak position and intensity imply that the growth of ice on naphthalene follows a distinct growth mode, in contrast to the ASW formation on the Ir(111) surface. This is likely attributed to the distinct adsorption preference of H₂O at the ice-naphthalene interface. Due to the conjugated π system, naphthalene functions as a proton acceptor, promoting the formation of the O-H $\cdots\pi$ bonds, as elucidated in the naphthalene-(H₂O)_{1,2,3} clusters from a previous gas-phase IR study (see Figure 7.1b) [210]. Recent experimental and theoretical investigations also suggested a similar binding preference at various water-PAH interfaces in the condensed phase

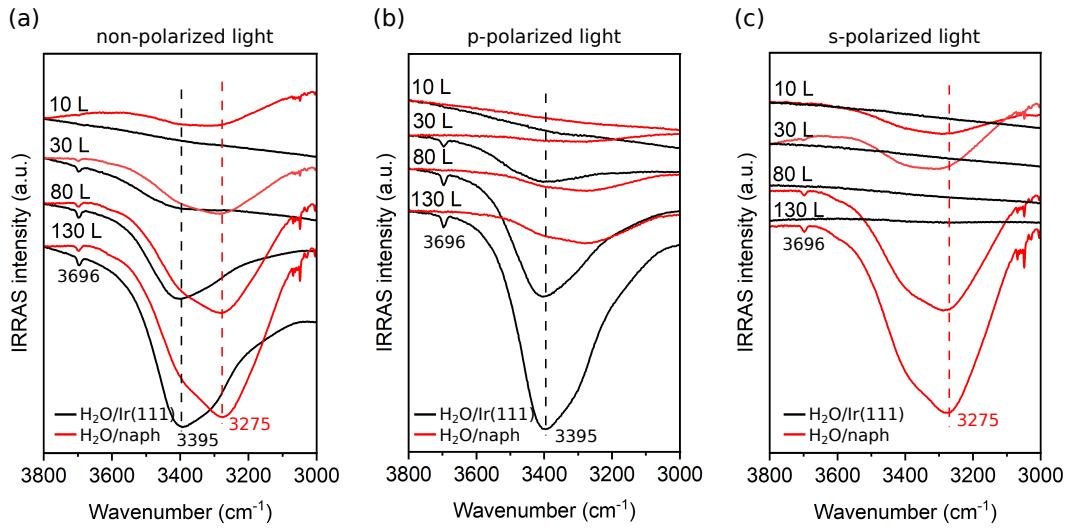


Figure 7.2: IRRAS spectra in the OH-stretching region as water (H₂O) adsorbs on the clean Ir(111) (black lines) or naphthalene (naph, red lines) surfaces at ~ 120 K. The spectra are labelled with the total exposure after each dosing step, which are measured with non- (a), p- (b), and s-polarized (c) IR light. The naphthalene interface is prepared on 130 L H₂O/Ir(111) with 130 L exposure of naphthalene.

[228, 229]. This sets naphthalene apart from other common surfaces. For instance, on metal surfaces, including Ir(111), water molecules in the contact layer lie flat (see Figure 7.1a), [197] as the surfaces serve as electron acceptor attracting the oxygen lone pairs of the water molecules. In the case of non-metal hydrophobic substrates, such as graphene [193] and carbon tetrachloride [221], water molecules orient with their oxygen atoms pointing toward the surfaces. Additionally, in the present study, by exposing the 130 L H₂O/Ir(111) sample to 0.5 L naphthalene, the dOH band at 3696 cm⁻¹ disappears completely, as presented in Figure 7.3a. The elimination of free O–H bonds evidently indicates that the three-coordinated water molecules are mainly situated in the ice overlayer and naphthalene favorably adsorbed onto these dangling O–H bonds via the hydrogen bonds. According to the measured IRRAS spectra for naphthalene on the Ir(111) surface

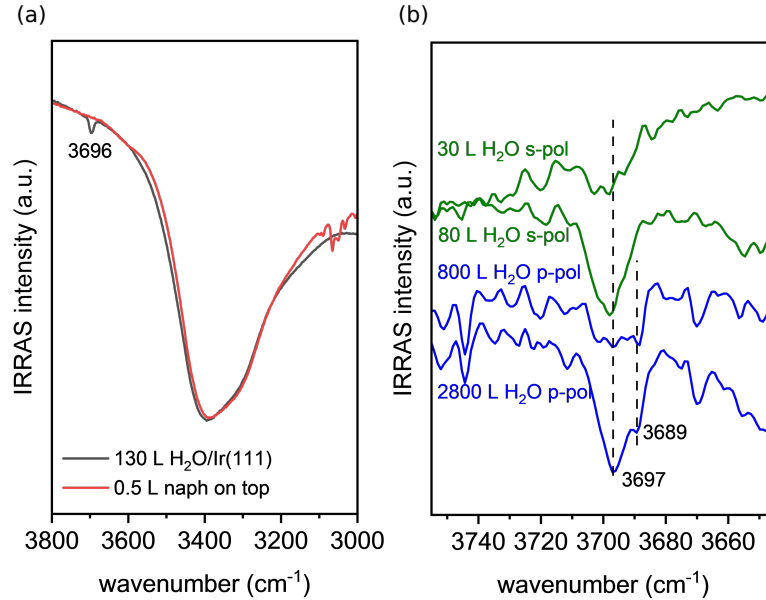


Figure 7.3: (a) Comparison of the non-polarized IRRAS spectra in the OH-stretching region before (black line) and after (red line) dosing 0.5 L naphthalene (naph) on the H₂O ice substrate at ~ 120 K, where the H₂O dOH band disappears completely with 0.5 L naphthalene on top. The ice surface is prepared by dosing 130 L H₂O on the clean Ir(111) surface. (b) The emergence of the H₂O dOH band in the s-polarized (green) and p-polarized (blue) spectra, respectively, when dosing H₂O on naphthalene. The naphthalene substrate is prepared by dosing 130 L naphthalene on the ice base described in (a). Similar spectra can be obtained using the 130 L nap/Ir(111) substrate.

and on the $\text{H}_2\text{O}/\text{Ir}(111)$ substrate (Figure 10.4 and 10.5 in the Appendix 10.4), the in-plane vibration bands of naphthalene, especially the in-plane C-H stretching features spanning from 2980 cm^{-1} to 3120 cm^{-1} , are more pronounced with s-polarized IR radiation, where the out-of-plane motions near 790 cm^{-1} are predominately probed with p-polarized light. Both suggest that the naphthalene rings are mainly lying flat on the $\text{Ir}(111)$ surface. As previously mentioned, when weakly bound to naphthalene, a single water molecule may rotate almost freely about its C_2 axis through quantum tunneling, as described in naphthalene- H_2O (Figure 7.1b) [200, 201]. Nevertheless, unlike the facile water diffusion on the non-confined $\text{Ir}(111)$ surface ($T > 20\text{ K}$), which leads to the formation of hydrogen-bonded ice films or clusters, the hydrogen edge of naphthalene confines the aromatic π system and makes water diffusion between naphthalene molecules energetically less favorable. When more water molecules accumulate over naphthalene, those making direct contact with naphthalene can adopt doubly or singly hydrogen-bonded ($\text{O}-\text{H} \cdots \pi$) arrangements, as shown in naphthalene- $(\text{H}_2\text{O})_2$ and naphthalene- $(\text{H}_2\text{O})_3$ (Figure 7.1b), respectively. Starting from these physisorbed water molecules, the formation of the complete ice monolayer and the continued growth of bulk ice are expected to undergo a different mode compared to the growth of ASW on $\text{Ir}(111)$. Since the selection rules for metal surfaces are no longer applicable to the naphthalene substrate, the water orientation in the ice was examined using the IRRAS spectra measured with p- and s-polarized IR radiation. In Figures 7.2b and 7.2c, the spectra evidently show that the ν_{OH} band strength obtained with the s-polarized light is much greater than that measured with the p-polarized light at each exposure step. Given that bulk ASW is isotropic, the polarization-dependent absorption feature indicates the anisotropy growth of ice films on the naphthalene substrate, in which the majority of O-H bonds align parallel with the $\text{Ir}(111)$ surface and the ring plane of naphthalene molecules [230]. This finding is consistent with previous observations with graphene/ $\text{Ir}(111)$ at high exposures ($>5\text{ L}$) under similar conditions [195]. Note that the ice grown on the graphene/ $\text{Pt}(111)$ substrate was proposed to exhibit a cubic crystalline ice (I_c) structure, which can also be observed within this study [193]. The anisotropic ice property on the naphthalene/ $\text{Ir}(111)$ surface is also reflected in the observation of the dOH band. Figure 7.3b highlights the emergence of the dOH feature with the s-polarized light at an H_2O exposure of 30 L, similar to that observed with bulk ASW on the $\text{Ir}(111)$ surface. In contrast, the detection of the dOH band with p-polarized light was only evident after an H_2O exposure of 800 L, indicating a limited number of O-H bonds dangling perpendicular to the $\text{Ir}(111)$ surface in the ice overlayer. The new side peak at 3689 cm^{-1} is presumably contributed from the dOH vibration in CI [231]. The early appearance of the dOH band with s-polarized light unveils the porous nature of the formed ice films. In this scenario, most of the three-coordinated water molecules are located at the internal surface of

the micropores, aligning their dangling O–H bonds parallel to the Ir(111) surface. This observation also sheds light on the intriguing difference between the confined carbon surface of naphthalene and the continuous carbon surface of graphene. The hydrogen edges of naphthalene molecules cause repulsion between the neighbouring molecules within the same layer. Consequently, the patched carbon surface in the naphthalene overlayer promotes the formation of ice islands on top of the naphthalene molecules at lower coverages, eventually evolving into porous ice structures. On the other hand, the naphthalene-water interactions have impact on the vibrational modes of naphthalene at the interface as well. Due to the interactions in the condensed phases, the spectral band positions and strengths are often varied compared with that obtained in the gas phase. As the structure of naphthalene is rather rigid, these effects are relatively modest so that peaks do not show significant shifts in position ($< 10 \text{ cm}^{-1}$) and changes in relative band strengths (by factors of 1–3) [205, 207, 232–235]. According to the IR spectra, the most sensitive band to the adsorbate-adsorbate and adsorbate-surface interactions arises from the out-of-plane C–H wagging motion, denoted as $\nu_{\text{CH,wag}}$. The transition dipole moment of this mode is perpendicular to the molecular plane of naphthalene. The band center is at 781.9 cm^{-1} in the gas phase [232], and 783 cm^{-1} in the solid phase [205] and inert gas matrices, respectively [233, 234]. In the present study, when dosing naphthalene on Ir(111) and $\text{H}_2\text{O}/\text{Ir}(111)$ surfaces at 120 K, the peak maximum of $\nu_{\text{CH,wag}}$ consistently appears at 787 cm^{-1} for high coverages (10 – 130 L) in both experiments (Figure 7.4). This peak position can be characterized as the absorption signature from the bulk phase of naphthalene. When compared to the peak maximum measured with low naphthalene coverage on Ir(111), a blueshift of 2 cm^{-1} is observed, which resembles the band variation observed with the growth of naphthalene on the Ag(111) surface at 150 K [236]. This blueshift is attributed to the formation of 3D multilayer islands after the completion of monolayer and metastable multilayers, following the Stranski-Krastanov growth mode. This interpretation is further supported by the appearance of the peak shoulder at 792 cm^{-1} , presumably arising from the $\nu_{\text{CH,wag}}$ vibration of the 3D multilayer islands. However, at the naphthalene-water interface, an opposite peak shift of approximately 3 cm^{-1} was observed for this $\nu_{\text{CH,wag}}$ vibration, which can be attributed to the O–H $\cdots \pi$ interactions occurring between naphthalene and water. A similar band shift is reported in a previous IRRAS study of naphthalene frozen within a solid H_2O matrix, and this shift was influenced by the concentration of naphthalene in the ice [207]. However, the co-deposition of naphthalene-water lead to the formation of bulk ASW, distinguishing it from the separate growth of naphthalene and ice.

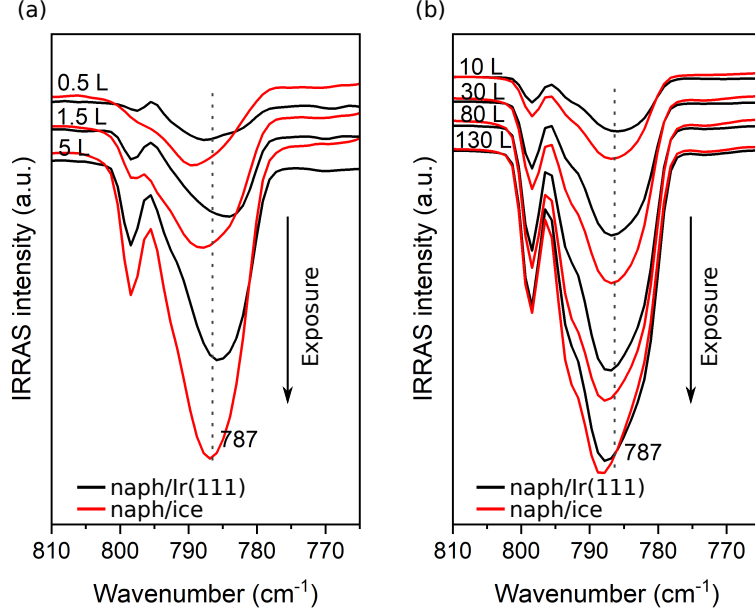


Figure 7.4: IRRAS spectra obtained with p-polarized IR light after exposing the clean Ir(111) (in black) or ice/Ir(111) (in red) sample to various doses of naphthalene (naph) at ~ 120 K in an UHV chamber. Panel (a) and (b) display the spectra with low and high naphthalene coverages, respectively, which are labelled with the accumulated exposure after each dosing step.

7.4 Summary

In summary, we studied ice growth on Ir(111) and naphthalene/Ir(111) surfaces under ultrahigh vacuum conditions at approximately 120 K using infrared reflection absorption spectroscopy (IRRAS) with p- and s-polarized IR radiation. Our finding regarding the water O–H stretching band demonstrates the formation of porous ice films on the naphthalene/Ir(111) substrate, whereas a bulk amorphous solid water structure was observed on the clean Ir(111) surface. Such difference is attributed to the varying molecule-surface interactions at the naphthalene-water and naphthalene-Ir(111) interfaces, respectively, leading to distinct structures in the ice monolayer. The former prefers to form the O–H $\cdots\pi$ between H₂O and the naphthalene rings, while water molecules adsorb on Ir(111) via the oxygen-metal interactions. As a result, the continued growth of bulk ice exhibits differing ice structures, revealed through the water O–H stretching mode measured with p- and s-polarized light. The observation of the dangling O–H band, arising from the three-coordinated water molecules, further suggests the porous structure in the ice films

formed on the naphthalene/Ir(111) sample. In addition, the molecule-surface interactions also modestly influence the out-of-plane wagging motion of naphthalene. From an astrochemical point of view, this study highlights the formation of different ice structures depending on the molecule-surface interaction. Our findings related to the formation of porous ice structures on the naphthalene/Ir(111) substrate could potentially influence surface chemistry on dust grains. This influence may arise from the increased surface area, enhanced local binding energies, and the potential trapping of molecules within the pores as ice mantles accumulate on the grains.

Chapter 8

Silicon chemistry under the harsh conditions of an electrical discharge

- A part of this chapter is based on experiments performed during a FELIX beamtime in Nijmegen, the Netherlands (August 2022), project titled, *Exploring the formation of silicon-containing PAH-like molecules under plasma conditions*. This project is a collaboration between G. Batra, D. Loru, A. K. Lemmens, P. Ferrari, B. Redlich, and M. Schnell.
- Own contributions:
 - participation in the measurements
 - quantum-chemical calculations
 - data analysis

8.1 Introduction

Silicon is one of the most abundant elements on the Earth's surface, accounting for around 27 % of the Earth's crust by mass (after oxygen representing 46.6%). However, due to the refractory nature of silicon, there are essentially no gas phase silicon-containing molecules in the Earth's terrestrial environment [171]. Silicon is also abundant in space, being only one order of magnitude less than C, N, and O [17]. A significant fraction of the elemental silicon is believed to be locked up in relatively volatile dust components [18], which provide the surface for the ice grain chemistry in the cold regions of interstellar medium (ISM). The presence of silicon in

the interstellar environments was first detected in Sagittarius B2 more than 50 years ago in the form of silicon monoxide (SiO) [19]. Since then, more than 15 silicon-containing molecules have been detected, ranging from diatomic silicon monoxide (SiO) to more complex molecules, such as methylsilane, CH_3SiH_3 [20]. Among the Si-containing molecules detected in space, organosilicon species and in particular silicon-carbon species Si_nC_m , are considered potential molecular building blocks in the chemical evolution of the interstellar medium [164, 237] and are associated with the formation of silicon-carbide dust grains in the outflow of circumstellar envelopes of asymptotic giant branch (AGB) star IRC+10216 [165, 238].

Organosilicon molecules are among the most abundant [182] molecular species in this region but their formation mechanisms have remained largely elusive. For instance, the line profiles of $c\text{-SiC}_3$ and SiC_4 found in IRC+10216 indicate that they are formed in the external regions of the envelope where other radicals are formed under the action of galactic ultraviolet fields [239], thus suggesting potential reaction pathways including neutral-radical or radical-radical recombination.

In addition to organosilicon molecules, Si_nC_m , hydrogenated Si-containing molecules such as silane SiH_4 have also been detected in IRC+10216 [240]. The derived abundance of silane (2×10^{-7} relative to H_2) [241] surpasses the abundance predicted by thermochemical equilibrium by several orders of magnitude. This mismatch in the observed and calculated abundance points towards the formation channels of silane that have not been included in the chemical models yet. For instance, one of the possible formation mechanisms for silane could be the catalytic reactions at the surface of grains, as suggested by Keady and Ridgway in 1993 [242]. The presence of silane in such high abundances could also lead to the formation of molecules containing SiH_3 and SiH_2 as functional groups, as suggested by the recent detections of methyl silane CH_3SiH_3 [241] and SiH_3CN [243] in IRC+10216. The formation of methylsilane in the outer layers of IRC+10216 is proposed to be driven by silyl and silylene radicals, SiH_3 and SiH_2 , and the methyl and methylene radicals, which could be produced by photodissociation of silane and methane, respectively [241].

Several studies in literature have explored reaction mechanisms leading to the formation of organosilicon molecules, including hydrogenated silicon carbides such as methylsilane [241] and cyanosilane [243], proposing radical-radical reactions. A recent investigation by Lucas *et al.* [244] delves into the gas phase reaction of phenyl radicals with silane, elucidating the formation mechanism of phenylsilane ($\text{C}_6\text{H}_5\text{SiH}_3$) under single collision conditions. Aromatic molecules are known to be quite ubiquitous in space, marked by the recent detections like that of benzonitrile in half a dozen molecular clouds [54], cyano substituted naphthalene [245], indene [139], cyano-indene [140], and probably more under way. Expanding upon the abundance of SiH_4 and the prevalence of aromatic molecules in the ISM, detecting silane-substituted aromatic compounds becomes a natural progression in exploring

the chemical complexity present in the interstellar medium. To aid the detection of molecules in space, laboratory data are required, and one way is to synthesize silicon containing molecules in laboratory by using electrical discharge sources [170, 171, 246], since they are known for *in situ* production of species of astronomical interests as a result of radicalization, fragmentation, and recombination. These molecules might be unstable in their pure form or not readily accessible commercially, for example, *o*-benzyne was formed *in situ* using electrical discharge [41] and subsequently examined through rotational spectroscopy to aid its detection in the ISM [39]. Coupling of the electrical discharge sources to spectroscopic techniques allows the formation of new species and their identification by spectroscopy [247–252]. Even though the experimental conditions of electrical discharge experiments do not exactly match with the conditions found in the star forming regions or different molecular clouds, nevertheless, identifying the intermediates and products formed in such experiments can help deduce possible formation pathways. For example, Lemmens *et al.* highlight different reaction mechanisms leading to the formation of larger PAHs starting from benzene in an electrical discharge experiment coupled with mass-resolved IR-UV ion dip spectroscopy [253]. Moreover, in an electrical discharge experiment of pure naphthalene, Loru *et al.* reported the formation of ethynyl benzene as a result of electrical discharge and probed by microwave spectroscopy, which further lead to its detection in TMC-1 [254]. In the present work, we emphasize on the importance of high-resolution spectroscopic techniques, such as IR-UV ion dip spectroscopy and rotational spectroscopy coupled with discharge sources. Since the two techniques are complementary to each other (as can be seen in section 8.3.3), one can use these results to obtain a broader overview of the chemical reactions between silicon and carbon containing moieties. We investigate the chemistry under electrical discharge conditions of phenylsilane, as this molecule can act as a source of an aromatic carbon ring and silicon in the form of silane.

8.2 Experimental and computational details

8.2.1 Electrical discharge coupled with IR-UV ion dip spectroscopy

The electrical discharge experiment of phenylsilane was performed at the FELIX laboratory [82] using mass-selective IR-UV ion dip spectroscopy coupled with an electrical discharge source. A thorough description of the spectrometer is given in Section 3.6. Phenylsilane was purchased from Sigma Aldrich (99 % purity), and it was used without any further purification. The sample of phenylsilane, which is liquid at room temperature, was loaded in a home-built heatable reservoir and heated

to 50 °C to obtain sufficient concentration of the molecules in the gaseous phase. Argon (~ 5 bar) was passed through the reservoir containing phenylsilane, and the molecular gas pulse was created using a general valve. Prior to supersonic expansion into the vacuum chamber, the gas pulse was subjected to a voltage of ~ 0.75 kV, which caused the ignition of a plasma. A current of ~ 50 mA was found optimal for the formation of molecular species with mass-to-charge (m/z) ratios larger than that of the precursor molecule. The design of the discharge nozzle was inspired from the one presented in references [247, 248]. The design and description of the discharge nozzle can be found in Section 3.4 and the explicit details of the discharge nozzle used for this experiment can be found in previous works by Lemmens *et al.* [40]. The expanding gas pulse containing a mixture of newly formed species, precursor molecule, and carrier gas was passed through a skimmer before it could interact with the three laser beams to perform IR-UV ion dip spectroscopy and mass spectroscopy. The formed products present in the molecular beam were ionized using $[1+1']$ resonant enhanced multiphoton ionization (REMPI) with excitation by a tunable dye laser and ionization with an ArF laser (193 nm). The excitation wavelength is resonant with an unresolved vibronic state of an electronic state of the formed discharge products. We used two different excitation wavelengths for our experiments, 266 and 269 nm, respectively, based on the UV absorption spectra recorded for a variety of new masses upon discharge observed using time-of-flight mass spectrometry, as shown in Figure 8.2. Excitation wavelengths in the range of 260 to 280 nm are known to enable a selective ionization of aromatic species [255], which is also in line with previous studies [40, 43, 253]. As can be seen from Figure 8.2, using two different excitation wavelengths can probe a broad range of discharge products, which in turn provides information about the chemical reactions taking place under the harsh conditions of the discharge experiment. The resonant IR absorption leading to the depopulation of molecules in the ground vibrational state is probed by the REMPI scheme (as described in section 3.6.1) and thereby recording their mass-selective IR-UV ion dip spectra [40]. The ionized species were then mass-separated and detected using a reflectron time-of-flight mass spectrometer equipped with a multi-channel plate ion detector. For each mass peak with sufficient signal-to-noise ratio in the $[1+1']$ REMPI mass spectrum, an IR spectrum was recorded in the 550-3200 cm^{-1} region in parts of 550-1000, 1000-1600, 1900-2400, and 2800-3200 cm^{-1} using the IR-UV ion dip method with the free electron laser FELIX-2 at the FELIX laboratory [82]. The repetition rate of the IR laser was set to half with respect to the rest of the experiment (10 Hz) to acquire alternating IR on and IR off shots to avoid shot-to-shot ion signal fluctuations.

To improve the SNR of the experimental data, several IR spectra were recorded and averaged together for each mass channel. For some of the mass channels with large absorption cross-sections, an attenuation of 5 dB and 10 dB were applied to FELIX

to avoid the saturation of the experimental IR spectra. The final IR spectra shown in this chapter are obtained after applying the 5-point adjacent-average smooth function to the average of the IR spectra for better visualization of the vibrational features.

The assignment of the IR spectra to a specific molecule was achieved by comparing the calculated IR spectra of multiple possible isomers with the experimental spectra of that particular mass. Some species could be discarded based on the mismatch between the calculated and experimental IR spectra. The theoretical spectra were calculated using ORCA 5.0 [60, 61] at the B3LYP-D3/def2-SVP level of theory. The basis set, def2-SVP, has been shown to be sufficient for the assignment of the experimental spectra. For example, we calculated the IR spectra for $m/z=184$ at different levels of theory and the comparison is shown in Figure 8.1, where the basis set def2-SVP performs better than others in reproducing the experimental spectrum. A scaling factor of 0.9671 was applied to the frequency scale of the theoretical harmonic spectra [256] and were subsequently convoluted to a Gaussian lineshape function having a full width at half maximum (FWHM) of 1% to match the FELIX bandwidth.

The final assignment was achieved by computing the IR spectra of several possible isomers corresponding to the same mass followed by their comparison with the experimental IR spectrum obtained for that particular mass.

8.2.2 Electrical discharge coupled with rotational spectroscopy

We analyzed the products resulting from the electrical discharge of a mixture of benzene and silane gas (1 % SiH_4 in Ne) using the CP-FTMW spectrometer COMPACT coupled with an electrical discharge source. The operation of the COMPACT spectrometer can be found in detail in Section 3.1. The rotational spectra were recorded across the frequency range of 2-8 GHz and 8-12 GHz [73, 75, 76]. A concise overview of the instrument’s operational sequence is provided hereafter. The sample of benzene (99.8 % purity) was purchased from Sigma-Aldrich and was used without any further purification. Benzene is liquid at room temperature, thus to increase its concentration in the gas phase, it was loaded in a heatable reservoir of a modified pulsed valve (General valve series 9), whereas a gas cylinder containing a mixture of 1 % silane in neon (used as a carrier gas) was attached externally to the instrument. The benzene and silane mixture was created by heating the reservoir containing benzene to 40 °C and flowing the silane (in Ne) gas over it with a backing pressure of 3 bar. Before the molecular gas pulse could supersonically expand into the vacuum chamber, it was flown through the discharge nozzle (containing two Cu electrodes with a potential difference) where the presence of the gas pulse containing the mixture of the precursors led to plasma ignition. A voltage between 1.2-1.3 kV

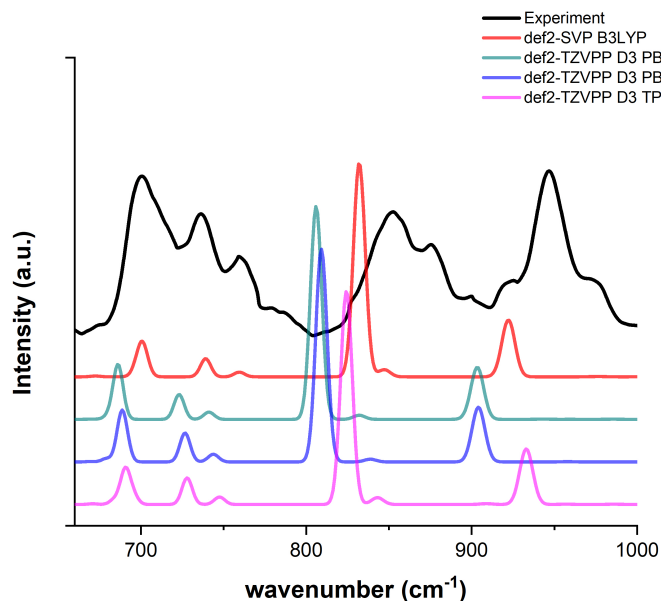


Figure 8.1: Comparison of the performance of different levels of theory for reproducing the experimental spectrum. The black trace depicts the experimental IR spectrum for $m/z = 184$ in $550\text{--}1000\text{ cm}^{-1}$ and the colored traces represent the calculations performed at different levels of theory.

producing around 100 mA was found optimal for the formation of molecular species of our interest. After passing through the nozzle, the gas pulse was supersonically expanded into the vacuum chamber.

A preliminary fit of the experimental rotational spectra of the newly formed species, was performed using the PGOPHER program [57]. The final spectroscopic parameters were obtained using the SPFIT/SPCAT suite of programs by Pickett [107].

8.3 Results and discussion

The results and discussions will be divided into two parts. The first part describes the results obtained using mass-resolved IR-UV ion dip spectroscopy”, while the second part focuses on the two specific discharge products phenylsilane and diphenylsilane, elucidating a bottom-up growth of silicon-containing aromatic molecules in the conditions of an electrical discharge.

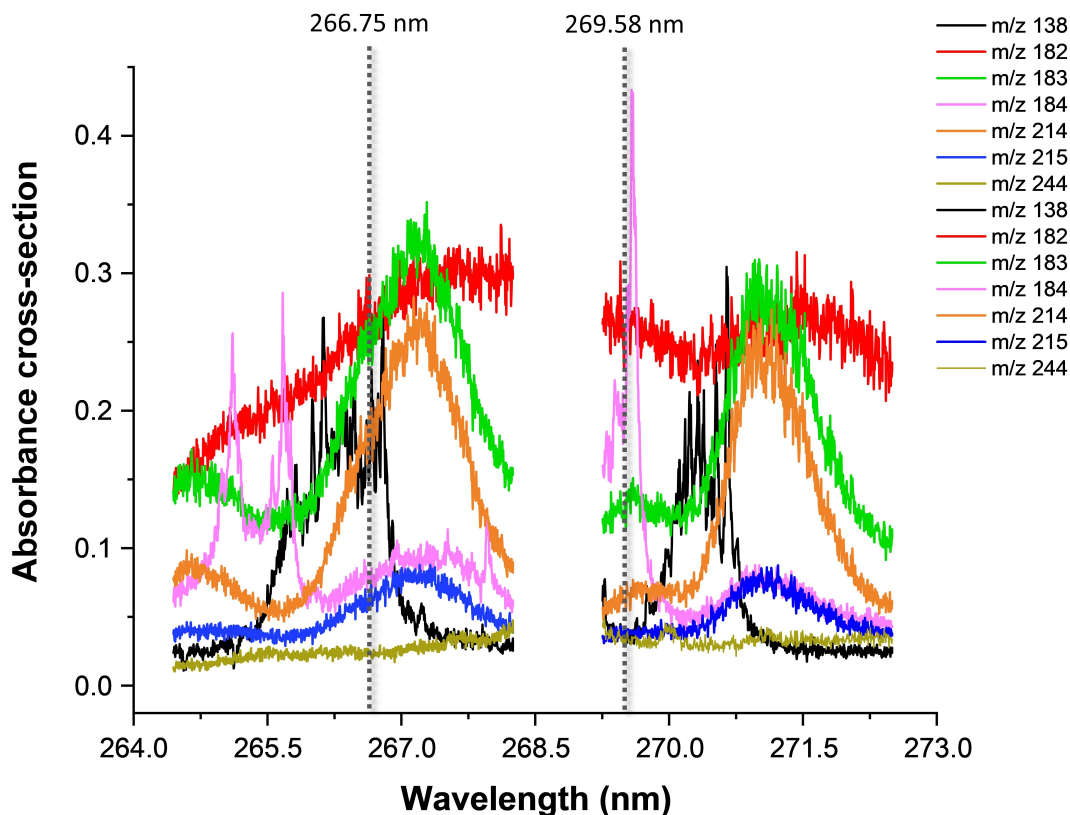


Figure 8.2: UV absorption spectra recorded for a variety of newly formed discharge products indicated by their m/z ratios on the right. The two vertical lines corresponds to the two wavelengths chosen for the excitation UV laser prior to ionization UV laser.

8.3.1 Electrical discharge of phenylsilane probed by mass-resolved IR-UV ion dip spectroscopy

Often the knowledge of the mass spectrum is not sufficient to deduce the chemical structures of the species involved, and additional spectroscopic information is required to ascertain the molecular formulae and/or structures. Especially for bigger molecules, as with increasing mass, the number of possible isomers increases dramatically and becomes more difficult to differentiate and assign among the isomers of the same mass. In order to obtain structural information for the different mass channels, we rely on a combination of mass-selective IR-UV ion dip spectroscopy and quantum chemical calculations.

The molecule phenylsilane contains a benzene ring and a silyl group attach to it.

When it is subjected to the conditions of electrical discharge it can result in two major classes of molecules: the ones arising solely from the benzene fragmentation followed by recombination and the other from the combination of both benzene and silane. To ease the identification of the new discharge products arising from the latter class of molecules, we compared the time of flight mass spectrum of the discharge of phenylsilane with that of pure benzene. The resulting products of an electrical discharge of pure benzene have been previously reported using mass selective IR-UV ion dip spectroscopy [40], which we employ here. Figure 8.3 displays a mass spectra of phenylsilane with and without the application of discharge (discharge ON and OFF) and pure benzene discharge spectrum probed via [1+1'] REMPI spectroscopy. Since the doubly ionized species are not expected with photo-ionization using 193 nm UV light, the m/z values reflect the masses of the species created in the discharge experiment. Upon comparison of the mass spectra obtained for benzene and phenylsilane, there are some m/z peaks in common. For these peaks, we compared the IR spectra to confirm if they arise from the same chemical species or the different ones. For example, the peak at $m/z = 152$ is common in both the discharge spectra of pure phenylsilane and pure benzene, but their experimental IR signatures are different, thus indicating the formation of different chemical species. The $m/z = 152$ in benzene discharge corresponds to the formation of ethylnaphthalene [40], whereas $m/z = 152$ in the discharge experiment of phenylsilane to methyl(silylphenyl)silane (see Figure 8.19b). Several new peaks corresponding to $m/z = 122, 134, 136, 138, 182, 183, 184, 185$, and 214 are observed in the mass spectrum of phenylsilane discharge. It is to be noted that the observed intensities in the mass spectra do not necessarily correspond to the relative abundances since the excitation and ionization cross sections may vary across the different chemical species formed in the experiment.

Considering that electrical discharge experiments are a source of radical formation, the C-Si bond can be assumed to be fairly easy to break due to the significant size difference between the atomic radii of C (0.77 Å) and Si (1.17 Å)*, therefore the presence of silyl and phenyl radicals can be assumed in fair abundance. This can be verified by reviewing the experimental bond enthalpies of some common bonds at 298 K, as given in Table 8.1. Following this, the assignment of $m/z = 138$ (Figure 8.4d) and $m/z = 184$ (Figure 8.7c) to phenyldisilane and diphenylsilane, respectively, was straightforward. In the former, the reaction product forms as a result of the substitution of H with SiH₃ radical to form phenyldisilane, and in the latter, it is the substitution of H with phenyl radical to form diphenylsilane. The assignment of diphenylsilane was further confirmed through a comparison of the recorded IR spectrum of diphenylsilane with that available on the NIST[†] Chemistry

*Atomic radii taken from reference [175]

[†]NIST/EPA Gas-Phase Infrared Database

website. Excellent agreement was observed between the $m/z=184$ and the reference spectrum of diphenylsilane, shown in the blue trace of Figure 8.7c.

Table 8.1: Experimental bond dissociation enthalpies at 298 K

Bond dissociation enthalpies at 298 K (kJ/mol)			
$\text{C}_6\text{H}_5\text{-H}$	472.4	C-C	347
$\text{CH}_3\text{-H}$	439.3	C-Si	318
$\text{SiH}_3\text{-H}$	383.7	Si-Si	218
C=C	610	$\text{C}\equiv\text{C}$	836

The bond dissociation enthalpies given above are taken from reference [257, 258]

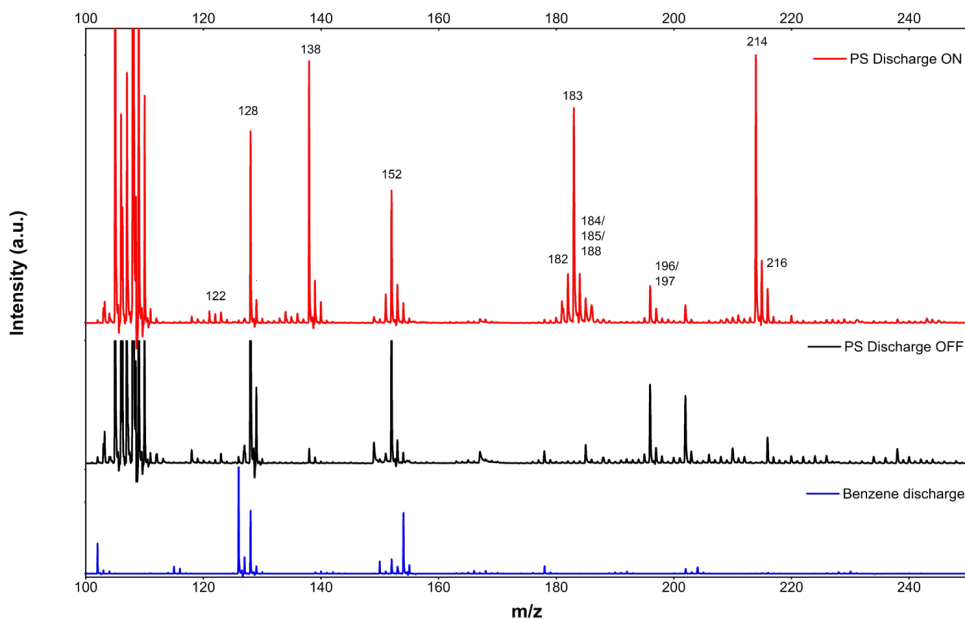


Figure 8.3: Comparison of the mass spectrum of phenylsilane (PS) with and without the application of electrical discharge (red and black trace, respectively), and with the mass spectrum obtained for the electrical discharge of benzene [253] (blue trace). The parent signal intensity of phenylsilane at $m/z=108$ is cut on the y-axis to highlight the peaks arising from the discharge products. The mass spectra of phenylsilane with discharge ON and discharge OFF were recorded with two-color REMPI (266+193 nm). The new products formed in the discharge experiment of phenylsilane are marked with their corresponding m/z values.

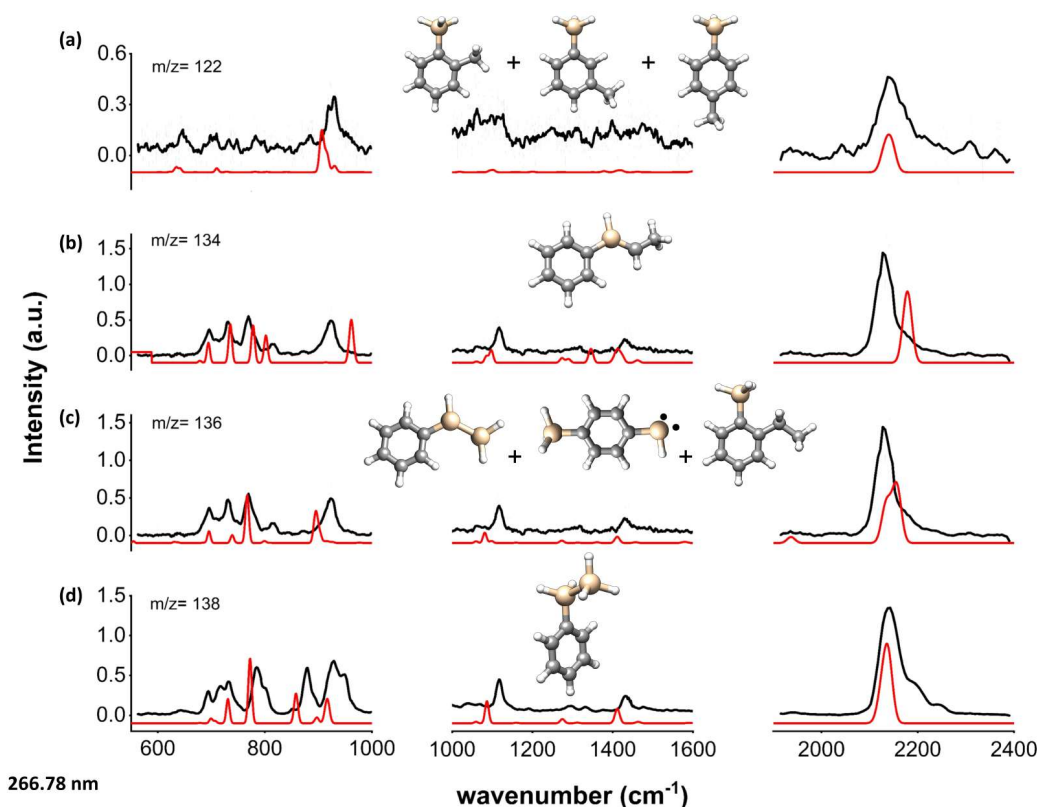


Figure 8.4: Comparison of the experimental IR spectra (black trace) recorded in the 550-2400 cm^{-1} frequency region for $m/z=122$, 134, 136, and 138 with the theoretical vibrational spectra (red trace) calculated at the B3LYP-D3/def2-SVP for the structures given above the spectra. The observed discharge products are probed with [1+1'] REMPI (266+193 nm). The black trace is obtained after applying a 5-point adjacent-average smooth function to the average of the IR spectra. The red trace provides the calculated spectra of one isomer ($m/z=134$ and 138) or the sum of the calculated spectra of the different structural isomers included ($m/z=122$ and 136) to account for the different vibrational bands. A scale factor of 0.9671 was applied to the frequency scale of the theoretical harmonic spectra [256] and was subsequently convoluted to a Gaussian lineshape function with a FWHM of 1% to match the FELIX bandwidth.

The IR regions between 550-1000 cm^{-1} and 1900-2400 cm^{-1} of the vibrational spectra are the most intense and diagnostic ones, often sufficient to assign a calculated spectrum of a particular molecular structure to the experimental spectrum. In fact, the intense band at $\sim 2200 \text{ cm}^{-1}$ arising from the asymmetric stretching motion of Si-H can act as a diagnostic tool for the identification of Si-H containing species. We used this band as a guide to focus on the discharge species containing Si. For in-

stance, $m/z=128$ corresponds to naphthalene having the molecular formula of $C_{10}H_8$ (also present as a contaminant in the commercial sample of phenylsilane) and hence no signature Si-H stretching band was observed and therefore was not considered for the analysis. The most intense vibrational bands in the spectral region of 1000-1600 cm^{-1} are generated by the scissoring motion (at $\sim 1100\text{ cm}^{-1}$) and rocking motion (at $\sim 1400\text{ cm}^{-1}$) of the H atoms attached to the aromatic ring. The vibrational bands in the region of 2800-3200 cm^{-1} depict the asymmetric stretching motion of the H atoms connected to the aromatic ring.

The experimental IR spectra corresponding to the mass channels 122, 134, 136, and 138 recorded with the UV excitation wavelength at 266 nm are shown in Figure 8.4. The black trace represents the experimental spectra and the red trace displays the theoretical spectra generated as a result of either one isomer or the combination of different structural isomers to account for all the vibrational bands exhibited by the experimental spectrum. The IR spectrum corresponding to $m/z=122$ (Figure 8.4a) has been assigned to the sum of three isomers, namely *o*-methyl phenylsilane, *m*-methyl phenylsilane, and *p*-methyl phenylsilane in 1:1:1 ratio. The sum spectrum and the individual contribution of all the three isomers is shown in Figure 8.5. Similarly, the IR spectrum for $m/z=136$ has been assigned to the sum of three isomers, namely phenyldisilane, (4-silylphenyl)silanylidene, and (2-ethylphenyl)silane in the ratio of 2:1:1, respectively to reproduce the experimental IR spectrum. The individual contribution of these species to the sum is shown Figure 8.18b in Appendix 8.4. Figure 8.4c shows the sum of the IR spectra of these three isomers (in red) against the experimental spectrum. Figure 8.4b and 8.4c in Appendix 8.4, displays the experimental and theoretical IR spectrum of $m/z=134$ and 138, where each of the experimental IR spectra could be reproduced by a single isomer: (E)-ethylidene(phenyl)silane and phenyldisilane, respectively.

The experimental IR spectra corresponding to mass channels 152, 183, 185, and 216 were recorded with the UV excitation wavelength set at 266 nm, and their assignment is summarized in Figure 8.6. It is to be noted that the $m/z=183$ and 185 are odd masses and hence (in the present experiment) correspond to open shell molecular species, *i.e.*, $m/z=183$ has been assigned to the 1:1 sum of diphenylsilyl and 4-silyl-1,1'-biphenyl-3-yl radical (Figure 8.6b) and $m/z=185$ to the 1-silyl-7H-benzoannulen-7-yl radical (Figure 8.6d). The IR spectra linked to $m/z=152$ and 216 have been assigned to the sum of two structural isomers in 1:1 ratio, methyl(3-silylphenyl)silane and methyl(4-silylphenyl)silane for $m/z=152$, and to the sum of (2,6-dimethyl-5-silylnaphthalen-1-yl)silane and (6,7-dimethyl-8-silylnaphthalen-2-yl)silane in 1:1 for $m/z=216$, as displayed in Figure 8.6a and 8.6d, respectively. In addition, we also performed another set of experiments where the UV excitation wavelength was fixed at 269 nm. The results of which are displayed in Figure 8.7, where the UV excitation wavelength was resonant with the unresolved vibrational

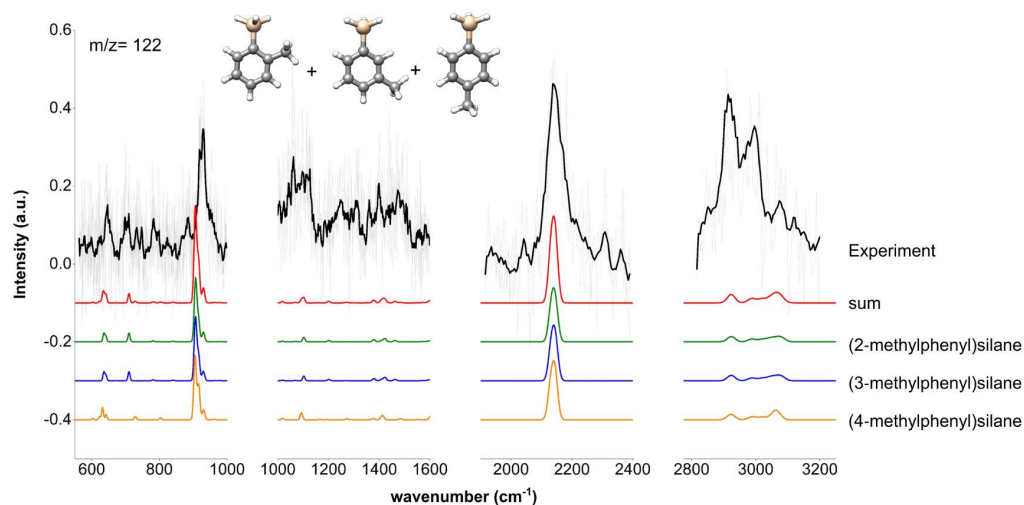


Figure 8.5: Comparison of the experimental IR spectrum (in black trace) recorded in the $550\text{--}2400\text{ cm}^{-1}$ frequency region for $m/z = 122$ with the theoretical vibrational spectra calculated at the B3LYP-D3/def2-SVP for the structures given above the spectra. This figure describes the assignment process, where the experimental IR spectrum of a particular mass is compared with different isomers of $m/z=122$ which have the similar vibrational features as that of the experimental IR spectrum. The final assignment includes the sum of all three isomers in 1:1:1 ratio (shown in red).

transitions of four new discharge products with $m/z = 138, 182, 184$, and 188 . The corresponding experimental IR spectra are displayed in the black trace, and the theoretical IR spectra are shown in the red trace of Figure 8.7.

It is interesting to note that the $m/z = 138$ has also been observed in the experiment performed with UV excitation wavelength fixed at 266 nm , but their IR signatures are different, as shown in Figure 8.8, thus indicating the formation of different molecules. The IR spectrum of $m/z = 138$ recorded with the UV excitation wavelength fixed at 269 nm corresponds to the sum of the theoretical IR spectra of (2-silylphenyl)silane and (4-silylphenyl)silane in a 1:1 ratio. On the other hand, the $m/z = 138$ observed with UV excitation wavelength fixed at 266 nm corresponds to the formation of disilylbenzene (Figure 8.19a, in Appendix 8.4). This signifies the importance of recording the UV absorption spectra of the discharge products, as it indicates the UV wavelengths where the excitation coefficients for the respective discharge species is at their maximum. This can then be employed to probe a broad range of molecules formed in the experiment.

The mass channels corresponding to $m/z = 182$ and 184 have been assigned to the biphenyl system condensing to form 9-silafluorene and to the diphenyl system, where the two phenyl rings are attached to the silicon atom: diphenylsilane, respectively.

The IR spectrum recorded for $m/z = 188$ is assigned to the sum of silane-substituted naphthalene units at two different positions, as shown in Figure 8.7d.

The IR spectra (both experimental and theoretical) of all the observed masses and their associated molecular species (both individual contribution and the sum spectra) are given in the Appendix at the end of this chapter.

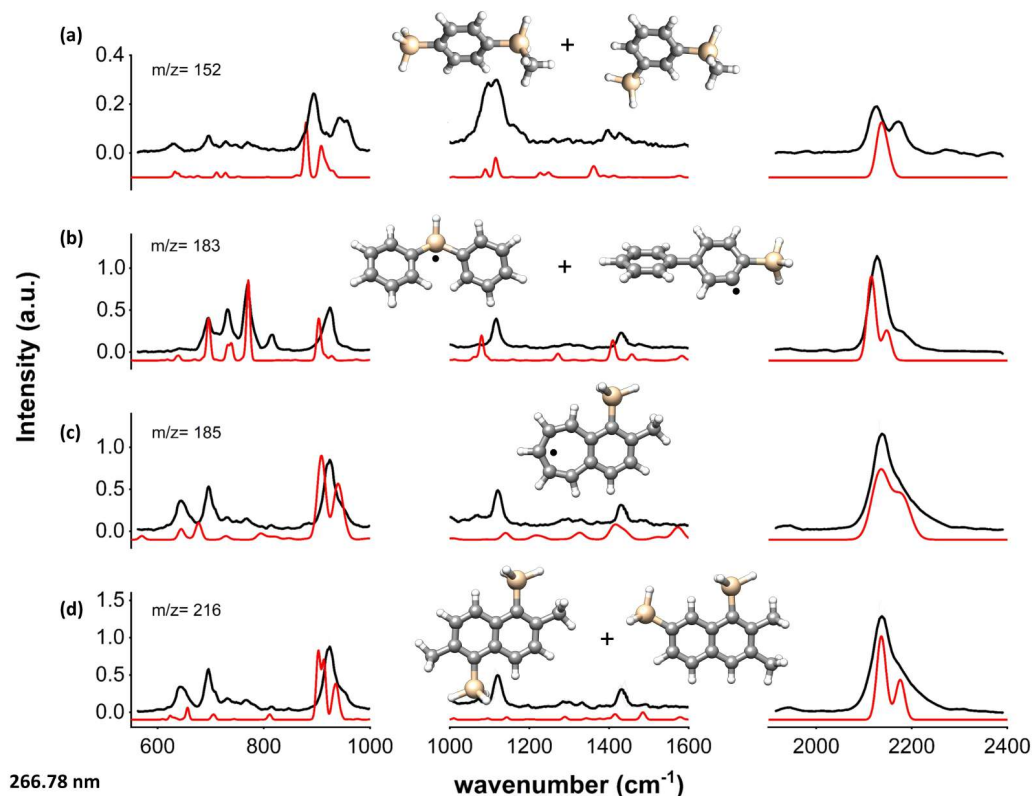


Figure 8.6: Comparison of the experimental IR spectrum (in black trace) recorded in the 550-2400 cm^{-1} frequency region for $m/z = 152$, 183, 185, and 216 with the theoretical vibrational spectra (in red trace) calculated at the B3LYP-D3/def2-SVP for the structures given above the spectra. The observed discharge products are probed with [1+1'] REMPI (266+193 nm). The black trace is obtained after applying a 5-point adjacent-average smooth function to the average of the IR spectra. The red trace provides the calculated spectrum of one isomer ($m/z = 185$) or the sum of the calculated spectra of the different structural isomers included ($m/z = 152$, 183, and 216) to account for the different vibrational bands. A scale factor of 0.9671 was applied to the frequency scale of the theoretical harmonic spectra [256] and was subsequently convoluted to a Gaussian lineshape function with a FWHM of 1% to match the FELIX bandwidth.

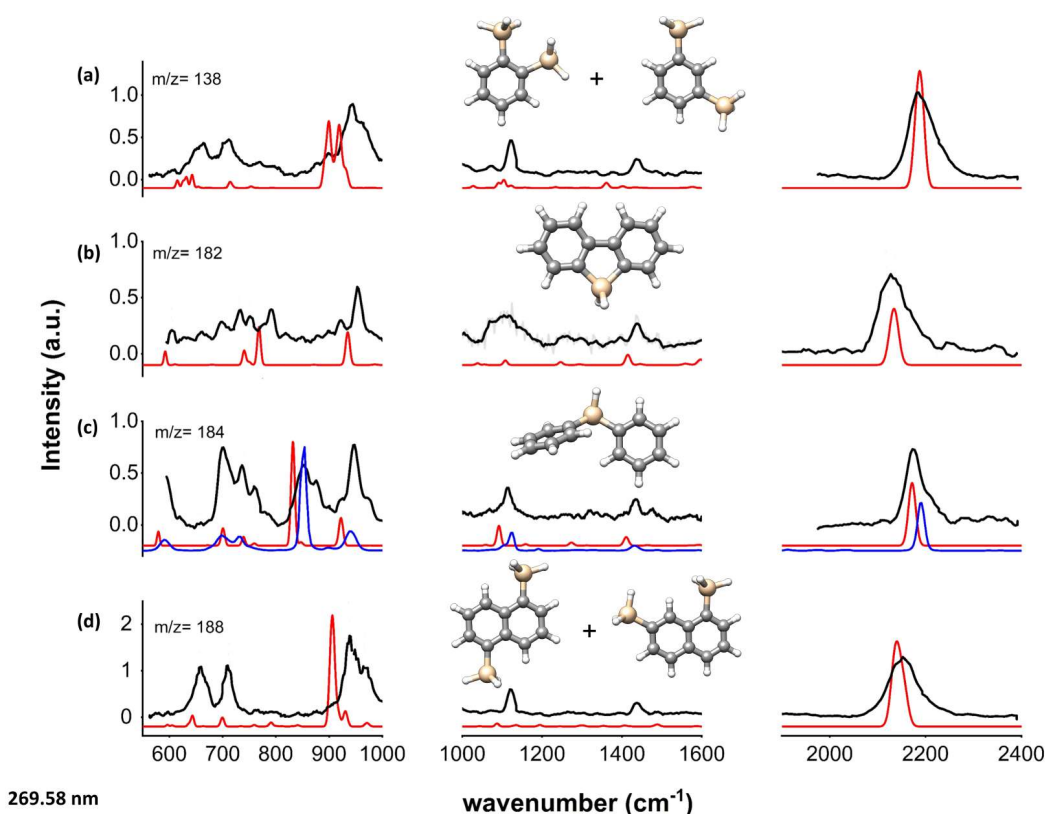


Figure 8.7: Comparison of the experimental IR spectrum (black trace) recorded in the 550-2400 cm^{-1} frequency region for $m/z=138$, 182, 184, and 188 with the theoretical vibrational spectra (in red trace) calculated at the B3LYP-D3/def2-SVP for the structures given above the spectra. The observed discharge products are probed with [1+1'] REMPI (269+193 nm). The black trace is obtained after applying a 5-point adjacent-average smooth function to the average of the IR spectra. The red trace provides the calculated spectrum of one isomer ($m/z=182$ and 184) or the sum of the calculated spectra of the different structural isomers included ($m/z=138$ and 188) to account for the different vibrational bands. A scale factor of 0.9671 was applied to the frequency scale of the theoretical harmonic spectra [256] and was subsequently convoluted to a Gaussian lineshape function with a FWHM of 1% to match the FELIX bandwidth.

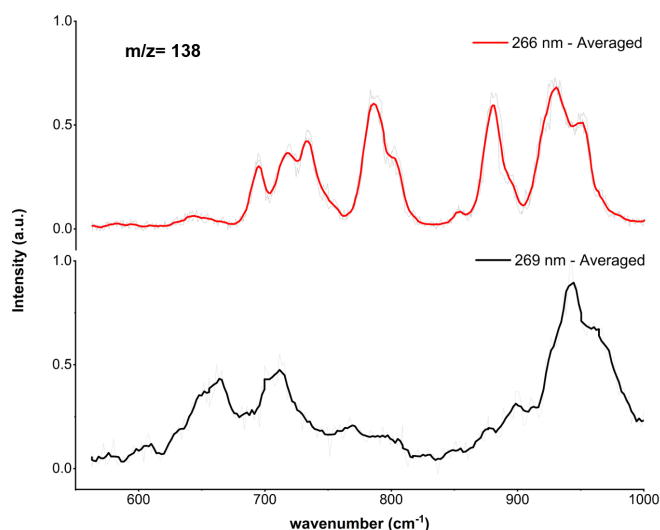


Figure 8.8: The comparison between the vibrational bands of $m/z=138$ ($550\text{--}1000\text{ cm}^{-1}$) at two different sets of UV wavelengths, (266+193 nm) and (269+193 nm). The red trace corresponds to the IR spectrum observed at the UV excitation wavelength of (266+193 nm) and the black trace to (269+193 nm).

In the analysis, we also observed similarities between the vibrational spectra of different masses, arising from the same vibrational motion. These mass channels are grouped together in Figure 8.9c to aid the visualization of the vibrational bands in discussion. The experimental IR spectra corresponding to mass channels 122, 185, 152, and 216 exhibit a similar profile of vibrational bands between 650 cm^{-1} and 750 cm^{-1} , which are generated by the hydrogen out-of-plane bending motion of substituted aromatic rings. The frequencies of these vibrational bands depend on the nature of the substituent and the position of the substitution. This explains the similarities in the vibrational frequencies of the $m/z=122, 152, 185$, and 216 , (as shown in Figure 8.9a) and also points towards the nature of the common substituent among all of these chemical species, which is a methyl group in this case. Similarly, Figure 8.9b), shows the molecules that exhibit similar vibrational features in the range of $790\text{--}880\text{ cm}^{-1}$, which arises from the wagging motion of the two hydrogen atoms connected to the Si atom. This consists of mass channels corresponding to 138, 152, 182, and 184, where $m/z=138$ and 182 show this vibrational band at $\sim 795\text{ cm}^{-1}$ and $m/z=184$ and 152 show this band at $\sim 850\text{ cm}^{-1}$ as displayed in Figure 8.9b. A distinctive vibrational band is also seen for $m/z=134, 136$, and 183 , at $\sim 770\text{ cm}^{-1}$ which arises from the wagging motion of a single H atom attached to the Si atom. In addition, a vibrational band that is present in all of the experimental IR spectra in the scope of this work is a symmetric stretching of the hydrogen atoms connected to the silicon atom, present at $\sim 950\text{ cm}^{-1}$, which (in most cases) arise

from the presence of the terminal SiH_3 group in the chemical species formed in the experiment.

Overall, a rich chemistry has been observed when phenylsilane was subjected to the conditions of electrical discharge. We have observed the reaction products as a result of hydrogen substitution by methyl, ethyl, silyl, methyl silyl, and a phenyl group. Furthermore, we do not only observe substitutions, but also the condensation of phenylsilane with another phenyl group, forming substituted naphthalene molecules and the ring growth from naphthalene to annulene units. All the reaction products observed in this work are exhibited in Figure 8.31. The reaction mechanisms for the hydrogen substitution reactions of silane with other moieties have been studied in detail previously, for example, the gas phase formation of SiH_3CN via a radical substitution mechanism by [259]. Yang *et al.* proposed a radical substitution mechanism via a single transition state containing a penta-coordinated silicon atom with a nearly co-linear geometry of the attacking cyano radical, the forming carbon-silicon bond, simultaneously with the cleaving silicon-hydrogen moiety.

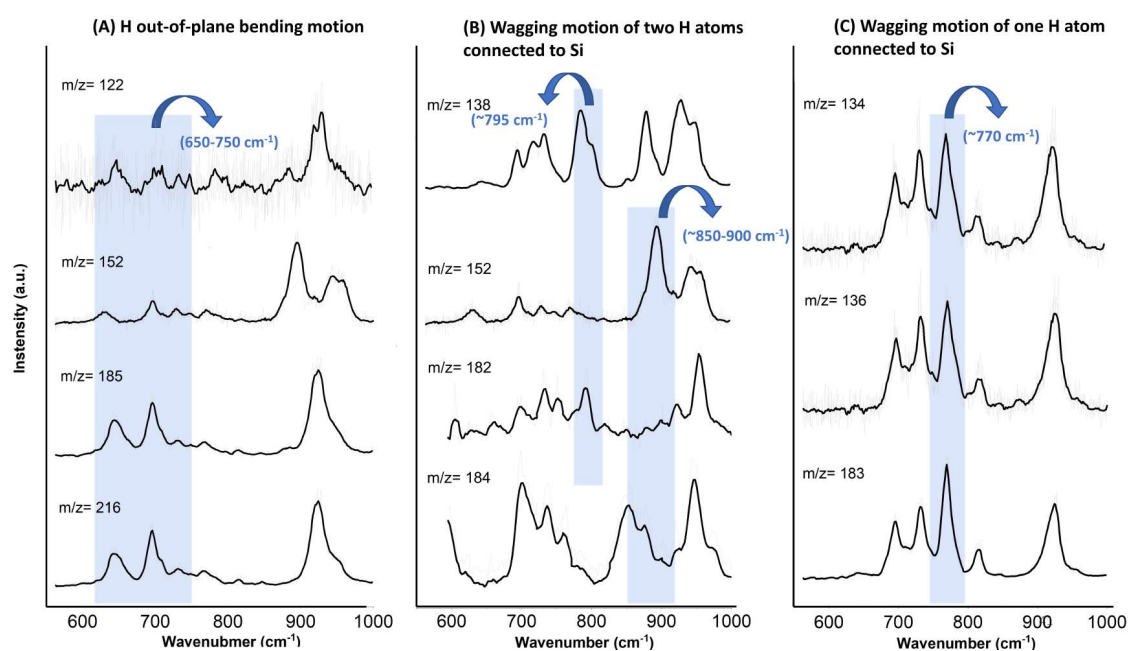


Figure 8.9: Grouping of the masses based on the similar vibrational features.

8.3.2 Summary

In summary, we have assigned twelve different mass channels to their corresponding chemical structures, as summarized in Figure 8.31. The information on the vibrational bands for these masses can then be used to search for them in the ISM. The commencement of the James Web Space Telescope (JWST) enables for the search of silicon-containing species observed here. Since the IR range that we studied overlaps with the range covered by JWST ($350\text{--}20000\text{ cm}^{-1}$), the work presented in this study can be a crucial step in the detection of the silicon-containing species. This was otherwise limited with the radio astronomy if the silicon-containing molecule has a low dipole moment. The study underscores the importance of the intense band at $\sim 2200\text{ cm}^{-1}$ arising from the Si-H stretch which acts as a diagnostic feature in the vibrational spectra of silicon-containing molecules. This band stands out as a valuable tool for identifying new silicon-containing species in diverse interstellar environments.

We were also able to explore the diverse chemistry arising from the electrical discharge of phenylsilane, revealing a range of reaction products resulting from hydrogen substitution by methyl, ethyl, silyl, methyl silyl, and a phenyl group. Moreover, notable findings include the condensation of phenylsilane with an additional phenyl group, resulting in the creation of substituted naphthalene molecules. Additionally, we observed the expansion of rings from benzene, leading to the formation of annulene structures. However, the incorporation of a silicon atom into the carbon backbone of aromatic molecules, which could potentially impact the stability of the molecular structures, was not observed in our study.

8.3.3 Bottom-up growth of silicon-containing aromatic molecules under the conditions of an electrical discharge

The utilization of electrical discharge for generating transient and exotic reaction products is widely recognized within the scientific community and has been extensively explored [139, 140, 170, 171, 245, 246]. Beyond the formation of novel molecules, electrical discharge experiments can serve as a valuable method for unraveling the reaction pathways leading to the formation of these reaction products in interstellar environments. While the experimental conditions during electrical discharge may not perfectly replicate those in the ISM, these discharge experiments can highlight the potential formation mechanisms that would otherwise remain elusive. Therefore, with the support of quantum chemical calculations, exothermic reactions whether barrier-free or with an accessible barrier height, can be unveiled, and their significance under astronomical conditions can be evaluated [40, 260].

In this part of the chapter, we emphasize on the formation of phenylsilane and

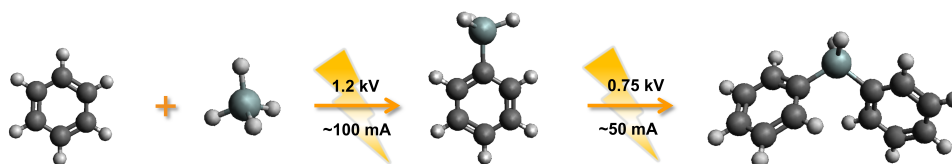


Figure 8.10: Scheme for the formation of phenylsilane from the electrical discharge of a benzene/silane mixture and the formation of diphenylsilane from the electrical discharge of phenylsilane.

diphenylsilane from the electrical discharge of a benzene/silane mixture and electrical discharge of phenylsilane, respectively. To achieve this, we leveraged the complementary nature of the two spectroscopic techniques used in this study. As microwave spectroscopy and IR-UV spectroscopy serve as complementary techniques, they can be employed collaboratively to target various molecular species. Microwave spectroscopy is sensitive to molecular structures, the magnitude of the molecule's permanent electric dipole moment, and its partition function. Conversely, in the case of IR-UV ion dip spectroscopy, which relies on the detection of ions generated through resonant UV radiation, the presence of chromophores is a prerequisite. Thus the two techniques can reveal the existence of different species which can give insights into the complex chemistry taking place. For instance, in the electrical discharge experiment of benzene by Lee *et al.* [42] using microwave spectroscopy, they observed the formation of chain or ring-chain combination molecules as favorable reaction products, while in the work by Lemmens *et al.* [253], the electrical discharge of benzene was probed using IR-UV ion dip spectroscopy, and the dominant pathway

was found to be the formation of aromatic systems extended with acetylene and diacetylene substitutions at the nucleophilic positions of the ring molecules. While both studies provided an exhaustive analysis of the species that were formed, the difference in the techniques can cover a broad range of discharge products formed and help elucidate various intermediate species.

In this part of the study, we investigated the discharge products arising from the electrical discharge of two precursor molecules: benzene, C_6H_6 (placed in an internal reservoir, heated at $40^\circ C$), and silane gas, SiH_4 (1 % silane in neon), in the 2-12 GHz frequency range using the COMPACT spectrometer (see Chapter 3). The 2-8 GHz experimental spectrum is shown in Figure 8.11, which exhibits rotational features arising from a variety of products generated as a result of electrical discharge of benzene, silane, and the combination of both. In this work, we specifically concentrate on the discharge products arising from the combination of benzene and silane, with the objective of exploring silicon-substituted aromatic molecules. The products of the electrical discharge experiment of benzene have been extensively studied previously by Lee *et al.* [42] where the authors identified more than 150 molecular species. In order to focus solely on the discharge products generated from the combination of benzene and silane, we removed the rotational transitions arising from the reported benzene discharge products from the recorded rotational spectrum, as shown in Figure 8.11(A). The negative trace (in red) is the simulation plotted for phenylsilane ($C_6H_5SiH_3$), based on the fitted rotational constants for the A state. Similarly, Figure 8.11 (C and D) shows the experimental spectrum recorded in 8-12 GHz before and after subtracting the transitions arising from the reaction products of the reported pure benzene discharge, against the simulation of phenyl silane. As the obtained signal-to-noise ratio for phenylsilane is not very high, the zoom-in of a few transitions is provided in Figure 8.12 to highlight its formation. In total, 12 transitions of phenylsilane were assigned in the 2-12 GHz frequency range, and the measured transition frequencies are listed in Table 8.2.

Exploring in detail the potential reaction mechanism for the formation of phenylsilane under discharge conditions, Lucas *et al.* [244] have previously proposed the formation pathway in a bimolecular reaction dynamics study. The authors reported the formation of phenylsilane in cross molecular beam experiment of phenyl radicals and silane molecule. They proposed the formation mechanism via a radical substitution pathway at a tetra-coordinated silicon atom, involving a trigonal bipyramidal transition state. This is due to the stronger tendency of silicon to form stable penta-coordinated transition states and intermediates relative to the carbon atom and hence favoring the formation of silicon-substituted molecules (H substitution) over the formation of benzene (H abstraction).

In addition to the benzene and silane discharge experiment, we also performed another discharge experiment where phenylsilane was used as a precursor molecule.

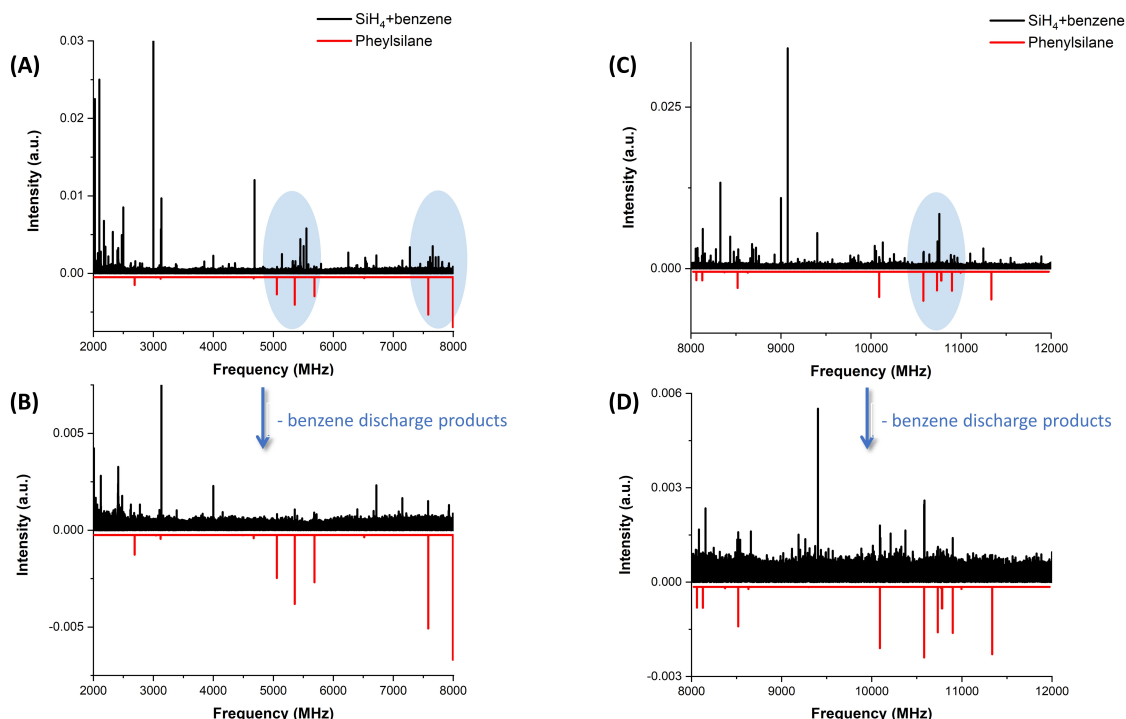


Figure 8.11: The rotational spectra obtained after applying electrical discharge to the mixture of benzene and silane (panels A and C) in the frequency range of 2-8 and 8-12 GHz, respectively. Panels B and C show the rotational spectra after removing the rotational transitions arising from the electrical discharge of benzene [42], highlighting the formation of phenylsilane, as shown in the red trace.

The aim of this experiment was to investigate and explore the formation of bigger silicon substituted aromatic or cyclic molecules than previously observed. For these experiments, we utilized the mass-resolved IR-UV ion-dip spectroscopy (see Chapter 3) coupled with electrical discharge at FELIX, Nijmegen, the Netherlands [82].

Table 8.2: List of rotational transitions observed for phenylsilane in the electrical discharge experiment in the 2-12 GHz of frequency range.

J	K_a	K_c	J'	K_a'	K_c'	Observed Freq. (MHz)
2	1	2	1	1	1	5060.9399
2	0	2	1	0	1	5356.6195
2	1	1	1	1	0	5685.8791
3	1	3	2	1	2	7581.1764
3	0	3	2	0	2	7993.3108
3	2	1	2	2	0	8126.9048
3	1	2	2	1	1	8518.0140
4	1	4	3	1	3	10089.9269
4	0	4	3	0	3	10581.8324
4	2	3	3	2	2	10733.7121
4	2	2	3	2	1	10898.6692
4	1	3	3	1	2	11336.4083

As seen before that in order to record a discharge spectrum of a molecule, the resulting discharge products must have a permanent electric dipole moment and it must be formed in abundance to obtain rotational transitions in decent signal-to-noise ratios. The advantage of performing mass-resolved IR-UV ion dip spectroscopy at the FELIX facility over rotational spectroscopy is three-fold. First, the low signal-to-noise ratio of silicon substituted aromatic molecules (due to small electric dipole moment and less fractional abundance) would not be a problem as long as enough ions travel to the multichannel plate detector for their corresponding m/z signal to be recorded. Second, the information on the mass-to-charge ratio (m/z) of the ions generated by REMPI contributes substantially to the assignment of the newly formed chemical species. Third, the characteristic IR feature in the 2000-2200 cm^{-1} range acts as a diagnostic tool for classifying molecules based the presence of a silicon-hydrogen bond. Here, the vibrational spectra of the resulting discharge products were investigated in the range of 550-3200 cm^{-1} using FELIX-2.

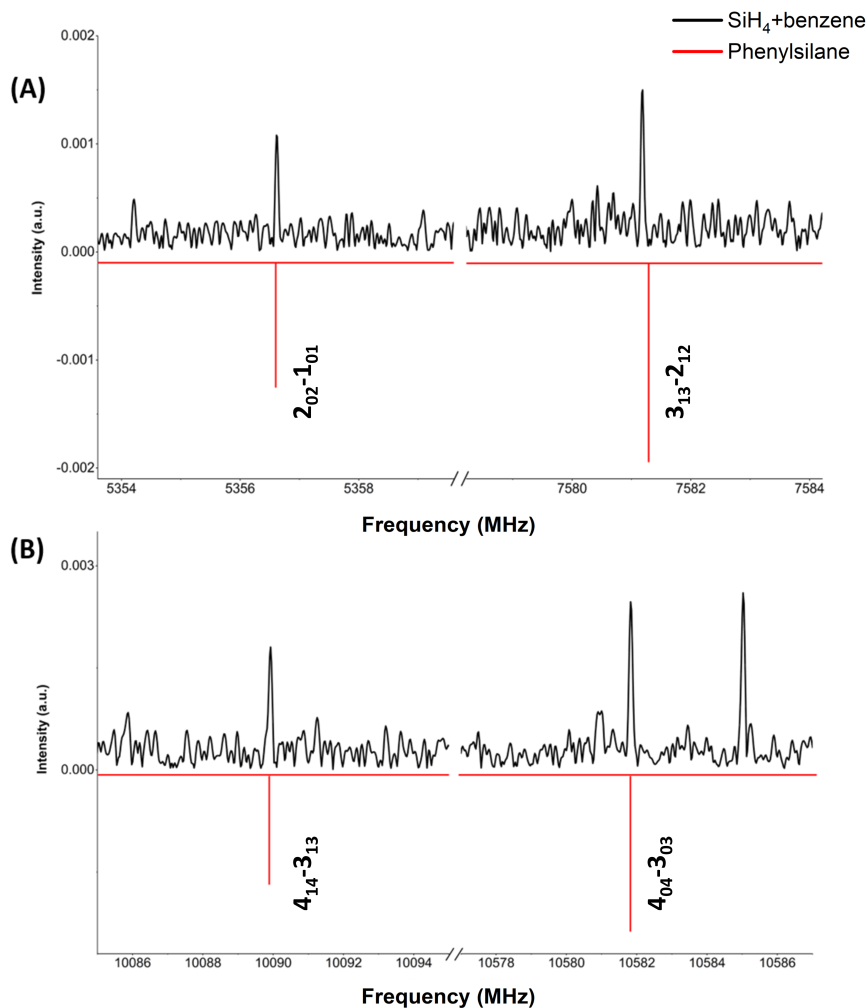


Figure 8.12: Zoom-in to highlight the rotational transitions ($J_{K_a, K_c} - J'_{K_{a'}, K_{c'}}$) observed for phenylsilane in the electrical discharge experiment of benzene and silane (A) in 2-8 GHz and (B) in 8-12 GHz of frequency range.

From the discharge experiment of phenylsilane probed by IR-UV ion dip spectroscopy, not only did we observe the rich silicon chemistry, where silicon is substituted at the aromatic ring system (refer to Section 8.3.1), we also noticed the formation of bigger molecular structures, i.e., diphenylsilane from phenylsilane. The formation of diphenylsilane was confirmed by comparing the experimental IR spectrum obtained for $m/z = 184$ with the IR spectrum computed for diphenylsilane and other isomers containing C, H, and Si in the structure. The depiction of various structural isomers attempted for $m/z=184$ is illustrated in Figure 8.14. The structures of the different isomers corresponding to $m/z= 184$ were optimized at

the B3LYP-D3/def2-SVP level of theory. In addition, the gas phase IR spectrum of diphenylsilane was also compared with the one available on the National Institute of Standard and Technology (NIST) website[‡] as shown in Figure 8.13 (illustrated by the blue trace).

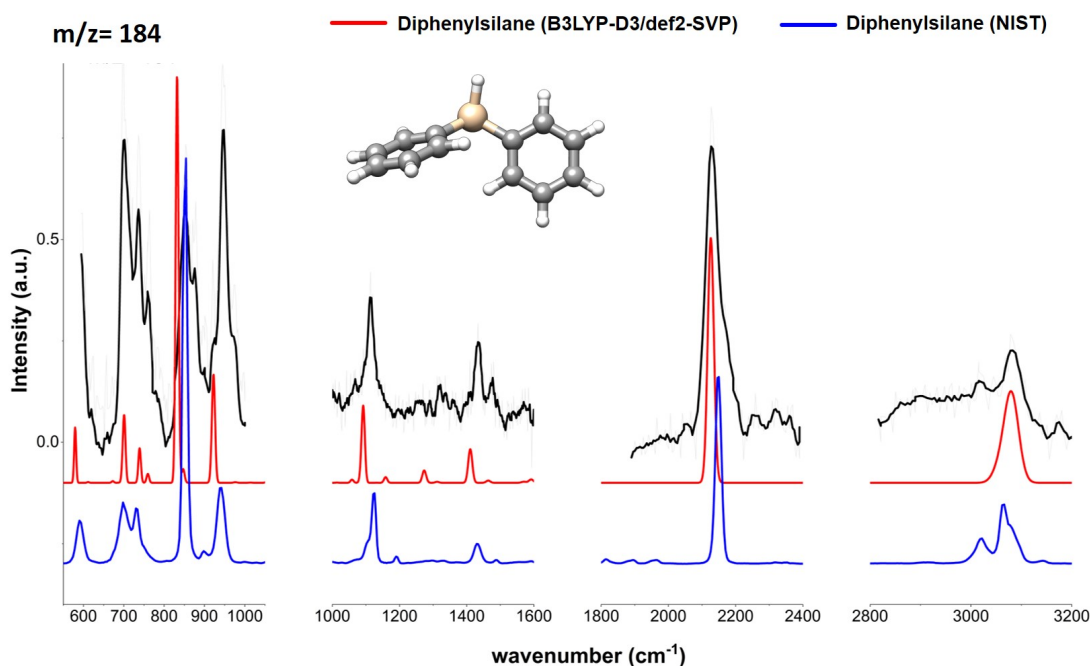


Figure 8.13: Comparison of the experimental IR spectrum (in black trace) recorded in the 550-2400 cm^{-1} frequency region for $m/z = 184$ with the theoretical vibrational spectra (in red trace) calculated at the B3LYP-D3/def2-SVP for the structure highlighted above the spectra. The excitation UV wavelength used in this experiment was fixed to 269 nm. The black trace is obtained after applying a 5-point adjacent-average smooth function to the average of IR spectra (shown in light grey). A scale factor of 0.9671 was applied to the frequency scale of the theoretical harmonic spectra [256] and was subsequently convoluted to a Gaussian lineshape function with a FWHM of 1% to match the FELIX bandwidth. The vibrational spectrum obtained from NIST is shown in the blue trace.

[‡]<https://www.nist.gov/>

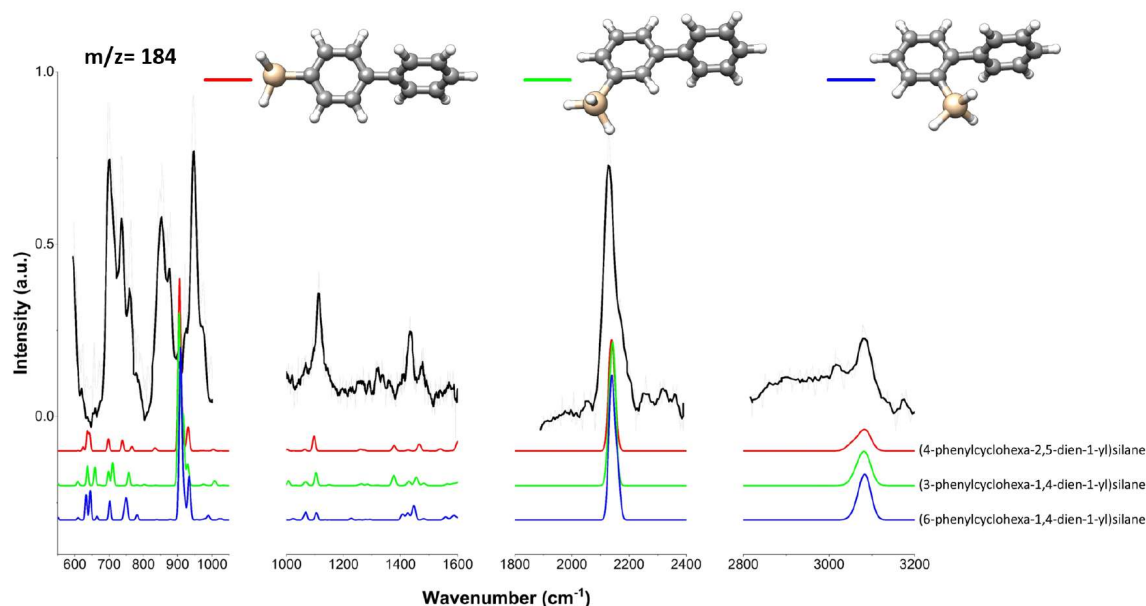


Figure 8.14: The vibrational spectra of different molecular structures corresponding to $m/z=184$. The black trace represents the vibrational spectrum observed experimentally, and the coloured traces represent the vibrational spectra obtained theoretically at B3LYP-D3/def2-SVP level of theory. The black trace is obtained after applying a 5-point adjacent-average smooth function to the average of IR spectra (shown in light grey). A scale factor of 0.9671 was applied to the frequency scale of the theoretical harmonic spectra [256] and was subsequently convoluted to a Gaussian lineshape function with a FWHM of 1% to match the FELIX bandwidth.

The reaction mechanism and the energetics involved in the formation of diphenylsilane from phenylsilane were examined by performing quantum-chemical calculations. The reaction follows a radical substitution mechanism involving simultaneous carbon-silicon bond formation and silicon-hydrogen bond breaking, as previously suggested by Lucas *et al.* [244]. The transition state takes on a trigonal bipyramidal geometry, owing to the tendency of silicon to form stable penta-coordinated transition states and intermediates relative to carbon, on account of stronger 3-center-4-electrons interactions [261, 262]. Using this approach, we performed structure optimization calculations for reactants (benzene radical and silane), transition states (penta-coordinated Si atom with two benzene rings and three hydrogen atoms) and the final product (diphenylsilane) at the B3LYP-D3/def2-TZVP level of theory. The proposed formation mechanism of diphenylsilane (Figure 8.15) is an exothermic reaction by ~ 5 kJ/mol with a barrier height of ~ 43 kJ/mol which can be accessible in the high energetic conditions of plasma.

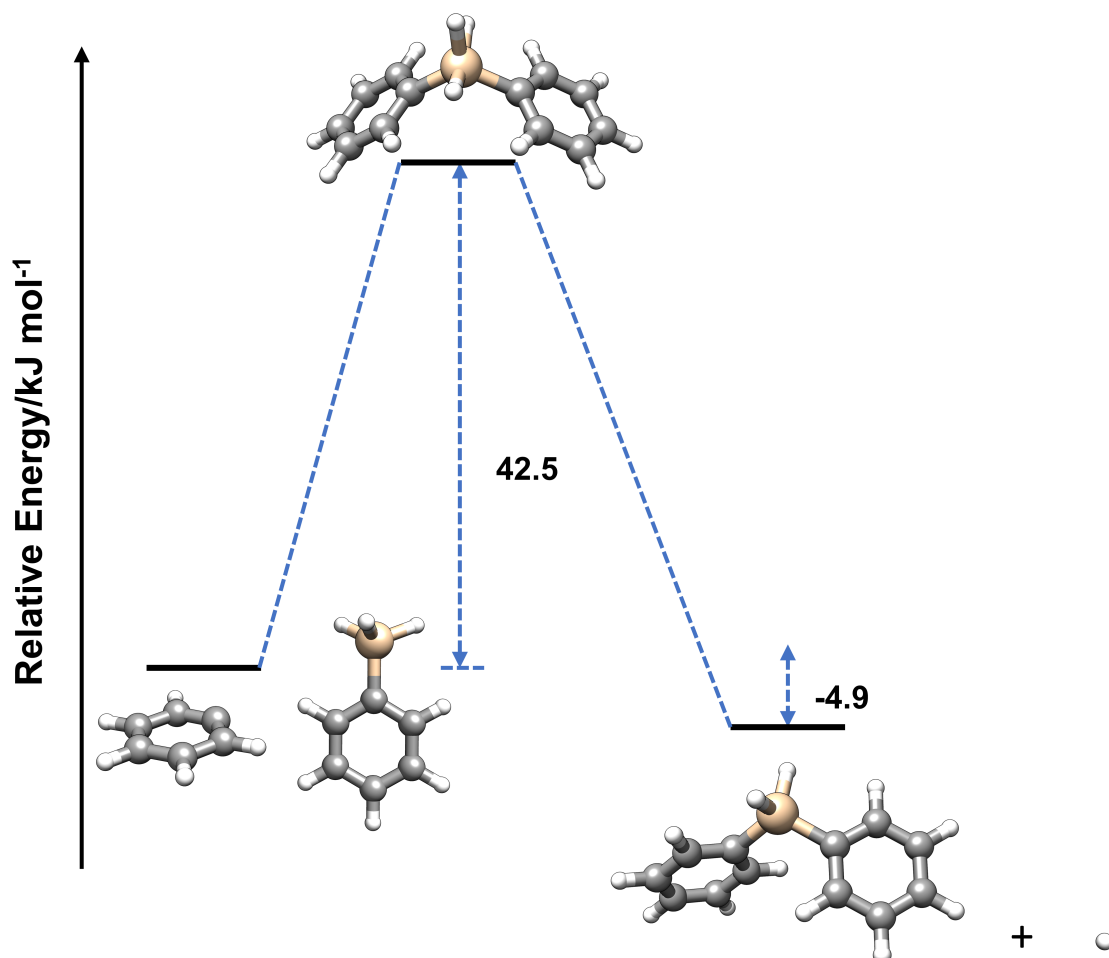


Figure 8.15: Proposed reaction pathway for the formation of diphenylsilane starting from the phenyl radical and the phenylsilane monomer via a trigonal bipyramidal transition state. The corresponding energies are given in kJ mol^{-1} , calculated at B3LYP-D3/def2-TZVP level of theory.

8.3.4 Facilitating astronomical searches

Given that phenylsilane and diphenylsilane are the primary discharge products observed in this work, it forms the basis for conducting their searches in the ISM where high energetic conditions like plasma are present, or, where other silicon-containing species, especially like SiH_4 , were detected beforehand. To aid the astronomical searches, we recorded the rotational spectra of phenylsilane and diphenylsilane in the laboratory up to 110 GHz, and at two different temperatures (3 and 300 K). For recording the rotational spectra, the following spectrometers were used,

namely COMPACT spectrometer [73, 75, 76], $T_{rot} = \sim 3$ K (2-18 GHz), the K-band spectrometer [76], $T_{rot} = \sim 3$ K (18-26 GHz), and the W-band spectrometer [79], $T_{rot} = \sim 300$ K (75-110 GHz). A thorough description of the above-mentioned rotational spectrometers is given in Chapter 3. The accurate rest frequencies up to 110 GHz and 50 GHz are provided for phenylsilane (A-state) and diphenylsilane, respectively.

Phenylsilane is a symmetric molecule with a six-fold barrier which leads to the splitting of each rotational transition into various components. The molecule has been investigated previously in 1975 with the help of rotational spectroscopy, see reference [178]. In the scope of this paper, only the A-state transitions were assigned and the line list for A state transitions of phenylsilane in the range of 2-8, 18-26, and 75-110 GHz are provided to aid the astronomical searches. In order for phenylsilane to be detected, its A state transitions must be observed. Therefore, this work forms a preliminary basis for the detection of phenylsilane in the ISM. A part of the rotational spectrum in the range of 75-110 GHz against the simulated spectrum of phenylsilane derived from the fitted rotational constants for the A-state [178] is shown in Figure 8.16. In addition to this, we were able to improve the accuracy and precision of the rotational constants available in literature. We also provide the accurate determination of the quartic and sextic centrifugal distortion constants by extending the measurement to the high frequency region along with the list of rotational transitions from 2-110 GHz. The determination of centrifugal distortion constants is of paramount importance for the prediction of accurate rest frequencies, as compared to the rigid-rotor model, in the high frequency regions.

For the case of diphenylsilane, the rotational spectroscopy study in the frequency range of 2-8 GHz at 3 K is discussed in Chapter 6). The assigned rotational constants, accurate rest frequencies and derived partition functions can be found therein. Here, we extend the study of diphenylsilane in the frequency region of 75-110 GHz at 300 K. Since the molecular size of diphenylsilane is quite big for the room-temperature measurement in 75-110 GHz, in addition to a dipole moment of 0.9 D, the analysis of the W-band data is not straight forward. Therefore, the analysis for the same is still ongoing. Based on the fitted rotational constants for both the molecules, we also derived the values of the rotational partition function at different temperatures as listed in the JPL database [110] is shown in Table 8.3. Note that the values of partition function for phenylsilane were derived based on the fit of the A state only.

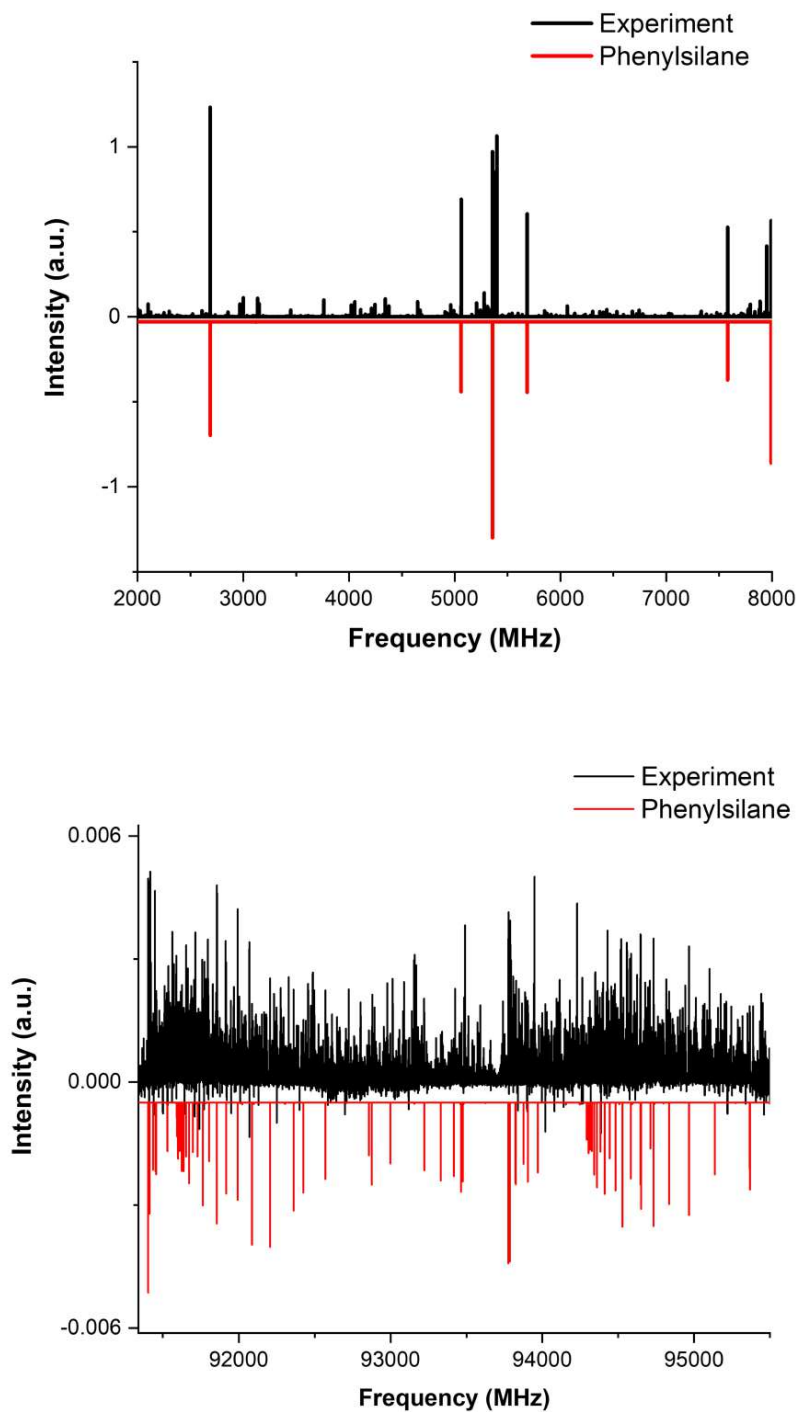


Figure 8.16: In panel (A) the rotational spectrum recorded for phenylsilane is described in the range of 2-8 GHz, with $T_{rot} \sim 3$ K. In Panel (B) a section of the W-band spectrum recorded for phenylsilane under room temperature conditions ($T_{rot} \sim 300$ K) is shown. The upper trace (in black) is the experimental spectrum while the bottom trace (in red) is the simulated spectrum based on the fitted rotational constants.

Table 8.3: Rotational and vibrational partition functions calculated for phenylsilane and diphenylsilane across the standard range of temperatures as implemented in the JPL database [110]

Rotational partition function (Q_{rot})		
T/K	Phenylsilane^a	Diphenylsilane
300	96197.0915	36932.2031
225	81308.7902	36070.3763
150	60278.4730	34434.9137
75	29953.1860	30147.1552
37.5	11961.6715	23683.9881
18.75	4295.5097	15770.2937
9.375	1521.2221	8461.5503
1.5	98.4425	687.7059

^a Rotational partition function calculated considering only the A-state transitions.

8.3.5 Summary

We report the experimental evidence of the formation of phenylsilane from the combination of benzene/silane in the electrical discharge experiment probed with rotational spectroscopy and the formation of diphenylsilane in the electrical discharge coupled with IR-UV ion dip spectroscopy. We also provide the comprehensive rotational spectroscopy data covering up to 110 GHz to aid the astronomical searches of these molecules in the regions of high energetic conditions. This work forms the ground work for astrochemistry and future detection of bigger organosilicon species than previously detected before. Observing larger molecules with radio astronomy poses a significant challenge due to their larger partition function values. The inverse relationship between the partition function and the intensities of rotational transitions adds complexity to their detection. With the constant improvements in the observational facilities, larger and complex molecules are becoming the targets of astronomical searches. The recent detections of cyano naphthalene [245] and indene [139, 140] are the examples.

The formation of phenylsilane and diphenylsilane in these experiments demonstrates the bottom-up growth mechanisms of complex silicon substituted aromatic hydrocarbons starting from simple precursors. This experiment also highlights the com-

plementary nature of the two techniques employed here: rotational spectroscopy and IR-UV ion dip spectroscopy. Both of these techniques target different class of molecules, For example, rotational spectroscopy depends of on the presence of a permanent electric dipole moment and the IR-UV ion dip spectroscopy relies on the presence of a chromophore in the molecule and a change in the dipole moment during vibration. This complementary nature of the two techniques allows one to probe a wide range of silicon-containing discharge products generated in the experiment. Moreover, the observation of phenylsilane and diphenylsilane in our experiment shed light on the plausible number of silicon-containing complex molecules that are yet to be explored in the ISM. The formation mechanisms of such species have already been proposed to undergo radical substitution reactions which inturn also explains the observations of methylsilane, CH_3SiH_3 and cyanosilane, SiH_3CN in the IRC+10216 region, while also suggesting the presence of other complex organosilicon molecules in interstellar and circumstellar environments.

8.4 Appendix for FELIX data

8.4.1 IR spectra of all the masses observed with the two-color REMPI (266+193 nm).

IR spectra: $m/z=122-216$

The black trace represents the experimental spectrum and the colored traces depict the simulated IR spectra for the corresponding isomer.

$m/z = 122$

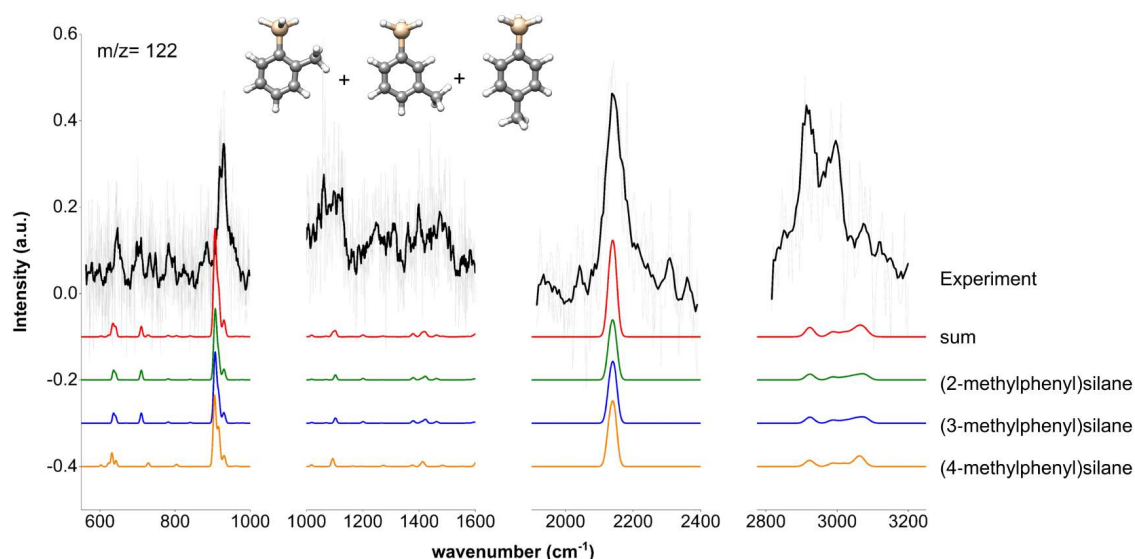
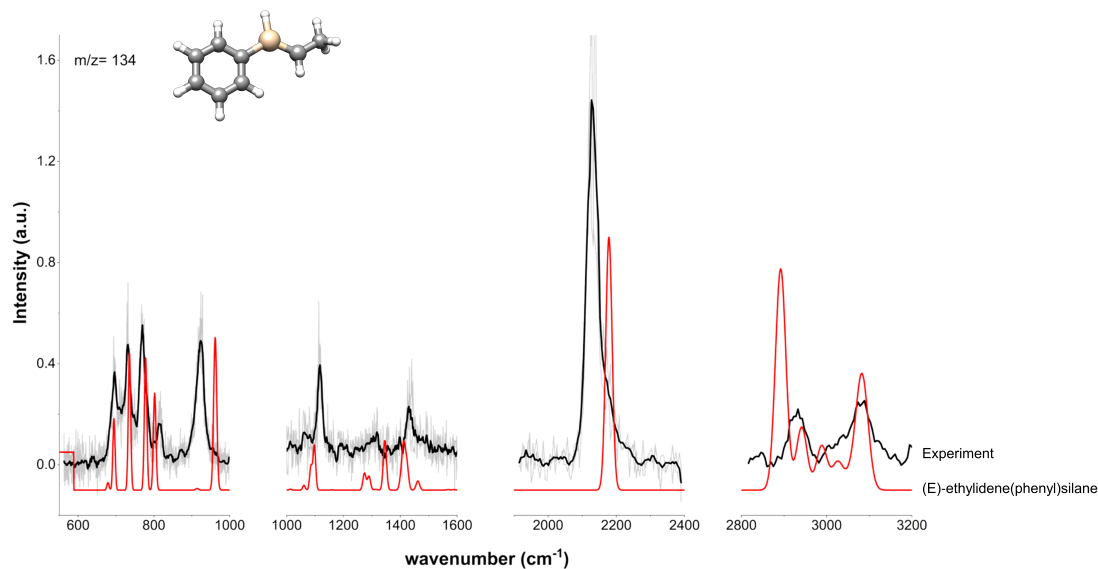


Figure 8.17: Comparison of the experimental IR spectrum (in black trace) recorded in the 550-3200 cm^{-1} frequency region for $m/z = 122$ with the theoretical vibrational spectra calculated at the B3LYP-D3/def2-SVP for the structures highlighted above the spectra.

(a) $m/z = 134$



(b) $m/z = 136$

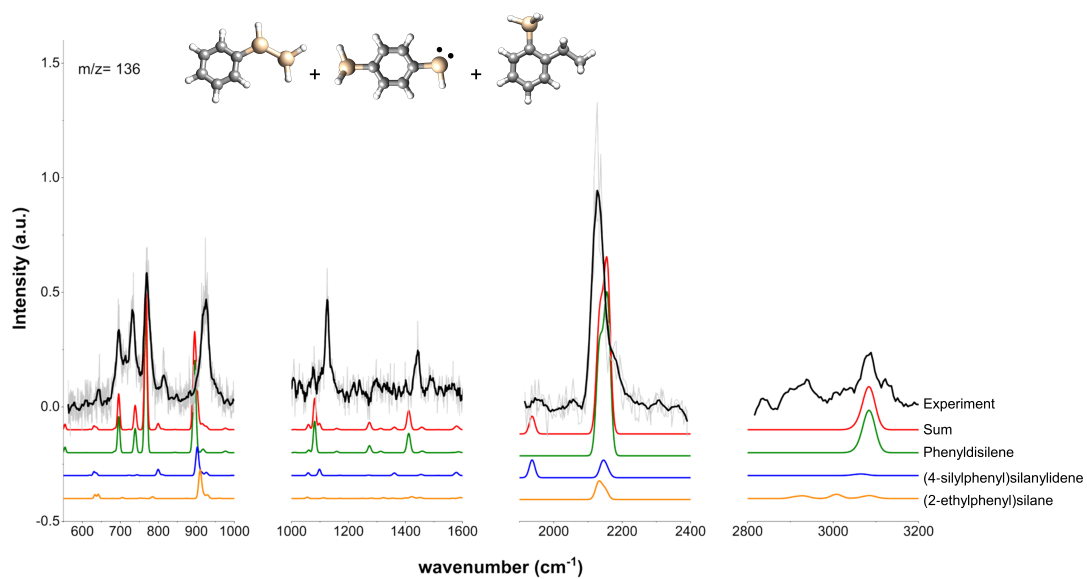


Figure 8.18: Comparison of the experimental IR spectrum (in black trace) recorded in the 550-3200 cm^{-1} frequency region for $m/z = 134$ and 136 with the theoretical vibrational spectra calculated at the B3LYP-D3/def2-SVP for the structures highlighted above the spectra.

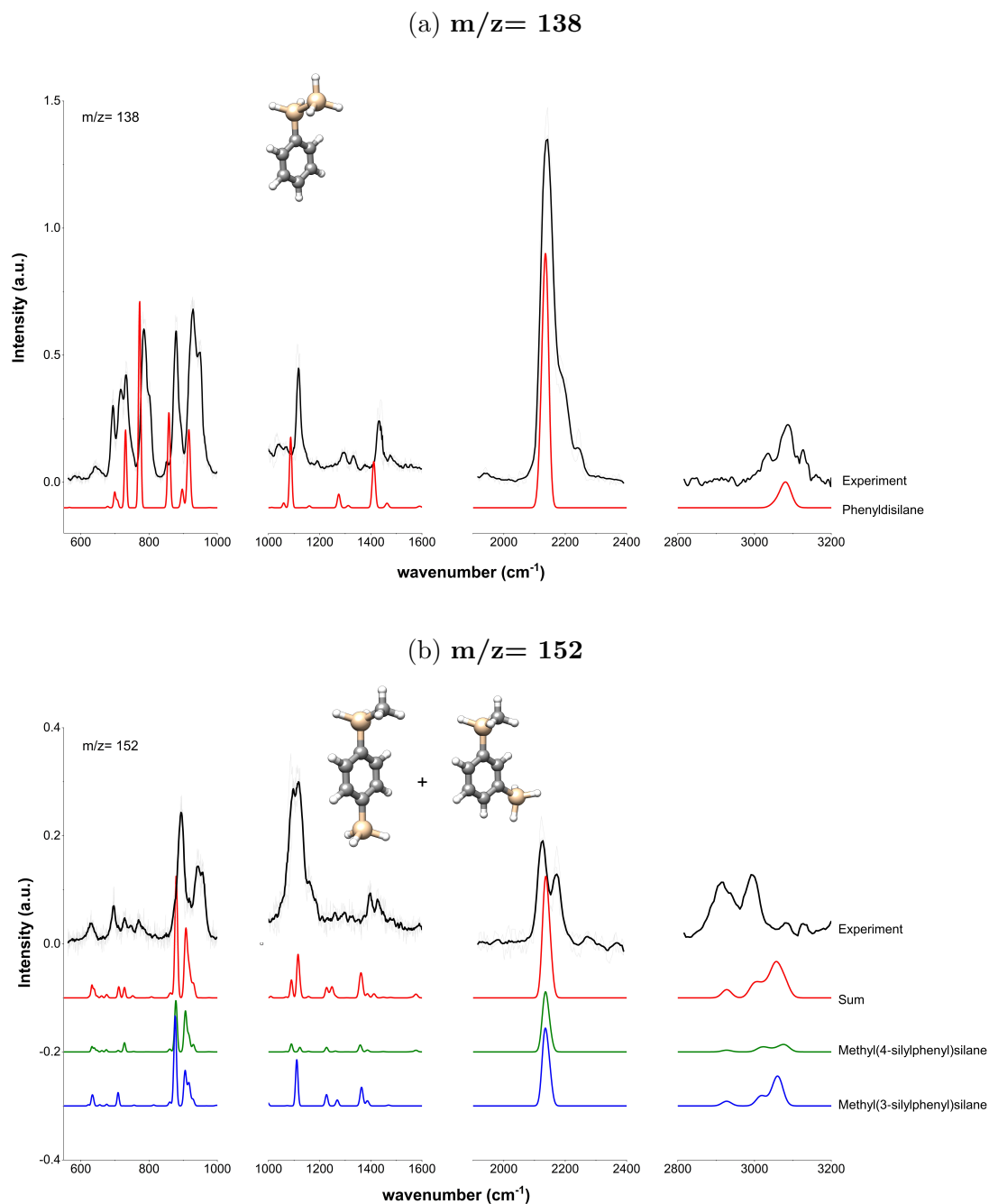
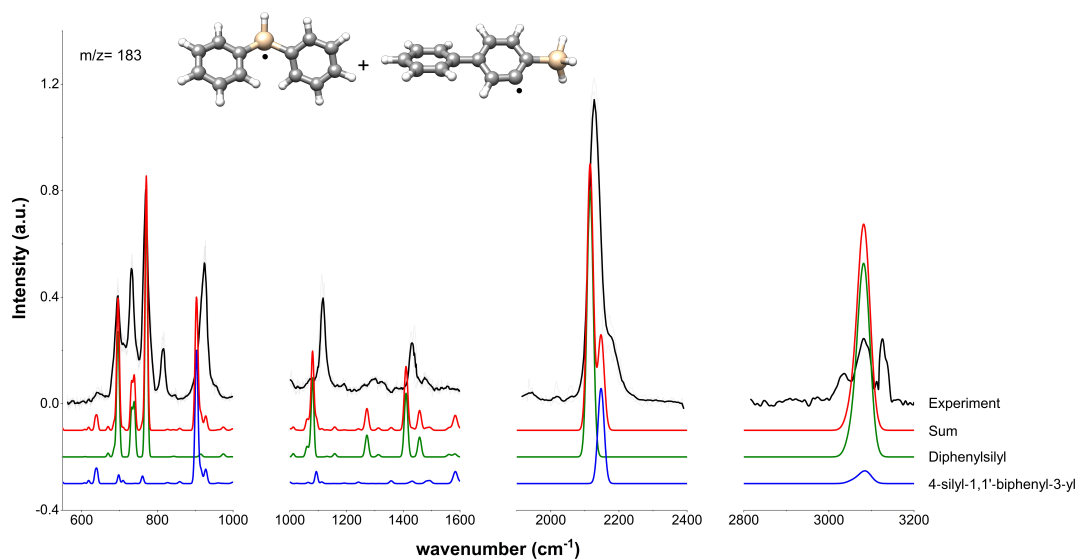


Figure 8.19: Comparison of the experimental IR spectrum (in black trace) recorded in the $550\text{--}3200\text{ cm}^{-1}$ frequency region for $m/z = 138$ and 152 with the theoretical vibrational spectra calculated at the B3LYP-D3/def2-SVP for the structures highlighted above the spectra.

(a) $m/z = 183$



(b) $m/z = 185$

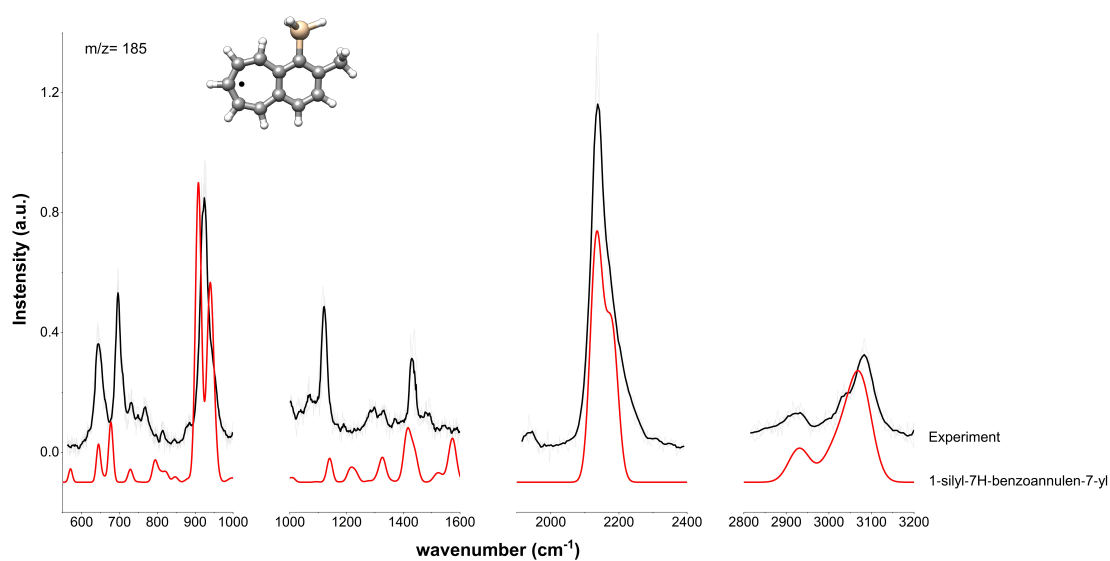


Figure 8.20: Comparison of the experimental IR spectrum (in black trace) recorded in the $550\text{--}3200\text{ cm}^{-1}$ frequency region for $m/z = 183$ and 185 with the theoretical vibrational spectra calculated at the B3LYP-D3/def2-SVP for the structures highlighted above the spectra.

$m/z = 216$

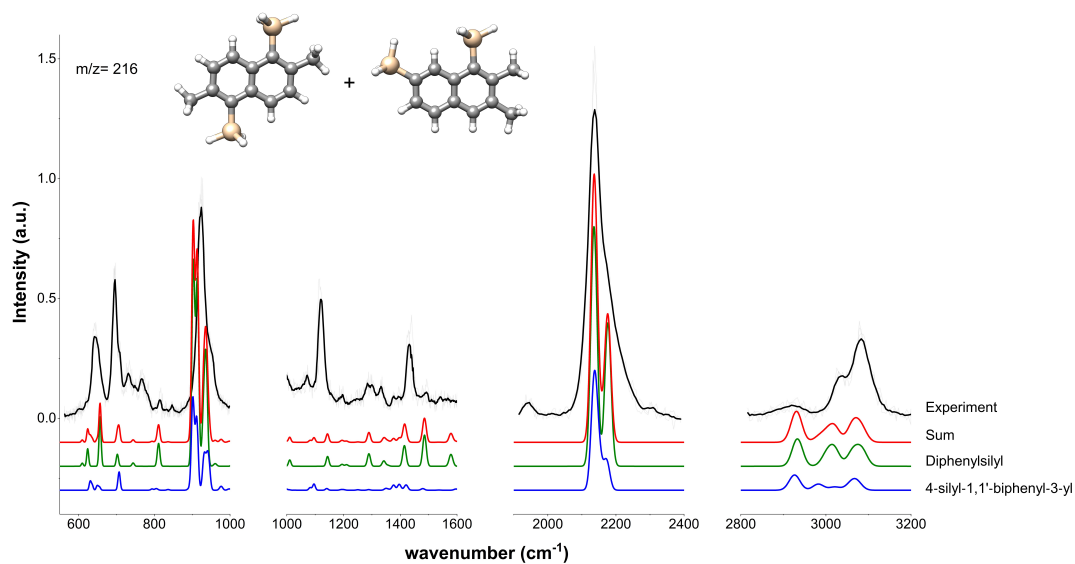


Figure 8.21: Comparison of the experimental IR spectrum (in black trace) recorded in the 550-3200 cm⁻¹ frequency region for $m/z=216$ with the theoretical vibrational spectra calculated at the B3LYP-D3/def2-SVP for the structures highlighted above the spectra.

8.4.2 IR spectra of all the masses observed with the two-color REMPI (269+193 nm).

IR spectra: $m/z=138-188$

The black trace represents the experimental spectrum and the colored traces depict the simulated IR spectra for the corresponding isomer.

$m/z = 138$

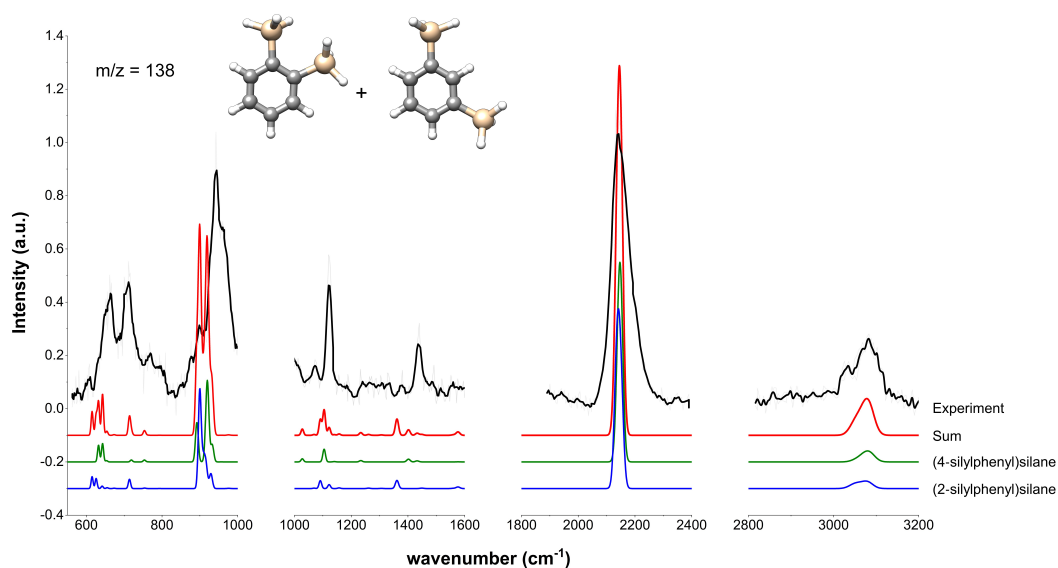
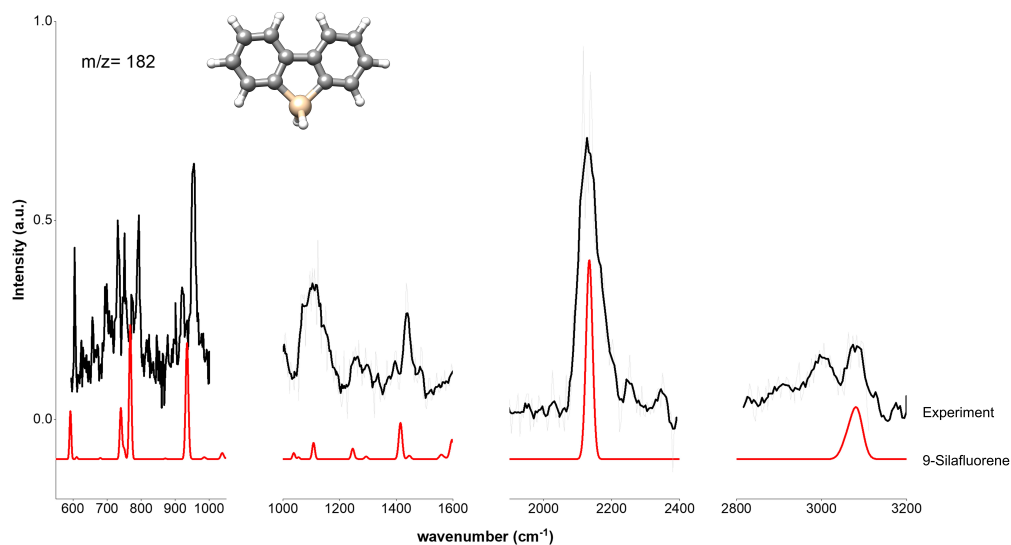


Figure 8.22: Comparison of the experimental IR spectrum (in black trace) recorded in the 550-3200 cm^{-1} frequency region for $m/z=138$ with the theoretical vibrational spectra calculated at the B3LYP-D3/def2-SVP for the structures highlighted above the spectra.

(a) $m/z = 182$



(b) $m/z = 184$

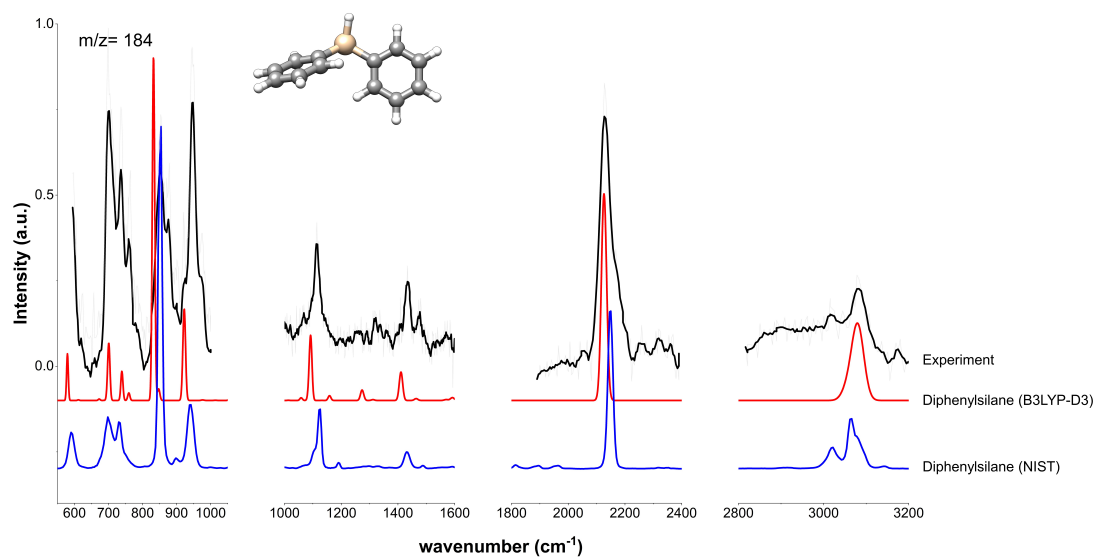


Figure 8.23: Comparison of the experimental IR spectrum (in black trace) recorded in the 550-3200 cm^{-1} frequency region for $m/z = 182$ and 184 with the theoretical vibrational spectra calculated at the B3LYP-D3/def2-SVP for the structures highlighted above the spectra.

$m/z = 188$

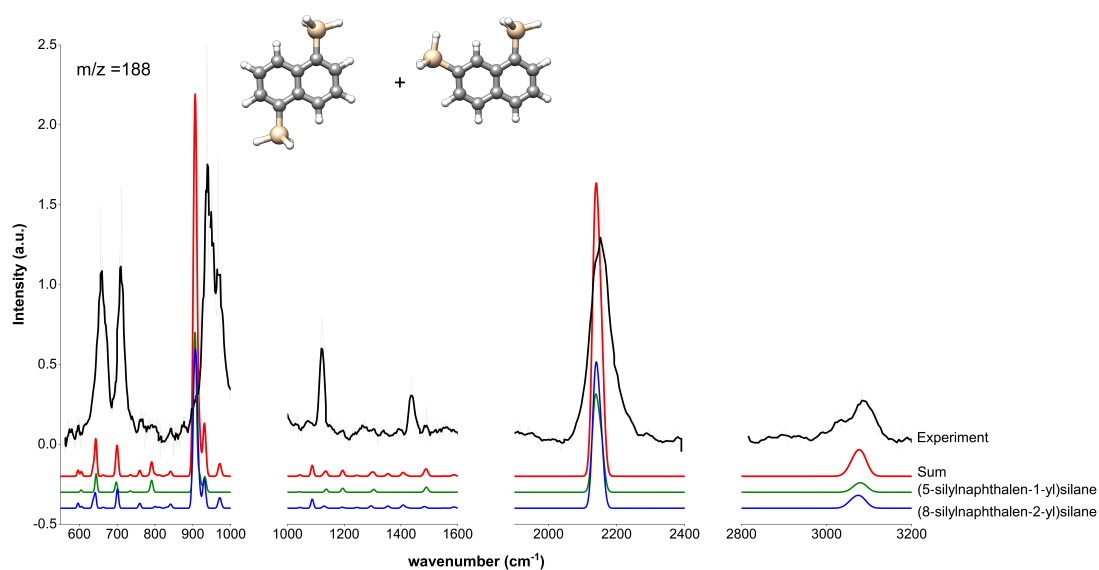


Figure 8.24: Comparison of the experimental IR spectrum (in black trace) recorded in the 550-3200 cm⁻¹ frequency region for $m/z=188$ with the theoretical vibrational spectra calculated at the B3LYP-D3/def2-SVP for the structures highlighted above the spectra.

8.4.3 Supplementary figures

Experimental IR spectra of the masses observed in the experiment along with the calculated IR spectra. The black trace represents the experimental spectrum and the colored traces depict the simulated IR spectra for the corresponding mass. This section describes the experimental vs. calculated IR spectra for the different structural isomers that did not reproduce the experimental IR spectra.

$m/z = 122$

Figure S2

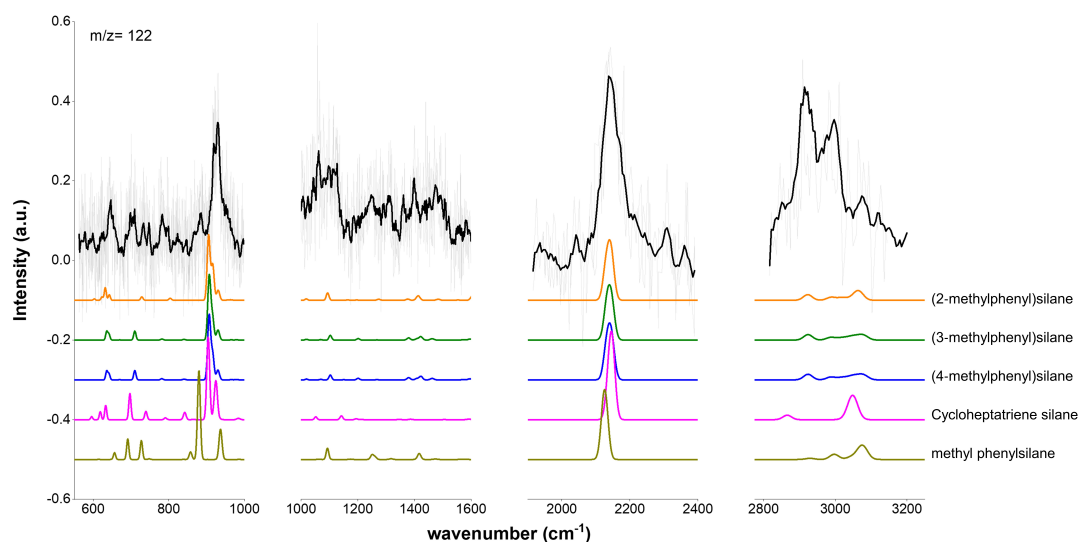


Figure 8.25: Comparison of the experimental IR spectrum (in black trace) recorded in the 550-3200 cm^{-1} frequency region for $m/z=122$ with the theoretical vibrational spectra calculated at the B3LYP-D3/def2-SVP for the molecules indicated next to their calculated spectra. .

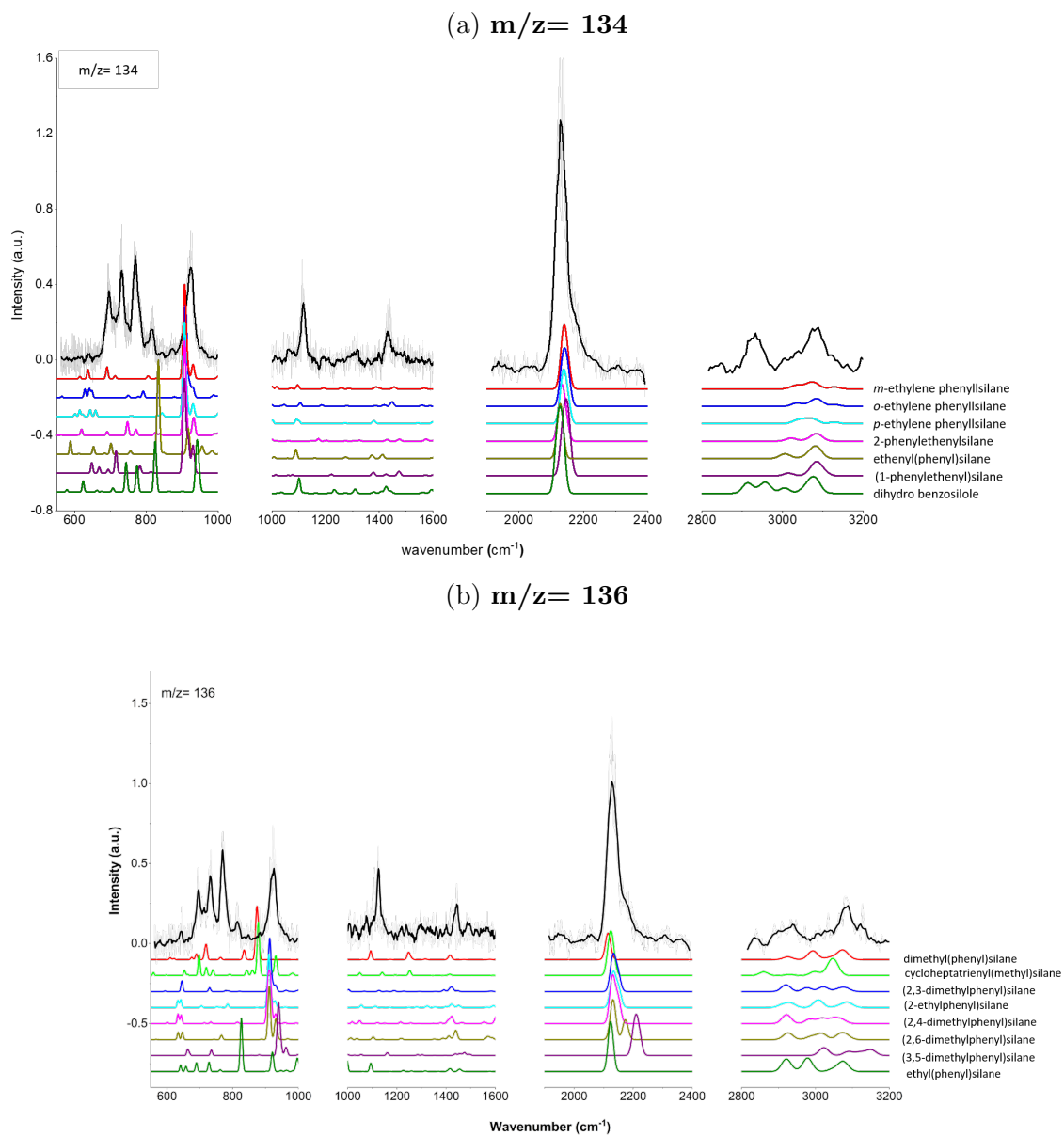
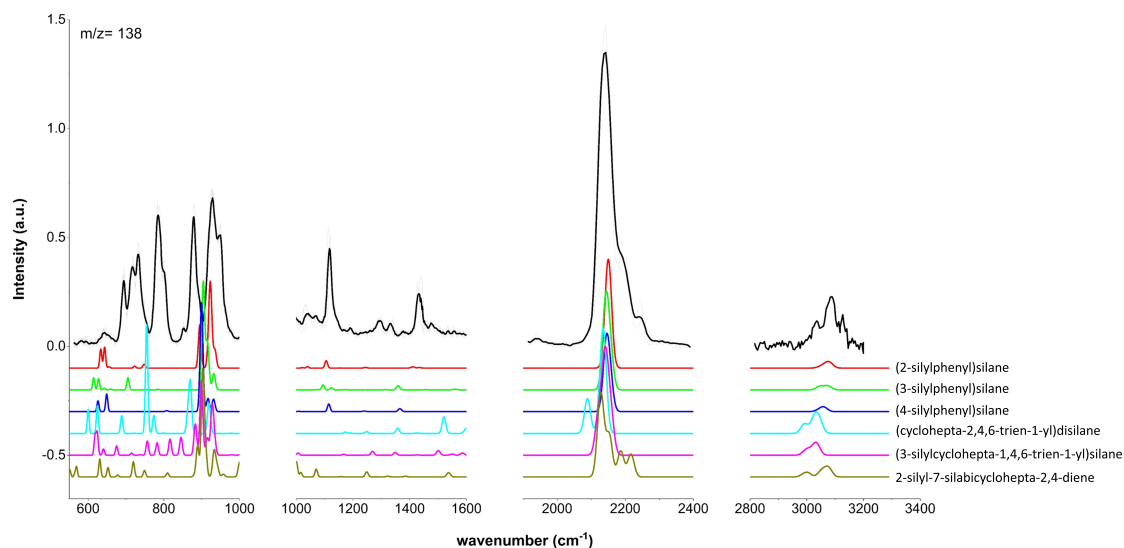


Figure 8.26: Comparison of the experimental IR spectrum (in black trace) recorded in the $550\text{--}3200\text{ cm}^{-1}$ frequency region for $m/z = 134$ and 136 with the theoretical vibrational spectra calculated at the B3LYP-D3/def2-SVP for the molecules indicated next to their calculated spectra.

(a) $m/z = 138$



(b) $m/z = 152$

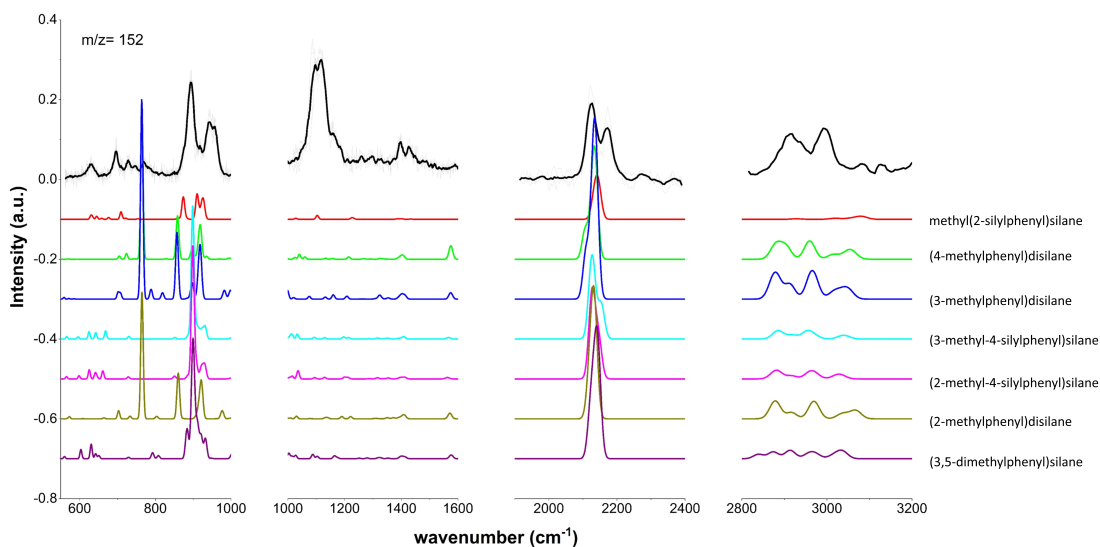
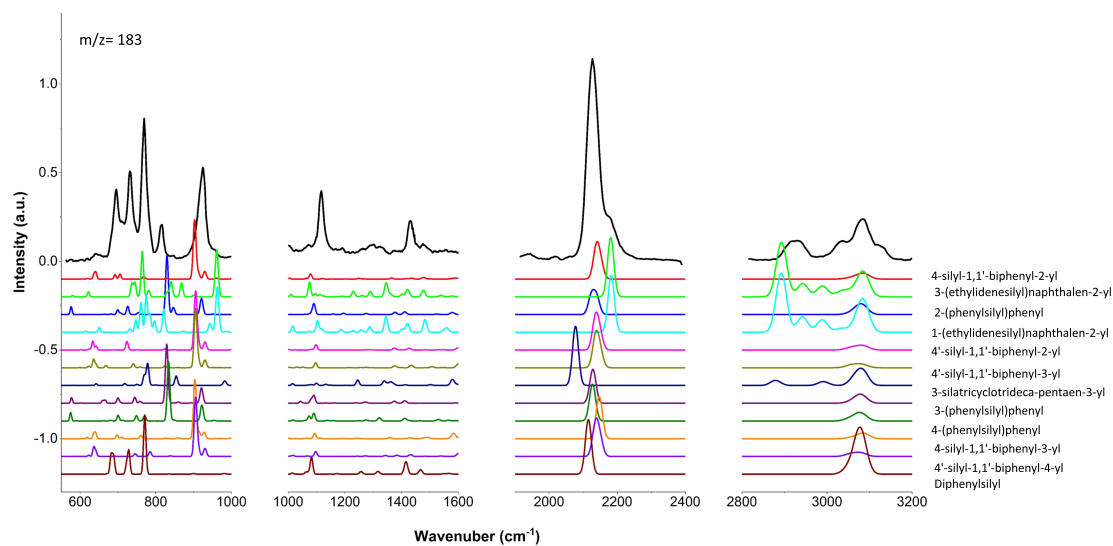


Figure 8.27: Comparison of the experimental IR spectrum (in black trace) recorded in the 550-3200 cm^{-1} frequency region for $m/z = 138$ and 152 with the theoretical vibrational spectra calculated at the B3LYP-D3/def2-SVP for the molecules indicated next to their calculated spectra.

(a) $m/z = 183$



(b) $m/z = 185$

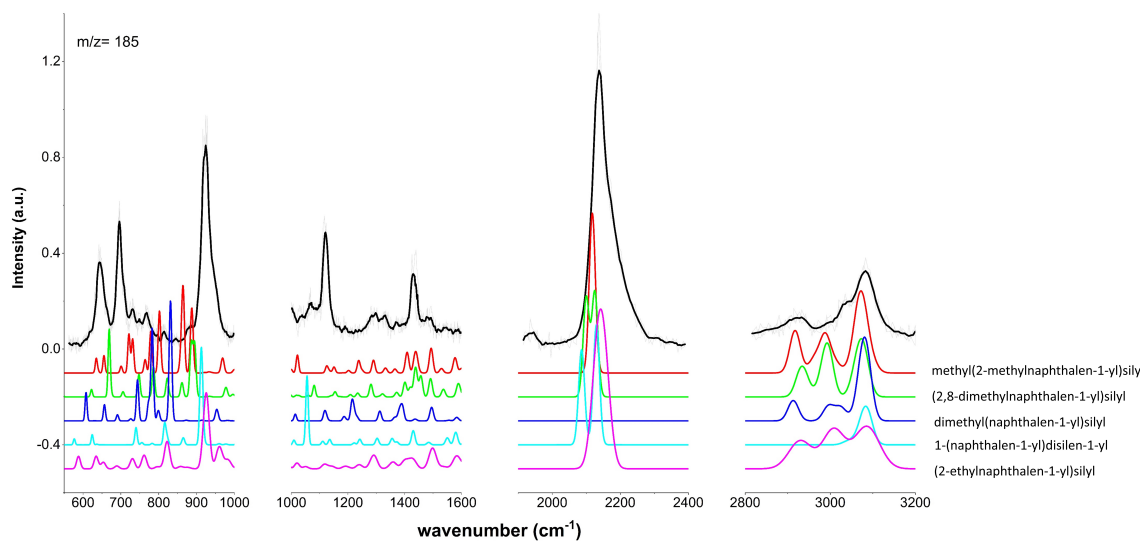
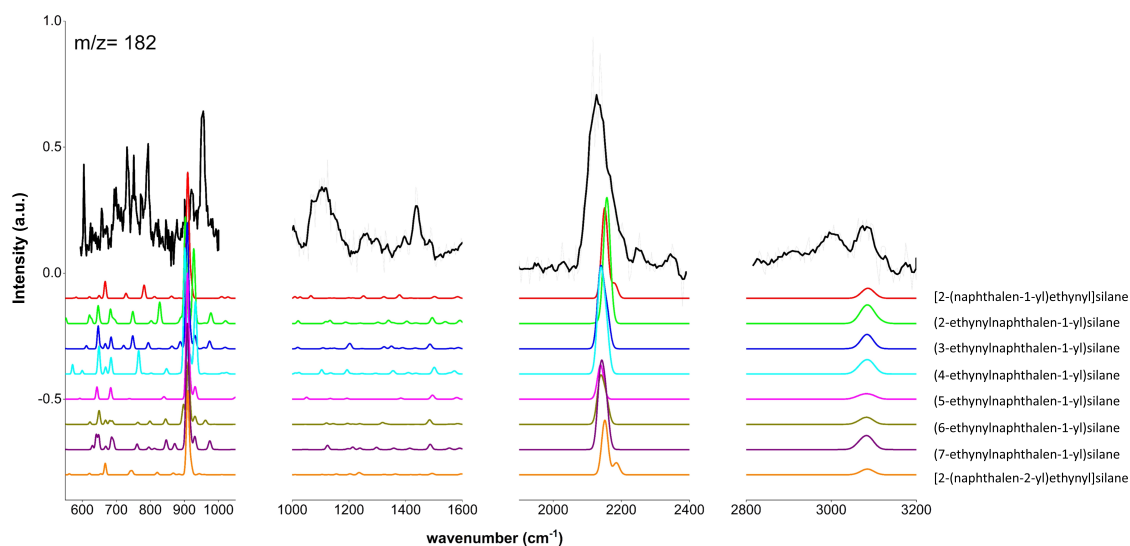


Figure 8.28: Comparison of the experimental IR spectrum (in black trace) recorded in the $550\text{--}3200\text{ cm}^{-1}$ frequency region for $m/z = 183$ and 185 with the theoretical vibrational spectra calculated at the B3LYP-D3/def2-SVP for the molecules indicated next to their calculated spectra.

(a) $m/z = 182$



(b) $m/z = 184$

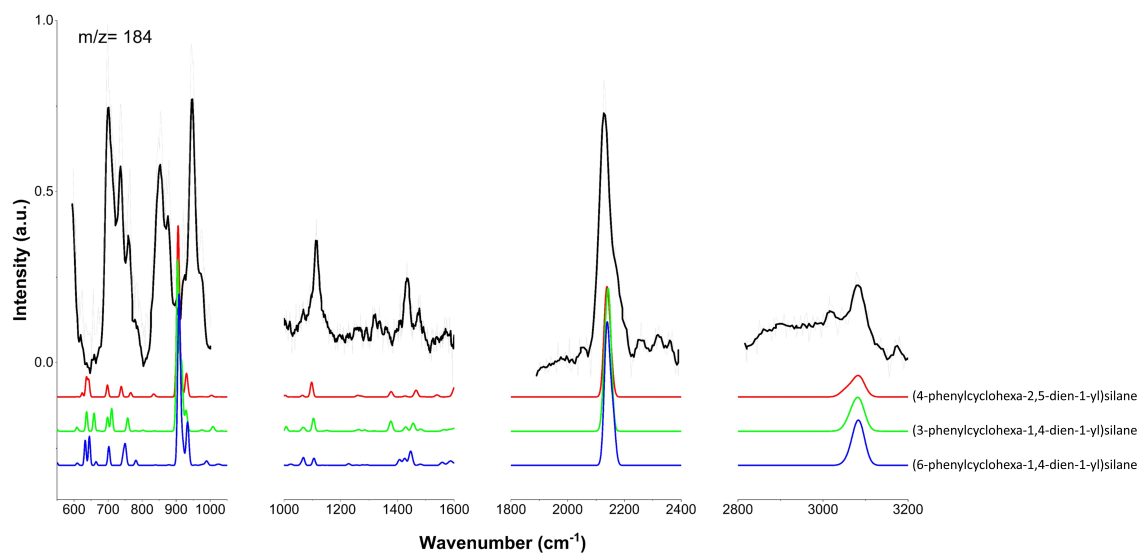
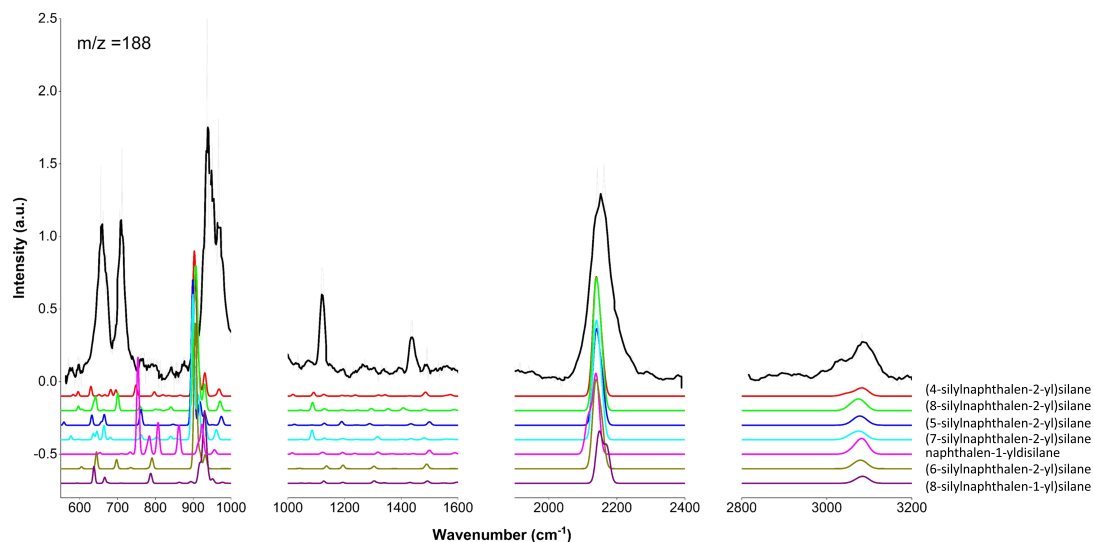


Figure 8.29: Comparison of the experimental IR spectrum (in black trace) recorded in the 550-3200 cm^{-1} frequency region for $m/z = 182$ and 184 with the theoretical vibrational spectra calculated at the B3LYP-D3/def2-SVP for the molecules indicated next to their calculated spectra.

(a) $m/z = 188$



(b) $m/z = 216$

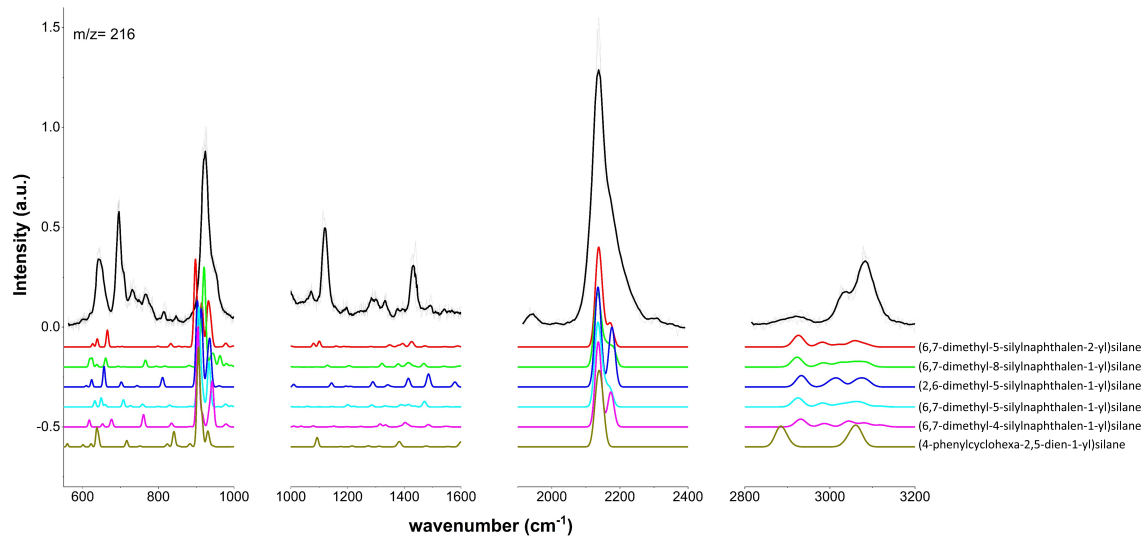


Figure 8.30: Comparison of the experimental IR spectrum (in black trace) recorded in the 550-3200 cm^{-1} frequency region for $m/z = 188$ and 216 with the theoretical vibrational spectra calculated at the B3LYP-D3/def2-SVP for the molecules indicated next to their calculated spectra.

Chapter 9

Summary and outlook

The objective of this thesis is to investigate molecules of astronomical interest with a multi-spectroscopic approach to allow the chemical inventory of interstellar molecules to be better determined. This will also contribute towards a more comprehensive understanding of their formation mechanisms in the ISM.

The major part of this thesis was done utilizing rotational spectroscopy. Analysis of rotational spectra delivers line lists and rotational constants for the molecules studied. Application of these to the observational data sets allows astronomers to search for the molecules in interstellar space. It is a very structure sensitive technique that not only conformer specific but also isotopologue specific.

The different frequency ranges covered by the rotational spectrometers, as described in detail in Chapter 3, overlaps with various radio telescopes. For example, the low-frequency data overlaps with facilities such as the Jansky Very Large Array and the Effelsberg 100m Radio Telescope. The W-band spectrometer overlaps with the Band 3 operating regime (86-114 GHz) of Atacama Large Millimeter/submillimeter Array (ALMA). This makes the laboratory data directly applicable to radio astronomy.

In addition to rotational spectroscopy, we also utilized IR spectroscopic techniques like Infrared reflection absorption spectroscopy and IR-UV ion dip spectroscopy, as discussed in the respective chapters. With the commencement of JWST, the data from the vibrational spectroscopy can be used for searching the vibrational features of the molecules of interest in the ISM. This is significant especially for molecules with very small or no dipole moment, as no rotational signatures can be recorded for those. While for infrared spectroscopy, a change in electric dipole moment is required for a vibrational mode to be IR-active.

In general, the experiments performed in this thesis has been categorized into three broad themes:

- Rotational spectroscopy of complex organic molecules like methyl cyanoacetate

(Chapter 4), 2,4,6-cycloheptatriene-1-carbonitrile (Chapter 5), and organosilicon molecules like phenylsilane (Chapter 8.3.4) and diphenylsilane (Chapter 6) to aid their detection in different regions of space. The spectra were measured in two different conditions, low rotational temperatures obtained with supersonic expansion ($T_{rot} = 1-3$ K) and room-temperature flow cell measurements ($T_{rot} \sim 300$ K).

- Infrared reflection absorption spectroscopy of naphthalene embedded in water ice in ultra-high vacuum conditions to understand the ice growth on dust particle and surface chemistry associated with ices in the ISM (Chapter 7).
- Electrical discharge experiments coupled with mass-resolved IR-UV ion dip spectroscopy of phenylsilane to explore the formation of silicon-substituted aromatic or cyclic molecules. This experiment was performed to aid the detection of silicon-containing species in the ISM with the help of JWST (Chapter 8). In addition to this electrical discharge experiment coupled with rotational spectroscopy was also performed in the 2-18 GHz frequency range. With benzene and silane (1% in neon) as precursors, the discharge chemistry was explored with the aim of forming silicon substituted aromatic molecules (Chapter 8).

A detailed summary of the chapters discussed in this thesis is as follows:

Chapter 4 describes a comprehensive laboratory investigation of the rotational spectra of the two lowest energy conformers of methyl cyanoacetylene (MCA). It exhibits methyl internal rotation and nuclear quadrupole coupling splittings owing to the presence of a methyl group and a ^{14}N nucleus, respectively. While the global minimum structure MCA_1, has been previously explored, our work extended the microwave investigation into the millimeter wave region and provided a detailed characterization of MCA_2, the next one in energy. The analysis included the assignment of rotational transition frequencies over a wide frequency range (2-26 GHz and 75-110 GHz), determining rotational parameters, and unveiling structural information for both conformers.

It is interesting to note that despite MCA_2 being slightly higher in energy than MCA_1, the intensities of MCA_2 transitions are generally more pronounced due to its higher electric dipole moment. This finding highlights the importance of considering higher-energy conformers for interstellar detection, particularly in warmer regions of the ISM. The work done on MCA predicted more than 250 transitions for MCA_1 and over 2000 transitions for MCA_2 with high accuracy (<40 kHz) in the ALMA Band 3 frequency range.

The two conformers of MCA were searched towards the G+0.693 molecular cloud in the Sagittarius B2 region of the Galactic Center, but none were observed. Such a comprehensive study, which covers the assignment of the rotational transitions

in the low and high frequency regime, is essential for interstellar searches, as the high frequency range (75-110 GHz) allows the experimental transition frequencies to be directly compared with the observational spectra. The detection of complex molecules such as MCA in the ISM will be a step forward in the direction of discovering the existing complexity of the molecules present in the ISM. In future, this molecule could be searched for in the Orion molecular cloud complex, where methyl acetate has been detected [96].

Chapter 5 delved into the rotational spectra of 2,4,6-cycloheptatriene-1-carbonitrile (CHT-1-CN), in the frequency ranges 2-8 GHz, 18-26 GHz, and 75-110 GHz. The analysis of the data led to the observation and assignment of the two lowest energy conformers, namely CHT-1-CN-1 and CHT-1-CN-2, in their ground state. Additionally, six vibrationally excited states of the lowest energy conformer CHT-1-CN-1 were identified, owing to the room-temperature measurement in 75-110 GHz frequency range.

The study provided rotational parameters including the quartic distortion constants and nuclear quadrupole coupling constants. Accurate determination of centrifugal distortion constants enables the computation of reliable rest frequencies in the high-frequency region. The observed uncertainties for CHT-1-CN-1 were well below 200 kHz for the majority of predicted transition frequencies up to 150 GHz.

This investigation recommends an astronomical search for CHT-1-CN-1 in TMC-1, a region where other cyclic molecules such as benzonitrile, *o*-benzyne, cyclopentadiene, derivatives, and indene have recently been detected.

In Chapter 6 the broadband rotational spectrum of diphenylsilane is presented in the frequency range of 2-8 GHz. During the analysis, the tunnelling barrier height and the central structure around the Si atom were compared with its oxygen analogue, diphenylether, thus providing insights into the impact of substituting the hetero atom from O to Si. The comparison was also extended to structural parameters, such as bond lengths, bond angles, and dihedral angles with other silicon-containing molecules. Notably, the tunnelling barrier in diphenylsilane was found to be nearly double than that of diphenylether, which indicated a lack of resolvable splitting in observed rotational transitions of diphenylsilane. Emphasis was also placed on the fact that one would expect a smaller tunnelling barrier for diphenylsilane than that of diphenylether, as the Si-C (1.855 ± 0.009 Å) bond length is considerably longer than that of O-C (1.406 ± 0.035 Å).

From an astronomical search point of view, this work could be extended into the high frequency utilizing the W-band spectrometer. The analysis of this molecule in 75-110 GHz region will lead to the determination of centrifugal distortion constants which are of great importance to astronomers for computing the rest frequencies in high-frequency regions. Also, the data obtained from the 75-110 GHz spectrum overlaps with ALMA Band 3, and can be directly used for the detection purposes.

Chapter 7 investigated the growth of water ice on Ir(111) and naphthalene/Ir(111) surfaces under ultrahigh vacuum conditions, employing infrared reflection absorption spectroscopy (IRRAS) with p- and s-polarized IR radiation. The aim of this work was to contribute to understanding the mechanism of ice growth on the dust particles in the space and subsequently the chemistry that takes place in and on the surface of these ices to produce complex organic molecules. The examination of the water O–H stretching band revealed the formation of porous ice films on the naphthalene/Ir(111) substrate and a bulk amorphous solid water structure on the clean Ir(111) surface. The observation is further supported by the presence of the vibrational signature of the dangling motion of O–H bond, stemming from three-coordinated water molecules grown on the naphthalene/Ir(111) sample. Additionally, this study sheds light on the intricacies of ice formation influenced by distinct surface environments and provides valuable insights into the structural characteristics of ice films on heterogeneous surfaces. In addition, this work presented here forms the basis of future experiments to investigate the ice chemistry and the reaction products under the influence of UV radiation.

Chapter 8 explored the diverse chemistry arising from the electrical discharge of phenylsilane, revealing a range of reaction products resulting from hydrogen substitution by methyl, ethyl, silyl, methyl silyl, and a phenyl group. Additionally, intriguing results included the condensation of phenylsilane with another phenyl group, leading to the formation of substituted naphthalene molecules, as well as the expansion of ring structures from naphthalene to annulene units.

In summary, twelve different chemical structures were assigned. The vibrational information associated with these masses holds potential for future searches in ISM with the help of JWST, as the IR range studied in this work overlaps with the range covered by JWST. This is a significant advancement, particularly when considering the limitations posed by radio astronomy for silicon-containing molecules with very low dipole moments.

The study underscores the importance of the intense Si–H band at $\sim 2200\text{ cm}^{-1}$, a diagnostic feature in the vibrational spectra of silicon-containing molecules. This band stands out as a valuable tool for identifying new silicon-containing species in diverse interstellar environments. The findings presented in this study provide essential insights into the potential detection and characterization of silicon-containing molecules, contributing to our understanding of the silicon chemistry in space. Reaction pathways to molecules can also be considered with the use of electrical discharge, thus deepening the understanding of chemical evolution in the ISM. In the second part of this chapter (Section 8.3.3), we observed the experimental evidence of the formation of phenylsilane from the combination of benzene and silane in the electrical discharge experiment probed with rotational spectroscopy, and the formation of diphenylsilane in the electrical discharge experiment coupled with IR-UV ion

dip spectroscopy. Hence, these results highlight the bottom-up growth of silicon-containing molecules under the conditions of electrical discharge experiments. Overall, this thesis employed Rotational and vibrational spectroscopy, coupled with electrical discharge sources to characterize the above-mentioned molecules and study their relevance to astrochemistry. The work underscores the significant role of laboratory studies of astrochemically relevant molecules to gain insights into the composition of the interstellar medium. The experimental data presented here lay groundwork for potentially detecting the investigated molecules in this thesis in various regions of space through astronomical observations.

Bibliography

- [1] A. G. Tielens, “Interstellar polycyclic aromatic hydrocarbon molecules”, *Annual Review of Astronomy and Astrophysics* **46**, 289–337 (2008).
- [2] P. M. Solomon, “Interstellar molecules”, *Physics today* **26**, 32–40 (1973).
- [3] M. Morris, B. Zuckerman, P. Palmer, and B. Turner, “Interstellar ammonia.”, *Astrophysical Journal*, Vol. 186, p. 501–528 **186**, 501–528 (1973).
- [4] A. Cheung, D. M. Rank, C. Townes, D. D. Thornton, and W. Welch, “Detection of water in interstellar regions by its microwave radiation”, *Nature* **221**, 626–628 (1969).
- [5] G. R. Carruthers, “Rocket observation of interstellar molecular hydrogen”, *Astrophysical Journal* **161**, L81 (1970).
- [6] J. Cami, J. Bernard-Salas, E. Peeters, and S. E. Malek, “Detection of C₆₀ and C₇₀ in a young planetary nebula”, *Science* **329**, 1180–1182 (2010).
- [7] B. A. McGuire, “2021 census of interstellar, circumstellar, extragalactic, protoplanetary disk, and exoplanetary molecules”, *The Astrophysical Journal Supplement Series* **259**, 30 (2022).
- [8] G. G. Brown, B. C. Dian, K. O. Douglass, S. M. Geyer, S. T. Shipman, and B. H. Pate, “A broadband Fourier transform microwave spectrometer based on chirped pulse excitation”, *Review of Scientific Instruments* **79**, 053103 (2008).
- [9] G. A. Blake, E. Sutton, C. Masson, and T. Phillips, “Molecular abundances in OMC-1: the chemical composition of interstellar molecular clouds and the influence of massive star formation”, *Astrophysical Journal* **315**, 621–645 (1987).
- [10] H. G. Arce, J. Santiago-García, J. K. Jørgensen, M. Tafalla, and R. Bachiller, “Complex molecules in the *L1157* molecular outflow”, *The Astrophysical Journal* **681**, L21 (2008).

- [11] S. Bottinelli, A. A. Boogert, J. Bouwman, M. Beckwith, E. F. Van Dishoeck, K. I. Öberg, K. M. Pontoppidan, H. Linnartz, G. A. Blake, N. J. Evans, et al., “The c2d spitzer spectroscopic survey of ices around low-mass young stellar objects. iv. NH_3 and CH_3OH ”, *The Astrophysical Journal* **718**, 1100 (2010).
- [12] K. I. Öberg, S. Bottinelli, J. K. Jørgensen, and E. F. Van Dishoeck, “A cold complex chemistry toward the low-mass protostar B1-b: evidence for complex molecule production in ices 1”, *The Astrophysical Journal* **716**, 825 (2010).
- [13] A. Bacmann, V. Taquet, A. Faure, C. Kahane, and C. Ceccarelli, “Detection of complex organic molecules in a prestellar core: a new challenge for astrochemical models”, *Astronomy and Astrophysics* **541** (2012).
- [14] E. C. Fayolle, K. I. Öberg, R. T. Garrod, E. F. van Dishoeck, and S. E. Bisschop, “Complex organic molecules in organic-poor massive young stellar objects”, *Astronomy & Astrophysics* **576**, A45 (2015).
- [15] R. A. Loomis, A. M. Burkhardt, C. N. Shingledecker, S. B. Charnley, M. A. Cordiner, E. Herbst, S. Kalenskii, K. L. K. Lee, E. R. Willis, C. Xue, et al., “An investigation of spectral line stacking techniques and application to the detection of HC_{11}N ”, *Nature Astronomy* **5**, 188–196 (2021).
- [16] J. Cernicharo, M. Agúndez, C. Cabezas, B. Tercero, N. Marcelino, J. R. Pardo, and P. De Vicente, “Pure hydrocarbon cycles in TMC-1: Discovery of ethynyl cyclopropenylidene, cyclopentadiene, and indene”, *Astronomy & Astrophysics* **649**, L15 (2021).
- [17] W. D. Langer and A. E. Glassgold, “Silicon chemistry in interstellar clouds”, *The Astrophysical Journal* **352**, 123 (1990).
- [18] A. G. G. M. Tielens, “Interstellar Depletions and the Life Cycle of Interstellar Dust”, *The Astrophysical Journal* **499**, 267 (1998).
- [19] R. W. Wilson, A. A. Penzias, K. B. Jefferts, M. Kutner, and P. Thaddeus, “Discovery of Interstellar Silicon Monoxide”, *The Astrophysical Journal* **167**, L97 (1971).
- [20] B. A. McGuire, “2021 Census of Interstellar, Circumstellar, Extragalactic, Protoplanetary Disk, and Exoplanetary Molecules”, *The Astrophysical Journal Supplement Series* **259**, 30 (2022).
- [21] D. Fulvio, A. Potapov, J. He, and T. Henning, “Astrochemical pathways to complex organic and prebiotic molecules: experimental perspectives for solid-state studies”, *Life* **11**, 568 (2021).
- [22] E. Herbst, “Three milieux for interstellar chemistry: gas, dust, and ice”, *Physical Chemistry Chemical Physics* **16**, 3344–3359 (2014).

- [23] E. Herbst, “The synthesis of large interstellar molecules”, *International Reviews in Physical Chemistry* **36**, 287–331 (2017).
- [24] T. I. Hasegawa, E. Herbst, and C. M. Leung, “Models of gas-grain chemistry in dense interstellar clouds with complex organic molecules”, *Astrophysical Journal Supplement Series* **82**, 167–195 (1992).
- [25] M. Jin and R. T. Garrod, “Formation of complex organic molecules in cold interstellar environments through nondiffusive grain-surface and ice-mantle chemistry”, *The Astrophysical Journal Supplement Series* **249**, 26 (2020).
- [26] E. Herbst, “Three milieux for interstellar chemistry: gas, dust, and ice”, *Physical Chemistry Chemical Physics* **16**, 3344–3359 (2014).
- [27] M. K. McClure, W. Rocha, K. Pontoppidan, N. Crouzet, L. E. Chu, E. Dartois, T. Lamberts, J. Noble, Y. Pendleton, G. Perotti, et al., “An ice age jwst inventory of dense molecular cloud ices”, *Nature astronomy*, 1–13 (2023).
- [28] A. Belloche, H. S. P. Müller, K. M. Menten, P. Schilke, and C. Comito, “Complex organic molecules in the interstellar medium: IRAM 30 m line survey of Sagittarius B2(N) and (M)”, *Astronomy & Astrophysics* **559**, A47 (2013).
- [29] E. F. van Dishoeck, “Laboratory astrophysics: key to understanding the universe”, *Proceedings of the International Astronomical Union* **15**, 3–14 (2019).
- [30] V. Taquet, E. F. van Dishoeck, M. Swayne, D. Harsono, J. K. Jørgensen, L. Maud, N. F. W. Ligterink, H. S. P. Müller, C. Codella, K. Altwegg, A. Bieler, A. Coutens, M. N. Drozdovskaya, K. Furuya, M. V. Persson, M. L. R. van’t Hoff, C. Walsh, and S. F. Wampfler, “Linking interstellar and cometary O₂: a deep search for ¹⁶O ¹⁸O in the solar-type protostar IRAS 16293–2422”, *Astronomy & Astrophysics* **618**, A11 (2018).
- [31] A. Belloche, R. T. Garrod, H. S. Müller, and K. M. Menten, “Detection of a branched alkyl molecule in the interstellar medium: iso-propyl cyanide”, *Science* **345**, 1584–1587 (2014).
- [32] B. E. Arenas, S. Gruet, A. L. Steber, B. M. Giuliano, and M. Schnell, “Chirped-pulse fourier transform millimeter-wave spectroscopy of ten vibrationally excited states of i-propyl cyanide: exploring the far-infrared region”, *Physical Chemistry Chemical Physics* **19**, 1751–1756 (2017).
- [33] B. E. Arenas, “High-resolution broadband rotational spectroscopy and electrical discharge experiments of astrochemically relevant molecules.”, PhD thesis (2020).

- [34] S. M. Fortman, I. R. Medvedev, C. F. Neese, and F. C. De Lucia, “How complete are astrophysical catalogs for the millimeter and submillimeter spectral region?”, *The Astrophysical Journal Letters* **725**, L11 (2010).
- [35] R. Motiyenko, B. Tercero, J. Cernicharo, and L. Margulès, “Rotational spectrum of formamide up to 1 THz and first ISM detection of its ν_{12} vibrational state”, *Astronomy & Astrophysics* **548**, A71 (2012).
- [36] K. Furuya, Y. Aikawa, N. Sakai, and S. Yamamoto, “Carbon isotope and isotopomer fractionation in cold dense cloud cores”, *The Astrophysical Journal* **731**, 38 (2011).
- [37] A. Remijan, H. N. Scolati, A. M. Burkhardt, P. B. Changala, S. B. Charnley, I. R. Cooke, M. A. Cordiner, H. Gupta, E. Herbst, K. L. K. Lee, et al., “Astronomical detection of the interstellar anion C_{10}H^- toward TMC-1 from the GOTHAM large program on the green bank telescope”, *The Astrophysical Journal Letters* **944**, L45 (2023).
- [38] A. Apponi, M. McCarthy, C. Gottlieb, and P. Thaddeus, “Astronomical detection of rhomboidal SiC_3 ”, *The Astrophysical Journal* **516**, L103 (1999).
- [39] J. Cernicharo, M. Agúndez, R. I. Kaiser, C. Cabezas, B. Tercero, N. Marcelino, J. R. Pardo, and P. d. Vicente, “Discovery of two isomers of ethynyl cyclopentadiene in TMC-1: Abundances of CCH and CN derivatives of hydrocarbon cycles”, *Astronomy & Astrophysics* **655**, L1 (2021).
- [40] A. K. Lemmens, D. B. Rap, J. M. Thunnissen, B. Willemsen, and A. M. Rijs, “Polycyclic aromatic hydrocarbon formation chemistry in a plasma jet revealed by IR-UV action spectroscopy”, *Nature communications* **11**, 269 (2020).
- [41] S. G. Kukolich, C. Tanjaroorn, M. C. McCarthy, and P. Thaddeus, “Microwave spectrum of *o*-benzyne produced in a discharge nozzle”, *The Journal of Chemical Physics* **119**, 4353–4359 (2003).
- [42] M. C. McCarthy, K. L. K. Lee, P. B. Carroll, J. P. Porterfield, P. B. Changala, J. H. Thorpe, and J. F. Stanton, “Exhaustive Product Analysis of Three Benzene Discharges by Microwave Spectroscopy”, *The Journal of Physical Chemistry A* **124**, 5170–5181 (2020).
- [43] D. Loru, A. L. Steber, J. M. Thunnissen, D. B. Rap, A. K. Lemmens, A. M. Rijs, and M. Schnell, “New potential candidates for astronomical searches discovered in the electrical discharge of the PAH naphthalene and acetonitrile”, *Journal of Molecular Spectroscopy* **386**, 111629 (2022).
- [44] M. Born and R. Oppenheimer, “Zur Quantentheorie der Molekeln”, *Annalen der Physik* **389**, 457–484 (1927).

- [45] W. Gordy and R. L. Cook, Microwave molecular spectra (New York: Wiley, 1984).
- [46] S. A. Cooke and P. Ohring, “Decoding pure rotational molecular spectra for asymmetric molecules”, *Journal of Spectroscopy* (2013).
- [47] B. S. Ray, “Über die Eigenwerte des asymmetrischen Kreisels”, *Zeitschrift für Physik* **78**, 74–91 (1932).
- [48] J. K. G. Watson, Vibrational spectra and structure, 3rd ed., Vol. 6, 1 (Amsterdam: Elsevier, 1977).
- [49] J. K. Watson, “Determination of centrifugal distortion coefficients of asymmetric-top molecules”, *The Journal of Chemical Physics* **46**, 1935–1949 (1967).
- [50] J. K. Watson, “Simplification of the molecular vibration-rotation hamiltonian”, *Molecular Physics* **15**, 479–490 (1968).
- [51] H. V. L. Nguyen, W. Caminati, and J.-U. Grabow, “The lam of the rings: large amplitude motions in aromatic molecules studied by microwave spectroscopy”, *Molecules* **27**, 3948 (2022).
- [52] H. Hartwig and H. Dreizler, “The microwave spectrum of trans-2, 3-dimethyloxirane in torsional excited states”, *Zeitschrift für Naturforschung A* **51**, 923–932 (1996).
- [53] Z. Kisiel, “PROSPE - Programs for Rotational Spectroscopy”, (2015).
- [54] B. A. McGuire, A. M. Burkhardt, S. Kalenskii, C. N. Shingledecker, A. J. Remijan, E. Herbst, and M. C. McCarthy, “Detection of the aromatic molecule benzonitrile ($c\text{-C}_6\text{H}_5\text{CN}$) in the interstellar medium”, *Science* **359**, 202–205 (2018).
- [55] P. W. Atkins and D. P. J., Physical chemistry, 9th edition (Oxford: Oxford University Press, 2010).
- [56] D. F. Plusquellic, R. Suenram, B. Mate, J. Jensen, and A. Samuels, “The conformational structures and dipole moments of ethyl sulfide in the gas phase”, *The Journal of Chemical Physics* **115**, 3057–3067 (2001).
- [57] C. M. Western, “PGOPHER: A program for simulating rotational, vibrational and electronic spectra”, *Journal of Quantitative Spectroscopy and Radiative Transfer* **186**, 221–242 (2017).
- [58] Z. Kisiel, L. Pszczółkowski, I. R. Medvedev, M. Winnewisser, F. C. De Lucia, and E. Herbst, “Rotational spectrum of trans–trans diethyl ether in the ground and three excited vibrational states”, *Journal of Molecular Spectroscopy* **233**, 231–243 (2005).

- [59] Z. Kisiel, L. Pszczółkowski, B. J. Drouin, C. S. Brauer, S. Yu, J. C. Pearson, I. R. Medvedev, S. Fortman, and C. Neese, “Broadband rotational spectroscopy of acrylonitrile: vibrational energies from perturbations”, *Journal of Molecular Spectroscopy* **280**, 134–144 (2012).
- [60] F. Neese, “The ORCA program system”, *WIREs Computational Molecular Science* **2**, 73–78 (2012).
- [61] F. Neese, “Software update: the ORCA program system, version 4.0”, *WIREs Computational Molecular Science* **8**, 10.1002/wcms.1327 (2018).
- [62] M. J. Frisch, G. W. Trucks, H. B. Schlegel, G. E. Scuseria, M. A. Robb, J. R. Cheeseman, G. Scalmani, V. Barone, G. A. Petersson, H. Nakatsuji, X. Li, M. Caricato, A. V. Marenich, J. Bloino, B. G. Janesko, R. Gomperts, B. Mennucci, H. P. Hratchian, J. V. Ortiz, A. F. Izmaylov, J. L. Sonnenberg, D. Williams-Young, F. Ding, F. Lipparini, F. Egidi, J. Goings, B. Peng, A. Petrone, T. Henderson, D. Ranasinghe, V. G. Zakrzewski, J. Gao, N. Rega, G. Zheng, W. Liang, M. Hada, M. Ehara, K. Toyota, R. Fukuda, J. Hasegawa, M. Ishida, T. Nakajima, Y. Honda, O. Kitao, H. Nakai, T. Vreven, K. Throssell, J. A. Montgomery Jr., J. E. Peralta, F. Ogliaro, M. J. Bearpark, J. J. Heyd, E. N. Brothers, K. N. Kudin, V. N. Staroverov, T. A. Keith, R. Kobayashi, J. Normand, K. Raghavachari, A. P. Rendell, J. C. Burant, S. S. Iyengar, J. Tomasi, M. Cossi, J. M. Millam, M. Klene, C. Adamo, R. Cammi, J. W. Ochterski, R. L. Martin, K. Morokuma, O. Farkas, J. B. Foresman, and D. J. Fox, “Gaussian~16 Revision C.01”, (2016).
- [63] Spartan 14.
- [64] J. Demaison, “Accurate structures of non-rigid molecules by microwave spectroscopy”, 239–256 (1993).
- [65] J. D. Dunitz, “Accurate molecular structures, their determination and importance.(iucr monograph on crystallography no. 1) edited by a. domenicano and i. hargittai”, *Acta Crystallographica Section B: Structural Science* **49**, 145–146 (1993).
- [66] J. Kraitchman, “Determination of Molecular Structure from Microwave Spectroscopic Data”, *American Journal of Physics* **21**, 17–24 (1953).
- [67] M. Creutzburg and A. Stierle, “Adsorption of carboxylic acids on magnetite single crystal surfaces”, (2020).
- [68] P. R. Griffiths and J. A. De Haseth, *Fourier Transform Infrared Spectrometry*, 1st ed. (Wiley, Apr. 2007).

- [69] Y. Wang, A. Glenz, M. Muhler, and C. Wöll, “A new dual-purpose ultrahigh vacuum infrared spectroscopy apparatus optimized for grazing-incidence reflection as well as for transmission geometries”, *Review of Scientific Instruments* **80**, 113108 (2009).
- [70] F. M. Hoffmann, “Infrared reflection-absorption spectroscopy of adsorbed molecules”, *Surface Science Reports* **3**, 107–192 (1983).
- [71] R. H. Page, Y. Shen, and Y.-T. Lee, “Local modes of benzene and benzene dimer, studied by infrared–ultraviolet double resonance in a supersonic beam”, *The Journal of chemical physics* **88**, 4621–4636 (1988).
- [72] A. M. Rijs, M. Kabeláč, A. Abo-Riziq, P. Hobza, and M. S. De Vries, “Isolated gramicidin peptides probed by ir spectroscopy”, *ChemPhysChem* **12**, 1816–1821 (2011).
- [73] D. Schmitz, V. A. Shubert, T. Betz, and M. Schnell, “Multi-resonance effects within a single chirp in broadband rotational spectroscopy: The rapid adiabatic passage regime for benzonitrile”, *Journal of Molecular Spectroscopy* **280**, 77–84 (2012).
- [74] J.-U. Grabow, “Fourier transform microwave spectroscopy measurement and instrumentation”, *Handbook of High-resolution Spectroscopy* (2011).
- [75] C. Pérez, A. Krin, A. L. Steber, J. C. López, Z. Kisiel, and M. Schnell, “Wetting camphor: Multi-isotopic substitution identifies the complementary roles of hydrogen bonding and dispersive forces”, *The Journal of Physical Chemistry Letters* **7**, 154–160 (2016).
- [76] M. Fatima, C. Pérez, B. E. Arenas, M. Schnell, and A. L. Steber, “Benchmarking a new segmented K-band chirped-pulse microwave spectrometer and its application to the conformationally rich amino alcohol isoleucinol”, *Physical Chemistry Chemical Physics* **22**, 17042–17051 (2020).
- [77] J. L. Neill, B. J. Harris, A. L. Steber, K. O. Douglass, D. F. Plusquellic, and B. H. Pate, “Segmented chirped-pulse Fourier transform submillimeter spectroscopy for broadband gas analysis”, *Optics Express* **21**, 19743 (2013).
- [78] A. L. Steber, B. J. Harris, J. L. Neill, and B. H. Pate, “An arbitrary waveform generator based chirped pulse fourier transform spectrometer operating from 260 to 295 GHz”, *Journal of Molecular Spectroscopy* **280**, 3–10 (2012).
- [79] B. E. Arenas, S. Gruet, A. L. Steber, B. M. Giuliano, and M. Schnell, “Chirped-pulse fourier transform millimeter-wave spectroscopy of ten vibrationally excited states of i-propyl cyanide: exploring the far-infrared region”, *Physical Chemistry Chemical Physics* **19**, 1751–1756 (2017).

- [80] M. McCarthy, W. Chen, M. Travers, and P. Thaddeus, “Microwave spectra of 11 polyyne carbon chains”, *The Astrophysical Journal Supplement Series* **129**, 611 (2000).
- [81] M. McCarthy, M. Travers, A. Kovács, C. Gottlieb, and P. Thaddeus, “Eight new carbon chain molecules”, *The Astrophysical Journal Supplement Series* **113**, 105 (1997).
- [82] D. Oepke, A. Van der Meer, and P. Van Amersfoort, “The free-electron-laser user facility FELIX”, *Infrared physics & technology* **36**, 297–308 (1995).
- [83] A. Kantrowitz and J. Grey, “A high intensity source for the molecular beam. Part I. Theoretical”, *Review of Scientific Instruments* **22**, 328–332 (1951).
- [84] J. Anderson, R. Andres, and J. Fenn, Supersonic nozzle beams (1966), p. 275.
- [85] R. Smalley, B. Ramakrishna, D. Levy, and L. Wharton, “Laser spectroscopy of supersonic molecular beams: application to the NO₂ spectrum”, *The Journal of Chemical Physics* **61**, 4363–4364 (1974).
- [86] D. H. Levy, “The spectroscopy of very cold gases”, *Science* **214**, 263–269 (1981).
- [87] A. Stierle, T. F. Keller, H. Noei, V. Vonk, and R. Roehlsberger, “Desy nanolab”, *Journal of large-scale research facilities JLSRF* **2**, A76–A76 (2016).
- [88] J. H. Moore, C. C. Davis, M. A. Coplan, and S. C. Greer, Building Scientific Apparatus, 4th ed. (Cambridge University Press, June 2009).
- [89] I. Kleiner, “Spectroscopy of Interstellar Internal Rotors: An Important Tool for Investigating Interstellar Chemistry”, *ACS Earth and Space Chemistry* **3**, 1812–1842 (2019).
- [90] N. Biver, D. Bockelée-Morvan, R. Moreno, J. Crovisier, P. Colom, D. C. Lis, A. Sandqvist, J. Boissier, D. Despois, and S. N. Milam, “Ethyl alcohol and sugar in comet C/2014 Q2 (Lovejoy)”, *Science Advances* **1**, e1500863 (2015).
- [91] E. Herbst and E. F. van Dishoeck, “Complex Organic Interstellar Molecules”, *Annual Review of Astronomy and Astrophysics* **47**, 427–480 (2009).
- [92] R. M. Walker and A. G. W. Cameron, Meteorites and the Early Solar System II, edited by D. S. Lauretta and H. Y. McSween (University of Arizona Press, July 2006).
- [93] D. Despois, N. Biver, D. Bockelée-Morvan, and J. Crovisier, “Observations of Molecules in Comets”, *International Astronomical Union* **1**, 469 (2006).
- [94] J. C. Pearson, K. V. L. N. Sastry, E. Herbst, and F. C. D. Lucia, “Gauche Ethyl Alcohol: Laboratory Assignments and Interstellar Identification”, *The Astrophysical Journal* **480**, 420 (1997).

- [95] B. Zuckerman, B. E. Turner, D. R. Johnson, F. J. Lovas, N. Fourikis, P. Palmer, M. Morris, A. E. Lilley, J. A. Ball, and F. O. Clark, “Detection of interstellar trans-ethyl alcohol”, *The Astrophysical Journal* **196**, L99 (1975).
- [96] B. Tercero, I. Kleiner, J. Cernicharo, H. V. L. Nguyen, A. López, and G. M. M. Caro, “Discovery of methyl acetate and gauche ethyl formate in Orion”, *The Astrophysical Journal* **770**, L13 (2013).
- [97] S. W. Charles, G. I. L. Jones, and N. L. Owen, “Vibrational spectra and rotational isomerism of methyl and ethyl cyanoacetate”, *Journal of the Chemical Society, Faraday Transactions 2* **69**, 1454 (1973).
- [98] D. Sinha and J. E. Katon, “The Vibrational Spectra of Methyl Cyanoacetate and Methyl Cyanoacetate- d_3 ”, *Canadian Journal of Chemistry* **52**, 3057–3062 (1974).
- [99] S. Leibowitz, J. Laane, C. Van Alsenoy, and B. van der Veken, “On the conformational analysis of methyl cyanoacetate”, *Journal of Molecular Structure* **248**, 251–273 (1991).
- [100] J. M. F. Neta and R. Fausto, “Molecular structure and vibrational spectra of methyl cyanoacetate: an FT-IR, raman and ab initio molecular orbital study”, *Journal of Molecular Structure* **443**, 41–56 (1998).
- [101] R. Prasad, Y. Mishra, and R. Gupta, “Spectroscopic and molecular mechanics study of the conformational properties of methyl cyanoacetate and ethyl cyanoacetate”, (1990).
- [102] I. D. Reva, S. V. Ilieva, and R. Fausto, “Conformational isomerism in methyl cyanoacetate: A combined matrix-isolation infrared spectroscopy and molecular orbital study”, *Physical Chemistry Chemical Physics* **3**, 4235–4241 (2001).
- [103] I. Reva, S. Stepanian, L. Adamowicz, and R. Fausto, “Missing conformers. Comparative study of conformational cooling in cyanoacetic acid and methyl cyanoacetate isolated in low temperature inert gas matrixes”, *Chemical Physics Letters* **374**, 631–638 (2003).
- [104] C. Gregory, W. G. D. P. Silva, and J. van Wijngaarden, “Rotational spectrum and quantum chemical calculations of methyl cyanoacetate: A compound of potential astrochemical interest”, *Journal of Molecular Spectroscopy* **377**, 111444 (2021).
- [105] V. M. Rivilla, M. T. Beltrán, J. Martín-Pintado, F. Fontani, P. Caselli, and R. Cesaroni, “On the chemical ladder of esters - Detection and formation of ethyl formate in the W51 e2 hot molecular core”, *Astronomy & Astrophysics* **599**, A26 (2017).

- [106] V. M. Rivilla, J. Martín-Pintado, I. Jiménez-Serra, S. Zeng, S. Martín, J. Armijos-Abendaño, M. A. Requena-Torres, R. Aladro, and D. Riquelme, “Abundant Z-cyanomethanimine in the interstellar medium: paving the way to the synthesis of adenine”, *Monthly Notices of the Royal Astronomical Society: Letters* **483**, L114–L119 (2019).
- [107] H. M. Pickett, “The fitting and prediction of vibration-rotation spectra with spin interactions”, *Journal of Molecular Spectroscopy* **148**, 371–377 (1991).
- [108] Z. Kisiel, L. Pszczółkowski, I. R. Medvedev, M. Winnewisser, F. C. De Lucia, and E. Herbst, “Rotational spectrum of trans–trans diethyl ether in the ground and three excited vibrational states”, *Journal of Molecular Spectroscopy* **233**, 231–243 (2005).
- [109] J. G. Mangum and Y. L. Shirley, “How to calculate molecular column density”, *Publications of the Astronomical Society of the Pacific* **127**, 266–298 (2015).
- [110] H. Pickett, R. Poynter, E. Cohen, M. Delitsky, J. Pearson, and H. Müller, “Submillimeter, millimeter, and microwave spectral line catalog”, *Journal of Quantitative Spectroscopy and Radiative Transfer* **60**, 883–890 (1998).
- [111] S. Zeng, I. Jiménez-Serra, V. M. Rivilla, S. Martín, J. Martín-Pintado, M. A. Requena-Torres, J. Armijos-Abendaño, D. Riquelme, and R. Aladro, “Complex organic molecules in the Galactic Centre: the N-bearing family”, *Monthly Notices of the Royal Astronomical Society* **478**, 2962–2975 (2018).
- [112] L. F. Rodríguez-Almeida, V. M. Rivilla, I. Jiménez-Serra, M. Melosso, L. Colzi, S. Zeng, B. Tercero, P. d. Vicente, S. Martín, M. A. Requena-Torres, F. Rico-Villas, and J. Martín-Pintado, “First detection of C₂H₅NCO in the ISM and search of other isocyanates towards the G+0.693-0.027 molecular cloud”, *Astronomy & Astrophysics* **654**, Publisher: EDP Sciences, L1 (2021).
- [113] V. M. Rivilla, L. Colzi, I. Jiménez-Serra, J. Martín-Pintado, A. Megías, M. Melosso, L. Bizzocchi, Á. López-Gallifa, A. Martínez-Henares, S. Massalkhi, B. Tercero, P. d. Vicente, J.-C. Guillemin, J. G. d. l. Concepción, F. Rico-Villas, S. Zeng, S. Martín, M. A. Requena-Torres, F. Tonolo, S. Alessandrini, L. Dore, V. Barone, and C. Puzzarini, “Precursors of the RNA World in Space: Detection of (Z)-1,2-ethenediol in the Interstellar Medium, a Key Intermediate in Sugar Formation”, *The Astrophysical Journal Letters* **929**, Publisher: American Astronomical Society, L11 (2022).
- [114] M. A. Requena-Torres, J. Martín-Pintado, A. Rodríguez-Franco, S. Martín, N. J. Rodríguez-Fernández, and P. d. Vicente, “Organic molecules in the Galactic center - Hot core chemistry without hot cores”, *Astronomy & Astrophysics* **455**, 971–985 (2006).

- [115] M. A. Requena-Torres, J. Martín-Pintado, S. Martín, and M. R. Morris, “The Galactic Center: The Largest Oxygen-bearing Organic Molecule Repository”, *The Astrophysical Journal* **672**, 352–360 (2008).
- [116] S. Zeng, Q. Zhang, I. Jiménez-Serra, B. Tercero, X. Lu, J. Martín-Pintado, P. de Vicente, V. M. Rivilla, and S. Li, “Cloud–cloud collision as drivers of the chemical complexity in Galactic Centre molecular clouds”, *Monthly Notices of the Royal Astronomical Society* **497**, 4896–4909 (2020).
- [117] V. M. Rivilla, I. Jiménez-Serra, J. Martín-Pintado, C. Briones, L. F. Rodríguez-Almeida, F. Rico-Villas, B. Tercero, S. Zeng, L. Colzi, P. de Vicente, S. Martín, and M. A. Requena-Torres, “Discovery in space of ethanolamine, the simplest phospholipid head group”, *Proceedings of the National Academy of Sciences* **118**, e2101314118 (2021).
- [118] S. Martín, J. Martín-Pintado, C. Blanco-Sánchez, V. M. Rivilla, A. Rodríguez-Franco, and F. Rico-Villas, “Spectral Line Identification and Modelling (SLIM) in the MAdrid Data CUBe Analysis (MADCUBA) package: Interactive software for data cube analysis”, *Astronomy & Astrophysics* **631**, A159 (2019).
- [119] Z. Kisiel, “Least-squares mass-dependence molecular structures for selected weakly bound intermolecular clusters”, *Journal of Molecular Spectroscopy* **218**, 58–67 (2003).
- [120] J. K. G. Watson, A. Roytburg, and W. Ulrich, “Least-Squares Mass-Dependence Molecular Structures”, *Journal of Molecular Spectroscopy* **196**, 102–119 (1999).
- [121] M. Sanz-Novo, I. León, E. R. Alonso, L. Kolesníková, and J. L. Alonso, “Laboratory Detection of Cyanoacetic Acid: A Jet-cooled Rotational Study”, *The Astrophysical Journal* **915**, 76 (2021).
- [122] M. C. McCarthy and B. A. McGuire, “Aromatics and Cyclic Molecules in Molecular Clouds: A New Dimension of Interstellar Organic Chemistry”, *The Journal of Physical Chemistry A* **125**, 3231–3243 (2021).
- [123] A. M. Burkhardt, R. A. Loomis, C. N. Shingledecker, K. L. K. Lee, A. J. Remijan, M. C. McCarthy, and B. A. McGuire, “Ubiquitous aromatic carbon chemistry at the earliest stages of star formation”, *Nature Astronomy* **5**, 181–187 (2021).
- [124] K. L. K. Lee, P. B. Changala, R. A. Loomis, A. M. Burkhardt, C. Xue, M. A. Cordiner, S. B. Charnley, M. C. McCarthy, and B. A. McGuire, “Interstellar Detection of 2-cyanocyclopentadiene, C₅H₅CN, a Second Five-membered Ring toward TMC-1”, *The Astrophysical Journal Letters* **910**, L2 (2021).

- [125] K. L. K. Lee, B. A. McGuire, and M. C. McCarthy, “Gas-phase synthetic pathways to benzene and benzonitrile: a combined microwave and thermochemical investigation”, *Physical Chemistry Chemical Physics* **21**, 2946–2956 (2019).
- [126] C. la Lau and H. de Ruyter, “Vibrational spectra and structure of the cycloheptatriene molecule”, *Spectrochimica Acta* **19**, 1559–1566 (1963).
- [127] S. S. Butcher, “Microwave Spectrum of 1,3,5-Cycloheptatriene”, *The Journal of Chemical Physics* **42**, 1833–1836 (1965).
- [128] W. Paulick, C. Jung, U. Kempka, J. Sühnel, and K. Gustav, “Interpretation of the vibrational spectra and calculation of the geometries of cycloheptatriene, 7-d-cycloheptatriene and phenyl substituted cycloheptatrienes”, *Journal of Molecular Structure: THEOCHEM* **85**, 235–240 (1981).
- [129] R. A. Creswell, “Microwave spectrum of tropone”, *Journal of Molecular Spectroscopy* **51**, 111–114 (1974).
- [130] L. M. Bateman, O. A. McNamara, N. R. Buckley, P. O’Leary, F. Harrington, N. Kelly, S. O’Keeffe, A. Stack, S. O’Neill, D. G. McCarthy, and A. R. Maguire, “A study of the norcaradiene–cycloheptatriene equilibrium in a series of azulenes by NMR spectroscopy; the impact of substitution on the position of equilibrium”, *Org. Biomol. Chem.* **13**, 11026–11038 (2015).
- [131] B. E. Arenas, G. Batra, A. L. Steber, L. Bizzocchi, A. P. Charmet, B. M. Giuliano, P. Caselli, B. J. Harris, B. H. Pate, J.-C. Guillemin, et al., “Rotational spectroscopy of imidazole: accurate spectroscopic information for three vibrationally excited states and the heavy-atom isotopologues up to 295 GHz”, *Journal of Molecular Spectroscopy* **378**, 111452 (2021).
- [132] B. M. Giuliano, L. Bizzocchi, A. Pietropolli Charmet, B. E. Arenas, A. L. Steber, M. Schnell, P. Caselli, B. J. Harris, B. H. Pate, J.-C. Guillemin, and A. Belloche, “Rotational spectroscopy of imidazole: improved rest frequencies for astrophysical searches”, *Astronomy & Astrophysics* **628**, A53 (2019).
- [133] J. Kraitchman, “Determination of Molecular Structure from Microwave Spectroscopic Data”, *American Journal of Physics* **21**, 17–24 (1953).
- [134] F. J. Lovas, A. J. Remijan, J. Hollis, P. Jewell, and L. E. Snyder, “Hyperfine structure identification of interstellar cyanoallene toward TMC-1”, *The Astrophysical Journal* **637**, L37 (2006).
- [135] J. Casado, L. Nygaard, and G. Sørensen, “Microwave spectra of isotopic benzonitriles. Refined molecular structure of benzonitrile”, *Journal of Molecular Structure* **8**, 211–224 (1971).

- [136] K. L. Kelvin Lee, P. B. Changala, R. A. Loomis, A. M. Burkhardt, C. Xue, M. A. Cordiner, S. B. Charnley, M. C. McCarthy, and B. A. McGuire, “Interstellar Detection of 2-cyanocyclopentadiene, C_5H_5CN , a Second Five-membered Ring toward TMC-1”, *The Astrophysical Journal Letters* **910**, L2 (2021).
- [137] J. Cernicharo, M. Agúndez, R. Kaiser, C. Cabezas, B. Tercero, N. Marcelino, J. Pardo, and P. De Vicente, “Discovery of benzyne, $o-C_6H_4$, in TMC-1 with the QUIJOTE line survey”, *Astronomy & Astrophysics* **652**, L9 (2021).
- [138] J. Cernicharo, R. Fuentetaja, M. Agúndez, R. I. Kaiser, C. Cabezas, N. Marcelino, B. Tercero, J. R. Pardo, and P. de Vicente, “Discovery of fulvenallene in TMC-1 with the QUIJOTE line survey”, *Astronomy & Astrophysics* **663**, L9 (2022).
- [139] A. M. Burkhardt, K. L. K. Lee, P. B. Changala, C. N. Shingledecker, I. R. Cooke, R. A. Loomis, H. Wei, S. B. Charnley, E. Herbst, M. C. McCarthy, et al., “Discovery of the pure polycyclic aromatic hydrocarbon indene ($c-C_9H_8$) with gotham observations of TMC-1”, *The Astrophysical Journal Letters* **913**, L18 (2021).
- [140] M. L. Sita, P. B. Changala, C. Xue, A. M. Burkhardt, C. N. Shingledecker, K. L. K. Lee, R. A. Loomis, E. Momjian, M. A. Siebert, D. Gupta, et al., “Discovery of interstellar 2-cyanoindene ($2-C_9H_7CN$) in gotham observations of tmc-1”, *The Astrophysical Journal Letters* **938**, L12 (2022).
- [141] H. E. Suess and H. C. Urey, “Abundances of the Elements”, *Rev. Mod. Phys.* **28**, 53–74 (1956).
- [142] M. Riordan and L. Hoddeson, “Origins of the pn junction”, *IEEE spectrum* **34**, 46–51 (1997).
- [143] W. Mönch, “Semiconductor surfaces and interfaces”, **26** (2013).
- [144] S. Fujii, “Expanding the chemical space of hydrophobic pharmacophores: the role of hydrophobic substructures in the development of novel transcription modulators”, *Med. Chem. Commun.* **7**, 1082–1092 (2016).
- [145] B. Vivet, F. Cavelier, and J. Martinez, “Synthesis of Silaproline, a New Proline Surrogate”, *Eur. J. Org. Chem.* **2000**, 807–811 (2000).
- [146] J. A. Salem, “Transparent Armor Ceramics as Spacecraft Windows”, *J. Am. Ceram. Soc.* **96**, edited by V. Sglavo, 281–289 (2013).
- [147] C. B. Carter and M. G. Norton, “Ceramics in biology and medicine”, *Ceramic Materials: Science and Engineering*, 635–651 (2007).
- [148] K. G. Babu and P. S. Prakash, “Efficiency of silica fume in concrete”, *Cement and concrete research* **25**, 1273–1283 (1995).

- [149] J. Ballato, T. Hawkins, P. Foy, R. Stolen, B. Kokuo, M. Ellison, C. McMillen, J. Reppert, A. Rao, and M. Daw, “Silicon optical fiber”, *Optics express* **16**, 18675–18683 (2008).
- [150] A. Snell, K. Mackenzie, W. Spear, P. LeComber, and A. Hughes, “Application of amorphous silicon field effect transistors in addressable liquid crystal display panels”, *Applied Physics A* **24**, 357–362 (1981).
- [151] R. R. LeVier, M. C. Harrison, R. R. Cook, and T. H. Lane, “What is silicone?”, *Journal of clinical Epidemiology* **48**, 513–517 (1995).
- [152] T. Ikeda, Y. Shionoiri, T. Atsumi, A. Ishikawa, H. Miyake, Y. Kurokawa, K. Kato, J. Koyama, S. Yamazaki, and K. Miyata, “21.2: Full-Functional System Liquid Crystal Display Using CG-Silicon Technology”, in, Vol. 35 (2004), pp. 860–863.
- [153] A. M. Muzafarov, “Silicon polymers”, **235** (2010).
- [154] R. D. Miller and J. Michl, “Polysilane high polymers”, *Chemical Reviews* **89**, 1359–1410 (1989).
- [155] R. J. Hofmann, M. Vlatković, and F. Wiesbrock, “Fifty years of hydrosilylation in polymer science: a review of current trends of low-cost transition-metal and metal-free catalysts, non-thermally triggered hydrosilylation reactions, and industrial applications”, *Polymers* **9**, 534 (2017).
- [156] W. Bains and R. Tacke, “Silicon chemistry as a novel source of chemical diversity in drug design.”, *Current Opinion in Drug Discovery & Development* **6**, 526–543 (2003).
- [157] R. Tacke and H. Zilch, “Sila-substitution—a useful strategy for drug design?”, *Endeavour* **10**, 191–197 (1986).
- [158] J. Millership and M. Shanks, “Prodrugs utilizing a reversible silyl linkage”, *International journal of pharmaceuticals* **28**, 1–9 (1986).
- [159] J. Soloducho, D. Zajac, K. Szychalska, S. Baluta, and J. Cabaj, “Conducting Silicone-Based Polymers and Their Application”, *Molecules* **26**, 2012 (2021).
- [160] N. Tanigaki, Y. Iwase, A. Kaito, Y. Okada, N. Yamahira, and K. Yase, “Oriented thin films of poly (diphenylsilane)”, *Molecular Crystals and Liquid Crystals Science and Technology. Section A. Molecular Crystals and Liquid Crystals* **370**, 219–222 (2001).
- [161] M. Iwase, T. Oku, A. Suzuki, T. Akiyama, K. Tokumitsu, M. Yamada, and M. Nakamura, “Fabrication and characterization of poly [diphenylsilane]-based solar cells”, in *Journal of physics: conference series*, Vol. 352, 1 (IOP Publishing, 2012), p. 012018.

- [162] L. Nielsen and T. Skrydstrup, “Sequential C-Si Bond Formations from Diphenylsilane: Application to Silanediol Peptide Isostere Precursors”, *J. Am. Chem. Soc.* **130**, 13145–13151 (2008).
- [163] L. M. Ziurys, “The chemistry in circumstellar envelopes of evolved stars: following the origin of the elements to the origin of life”, *Proceedings of the National Academy of Sciences* **103**, 12274–12279 (2006).
- [164] J. Cernicharo, L. B. F. M. Waters, L. Decin, P. Encrenaz, A. G. G. M. Tielens, M. Agúndez, E. D. Beck, H. S. P. Müller, J. R. Goicoechea, M. J. Barlow, A. Benz, N. Crimier, F. Daniel, A. M. D. Giorgio, M. Fich, T. Gaier, P. García-Lario, A. d. Koter, T. Khouiri, R. Liseau, R. Lombaert, N. Erickson, J. R. Pardo, J. C. Pearson, R. Shipman, C. S. Contreras, and D. Teyssier, “A high-resolution line survey of IRC +10216 with Herschel/HIFI - First results: Detection of warm silicon dicarbide (SiC)”, *Astronomy & Astrophysics* **521**, L8 (2010).
- [165] A. P. Jones, “Interstellar and circumstellar grain formation and survival”, *Philosophical Transactions of the Royal Society of London. Series A: Mathematical, Physical and Engineering Sciences* **359**, edited by R. Hutchison, C. Pillinger, G. Turner, and S. Russell, 1961–1972 (2001).
- [166] D. S. N. Parker, A. V. Wilson, R. I. Kaiser, N. J. Mayhall, M. Head-Gordon, and A. G. G. M. Tielens, “On the formation of silacyclopropenyldiene ($c\text{-SiC}_2\text{H}_2$) and its role in the organosilicon chemistry in the interstellar medium”, *The Astrophysical Journal* **770**, 33 (2013).
- [167] M. Ohishi, N. Kaifu, K. Kawaguchi, A. Murakami, S. Saito, S. Yamamoto, S.-I. Ishikawa, Y. Fujita, Y. Shiratori, and W. M. Irvine, “Detection of a new circumstellar carbon chain molecule, C_4Si ”, *The Astrophysical Journal* **345**, L83 (1989).
- [168] J. Cernicharo, M. Agúndez, L. Velilla Prieto, M. Guélin, J. R. Pardo, C. Kahane, C. Marka, C. Kramer, S. Navarro, G. Quintana-Lacaci, J. P. Fonfría, N. Marcelino, B. Tercero, E. Moreno, S. Massalkhi, M. Santander-García, M. C. McCarthy, C. A. Gottlieb, and J. L. Alonso, “Discovery of methyl silane and confirmation of silyl cyanide in IRC +10216”, *Astronomy & Astrophysics* **606**, L5 (2017).
- [169] M. C. McCarthy, A. J. Apponi, C. A. Gottlieb, and P. Thaddeus, “Rotational spectra of SiCN, SiNC, and the SiC_nH , $n=2, 4-6 \dots$ radicals”, *Journal of Chemical Physics* **115**, 8 (2001).
- [170] M. McCarthy, A. Apponi, C. Gottlieb, and P. Thaddeus, “Laboratory detection of five new linear silicon carbides: SiC_3 , SiC_5 , SiC_6 , SiC_7 , and SiC_8 ”, *The Astrophysical Journal* **538**, 766 (2000).

- [171] M. McCarthy, C. Gottlieb, and P. Thaddeus, “Silicon molecules in space and in the laboratory”, *Molecular Physics* **101**, 697–704 (2003).
- [172] V. D. Gordon, E. S. Nathan, A. J. Apponi, M. C. McCarthy, P. Thaddeus, and P. Botschwina, “Structures of the linear silicon carbides SiC_4 and SiC_6 : Isotopic substitution and Ab Initio theory”, 11 (2014).
- [173] M. C. McCarthy, J. H. Baraban, P. B. Changala, J. F. Stanton, M.-A. Martin-Drumel, S. Thorwirth, C. A. Gottlieb, and N. J. Reilly, “Discovery of a Missing Link: Detection and Structure of the Elusive Disilicon Carbide Cluster”, *The Journal of Physical Chemistry Letters* **6**, 2107–2111 (2015).
- [174] M. Fatima, D. Maué, C. Pérez, D. S. Tikhonov, D. Bernhard, A. Stamm, C. Medcraft, M. Gerhards, and M. Schnell, “Structures and internal dynamics of diphenylether and its aggregates with water”, *Physical Chemistry Chemical Physics* **22**, 27966–27978 (2020).
- [175] H. F. Holtzclaw, H. F. Holtzelaw Jr, W. R. Robinson, and J. D. Odom, “General chemistry”, (1988).
- [176] M. C. McCarthy, A. J. Apponi, and P. Thaddeus, “A second rhomboidal isomer of SiC_3 ”, *The Journal of Chemical Physics* **111**, 7175–7178 (1999).
- [177] I. Merke, W. Stahl, S. Kass, D. Petitprez, and G. Wlodarczak, “Internal Rotation, Quadrupole Coupling, and Structure of $(\text{CH}_3)_3\text{SiCl}$ Studied by Microwave Spectroscopy and ab Initio Calculation”, *Journal of Molecular Spectroscopy* **216**, 437–446 (2002).
- [178] W. Caminati, G. Cazzoli, and A. Mirri, “Internal rotation barrier and dipole moment of phenylsilane by microwave spectroscopy”, *Chemical Physics Letters* **35**, 475–478 (1975).
- [179] J. Lei, J. Chen, Z. Yang, G. Feng, Z. Xia, and Q. Gou, “Rotational spectrum, internal dynamics, and molecular structure of methylphenylsilane”, *Journal of Chemical Physics* **150**, 234302 (2019).
- [180] G. Portalone, F. Ramondo, A. Domenicano, and I. Hargittai, “Molecular structure of phenylsilane: a study by gas-phase electron diffraction and ab initio molecular orbital calculations”, *Journal of organometallic chemistry* **560**, 183–190 (1998).
- [181] S. Claude, P. Dindo, D. Erickson, N. Jiang, K. Yeung, D. Derdall, D. Duncan, D. Garcia, D. Henke, B. Leckie, A. Lichtenberger, P. Niranjanan, S.-K. Pan, M. Pflieger, G. Rodrigues, K. Szeto, P. Welle, and K. Caputa, “The band 3 receiver (84-116 GHz) for ALMA”, in , Vol. 2 (Oct. 2005), 407–408 vol. 2.

- [182] D. Keller, “Molecules in the circumstellar envelope of the evolved carbon-rich star IRC+ 10216”, PhD thesis (Universitäts-und Landesbibliothek Bonn, 2017).
- [183] M. K. McClure, W. Rocha, K. Pontoppidan, N. Crouzet, L. E. Chu, E. Dartois, T. Lamberts, J. Noble, Y. Pendleton, G. Perotti, et al., “An ice age jwst inventory of dense molecular cloud ices”, *Nature Astronomy*, 1–13 (2023).
- [184] K. I. Öberg, “Photochemistry and astrochemistry: photochemical pathways to interstellar complex organic molecules”, *Chemical reviews* **116**, 9631–9663 (2016).
- [185] J. Noble, E. Michoulier, C. Aupetit, and J. Mascetti, “Influence of ice structure on the soft uv photochemistry of pahs embedded in solid water”, *Astron. Astrophys.* **644**, A22 (2020).
- [186] R. Mastrapa, S. Sandford, T. Roush, D. Cruikshank, and C. Dalle Ore, “Optical constants of amorphous and crystalline H₂O-ice: 2.5–22 μ m (4000–455 cm^{−1}) optical constants of H₂O-ice”, *The Astrophysical Journal* **701**, 1347 (2009).
- [187] J. A. Noble, C. Martin, H. J. Fraser, P. Roubin, and S. Coussan, “Unveiling the surface structure of amorphous solid water via selective infrared irradiation of oh stretching modes”, *The journal of physical chemistry letters* **5**, 826–829 (2014).
- [188] A. G. Tielens, “Interstellar polycyclic aromatic hydrocarbon molecules”, *Annual Review of Astronomy and Astrophysics* **46**, 289–337 (2008).
- [189] A. Li, “Spitzer’s perspective of polycyclic aromatic hydrocarbons in galaxies”, *Nature Astronomy* **4**, 339–351 (2020).
- [190] J. S. Spilker, K. A. Phadke, M. Aravena, M. Archipley, M. B. Bayliss, J. E. Birkin, M. Béthermin, J. Burgoyne, J. Cathey, S. C. Chapman, et al., “Spatial variations in aromatic hydrocarbon emission in a dust-rich galaxy”, *Nature*, 1–4 (2023).
- [191] A. G. G. M. Tielens and L. J. Allamandola, “Evolution of interstellar dust”, in *Physical processes in interstellar clouds*, edited by G. E. Morfill and M. Scholer (Springer Netherlands, Dordrecht, 1987), pp. 333–376.
- [192] E. Dwek and I. Cherchneff, “The origin of dust in the early universe: probing the star formation history of galaxies by their dust content”, *The Astrophysical Journal* **727**, 63 (2011).

- [193] G. A. Kimmel, J. Matthiesen, M. Baer, C. J. Mundy, N. G. Petrik, R. S. Smith, Z. Dohnalek, and B. D. Kay, “No confinement needed: observation of a metastable hydrophobic wetting two-layer ice on graphene”, *J. Am. Chem. Soc.* **131**, 12838–44 (2009).
- [194] S. Standop, T. Michely, and C. Busse, “H₂O on Graphene/Ir (111): a periodic array of frozen droplets”, *The Journal of Physical Chemistry C* **119**, 1418–1423 (2015).
- [195] R. Gleißner, M. Creutzburg, H. Noei, and A. Stierle, “Interaction of water with Graphene/Ir(111) studied by vibrational spectroscopy”, *Langmuir* **35**, 11285–11290 (2019).
- [196] S. Standop, “Water adsorption and ion induced defect formation: a comparative study of graphene and noble metal surfaces.”, Thesis (2013).
- [197] J. Carrasco, A. Hodgson, and A. Michaelides, “A molecular perspective of water at metal interfaces”, *Nature Materials* **11**, 667–674 (2012).
- [198] A. Jones, A. Tielens, and D. Hollenbach, “Grain shattering in shocks: the interstellar grain size distribution”, *The Astrophysical Journal* **469**, 740 (1996).
- [199] J. Y. Seok, H. Hirashita, and R. S. Asano, “Formation history of polycyclic aromatic hydrocarbons in galaxies”, *Monthly Notices of the Royal Astronomical Society* **439**, 2186–2196 (2014).
- [200] C. Pérez, A. L. Steber, A. M. Rijs, B. Temelso, G. C. Shields, J. C. Lopez, Z. Kisiel, and M. Schnell, “Corannulene and its complex with water: a tiny cup of water”, *Physical Chemistry Chemical Physics* **19**, 14214–14223 (2017).
- [201] D. Loru, A. L. Steber, C. Pérez, D. A. Obenchain, B. Temelso, J. C. López, and M. Schnell, “Quantum tunneling facilitates water motion across the surface of phenanthrene”, *J. Am. Chem. Soc.* **145**, 17201–17210 (2023).
- [202] S. Schlemmer, D. J. Cook, J. A. Harrison, B. Wurfel, W. Chapman, and R. J. Saykally, “The unidentified interstellar infrared bands: PAHs as carriers?”, *Science* **265**, 1686–1689 (1994).
- [203] B. A. McGuire, R. A. Loomis, A. M. Burkhardt, K. L. K. Lee, C. N. Shingledecker, S. B. Charnley, I. R. Cooke, M. A. Cordiner, E. Herbst, S. Kalenskii, et al., “Detection of two interstellar polycyclic aromatic hydrocarbons via spectral matched filtering”, *Science* **371**, 1265–1269 (2021).
- [204] E. Cané, P. Palmer, R. Tarroni, A. Trombetti, and N. Handy, “The high-resolution infrared spectra of naphthalene-h₈ and naphthalene-d₈: comparison of scaled scf and density functional force fields”, *Gazzetta Chimica Italiana* **126**, 289–296 (1996).

- [205] E. R. Lippincott and E. J. O'Reilly, "Vibrational spectra and assignment of naphthalene and naphthalene-*d*-8", *Journal of Chemical Physics* **23**, 238–244 (1955).
- [206] D. M. Hudgins and S. A. Sandford, "Infrared spectroscopy of matrix isolated polycyclic aromatic hydrocarbons. 1. pahs containing two to four rings", *The Journal of Physical Chemistry A* **102**, 329–343 (1998).
- [207] S. A. Sandford, M. P. Bernstein, and L. J. Allamandola, "The Mid-Infrared Laboratory Spectra of Naphthalene ($C_{10}H_8$) in Solid H_2O ", *The Astrophysical Journal* **607**, 346–360 (2004).
- [208] A. Stierle, T. F. Keller, H. Noei, V. Vonk, and R. Roehlsberger, "DESY NanoLab", *Journal of large-scale research facilities JLSRF* **2**, A76 (2016).
- [209] H. Noei, H. Qiu, Y. Wang, E. Löffler, C. Wöll, and M. Muhler, "The identification of hydroxyl groups on ZnO nanoparticles by infrared spectroscopy", *Physical Chemistry Chemical Physics* **10**, 7092–7097 (2008).
- [210] K. Chatterjee, T. K. Roy, J. Khatri, G. Schwaab, and M. Havenith, "Unravelling the microhydration frameworks of prototype pah by infrared spectroscopy: naphthalene-(water) $_{1-3}$ ", *Physical Chemistry Chemical Physics* **23**, 14016–14026 (2021).
- [211] P. Vassilev, R. A. van Santen, and M. T. Koper, "Ab initio studies of a water layer at transition metal surfaces", *Journal of Chemical Physics* **122**, 54701 (2005).
- [212] H. Ogasawara, B. Brena, D. Nordlund, M. Nyberg, A. Pelmenschikov, L. G. Pettersson, and A. Nilsson, "Structure and bonding of water on Pt(111)", *Physical Review Letters* **89**, 276102 (2002).
- [213] T. Yamada, S. Tamamori, H. Okuyama, and T. Aruga, "Anisotropic water chain growth on Cu(110) observed with scanning tunneling microscopy", *Physical Review Letters* **96**, 036105 (2006).
- [214] G. A. Kimmel, N. G. Petrik, Z. Dohnálek, and B. D. Kay, "Crystalline ice growth on Pt(111): observation of a hydrophobic water monolayer", *Physical Review Letters* **95**, 166102 (2005).
- [215] M. Mehlhorn and K. Morgenstern, "Faceting during the transformation of amorphous to crystalline ice", *Physical Review Letters* **99**, 246101 (2007).
- [216] K. Thurmer and N. C. Bartelt, "Nucleation-limited dewetting of ice films on Pt(111)", *Physical Review Letters* **100**, 186101 (2008).
- [217] G. A. Kimmel, N. G. Petrik, Z. Dohnálek, and B. D. Kay, "Layer-by-layer growth of thin amorphous solid water films on Pt(111) and Pd(111)", *Journal of Chemical Physics* **125**, 44713 (2006).

- [218] S. Kaya, J. Weissenrieder, D. Stacchiola, S. Shaikhutdinov, and H. J. Freund, “Formation of an ordered ice layer on a thin silica film”, *The Journal of Physical Chemistry C* **111**, 759–764 (2006).
- [219] R. S. Smith, T. Zubkov, Z. Dohnálek, and B. D. Kay, “The effect of the incident collision energy on the porosity of vapor-deposited amorphous solid water films”, *The Journal of Physical Chemistry B* **113**, 4000–4007 (2009).
- [220] P. J. Feibelman, G. A. Kimmel, R. S. Smith, N. G. Petrik, T. Zubkov, and B. D. Kay, “A unique vibrational signature of rotated water monolayers on Pt(111): predicted and observed”, *Journal of Chemical Physics* **134**, 204702 (2011).
- [221] R. A. May, R. S. Smith, and B. D. Kay, “Probing the interaction of amorphous solid water on a hydrophobic surface: dewetting and crystallization kinetics of ASW on carbon tetrachloride”, *Physical Chemistry Chemical Physics* **13**, 19848–19855 (2011).
- [222] G. A. Kimmel, T. Zubkov, R. S. Smith, N. G. Petrik, and B. D. Kay, “Turning things downside up: adsorbate induced water flipping on Pt(111)”, *Journal of Chemical Physics* **141**, 18C515 (2014).
- [223] D. Klug, O. Mishima, and E. Whalley, “High-density amorphous ice. iv. raman spectrum of the uncoupled O–H and O–D oscillators”, *The Journal of chemical physics* **86**, 5323–5328 (1987).
- [224] M. Moskovits, “Surface selection rules”, *Journal of Chemical Physics* **77**, 4408–4416 (1982).
- [225] V. Buch and J. P. Devlin, “Spectra of dangling OH bonds in amorphous ice: assignment to 2- and 3-coordinated surface molecules”, *Journal of Chemical Physics* **94**, 4091–4092 (1991).
- [226] W. Hagen, A. G. G. M. Tielens, and J. M. Greenberg, “The infrared spectra of amorphous solid water and ice I_c between 10 and 140 K”, *Chem. Phys.* **56**, 367–379 (1981).
- [227] C. C. Pradzynski, R. M. Forck, T. Zeuch, P. Slavíček, and U. Buck, “A fully size-resolved perspective on the crystallization of water clusters”, *Science* **337**, 1529–1532 (2012).
- [228] E. Michoulier, N. Ben Amor, M. Rapacioli, J. A. Noble, J. Mascetti, C. Toubin, and A. Simon, “Theoretical determination of adsorption and ionisation energies of polycyclic aromatic hydrocarbons on water ice”, *Physical Chemistry Chemical Physics* **20**, 11941–11953 (2018).

- [229] E. Michoulier, C. Toubin, A. Simon, J. Mascetti, C. Aupetit, and J. A. Noble, “Perturbation of the surface of amorphous solid water by the adsorption of polycyclic aromatic hydrocarbons”, *The Journal of Physical Chemistry C* **124**, 2994–3001 (2019).
- [230] C. Bu, J. Shi, U. Raut, E. H. Mitchell, and R. A. Baragiola, “Effect of microstructure on spontaneous polarization in amorphous solid water films”, *Journal of Chemical Physics* **142** (2015).
- [231] Y. Xu, C. J. Dibble, N. G. Petrik, R. S. Smith, B. D. Kay, and G. A. Kimmel, “Complete wetting of Pt(111) by nanoscale liquid water films”, *The Journal of Physical Chemistry Letters* **7**, 541–7 (2016).
- [232] S. Chakraborty, S. Banik, and P. K. Das, “Anharmonicity in the vibrational spectra of naphthalene and naphthalene-*d*₈: experiment and theory”, *The Journal of Physical Chemistry A* **120**, 9707–9718 (2016).
- [233] D. M. Hudgins, S. A. Sandford, and L. J. Allamandola, “Infrared spectroscopy of polycyclic aromatic hydrocarbon cations. 1. matrix-isolated naphthalene and perdeuterated naphthalene”, *The Journal of Physical Chemistry A* **98**, 4243–4253 (1994).
- [234] J. E. Roser and L. J. Allamandola, “Infrared spectroscopy of naphthalene aggregation and cluster formation in argon matrices”, *The Astrophysical Journal* **722**, 1932–1938 (2010).
- [235] M. P. Bernstein, S. A. Sandford, and L. J. Allamandola, “The mid-infrared absorption spectra of neutral polycyclic aromatic hydrocarbons in conditions relevant to dense interstellar clouds”, *The Astrophysical Journal Supplement Series* **161**, 53–64 (2005).
- [236] W. X. Huang and J. M. White, “Growth and orientation of naphthalene films on Ag(111)”, *The Journal of Physical Chemistry B* **108**, 5060–5065 (2004).
- [237] L. M. Ziurys, “The chemistry in circumstellar envelopes of evolved stars: Following the origin of the elements to the origin of life”, *Proceedings of the National Academy of Sciences* **103**, 12274–12279 (2006).
- [238] M. C. McCarthy, C. A. Gottlieb, and J. Cernicharo, “Building blocks of dust: a coordinated laboratory and astronomical study of the archetype agb carbon star irc+ 10216”, *Journal of molecular spectroscopy* **356**, 7–20 (2019).
- [239] M. Guélin, R. Lucas, and J. Cernicharo, “MgNC and the carbon-chain radicals in IRC+ 10216”, *Astronomy and Astrophysics* **280**, L19–L22 (1993).
- [240] D. M. Goldhaber and A. L. Betz, “Silane in IRC +10216.”, *The Astrophysical Journal* **279**, L55–L58 (1984).

- [241] J. Cernicharo, M. Agúndez, L. V. Prieto, M. Guélin, J. R. Pardo, C. Kahane, C. Marka, C. Kramer, S. Navarro, G. Quintana-Lacaci, J. P. Fonfría, N. Marcelino, B. Tercero, E. Moreno, S. Massalkhi, M. Santander-García, M. C. McCarthy, C. A. Gottlieb, and J. L. Alonso, “Discovery of methyl silane and confirmation of silyl cyanide in IRC +10216”, *Astronomy & Astrophysics* **606**, L5 (2017).
- [242] J. J. Keady and S. T. Ridgway, “The IRC +10216 Circumstellar Envelope. III. Infrared Molecular Line Profiles”, *The Astrophysical Journal* **406**, 199 (1993).
- [243] M. Agúndez, J. Cernicharo, and M. Guélin, “New molecules in IRC+10216: confirmation of C₅S and tentative identification of MgCCH, NCCP, and SiH₃CN”, *Astronomy & Astrophysics* **570**, A45 (2014).
- [244] M. Lucas, A. M. Thomas, T. Yang, R. I. Kaiser, A. M. Mebel, D. Hait, and M. Head-Gordon, “Bimolecular Reaction Dynamics in the Phenyl–Silane System: Exploring the Prototype of a Radical Substitution Mechanism”, *The Journal of Physical Chemistry Letters* **9**, 5135–5142 (2018).
- [245] B. A. McGuire, R. A. Loomis, A. M. Burkhardt, K. L. K. Lee, C. N. Shinglededecker, S. B. Charnley, I. R. Cooke, M. A. Cordiner, E. Herbst, S. Kalenskii, et al., “Detection of two interstellar polycyclic aromatic hydrocarbons via spectral matched filtering”, *Science* **371**, 1265–1269 (2021).
- [246] M. McCarthy, A. Apponi, C. Gottlieb, and P. Thaddeus, “Rotational spectra of SiCN, SiNC, and the SiC_nH (n= 2, 4–6) radicals”, *The Journal of Chemical Physics* **115**, 870–877 (2001).
- [247] M. C. McCarthy, M. J. Travers, A. Kovács, C. A. Gottlieb, and P. Thaddeus, “Eight New Carbon Chain Molecules”, *The Astrophysical Journal Supplement Series* **113**, 105 (1997).
- [248] M. C. McCarthy, W. Chen, M. J. Travers, and P. Thaddeus, “Microwave Spectra of 11 Polyne Carbon Chains”, *The Astrophysical Journal Supplement Series* **129**, 611 (2000).
- [249] M. Alliat, D. Donaghy, X. Tu, and J. W. Bradley, “Ionic Species in a Naphthalene Plasma: Understanding Fragmentation Patterns and Growth of PAHs”, *The Journal of Physical Chemistry A* **123**, 2107–2113 (2019).
- [250] X. Gillon and L. Houssiau, “Plasma polymerization chemistry of unsaturated hydrocarbons: neutral species identification by mass spectrometry”, *Plasma Sources Sci. Technol.* **23**, 045010 (2014).
- [251] L. He, W. Shen, and M. Sulkes, “Early chemical intermediates following corona discharge on benzene derivatives: CH addition favored products”, *Chemical Physics Letters* **471**, 210–215 (2009).

- [252] C. S. Contreras and F. Salama, “Laboratory investigations of polycyclic aromatic hydrocarbon formation and destruction in the circumstellar outflows of carbon stars”, *The Astrophysical Journal Supplement Series* **208**, 6 (2013).
- [253] A. K. Lemmens, D. B. Rap, S. Brünken, W. J. Buma, and A. M. Rijs, “Polycyclic aromatic hydrocarbon growth in a benzene discharge explored by IR-UV action spectroscopy”, *Physical Chemistry Chemical Physics* **24**, 14816–14824 (2022).
- [254] D. Loru, C. Cabezas, J. Cernicharo, M. Schnell, and A. L. Steber, “Detection of ethynylbenzene in TMC-1 and the interstellar search for 1,2-diethynylbenzene”, *Astronomy & Astrophysics* **677**, A166 (2023).
- [255] T. Streibel and R. Zimmermann, “Resonance-Enhanced Multiphoton Ionization Mass Spectrometry (REMPI-MS): Applications for Process Analysis”, *Annual Review of Analytical Chemistry* **7**, 361–381 (2014).
- [256] M. K. Kesharwani, B. Brauer, and J. M. L. Martin, “Frequency and Zero-Point Vibrational Energy Scale Factors for Double-Hybrid Density Functionals (and Other Selected Methods): Can Anharmonic Force Fields Be Avoided?”, *The Journal of Physical Chemistry A* **119**, 1701–1714 (2015).
- [257] W. Reusch, “Virtual textbook of organic chemistry”, (1999).
- [258] R. Sanderson, *Chemical bonds and bonds energy*, Vol. 21 (Elsevier, 2012).
- [259] Z. Yang, C. He, S. J. Goettl, D. Paul, R. I. Kaiser, M. X. Silva, and B. R. Galvão, “Gas-phase preparation of silyl cyanide (SiH_3CN) via a radical substitution mechanism”, *Journal of the American Chemical Society* **144**, 8649–8657 (2022).
- [260] R. I. Kaiser, D. S. Parker, and A. M. Mebel, “Reaction dynamics in astrochemistry: low-temperature pathways to polycyclic aromatic hydrocarbons in the interstellar medium”, *Annual Review of Physical Chemistry* **66**, 43–67 (2015).
- [261] G. Sini, G. Ohanessian, P. C. Hiberty, and S. S. Shaik, “Why is SiH_5^- a stable intermediate while CH_5^- is a transition state? A quantitative curve crossing valence bond study”, *Journal of the American Chemical Society* **112**, 1407 (1990).
- [262] T. A. Albright, J. K. Burdett, and M.-H. Whangbo, *Orbital Interactions in Chemistry*, 1st ed. (Wiley, Apr. 2013).

Chapter 10

Appendices

10.1 The missing conformer: A comprehensive rotational spectroscopy study and astronomical search of two conformers of methyl cyanoacetate

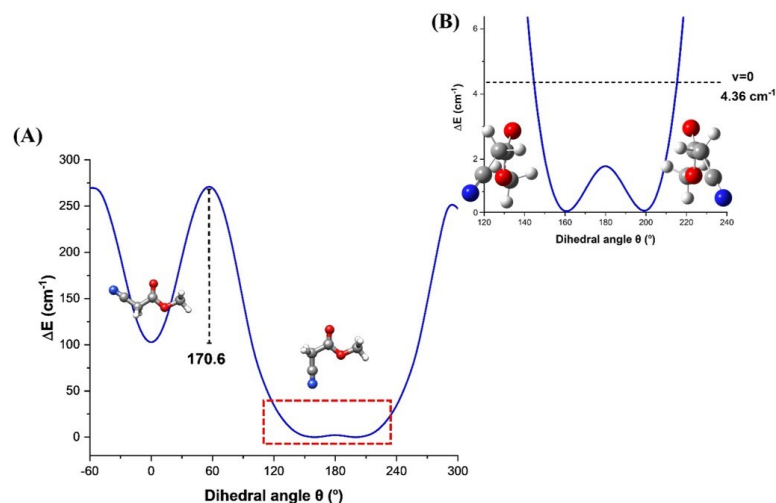


Figure 10.1: (A) One dimensional potential energy scan of the dihedral angle θ , given by NC-CH₂-C=O. The scan was performed at B3LYP-D3/aug-cc-pVTZ level of theory, with the step size of 10°. (B) Zoom-in to show the interconversion barrier between the enantiomeric pair of MCA₁ with respect to the vibronic ground state.

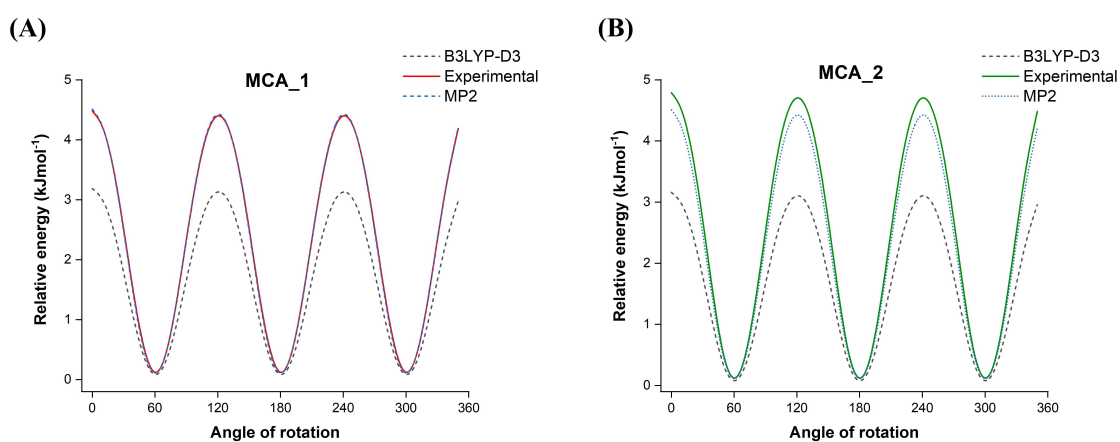


Figure 10.2: One dimensional potential energy scan for the internal rotation of the methyl top in (A) MCA_1 and (B)MCA_2. The scan was performed for dihedral angle ϕ , given by NC-CH₂-C=O, at two different levels of theory: B3LYP-D3/aug-cc-pVTZ and MP2/ aug-cc-pVTZ, with a step size of 10°. The bold line shows the experimentally obtained barrier height and the dashed line shows the theoretically obtained barrier height at two different levels of theory.

Table 10.1: Experimental rotational constants obtained for the parent and the observed isotopologues of MCA_1. Parameters obtained from a fit of the A-state using SPFIT in the 2-26 GHz region.

Rotational parameters	Parent	¹³ C1	¹³ C3	¹³ C5	¹³ C6	¹⁵ N7
A (MHz) ^a	5069.78816(66)	4986.4697(84)	5055.585(53)	5014.768(45)	5069.585(61)	5041.423(35)
B (MHz)	1842.95654(37)	1816.2130(15)	1840.7430(18)	1838.0052(12)	1819.6142(17)	1794.7896(17)
C (MHz)	1383.83241(32)	1362.5285(17)	1381.5191(16)	1377.1700(12)	1370.5870(15)	1354.5013(13)
D _J ^b (KHz)	0.4838(45)	0.4630(77)	0.5060(98)	0.4607(84)	0.444(10)	0.4808(94)
D _{JK} (KHz)	1.220(19)	[1.220]c	[1.220]	[1.220]	[1.220]	[1.220]
D _K (KHz)	4.352(57)	[4.352]	[4.352]	[4.352]	[4.352]	[4.352]
d ₁ (KHz)	-0.1782(30)	0.195(10)	-0.153(10)	-0.1967(96)	-0.160(11)	-0.1355(94)
d ₂ (KHz)	-0.0253(43)	0.0547(87)	[-0.0253]	-0.047(11)	-0.102(15)	[-0.0253]
χ _{aa} ^c (MHz)	-1.1895(44)	-1.103(9)	-1.204(12)	-1.157(11)	-1.173(14)	-
χ _{bb-cc} (MHz)	-2.7592(84)	-2.769(28)	-2.772(35)	-2.774(26)	-3.312(72)	-
No. of lines	320	55	57	66	58	25
σ ^d (kHz)	14.5	11	14.2	12.9	14.3	11.1

^a A, B, and C are the rotational constants

^b D_J, D_{JK}, D_J, d₁, and D₂ are the quartic centrifugal distortion constants.

^c χ_{aa}, χ_{bb}, and χ_{cc} represent the diagonal elements of the ¹⁴N nuclear quadrupole coupling tensor.

^d Microwave root-mean-square deviation of the fit.

Table 10.2: Experimental rotational constants obtained for the parent and the observed isotopologues of MCA_2. Parameters obtained from a fit of the A-state using SPFIT in the 2-26 GHz region.

Rotational parameters	Parent	¹³ C1	¹³ C3	¹³ C5	¹³ C6	¹⁵ N7
A (MHz) ^a	9430.6654(32)b	9427.7533(75)	9431.037(61)	9289.6717(73)	9422.6546(80)	9415.2687(85)
B (MHz)	1413.54814(45)	1384.1964(23)	1412.9177(19)	1411.3114(10)	1397.3314(17)	1377.5203(11)
C (MHz)	1249.84446(41)	1226.7903(15)	1249.3600(16)	1245.6090(10)	1237.0170(11)	1221.3503(10)
D _J ^b (KHz)	0.1457(28)	0.172(13)	0.1424(93)	0.1524(65)	0.1310(84)	0.1509(79)
D _{JK} (KHz)	-0.444(28)	-1.77(36)	[-0.444]	[-0.444]	[-0.444]	[-0.444]
D _K (KHz)	12.69(68)	[12.69]d	[12.69]	[12.69]	[12.69]	[12.69]
d ₁ (KHz)	-0.0187(15)	-0.076(12)	[-0.0187]	[-0.0187]	[-0.0187]	[-0.0187]
d ₂ (KHz)	[-0.001]c	[-0.001]	[-0.001]	[-0.001]	[-0.001]	[-0.001]
χ _{aa} ^c (MHz)	-2.959(7)	-2.953(29)	-3.07(19)	-2.955(64)	-2.848(46)	-
χ _{bb-cc} (MHz)	-1.115(16)	-1.124(60)	-1.56(68)	-1.092(88)	-1.216(76)	-
No. of lines	319	58	50	65	46	22
σ ^d (kHz)	20.3	17.2	21.2	20.5	18.3	17.4

^a A, B, and C are the rotational constants

^b D_J, D_{JK}, D_J, d₁, and D₂ are the quartic centrifugal distortion constants.

^c χ_{aa}, χ_{bb}, and χ_{cc} represent the diagonal elements of the ¹⁴N nuclear quadrupole coupling tensor.

^d Microwave root-mean-square deviation of the fit.

Table 10.3: Molecular bond distances, angles, and dihedral angles for MCA_1 obtained from r_e , r_s , and r_m^1 structures.

Bond distances (Å)	r_e	r_s	r_m^1
C1-O2	1.44	-	1.42(1)
O2-C3	1.33	-	1.33(2)
C3-O4	1.2	-	1.21(2)
C3-C5	1.53	1.50(3)	1.53(2)
C5-C6	1.45	1.41(1)	1.44(2)
C6-N7	1.15	1.20(1)	1.16(2)
Angles (°)	r_e	r_s	r_m^1
C1-O2-C3	115.8	-	[115.8]
O2-C3-O4	125.4	-	126(2)
O2-C3-C5	112.6	-	113.8(7)
C3-C5-C6	116.2	118.23(5)	116.2(9)
C5-C6-N7	178.6	176.79(1)	179(2)
Dihedral angles (°)	r_e	r_s^*	r_m^1
C1-O2-C3-O4	0	-	-
C1-O2-C3-C5	-179.9	-	-
O2-C3-O4-C6	-1	-	-
C3-C5-C6-N7	-174.5	[0]	-
C1-C3-C5-C6	-1	[0]	-
C1-C5-C6-N7	-174.9	[0]	-

* The dihedral angles were calculated to be zero as a result of fixing the atomic coordinate c to zero, due to high uncertainties observed in the calculation of this coordinate.

Table 10.4: Molecular bond distances, angles, and dihedral angles for MCA_1 obtained from r_e , r_s , and r_m^1 structures.

Bond distances (Å)	r_e	r_s	r_m^1
C1-O2	1.44	-	1.45(2)
O2-C3	1.34	-	1.36(3)
C3-O4	1.2	-	1.19(2)
C3-C5	1.52	1.47(2)	1.51(1)
C5-C6	1.45	1.46(2)	1.46(1)
C6-N7	1.15	1.16(1)	1.16(1)
Angles (°)	r_e	r_s	r_m^1
C1-O2-C3	115.4	-	113(1)
O2-C3-O4	125.1	-	[125.1]
O2-C3-C5	109	-	108(1)
C3-C5-C6	113.3	113.71(1)	112.8(9)
C5-C6-N7	178.2	176.3(42)	179(2)
Dihedral angles (°)	r_e	r_s^*	r_m^1
C1-O2-C3-O4	0	-	-
C1-O2-C3-C5	180	-	-
O2-C3-C5-C6	180	-	-
C3-C5-C6-N7	163.3	[180]	-
C1-C3-C5-C6	180	[180]	-
C1-C5-C6-N7	163.3	[180]	-

* The dihedral angles were calculated to be zero as a result of fixing the atomic coordinate c to zero, due to high uncertainties observed in the calculation of this coordinate.

Table 10.5: Single point energy calculations for MCA_1 and MCA_2 at higher levels of theory in comparison to the B3LYP-D3/aug-cc-pVTZ level of theory as indicated in the chapter.

Method	$\Delta E = E(\text{MCA_2}) - E(\text{MCA_1})$
B3LYP-D3/aug-cc-pVTZ	1.4 kJ/mol
RI-MP2/cc-pVTZ	0.4 kJ/mol
DLPNO-CCSD(T)/CBS extrapolation based on aug-cc-pVnZ (n=T,Q) calculations, with TightPNO settings	0.1 kJ/mol

10.2 Rotational spectroscopy of 2,4,6-cycloheptatriene-1-carbonitrile: Facilitating the search for complex cyclic molecules in the ISM

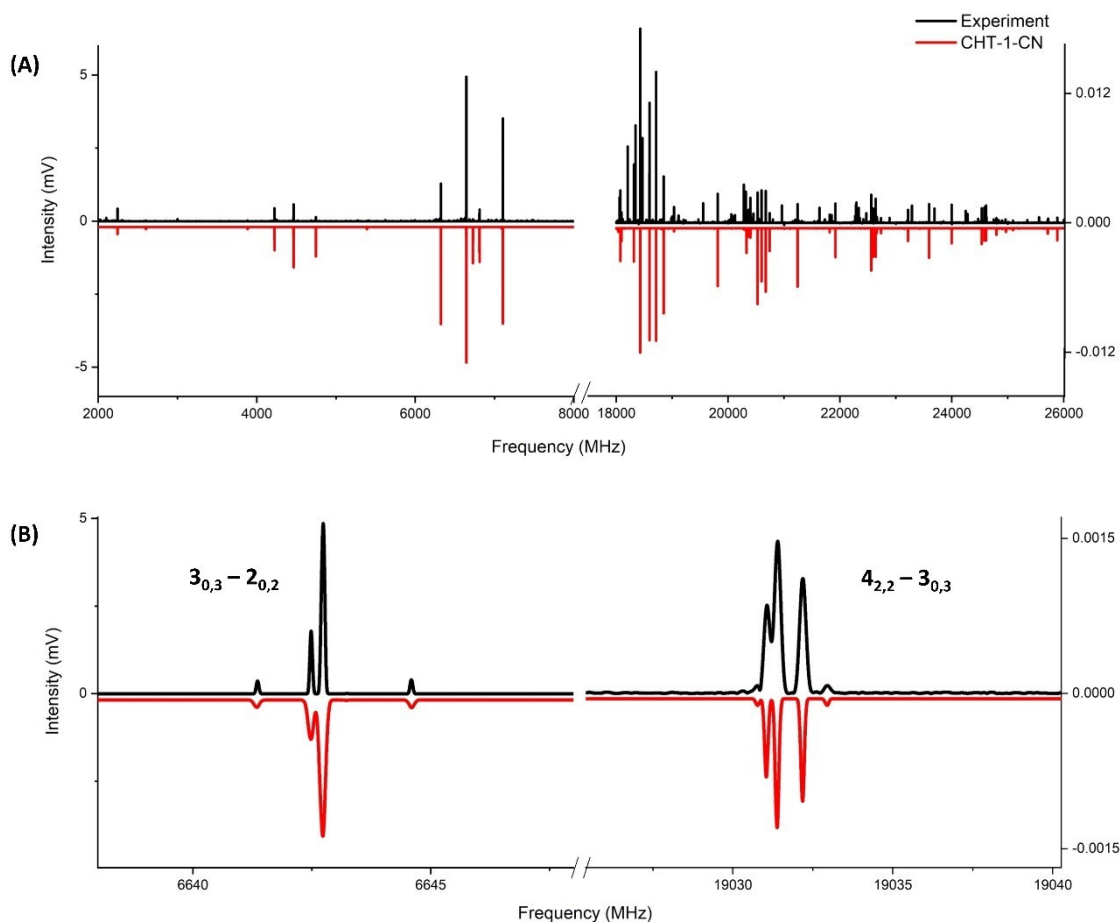


Figure 10.3: Panel (A) shows the rotational spectra of CHT-1-CN in the frequency range of 2-8, 18-26 GHz. The black trace represents the experimental spectra, and the red trace is the simulated spectra based on the fitted rotational constants at 3 K. Panel (B) shows the zoom-in of the rotational transitions ($J_{Ka,Kc} - J'_{Ka',Kc'}$) $3_{0,3} - 2_{0,2}$ and $4_{2,2} - 3_{0,3}$ to highlight the hyperfine splitting observed due to the nuclear quadrupole coupling. To note: the left and right intensity axes correspond to the experiments performed in the different frequency regions.

Table 10.6: The experimental and theoretical rotational constants for the observed six low-lying vibrationally excited states of CHT-1-CN-1. The rotational constants A_{theory} , B_{theory} , and C_{theory} were corrected by 23.37 MHz, -4.14 MHz, and -3.85 MHz, respectively, to account for the differences in the experimental and theoretical rotational constants of the vibronic ground state. E_h and E_a are the harmonic and anharmonic energies of the vibrational states.

Vibrationally excited states of CHT-1-CN-1						
Rotational parameters	ν_{42}	ν_{41}	$2\nu_{42}$	$\nu_{42} + \nu_{41}$	ν_{40}	ν_{38}
E_h / cm^{-1}	110.2	149.4	220.4	259.9	271.3	320.4
E_a / cm^{-1}	110.4	145.8	219.9	255.4	269.8	318.3
$A_{theory}^a / \text{MHz}$	3513.36	3565.02	3488.57	3540.26	3543.4	3537.92
B_{theory} / MHz	1251.37	1253.11	1251.34	1253.08	1251.25	1251.97
C_{theory} / MHz	990.65	991.04	990.68	991.07	990.14	990.26
A / MHz	3511.3491(46)	3565.8196(44)	3490.087(64)	3540.123(25)	3540.123(25)	3481.56(80)
B / MHz	1251.32759(32)	1253.25308(43)	1250.9389(69)	1251.7762(26)	1251.7762(26)	1249.437(85)
C / MHz	990.57016(28)	991.31445(24)	990.50584(42)	990.21198(40)	990.21198(40)	990.41961(25)
Δ_J^b / kHz	0.055728(49)	0.056761(74)	0.056988(89)	0.055413(90)	0.055413(90)	0.058143(51)
Δ_{JK} / kHz	0.15257(23)	0.2491(11)	0.123(16)	0.384(18)	0.384(18)	[0.20088039]
Δ_K / kHz	[0.83]	[0.83]	[0.83]	[0.83]	[0.83]	[0.766306647]
δ_J / kHz	-0.006529(36)	-0.007072(45)	[-0.006736]	[-0.006736]	[-0.006736]	[0.006736]
δ_K / kHz	-0.2151(13)	-0.3439(14)	-0.2002(84)	-0.3828(94)	-0.3828(94)	[0.277093198]
σ^c / kHz	92	120	112	100	150	76
No. of lines	714	361	123	107	63	96
J/K_a^d	54/31	54/13	54/6	54/6	47/4	44/3

^a A, B, and C are the rotational constants.

^b Δ_J , Δ_{JK} , Δ_K , δ_J , and δ_K are the quartic centrifugal distortion constants.

^c Microwave root-mean-square deviation of the fit.

^d Maximum values of J and K_a assigned in the fit.

Table 10.7: Experimental rotational constants obtained for the parent and the observed isotopologues of CHT-1-CN-1. Parameters are obtained by using SPFIT program for the 2-26 GHz region.

Rotational parameters	$^{13}\text{C1}$	$^{13}\text{C2}$	$^{13}\text{C3}$	$^{13}\text{C4}$	$^{13}\text{C8}$	$^{15}\text{N7}$
A^a/MHz	3536.684(45)	3497.122(23)	3480.336(25)	3523.275(27)	3536.827(64)	3537.177(34)
$B (\text{MHz})$	1249.65504(70)	1250.77571(70)	1247.06586(48)	1237.20758(55)	1236.6123(12)	1217.87199(73)
$C (\text{MHz})$	989.65546(53)	987.70952(45)	983.63065(36)	981.12660(47)	981.4223(12)	969.55357(64)
Δ_J^b/kHz	[0.055512]	[0.055512]	[0.055512]	[0.055512]	[0.055512]	[0.055512]
Δ_{JK}/kHz	[0.20096]	[0.20096]	[0.20096]	[0.20096]	[0.20096]	[0.20096]
Δ_K/kHz	[0.83]	[0.83]	[0.83]	[0.83]	[0.83]	[0.83]
δ_J/kHz	[-0.0067]	[-0.0067]	[-0.0067]	[-0.0067]	[-0.0067]	[-0.0067]
δ_K/kHz	[-0.27771]	[-0.27771]	[-0.27771]	[-0.27771]	[-0.27771]	[-0.27771]
χ_{aa}^c/MHz	-4.245(14)	-4.242(14)	-4.241(10)	-4.241(13)	-4.234(22)	-
χ_{bb-cc}/MHz	[0.00772]	[0.00772]	[0.00772]	[0.00772]	[0.00772]	-

^a A, B, and C are the rotational constants

^b Δ_J , Δ_{JK} , Δ_K , δ_J , and δ_K are the quartic centrifugal distortion constants.

^c χ_{aa} , χ_{bb} , and χ_{cc} represent the diagonal elements of the ^{14}N nuclear quadrupole coupling tensor.

10.3 Insights into the gas phase structure and rotational dynamics of diphenylsilane: A broadband rotational spectroscopy study

Table 10.8: The relevant bond lengths, bond angles, and dihedral angles for the gas phase structure of diphenylsilane. The structural parameters were calculated using the r_g method.

Bond lengths (Å)	
C1-C2	1.389 (2)
C2-C3	1.407 (8)
C3-C4	1.397 (34)
C4-C5	1.385 (22)
C5-C6	1.443 (10)
C6-Si	1.856 (10)
Bond angles (°)	
C1-C6-C5	117.1(2)
Si-C6-C5	120.7(7)
C6-Si-C6'	109.6(2)
Dihedral angle (°)	
C6'-Si-C6-C1	47(2)

Table 10.9: Experimental rotational constants obtained for the observed isotopologues of diphenylsilane. Parameters are obtained by using SPFIT program for the 2-8 GHz region.

Rotational parameters	²⁹ Si	³⁰ Si	¹³ C1	¹³ C2	¹³ C3	¹³ C4	¹³ C5	¹³ C6
A^a/MHz	1689.10071(27)	1675.61231(31)	1696.33488(53)	1686.74297(35)	1696.23332(43)	1700.45898(44)	1696.2776(11)	1701.53655(70)
B/MHz	366.70091(19)	366.70388(21)	365.81859(32)	364.475180(21)	362.78387(25)	362.76939(36)	364.70283(50)	366.08671(36)
C/MHz	335.27005(13)	334.74088(14)	335.14622(19)	333.688440(17)	332.27089(19)	332.60598(19)	334.10348(46)	335.24340(26)
Δ_J^b/kHz	[0.035078254]	[0.035078254]	[0.035078254]	[0.035078254]	[0.035078254]	[0.035078254]	[0.035078254]	[0.035078254]
Δ_{JK}/kHz	[0.209956496]	[0.209956496]	[0.209956496]	[0.209956496]	[0.209956496]	[0.209956496]	[0.209956496]	[0.209956496]
Δ_K/kHz	[1.680165342]	[1.680165342]	[1.680165342]	[1.680165342]	[1.680165342]	[1.680165342]	[1.680165342]	[1.680165342]
σ^c/kHz	5	5	5	5	6	6	5	8
No. of lines	40	31	20	28	25	24	25	25

^a A, B, and C are the rotational constants.

^b Δ_J, Δ_{JK}, Δ_K are the quartic centrifugal distortion constants.

^c Microwave root-mean-square deviation of the fit.

10.4 Infrared reflection absorption spectroscopy of water ice and naphthalene

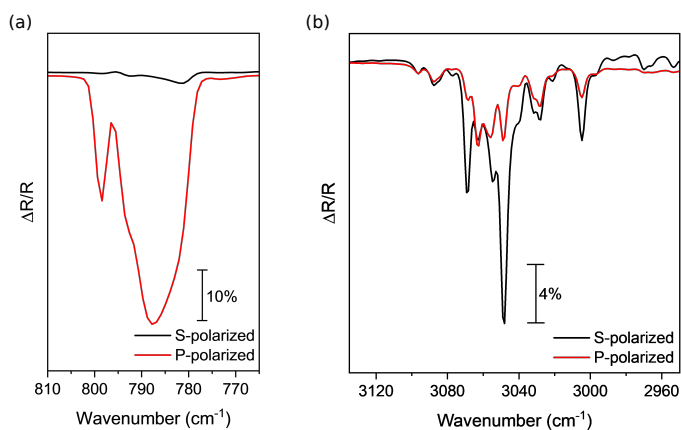


Figure 10.4: IRRAS spectra of 130 L naphthalene on the clean Ir(111) surface, measured with s- and p-polarized IR light. Panel (a) and (b) display the regions corresponding to the out-of-plane C-H wagging motion (788 cm^{-1}) and in-plane C-H stretching modes, respectively.

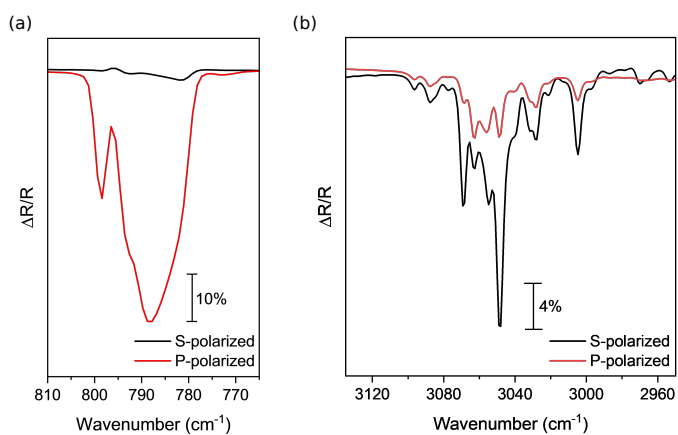


Figure 10.5: IRRAS spectra of 130 L naphthalene on the H_2O ice surface, which was prepared with 130 L H_2O on the clean Ir(111) surface, measured with s- and p-polarized IR light. Panel (a) and (b) display the regions corresponding to the out-of-plane C-H wagging motion (788 cm^{-1}) and in-plane C-H stretching modes, respectively.

Acknowledgements

Everyone has to go through some good and some tough times in their life. In my case, I feel incredibly fortunate to be able to do that with the most amazing friends and colleagues, who accepted and loved me for who I am. I would like to extend my thanks to all of you, this journey would not have been possible without you.

I would like to express my gratitude to all of my teachers, with special acknowledgments to Dr. Manisha Jain, Prof. Dr. Chayan Kanti Nandi, Dr. Aditi Halder, Dr. Amit Jaiswal, Dr. Vishwanath, and Dr. Syamantak Khan. Their dedication to science and their encouragement have inspired me to pursue a Ph.D.

I am particularly grateful to my Ph.D. supervisor, Prof. Dr. Melanie Schnell. I extend my sincere appreciation for pushing me when I was demotivated and for calming me when I was extremely excited. For all the professional and personal discussions that got me through some of the toughest times. For being the best boss ever, for always being open to new ideas. I am truly thankful for your guidance.

I extend my heartfelt thanks to my close friends: Shweta, Anika, GK, Shivani, Neeraj, and Sakshi – it's almost been ten years since we have been friends and not a single day has gone by when I haven't cherished my friendship with you. Despite meeting almost once in a year, our friendship picks up right where we left off. I want to give a special shout-out to Vishwajeet, Sai Sandeep, and Mehul. Meeting you guys during the sports meet was one of the best things that happened to me, and I'm incredibly grateful for our friendship. Whether continents apart or dealing with challenging time zones, you've consistently been there for me. I've always known I can count on your support, regardless of the situation. Thank you for the abundant love, motivation, and encouragement. A part of me still believes in the extremely slim chance of all of us living in the same neighbourhood when we grow old :P

I want to express my gratitude to my master's research group led by Prof. Dr. Chayan Kanti Nandi. Being part of this group taught me the dedication required for research and the spirit of working together as a team. Special thanks to Dr. Syamantak Khan, Dr. Aditya Yadav, Dr. Chethna Rao, and Dr. Navneet Sharma, for always being ready to engage in discussions and collaborative research efforts.

This leads me to my current research group, FS-SMP and the friendships that I've cultivated in Hamburg during my Ph.D. under the guidance of Prof. Dr. Melanie

Schnell. I will start with saying thanks to Amanda for your guidance during the initial stages of my Ph.D.

I extend my sincere thanks to Ben, who stands out as one of the most exceptional teachers. You have made me a better researcher. The time I spent working with you was the time when not only I learnt about science but also the passion it demands to be in science. Thanks for being my mentor! To dearest Pablo, Teresa, Pragya, Diksha, and Maider- Thanks for being my family here, away from home. Despite some of you moving to different countries, I hope we can continue to be a family for each other. To Pablo and Dona, I learnt a lot from you including how to be always being ready to lend a helping hand, be it experiments, analysis, or by just being there when someone needs you. Thanks a lot.

Dear Pragya, I have been fortunate enough to have lived with you, fought with you, and then laughed with you. I feel blessed to know that I can reach out to you at any time, and you will always be there for me. Thanks for being there. To my awesome officemates, Dona, Eva, Christina, and Comet (our office dog): Thank you for transforming the office into a fantastic space where we can spend our days working, laughing, engaging in scientific discussions, and, of course, me sharing those obligatory hugs. Thanks, Eva, for bringing Comet in my life, I never anticipated falling so deeply in love with Comet. And, Comet, thank you for being a constant source of motivation as you stay behind my desk, encouraging me to keep working and only taking breaks for cuddles. To Lars, who started as a office neighbour and became an amazing friend in no time. A shout-out to our enduring friendship, forged through thick and thin, numerous sportspaß training sessions, countless coffee dates, and to plans of buying a house in Goa. I want to extend my gratitude to Denis for endless supply of chocolates and wisdom, to Laura, Swantje, and Freya for sharing the same level of crazy. To Maureen for always taking care of all the admin jobs. To Sonu, for always being ready to go out for Indian food. To Himanshi, Wenhao, and Fan it for wonderful working and/or hanging out times together. To Isak, for being a great flatmate and for sharing science ideas in the middle of the night.

A special thanks to Holger, for helping me navigate through all the crazy times (good or bad) and for being a great friend. A big thanks to all my past group members for sharing the wonderful time together working, learning, and going to Christmas markets together: Maria, Sergio, Amanda, Cristobal, Alcides, Jason, and Dan.

Dear Loris, thanks for being the calming presence in my life over the last six months, for giving me company with pulling long hours in the library and for showing me what it means to be there for someone, no matter the circumstances. I can never thank you enough!

Most importantly, I would like to express my gratitude and love to my mother, Mrs. Anupam Batra for making me the woman I am today, for being my strength when I

am down and for being my biggest cheerleader always. I am forever grateful to you. To my amazing siblings, Swati and Tejasavi and to my uncle, Dr. Deepak Batra for giving me the best memories of my childhood and for always having my back. To my paternal grandparents, I miss you. I wish I could have shown you my thesis and see you feel proud.

Declaration

I, Gayatri Batra, hereby declare under oath that apart from the advice of Prof. Dr. Melanie Schnell, the content and design of the thesis is all my own work. I have duly acknowledged all the sources of information which have been used in this thesis.

This work has not been submitted either partially or wholly as part of a doctoral degree to another examining body. The complete work has neither been published nor has it been submitted for publication.

A part of this work has been submitted for publication in academic journals. This relates to Chapter 4 "The missing conformer: A comprehensive rotational spectroscopy study and astronomical search of two conformers of methyl cyanoacetate":

G. Batra, P. Pinacho, A. L. Steber, V. M. Rivilla, J. M. Pintado, I. J. Serra, M. Schnell *The missing conformer: A comprehensive rotational spectroscopy study and astronomical search of two conformers of methyl cyanoacetate*, *Frontiers in Astronomy and Space Sciences*, **9**, 977488 (2022).

Chapter 8 is based on experiments performed during a FELIX beamtime in Nijmegen, the Netherlands (August 2022), project titled, *Exploring the formation of silicon-containing PAH-like molecules under plasma conditions*. This project is a collaboration between G. Batra, D. Loru, A. K. Lemmens, P. Ferrari, B. Redlich, and M. Schnell.

This work is in compliance with the Rules of Good Scientific Practice of the German Research Foundation.

No academic degree of mine has ever been withdrawn.

Gayatri Batra

15-12-2023

Hamburg, Germany